Durham E-Theses

Growth and Defect Formation in Graphene

WELLS, GEORGE,HENRY

Growth and Defect Formation in Graphene

George H. Wells

A thesis submitted in partial fulfilment of the requirements for the
degree of
Doctor of Philosophy

Supervised by Dr Michael R. C. Hunt
Department of Physics
University of Durham
UK
March 2016

Growth and the Formation of Defects in Graphene

George Henry Wells

Abstract

In this work, few-layer graphene (FLG) was grown from SiC(0001) with temperature, growth time and cooling rate as variables. Samples were characterised by Scanning Tunnelling Microscopy (STM), Low Energy Electron Diffraction (LEED), Auger Electron Spectroscopy (AES) and Raman Spectroscopy (RS) to determine graphene quality. The information obtained from these techniques was then used to determine optimal conditions for growing graphene from SiC(0001). Contamination on graphene films is also discussed and a facile method for the removal of large scale metal contaminant layers from the surface is described.

To study adhesion of FLG to a substrate, a continuum energy model was developed to obtain the adhesion energy via the measurement of pleat defects by STM. This model was applied to graphene grown from SiC(0001) and its adhesion energy was found to be significantly larger than the those measured for graphene on other substrates. Variation of pleat defects on graphene grown from SiC(0001) with different growth parameters was also studied by STM. The factors that affect the dimensions and concentration of pleats were determined and discussed in relation to the quality of the film. Further investigation was conducted on the stability of pleat defects under STM imaging, with the presence of contamination and defects found to have a significant effect in reducing the dragging of pleats by the probe tip.

A comparative study of the dynamics of extrinsic defects on FLG and graphite is also presented in this work. Samples were bombarded with 0.2 keV Ar^+ ions, heated to different temperatures and studied with STM. The concentration, mobility, agglomeration and alignment of defects was examined and mechanisms suggested for the behaviour observed. The Local Density of States (LDOS) at defect sites of both graphite and FLG were studied by Scanning Tunnelling Spectroscopy (STS) to determine if significant differences in electronic structure due to defects were observed between the two systems.

Preliminary experiments to optimise the growth of graphene on Cu substrates by "hot-wall" and "cold-wall" methods have been performed, to determine whether cold-wall growth presents a viable alternative to hot-wall for the production of high quality graphene. Graphene was grown by both methods using different growth periods to determine the optimal growth time for each method. The use of evaporated Cu on SiO_2 as growth substrates is also discussed. Samples produced by both methods were studied by Scanning Electron Microscopy (SEM) to determine their quality. Electron Back-Scatter Diffraction (EBSD) measurements were also performed on samples produced by both methods to determine the extent to which Cu grain orientation affects the growth of graphene.

Contents

List of Figures

Declaration

No part of this thesis has been submitted elsewhere for any other degree or qualification. The content of this thesis is the author's own work, unless otherwise stated in the text. All measurements and analysis were carried out by the author, with the exception of the following measurements: Chapter 4 RS measurements were taken by Dr Enrique Escobedo-Cousin in the School of Electrical and Electronic Engineering, Newcastle University. This data is presented in Figures 4.7 and 4.9. AFM images in Chapter 4 were obtained by Dr Toby Hopf also at the School of Electrical and Electronic Engineering, Newcastle University, these can be found in Fig. 4.4(d) and 4.13(a). The Raman spectrum used in Chapter 6 was obtained by Dr Michael Hunt at Durham University, this can be found in Fig. 6.9.

Publications

- **G. H. Wells**, T. Hopf, K. V. Vassilevski and E. Escobedo-Cousin, N. G. Wright, A. B. Horsfall, J. P. Goss, A. G. O'Neill and M. R. C. Hunt. "Determination of the adhesion energy of graphene on SiC(0001) via measurement of pleat defects". *Appl. Phys. Lett.*, **105**(19), 193109 (2014).

- **G. H. Wells**, T. Hopf, K. V. Vassilevski and E. Escobedo-Cousin, A. B. Horsfall, J. P. Goss, A. G. O'Neill and M. R. C. Hunt. "Facile technique for the removal of metal contamination from graphene". *J. Vac. Sci. Technol. B*, **33**(5), 051802 (2015).

- T. Hopf, K. V. Vassilevski and E. Escobedo-Cousin, P. J. King, N. G. Wright, A. G. O'Neill, A. B. Horsfall, J. P. Goss, **G. H. Wells** and M. R. C. Hunt. "Dirac point and transconductance of top-gated graphene field-effect transistors operating at elevated temperature". *J. Appl. Phys.*, **116**(15), 154504 (2014).

- T. Hopf, K. V. Vassilevski and E. Escobedo-Cousin, N. G. Wright, A. G. O'Neill, A. B. Horsfall, J. P. Goss, A. Barlow, **G. H. Wells** and M. R. C. Hunt. "Optimizing the vacuum growth of epitaxial graphene on 6H-SiC". *Mater. Sci. Forum*, **778-780**, 1154-1157 (2014).

- T. Hopf, K. V. Vassilevski and E. Escobedo-Cousin, P. J. King, N. G. Wright, A. G. O'Neill, A. B. Horsfall, J. P. Goss, **G. H. Wells** and M. R. C. Hunt. "Electrical Characterisation of epitaxial graphene field-effect transistors with high-κ Al_2O_3 gate dielectric fabricated on SiC substrates". *Mater. Sci. Forum*, **812-823**, 937-940 (2015).

Acknowledgments

This thesis is the culmination of three and a half years of hard work. However, it would not have been possible without the help of many people, whom particular thanks should be extended to:

Dr Michael Hunt for his supervision throughout the PhD, the opportunity to study here at Durham University and his initial trust in me, despite my lack of experience.

Dr Toby Hopf and Dr Konstantin Vassilevski at Newcastle University whose collaboration helped yield such excellent results.

The technical staff in the Department of Physics, Durham University, who were always at hand to help fix the systems that invariably broke.

My house mates Rob and Rich, whose support and understanding was always a comfort.

Bill and Ashley, for dragging me to the pub to let off steam when I needed it the most.

My friends, both in the Physics Department and in University College, who were always happy to help distract me from my work.

Fiona for her constant support, despite my regular moaning, and helping me to escape Durham regularly and put everything into perspective.

Finally, my parents, Gillian and Alan, whom without their support from a young age I would never have made it this far.

Nature doesn't owe you an explanation. - Anon.

Chapter 1

Introduction

This chapter provides an introduction to both isolated and epitaxially grown graphene and their electronic and mechanical properties. The different graphene production methods of mechanical exfoliation, Chemical Vapour Deposition (CVD) and thermal decomposition of SiC are outlined. Defects in carbon nanostructures are discussed along with their effects on the properties of graphene. Current and potential applications of graphene are also briefly discussed to provide the motivation of the work carried out herein.

1.1 Graphene: Introduction

Carbon nanostructures have been the subject of significant research since the discovery of the truncated icosahedral fullerene molecule, C_{60}, in 1985 [1]. This was followed some years later by the discovery and isolation of carbon nanotubes, extended fullerenes one or two layers thick which can extend up to many cm in length [2]. Each of these areas has led to the proposition of new technologies at the nanoscale [3, 4]. However, despite the large amount of research and potential applications, the conceptual building block of these nanostructures was not isolated until many years later when Novoselov and Geim produced the first atomically thin carbon layers [5]. The isolation of stable carbon films was somewhat surprising due to early experimental and theoretical work arguing that two-dimensional crystals would be thermodynamically unstable, due to the significance of thermal fluctuations at low thicknesses [3, 6]. However, the combination of strong intermolecular bonding and small vertical rippling allows this issue to be overcome [7, 8]. Since this discovery, graphene based research has developed into a large field with many potential technological applications, some of which are discussed below.

1.2 Properties of Isolated Graphene
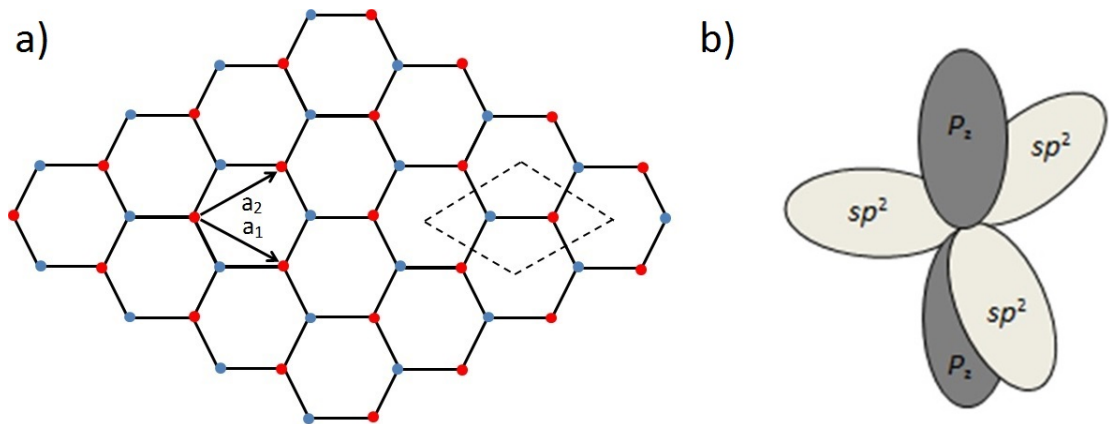
Figure 1.1: (a) Hexagonal atomic structure of the pristine heaxgonal graphene lattice. Atoms in each triangular sublattice are shown as red or blue circles. The graphene primitive unit cell is outlined by the dotted line and the two primitive vectors are shown as arrows. (b) Arrangement of the sp^2-hybridised orbitals in graphene; $2p_z$ orbitals are oriented perpendicular to the sheet surface.

Figure 1.1(a) shows the honeycomb lattice of carbon atoms which make up the 2D monolayer graphene sheet. The sheet consists purely of carbon atoms arranged

in a sixfold symmetric structure with a bond length of 0.142 nm. Although the carbon atoms are located at the vertices of interlocking hexagons, the lattice in fact is comprised of two intersecting triangular sub-lattices. These two sub lattices are outlined in Fig. 1.1(a) by red and blue atoms. Consequently, the graphene unit cell contains two atoms, one from each sub-lattice with unit cell vectors a_1 and a_2 between atoms within the same sub-lattice. The origin of the hexagonal atomic arrangement can be understood by considering the bonding between atoms. The carbon atomic $2s$ orbitals mix with two of the $2p$ orbitals to form three sp^2 hybridised orbitals arranged at $120°$ in plane. Upon overlap of sp^2 orbitals on neighbouring atoms strong localised σ bonds are formed. These strong covalent bonds directly result in graphene exhibiting the highest intrinsic strength of any material ever measured. This was demonstrated by Lee *et al.* via nanoindentation using an atomic force microscope (AFM), in which an intrinsic breaking strength of 42 Nm^{-1} was determined [9].

Although the excellent mechanical properties of graphene arise from the in plane σ bonding, the electronic conductivity arises from spatially de-localised π bonds, which arise from the overlap of unhybridised p_z orbitals on neighbouring atoms (Fig. 1.1(b)). These bonds, at T = 0, form a completely filled π band and a completely empty π^* band derived from anti-bonding states. With the complete filling of the π (valence) band and a completely empty π^* (conduction) band, graphene acts as a zero-bandgap semiconductor [10]. The sp^2 hybridised states form both occupied (and empty) bands in the graphene band structure well above (below) E_F, however the π/π^* states produce bands which touch at the K and K$'$ points, located at the corners of the first Brillouin zone, these points are known as Dirac points (Fig. 1.2(a)) [11, 12]. First discussed by Wallace, these crossing points are a direct result of the two triangular sublattices, whose structure is reflected in the graphene reciprocal lattice [13]. As such, in the nearest neighbour approximation, the hopping of electrons and holes occurs purely between the two lattices, with Dirac cones produced at the high symmetry points of the reciprocal lattice (Fig. 1.2(b) and (c)). These Dirac cones are of significant interest as they display a linear electronic dispersion close to the Fermi level, causing electrons to exhibit zero effective mass in this region. The linear dispersion results in holes and electrons no longer resembling the charge carriers observed in typical semiconductors, but instead they behave as relativistic quasi-particles and hence follow the Dirac equation for relativistic particles [14]. As a result of this unique band structure, graphene can exhibit phenomena not observable within typical solids, such as Berry's phase and the half-integer quantum hall effect [15, 16].
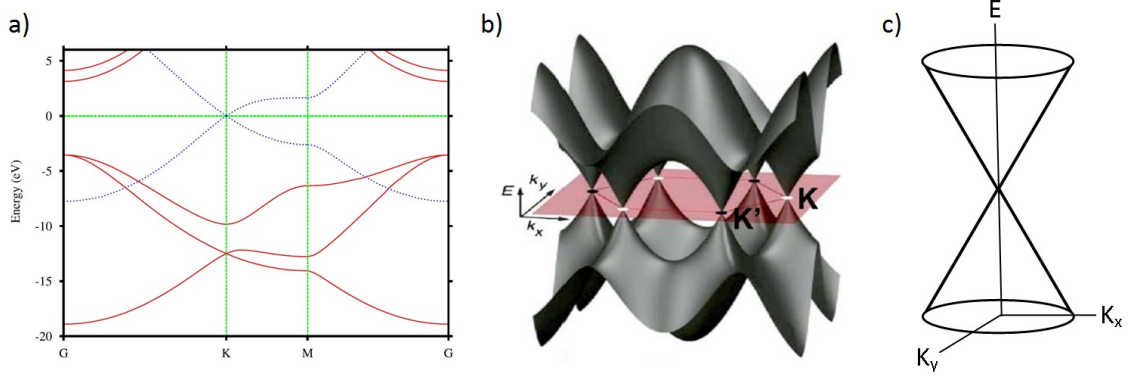
Figure 1.2: (a) The graphene bandstructure showing both σ (red) and π bands (blue), including the Dirac point at E = 0 eV [11]. (b) 3D representation of the graphene electronic energy spectrum [17]. (c) Schematic of a region close to the E_F of the Dirac cone at K, showing linear dispersion.

As a further consequence of the two sublattices, the distribution of electrons across the two sublattices can be described by pseudospin. The pseudospin is oriented parallel to the direction of motion for electrons and anti-parallel for holes, resulting in chiral and helical states respectively [14]. The requirement for the conservation of pseudospin prevents electron scattering from the K to K′ point in reciprocal space, resulting in ballistic transport over very large distances due to minimal scattering [18]. Due to the confinement of charge carriers within the plane of the sheet, charge carriers behave as a two-dimensional electron gas (2DEG), in which electrons/holes are free to move throughout the plane, whilst simultaneously motion is prevented in the third dimension. This confinement, combined with minimal scattering results in extremely high carrier mobilities (200,000 $cm^2V^{-1}s^{-1}$), which are of significant interest for electronic applications [19, 20].

Although the main focus of research is on the mechanical and electronic properties of graphene, significant work has also been conducted into its chemical, thermal and optical behaviour. Graphene, while derived from graphite in structure, does not share the latter's chemical inertness. An example of this is seen by the study by Elias *et al.* in which hydrogenation of graphene flakes led to a transition from a zero-bandgap semiconductor to an insulator [21]. Furthermore, increased chemical reactivity can be observed at graphene edges due to the presence of dangling bonds, which provide a further avenue to chemical engineering [22]. In particular, Wang *et al.* were able to *n*-dope graphene nano-ribbons via high temperature annealing in the presence of ammonia, resulting in carbon-nitrogen bonding [2]. However, despite this reactivity at edges and electronic structure manipulation via hydrogenation, graphene can also show a large degree of impermeability. Graphene layers have

been shown to be impermeable to inert gases, which, when combined with its high intrinsic strength, makes graphene ideal as an atomic membrane for gas storage and separation [23]. While the chemical properties of graphene are of significant interest, they are also combined with excellent thermal conductivity ($(4.84\pm0.44)\times10^3$ to $(5.3\pm0.48)\times10^3$ Wm^{-1}K^{-1}), higher even than carbon nanotubes [24, 25], which arises from the exceptionally high crystal quality, ensuring that the only limiting factor on thermal conductivity is scattering from acoustic phonons. Furthermore, due to the small opacity ($2.3\pm0.1\%$) of monolayer graphene (MLG), potential applications in transparent electronics are also possible [26, 27].
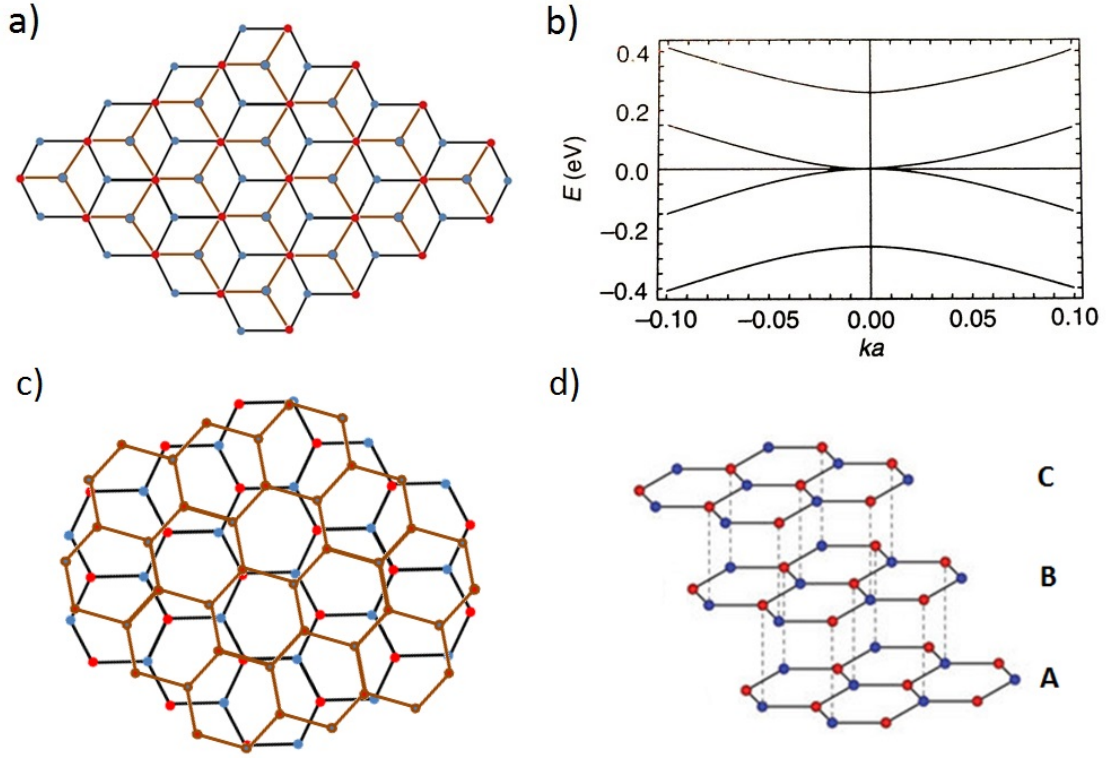
Figure 1.3: (a) Bernal stacking structure of bi-layer graphene; the upper layer is shown in orange, with the lower layer shown in black. Atoms on lattice site A are marked in red, whilst atoms on lattice site B are blue. (b) DOS of bi-layer graphene [12]. (c) Turbostratically stacked bilayer graphene; the upper layer is shown in orange rotated randomly with respect to the lower black layer. (d) Rhombohedrally stacked tri-layer graphene.

Although MLG has received particular attention due to its "true" 2D structure, Bi-layer (BLG) and few layer (FLG) graphene have also seen significant interest, as they share many properties with MLG, whilst also presenting a number of unique properties. Figure 1.3(a) shows the BLG crystal structure, in which a second graphene layer sits, with a sheet separation of 3.35 Å, above the first, at a $60°$ angle, resulting in the atoms in sublattice A sitting above their sublattice A

counterparts in the lower layer, whilst the atoms in sublattice B sit directly above the centre of a hexagon in the first graphene sheet. This particular structuring is known as Bernal stacking and is the most common form of stacking in graphite since it requires the least energy to form [28]. As a result of the positioning of these atoms, hopping can now occur between the atoms in each layer, but only between the atoms in sublattice A [12], leading to significant variation in electronic properties, though many properties such as high intrinsic carrier mobilities remain due to the very low electron-phonon scattering [20, 29, 30]. The electronic structure of BLG, produced from a simple nearest neighbour hopping model, is shown in figure 1.3(b) [12]. There is a parabolic, rather than linear dispersion close to the Fermi level, though the zero-bandgap semiconducting behaviour is retained. Interestingly, a bandgap can be induced by the perpendicular application of a bias potential, which is not possible in MLG. The potential breaks the equivalence symmetry of the sublattices causing a bandgap to open [30]. The magnitude of the bandgap is proportional to the magnitude of the applied potential and therefore provides an excellent route towards graphene based digital electronics [31, 32].

Although Bernal stacked BLG is often observed due to its energetically favourable structure, other forms of stacking have also been observed. In turbostratically stacked BLG the basal planes slip out of alignment resulting in atoms of both sublattices in the upper layer having no specific sites in which they sit above the lower graphene layer (Fig. 1.3(c)). In contrast to Bernal stacked BLG this lack of alignment results in the graphene layers acting as isolated single sheets, due to its decoupling of the electronic states of adjacent layers [33, 34]. Further differences in electronic properties are observed in the case of rhombohedrally stacked tri-layer graphene (TLG) (Fig. 1.3(d)), where one sublattice of the uppermost layer sits above the centre of hexagons in the bottom layer [35]. This in turn results in a tunable semi-conducting bandstructure, indicating that even small changes in the ordering of graphene layers result in significant variance in graphene properties.

1.3   Graphene Production Methods

As a result of the many exceptional properties graphene exhibits, the production of graphene, both for research and industrial purposes, has also been a focus of intense interest [3, 36–38]. The first successful isolation of monolayer graphene was performed by Geim and Novoselov in 2004 [5]. Their method consisted of applying

adhesive tape to the surface of a slab of highly oriented pyrolytic graphite (HOPG) and removing the upper most layers when peeling away, known as mechanical exfoliation. Repetition of this process on the exfoliated layers, allows for the production of single atomic layer flakes up to 20 μm in lateral size, whilst flakes 100 μm in size are possible for 2-3 layer flakes. One of the many advantages of graphene produced via this method is the extremely high crystal quality [18]. Although producing the best quality graphene, mechanical exfoliation suffers from limitations in potential for scaling, a critical issue when considering the use of graphene for technological purposes on an industrial scale. Furthermore, the size of crystals is intrinsically limited to a few 100 μm due to the damage caused by the exfoliation process. Therefore, increasing graphene production up to full sheets of the order of centimetre linear dimensions becomes impossible.
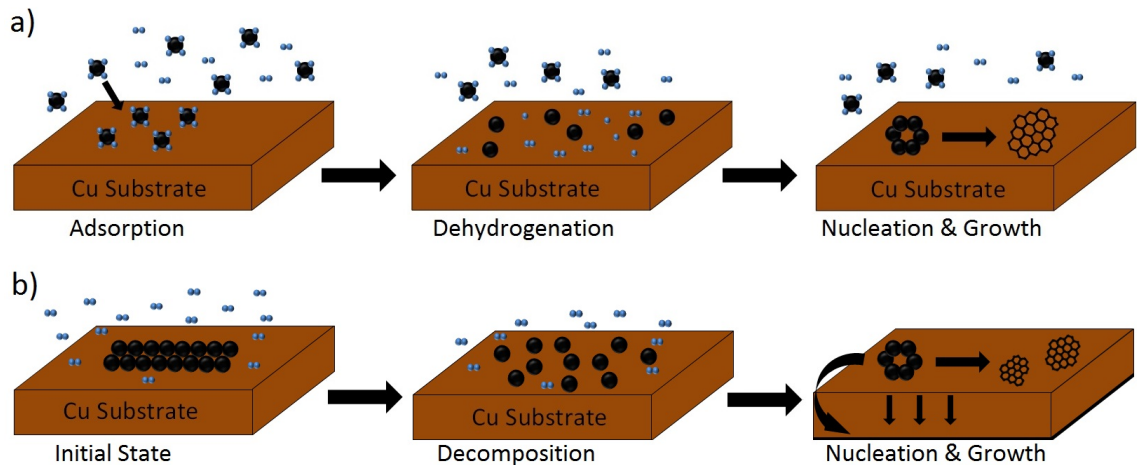
Figure 1.4: (a) CVD growth of graphene on Cu. A Cu substrate is heated in the presence of hydrogen (blue) and a carbon (black) based gas such as methane. The carbon containing gas dehydrogenates at the hot Cu surface. During cooling carbon reorganises on the surface to form graphene. (b) Graphene growth from solid carbon precursors. Solid carbon sources heated in the presence of hydrogen decompose on the Cu substrate. Nucleation of carbon atoms occurs on both sides of the Cu foil, as a small amount of carbon diffuses through the substrate forming graphene layers.

As a result of the limitations presented by mechanical exfoliation, alternatives have been developed, which have better potential to be scaled to industrial production. A method that has shown particular promise in this endeavour is the growth of graphene on metals via chemical vapour deposition (CVD). CVD methods employ a metal substrate, which is cleaned and then annealed in the presence of hydrogen and a carbon containing precursor gas, such as methane (CH_4). The precursor gas decomposes upon coming into contact with the hot substrate surface and typically carbon diffuses into the metal. Upon cooling, the carbon atoms that have diffused

into the substrate diffuse out to the surface forming graphene layers, this full process can be seen schematically in figure 1.4(a). CVD growth has been successfully performed on many different metal substrates including Pt [39], Ni [40] and Ir [41], however the majority of growth has been performed on Cu substrates [37, 42–44]. Cu of all metal substrates has shown the most promise in producing high quality graphene, as its very low carbon solubility causes carbon atoms to remain on the surface ensuring a self-limiting growth that results in the formation of high quality graphene of purely monolayer thickness [37]. Combined with the ease at which this method can be scaled up to industrial levels, the CVD method has been the subject of intense research to optimise all aspects of the process, including, but not limited to atmospheric hydrogen concentration [45], carbon precursor [46], growth time [47] and growth temperature [42].

Despite the promise shown by CVD growth, some deficiencies are apparent. One of the most significant hindrances is the polycrystalline nature of the graphene produced via this method. As growth proceeds from the formation of many carbon nuclei, which gradually grow into larger domains as more carbon diffuses out of the substrate, a large number of differently oriented domains are produced [42]. For single graphene flakes these differently oriented domains do not cause significant issues, but as they grow and meet to form a larger graphene film of the order of centimetre length scales, the regions at which two differently oriented islands meet results in the formation of grain boundaries. As discussed above, one of graphene's most exceptional properties is high carrier mobility, which result from minimal scattering due to electron-phonon interactions. However, the presence of grain boundaries, much like other lattice defects discussed later, causes significant levels of electron scattering, resulting in diminished carrier mobilities [48]. In efforts to reduce the number of grain boundaries, adaptations of the CVD method have been investigated. One particular method reported is the use of liquid metal substrates as a potential solution, as the liquid surface removes substrate grain boundaries, resulting in reduced but uniform nucleation [49, 50]. As a result of these methods graphene flakes inches in lateral dimension have been successfully grown [51].

Solid phase growth has also been explored, due to the limitations of CVD posed by using purely gaseous carbon sources [52]. This method shows similarities to CVD, in that carbon species are decomposed at high temperatures in the presence of hydrogen subsequently followed by nucleation and segregation during cooling. However, the use of solid precursors requires lower temperatures and graphene forms on both sides of the substrate as carbon atoms diffuse through the substrate (Fig.

1.4(b)). This has been shown to excellent effect by Ruan *et al.*, who produced high quality graphene from a diverse variety of sources, such as insects, grass and chocolate, which opens up the possibility of graphene mass production from waste materials [53]. As a result of the advantages of CVD, roll-to-roll graphene grown may be produced by this method, for larger scale graphene electronics. However, due to the higher concentration of grain boundaries, which act to degrade the electronic properties of films, CVD becomes less useful when attempting to produce graphene based nano-electronics.

Despite the progress made in these growth methods, a key issue remains in that in order to obtain isolated graphene on a larger scale, it must be successfully separated from its growth substrate. Successful transfer has been reported involving the support of the graphene film followed by etching of the metal substrate and subsequent water based transfer to arbitrary insulating substrates [54]. Although this method does allow for rapid transfer of graphene films, significant levels of contamination are introduced, typically Fe or Ni depending on the etching procedure utilised [55, 56]. This is also often combined with significant transfer defects such as cracks, folds and wrinkles caused by tension experienced by the film during the water suspension step of the process [57]. The presence of both contamination and defects will dramatically reduce the quality of graphene due to the inhomogeneous charge densities and scattering sites produced at these points [10, 58]. An alternative transfer method was outlined by Suk *et al.* in which graphene transfer was performed using ammonium persulfate etching, which was found to reduce the contamination on transferred films, improving overall quality, however wrinkles and tears still persist after using this method [59]. Therefore, a growth method that removes the need for a transfer process, whilst also producing a high quality graphene film with minimal grain boundaries is of substantial value.
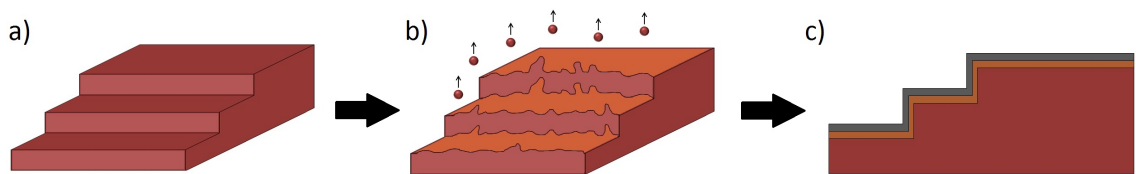
Figure 1.5: Schematic diagram of the growth of graphene from a SiC(0001) wafer. (a) A stepped SiC(0001) (red) surface is annealed under a H_2 atmosphere, producing a smooth stepped surface. (b) Si atoms sublime from the surface causing some steps to retract and a $(6\sqrt{3} \times 6\sqrt{3})$R30° buffer layer (orange) to form. (c) Graphene layers (grey) form on top of the buffer layer after extended annealing.

Such a method exists in the form of thermal decomposition of SiC(0001) wafers

(Fig. 1.5) [36, 38, 60]. Graphene growth from SiC consists of etching a SiC surface in a H_2/Ar atmosphere and heating under a Si flux, followed by annealing at higher temperatures [61]. The SiC(0001) surface goes through a number surface reconstructions during annealing under the Si flux, eventually producing a $(\sqrt{3} \times \sqrt{3})R30°$ precursor reconstruction, which upon further annealing results in a carbon rich $(6\sqrt{3} \times 6\sqrt{3})R30°$ surface upon which high quality graphene layers form with further annealing [61,62]. The graphene layers grown via this method exhibit a single crystallographic orientation, thereby reducing issues with grain boundaries that reduce the effectiveness of graphene grown by CVD. Furthermore, as a wide bandgap semiconductor, SiC provides a semi-insulating substrate with excellent thermal conductivity, which allows device processing to be performed without the need for graphene transfer [38]. Further advantages to this growth method, particularly modifications to the graphene band structure, arise from the presence of the SiC substrate which will be discussed later.

As with all graphene growth methods there are, nonetheless some drawbacks associated with thermal decomposition of SiC. First, control over graphene thickness remains a significant challenge, with MLG films particularly difficult to produce, with multilayer islands prevalent, though some studies have reported films up to 85% MLG [61]. A further issue arises from the presence of the carbon rich buffer layer, as carrier mobilities in the graphene are significantly reduced compared to isolated films [61]. This loss in mobility is attributed to the strong coupling between the buffer layer and the SiC(0001) substrate, which is required to allow true graphene layers to form unhindered. A final drawback is the significant cost of SiC wafers in comparison to Cu foils used in CVD, which will also reduce the economic viability of this method, when considering the demand for electronic devices. Therefore because of these disadvantages, it is clear that in order to successfully produce graphene of high enough quality for devices, significant optimisation of the growth method is still required.

When weighing up the advantages and disadvantaged of each graphene production method, it rapidly becomes clear that no method is preferable above all others to produce graphene for use in experiments, material composites and nano electronics. As a result of the specific pros and cons to each method it becomes apparent in the case of nano-electronics, growth from SiC is highly preferable due to its reproducibility and its single orientation, whilst CVD grown graphene on Cu becomes more favourable when scaling up production to create graphene composite materials and roll-to-roll graphene films [63].

1.4 Properties of Epitaxially Grown Graphene

Although isolated graphene, both in its single and bi-layer forms, shows great promise as a replacement for Si based electronics, the ease of growth on a number of substrates has led to several investigations into the graphene-substrate interaction. Ni(111) [64], Ru(0001) [65,66], Ir(111) [41] and Pt(111) [67] are just a few of the substrates on which graphene has been grown. Each enable production of high quality epitaxial graphene. In particular, moiré structures with large periodicities form due to the lattice mismatch between the graphene and the substrate [68]. The impressive uniformity of these moiré patterns points to possible uses as templates to produce layered devices [69].

The graphene substrate bond differs quite significantly between different metal substrates, with two main binding cases apparent. On substrates such as Ru(0001) and Ni(111), a strong graphene-substrate interaction is observed combined with a small spacing of $\sim$2 Å between overlayer and metal. This results in significant changes to the graphene band structure and a bandgap of $\sim$2 eV opens, due to a downward shift in the π band [68]. In contrast, graphene grown epitaxially on Pt and Ir exhibits a much larger distance between graphene and substrate, of $\sim$3.35 Å, and leaves the electronic structure predominantly unchanged, though small bandgaps of 0.1 eV have been reported [67, 70]. The difference in the strength of interaction observed between graphene and these substrates, and the modifications to the electronic structure provide a potential route towards further tailoring graphene's electronic structure. However, for applications such as field effect transistors (FETs) a semi-insulating substrate is required.

Consequently, it is growth from SiC, a semi-insulating substrate, which may provide the most effective route towards graphene electronics. As discussed above, one of the key features of isolated graphene is its lack of a bandgap, which prevents effective use in digital devices such as FETs due to the poor on-off ratios obtainable. Therefore, the ability to produce a bandgap in the graphene DOS is of great value. This can be reproducibly achieved using SiC(0001) substrates, which are capable of inducing a gap of $\sim$0.26 eV. The bandgap opens by reduction of graphene's six-fold rotational symmetry to three-fold through the presence of the buffer layer, which breaks the equivalence of the graphene sublattices. Symmetry breaking results in the rehybridisation of the valence and conduction band states, opening a bandgap [71]. With an induced bandgap, typical on/off ratios for graphene FETs should see rapid improvement from those observed using isolated graphene [72,73]. Hence, the

advantages inherent to the growth process, namely the presence of a semi-insulating substrate negating the need for transfer processes and the induced bandgap mean that graphene growth from SiC(0001) is ideal for the fabrication of devices.

1.5   Defects in Carbon Nanostructures
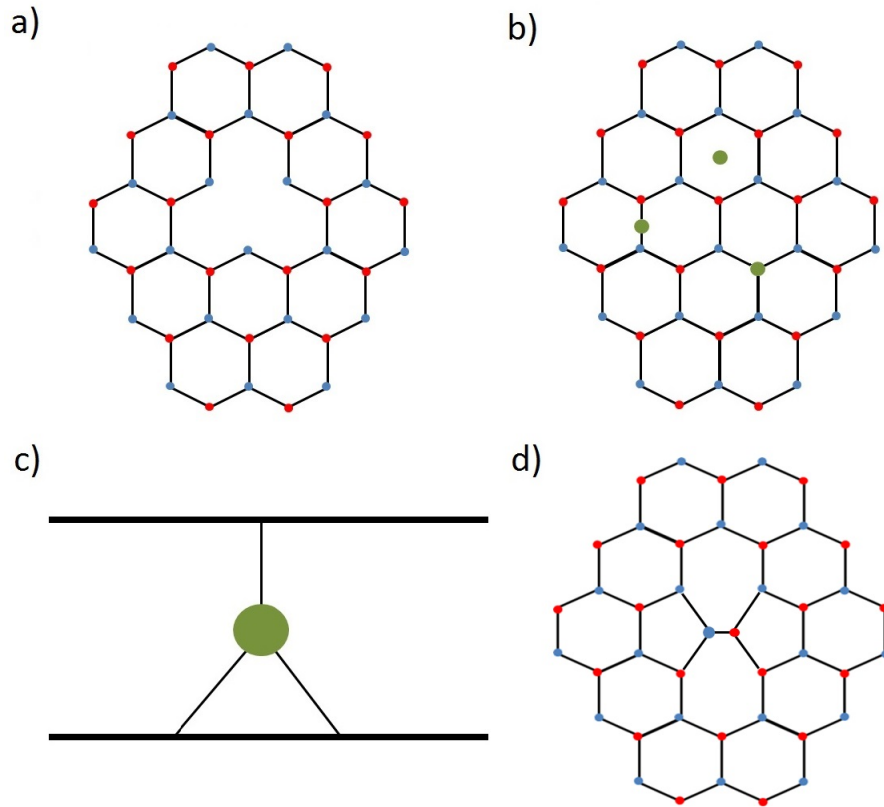
Figure 1.6: (a) Schematics of a vacancy defect in graphene; (b) an adatom (green circle) bound at three different lattice sites; (c) an interstial atom between two graphene layers. (d) Stone-Wales defect produced by a 90° bond rotation.

It is the pristine planar sheets of sp^2 hybridised carbon that lead to the excellent properties of carbon nanostructures like graphene and carbon nanotubes. However, defect structures may occur in the otherwise perfect hexagonal lattice, arising either from the growth process or via external input [58]. These vary from point defects, to large extended defects such as grain boundaries involving hundreds of atoms. Figure 1.6 shows three lattice defects that can occur in carbon nanostructures; a vacancy (a), an adatom (b) and an interstitial atom (c). A vacancy defect is produced when a single carbon atom is removed from the lattice, leaving three dangling bonds. In contrast, an adatom defect is created by an additional atom sitting in the graphene

plane, and can be thought of as an opposite sign of defect to a vacancy. The adatom can sit in many different high symmetry locations on the surface, as shown by Fig. 1.6(b) with each site having an associated binding energy [58]. The interstitial atom defect (Fig. 1.6(c)), though similar to the adatom, differs in that it requires more than one graphitic layer, which the extra atom sits between. Obviously, this type of defect is not observed on isolated graphene sheets, but may be observed on FLG, multi-walled carbon nanotubes (MWCNT) and in graphite [74–76].

A final defect type must also be considered, which is often observed in combination with those outlined above. Bond rotations are regularly observed in graphitic materials, either spontaneously or due to the presence of another defect such as a vacancy [58, 77]. A commonly observed structure that results from a bond rotation is the Stone-Wales defect, which arises from the 90° rotation of a C-C bond, resulting in the formation of two seven membered and two five membered rings (Fig. 1.6(d)) [78]. Bond rotations are vital in defect formation in graphene as the structural distortions they produce allows the free energy of defect regions to be significantly decreased, resulting in far more stable defect structures to be produced [79]. These rotations are known as Jahn-Teller distortions and result in the significantly increased stability of defects in graphene [80].

Although the initial formation of these defects occurs almost instantaneously, to remain stable, reconstruction of the surface can occur in which non-six membered rings are produced, a unique property of graphitic structures [58]. When a mono-vacancy is produced, dangling bonds are present where the carbon atom is removed; in order to achieve the most energetically stable configuration, two of these bonds saturate producing a 5-membered ring, leaving only a single dangling bond (Fig. 1.7(a) and (b)) [82]. In the case of a di-vacancy, in which two atoms are removed from the lattice, a more energetically stable configuration of 5-8-5 carbon atom rings can be achieved, ensuring no dangling bonds remain (Fig. 1.6(c) and (d)). This reconstruction, though more energetically favourable to dangling bonds, often reconstructs further, via bond rotations, to produce other lower energy defects [77, 83–86]. This can lead to an even wider range of defect types, for example the 555-777 and two-hexagon addimer defects seen in figure 1.7(e) and (f) respectively. Although these defect structures may be described as stable, they are often mobile on the surface should enough energy be available to consistently break and reform the bonds. This results in each defect having an associated migration energy that describes its ability to diffuse [87]. When two or more defects combine, larger defect agglomerations may be produced which reduce the free energy of the structure, or
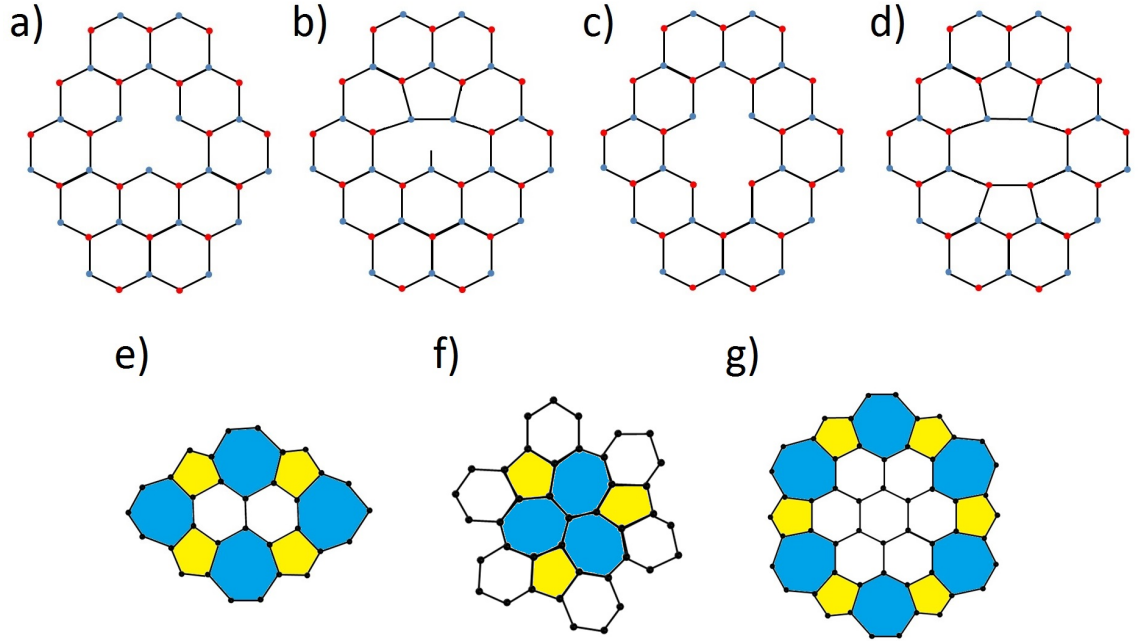
Figure 1.7: (a) Typical mono-vacancy on graphene shortly after production. (b) Reconstruction of the graphene lattice at a vacancy site. Two bonds saturate producing a pentagonal ring, leaving a single dangling bond. (c) Typical di-vacancy defect shortly after production. (d) Reconstruction of the graphene lattice into non-six membered rings to saturate dangling bonds. (e) Two-hexagon addimer defect [81]. (f) 555-777 reconstructed di-vacancy defect. (g) Large lattice reconstruction "flower" defect [81].

conversely if the defects are of opposite "sign", they may recombine to heal the lattice [58].

Despite reconstruction, the presence of dangling bonds, adatoms, bond rotations, and non-six membered rings does have a significant effect on the properties of the material, both locally and macroscopically. In particular, graphene's electronic properties see significant modification as the defect sites, even with reconstruction, provide highly reactive regions. Due to the added strain introduced by the defect, rehybridisation of the lattice occurs resulting in significant changes in the local electronic structure, which in turn leads to the scattering of electrons [88]. When imaging via STM these perturbations can be clearly seen in the form of Friedel oscillations in the vicinity of the defects, extending over many lattice spacings [39]. The presence of defects is the primary cause of reduced electron mobilities in graphitic materials. Furthermore, the rehybridisation of the lattice by defects causes significant degradation of the mechanical properties of carbon nanostructures, with the presence of both point defects and grain boundaries resulting in a reduction in intrinsic strength of both graphene and carbon nanotubes [89, 90].

Although defects are often unwanted, their controlled introduction also presents an avenue for tailoring the local properties of graphene for specific applications [58]. An example is the potential to functionalise graphene sheets through the increased reactivity produced by dangling bonds at defect sites [11]. Modification of the electronic structure and the introduction of dopants is also possible through the controlled creation of defects [91, 92]. To ensure that these potential applications can be thoroughly investigated an in-depth knowledge of the behaviour of defect structures is important, therefore, further research to understand their formation mechanisms and dynamics is of great value.

1.6 Applications and Motivation

Graphene has described as a "wonder" material with a huge number of potential applications [3]. As outlined in this chapter, graphene exhibits a number of unique and exceptional properties. These qualities have been used, for example in "bench top" experiments to probe quantum electrodynamics (QED) phenomena, due to the relativistic behaviour of electrons within graphene sheets [16]. However, it is the potential technological uses for graphene that provide the greatest motivation for much research in this field. The use of graphene in gas sensors, sensitive to the point of detecting single dopants has been reported [93], whilst graphene composite materials have shown significant potential due to exceptional mechanical strength and thermal conductivity [94]. Perhaps the most important of these applications is graphene's potential use in post-Si electronics. If graphene is to realise all of these applications, pristine graphene films will be required. Many methods to grow high quality graphene have been developed, but it is growth from SiC(0001) substrates that presents perhaps the clearest path to graphene-based electronic devices that can surpass their current Si counterparts. As such, optimisation of the growth of graphene from SiC(0001) to ensure the highest quality graphene is required. Hence, an in-depth study of the growth of graphene on SiC(0001) and identification of the factors affecting quality is of significant value to the scientific community.

Although a large amount of research has been directed at purely graphene based electronics, recent interest and development of layered devices shows significant promise [95–97]. As discussed above, the effect of the substrate to which graphene is attached can play a large role in producing desirable effects. Therefore, understanding the interaction of graphene with different materials is of great importance.

Although the adhesion of graphene to a number of different substrates has been determined, many more adhesion energies remain unknown, a particularly important example being graphene grown from SiC(0001), due to the significant level of research interest in this system. Furthermore, methods used to determine adhesion energies vary significantly and often require highly specialised approaches [98, 99], suggesting that a simple process or model to obtain these values would be useful.

Whichever way graphene is grown and whichever material it adheres to, the many defect structures that arise, whether during growth, transfer or purposeful introduction, will have a significant effect on the membrane's properties. While reducing the concentration of these defects has been the general approach in research on graphene, a number of other studies have looked at the controlled creation of defects for technological applications. These studies range from doping by attaching atoms or species at defect sites where localised reactivity is high [58, 100], through the binding of larger molecules at reactive sites to functionalise graphene sheets, to the creation of impermeable graphene membranes with further tailoring via defects [76, 101]. In order for these applications to be viable, detailed knowledge of the effects of defect formation on behaviour and mechanisms that control the dynamics of defect structures must be known. A large body of research exists on the formation and migration of defects on carbon structures, particularly graphite, but some questions pertaining to the agglomeration of defects remain. Do defect agglomerations typically exhibit the same effects on electronic structure? How do different temperatures affect the agglomeration of defects and is agglomeration affected strongly by other factors such as grain boundaries? Furthermore, considering the large amount of attention directed towards graphene on SiC(0001), only isolated studies have been reported on the formation of defect structures either naturally [39] or via bombardment. Moreover, the dynamics of these defects are unknown and whether they can be treated much the same as those in graphite still remains unanswered.

1.7 Organisation of Thesis

Taking into consideration the motivations outlined above, this thesis is organised as follows: The theoretical background of the various analytical techniques which were employed during the studies presented here is provided in Chapter 2. A particular emphasis is placed on their use to study graphene and carbon nanostructures. The experimental apparatus used to perform the experiments described in this thesis are

outlined in Chapter 3. Chapter 4 discusses the results of experiments investigating the effects of various growth parameters on the quality of graphene produced via thermal decomposition of SiC(0001). A method for removing contamination from the graphene is also presented within this chapter. Chapter 5 examines pleat defects which form during graphene growth. The orientation, concentration and stability of pleats is discussed and a continuum energy model is developed and implemented to obtain the adhesion energy of graphene on SiC. Chapter 6 details the results of annealing on defects produced via ion bombardment on both graphite and graphene samples. The final research chapter, Chapter 7 explores the quality of graphene produced via cold-wall and hot-wall growth methods. These samples are also studied via SEM and EBSD to examine whether different crystallographic Cu faces have an effect on graphene quality. Finally, Chapter 8, reviews the conclusions drawn from this thesis and presents ideas for further work that may be implemented to extend the research presented here.

1.8 Summary

In this chapter, the mechanical and electronic properties of graphene were discussed. Various growth methods currently used to produce graphene and their respective advantages and disadvantages are described. Defect structures that can form on graphene and other analogous carbon nanostructures are also outlined with the potential advantages and limitations they put on graphene's intrinsic properties examined. Finally, a number of different applications for graphene have been discussed and the motivation and organisation of this thesis has been given.

1.9 References

[1] H. W. Kroto, J. R. Heath, S. C. O'Brien, R. F. Curl and R. E. Smalley, *Nature*, **318**(6042), 162–163 (1985).

[2] X. Wang, Q. Li, J. Xie, Z. Jin, J. Wang, Y. Li, K. Jiang and S. Fan, *Nano Lett.*, **9**(9), 3137–3141 (2009).

[3] A. K. Geim and K. S. Novoselov, *Nature Mater.*, **6**(3), 183–191 (2007).

[4] W. Choi, I. Lahiri, R. Seelaboyina and Y. S. Kang, *Crit. Rev. Sol. State*, **35**(1) (2010).

[5] K. S. Novoselov, A. K. Geim, S. V. Morozov, D. Jiang, Y. Zhang, S. V. Dubonos, I. V. Grigorieva and A. A. Firsov, *Science*, **306**(5696), 666–669 (2004).

[6] L. D. Landau and E. M. Lifshitz, *Statistical Physics, Part 1*, Pergamon, Oxford (1980).

[7] J. C. Meyer, A. K. Geim, M. I. Katsnelson, K. S. Novoselov, T. J. Booth and S. Roth, *Nature*, **446**(7131), 60–63 (2007).

[8] N. D. Mermin, *Phys. Rev.*, **176**(1), 250–254 (1968).

[9] C. Lee, X. Wei, J. W. Kysar and J. Hone, *Science*, **321**(5887), 385–388 (2008).

[10] S. Adam, E. H. Hwang, V. M. Galitski and S. D. Sarma, *Proc. Nat. Aca. Sci. USA*, **104**(47), 18392–7 (2007).

[11] D. W. Boukhvalov, M. I. Katsnelson and A. I. Lichtenstein, *Phys. Rev. B*, **77**(3), 035427 (2008).

[12] M. I. Katsnelson, *Graphene: Carbon in Two Dimensions*, Cambridge University Press, Cambridge (2012).

[13] P. Wallace, *Phys. Rev.*, **71**(9), 622–634 (1947).

[14] M. I. Katsnelson, K. S. Novoselov and A. K. Geim, *Nature Phys.*, **2**(9), 620–625 (2006).

[15] Y. Zhang, Y.-W. Tan, H. L. Stormer and P. Kim, *Nature*, **438**(7065), 201–204 (2005).

[16] M. I. Katsnelson and K. S. Novoselov, *Solid State Comm.*, **143**, 3–13 (2007).

[17] J. Yao, Y. Sun, M. Yang and Y. Duan, *J. Mat. Chem.*, **22**(29), 14313–14329 (2012).

[18] K. S. Novoselov, A. K. Geim, S. V. Morozov, D. Jiang, M. I. Katnelson, I. V. Grigorieva, S. V. Dubonos and A. A. Firsov, *Nature*, **438**(7065), 197–200 (2005).

[19] K. I. Bolotin, K. J. Sikes, Z. Jiang, M. Kilma, G. Fudenberg, J. Jone, P. Kim and H. L. Stormer, *Solid State Comm.*, **146**(9-10), 351–355 (2008).

[20] S. V. Morozov, K. S. Novoselov, M. I. Katsnelson, F. Schedin, D. C. Elias, J. A. Jaszczak and A. K. Geim, *Phys. Rev. Lett.*, **100**(1), 016602 (2008).

[21] D. C. Elias, R. R. Nair, T. M. G. Mohiuddin, S. V. Morozov, P. Blake, M. P. Halsall, A. C. Ferrari, D. W. Boukhvalov, M. I. Katsnelson, A. K. Geim and K. S. Novoselov, *Science*, **323**(5914), 610–613 (2009).

[22] Y. Shao, J. Wang, H. Wu, J. Liu, I. A. Aksay and Y. Lin, *Electroanalysis*, **22**(10), 1027–1036 (2010).

[23] J. S. Bunch, S. S. Verbridge, J. S. Alden, A. M. V. der Zande, J. M. Parpia, H. G. Craighead and P. L. McEuen, *Nano Lett.*, **8**(8), 2458–2462 (2008).

[24] A. A. Balandin, S. Ghosh, W. Z. Bao, I. Calizo, D. Teweldebrhan, F. Miao and C. N. Lau, *Nano Lett.*, **8**(3), 902–907 (2008).

[25] P. Kim, L. Shi, A. Majumdar and P. L. Euen, *Phys. Rev. Lett.*, **87**(21), 215502 (2001).

[26] R. R. Nair, P. Blake, A. N. Grigorenko, K. S. Novoselov, T. J. Booth, T. Stauber, N. M. R. Peres and A. K. Geim, *Science*, **320**(5881), 1308 (2008).

[27] Y. Zhu, Z. Sun, Z. Yan, Z. Jin and J. M. Tour, *ACS Nano*, **5**(8), 6472–6479 (2011).

[28] R. Haering, *Can. J. Phys.*, **36**, 352–362 (1958).

[29] J. Nilsson, A. H. C. Neto, N. M. R. Peres and F. Guinea, *Phys. Rev. B*, **73**(21), 214418 (2006).

[30] A. H. Castro-Neto, F. Guinea, N. M. R. Peres, K. S. Novoselov and A. K. Geim, *Rev. Mod. Phys.*, **81**(1), 109–162 (2009).

[31] E. V. Castro, K. S. Novoselov, S. V. Morozov, N. M. R. Peres, J. M. B. L. dos Santos, J. Nilsson, F. Guinea, A. K. Geim and A. H. C. Neto, *Phys. Rev. Lett.*, **99**(21), 216802 (2007).

[32] E. McCann and V. I. Fal'ko, *Phys. Rev. Lett.*, **96**(8), 086805 (2006).

[33] S. Shallcross, S. Sharma, E. Kandelaki and O. A. Pankratov, *Phys. Rev. B*, **81**(1), 165105 (2010).

[34] J. A. Garlow, L. K. Barrett, L. Wu, K. Kisslinger, Y. Zhu and J. F. Pulecio, *Sci. Rep.*, **6**(19804) (2016).

[35] W. Bao, L. Jing, J. Velasco, Y. Lee, G. Liu, D. Tran, B. Standley, M. Aykol, S. B. Cronin, D. Smirnov, M. Koshino, E. McCann, M. Bockrath and C. N. Lau, *Nature Phys.*, **7**(12), 948–952 (2011).

[36] W. A. de Heer, C. Berger, X. Wu, P. N. First, E. H. Conrad, X. Li, T. Li, M. Sprinkle, J. Hass, M. L. Sadowski, M. Potemski and G. Martinez, *Solid State Commun.*, **143**(1-2), 92–100 (2007).

[37] X. Li, W. Cai, J. An, S. Kim, J. Nah, D. Yang, R. Piner, A. Velamakanni, I. Jung, E. Tutuc, S. K. Banerjee, L. Colombo and R. S. Ruoff, *Science*, **324**(5932), 1312–1314 (2009).

[38] T. Hopf, K. V. Vassilevski, E. Escobedo-Cousin, N. G. Wright, A. G. O'Neill, A. B. Horsfall, J. P. Goss, A. Barlow, G. H. Wells and M. R. C. Hunt, *Mater. Sci. Forum*, **778-780**, 1154–1157 (2014).

[39] G. M. Rutter, N. P. Guisinger, J. N. Crain, E. A. A. Jarvis, M. D. Stiles, T. Li, P. N. First and J. A. Stroscio, *Phys. Rev. B*, **76**(23), 235416 (2007).

[40] J. Lahiri, T. S. Miller, A. J. Ross, L. Adamska, I. I. Oleynik and M. Batzill, *New J. Phys.*, **13**(2), 025001 (2011).

[41] A. T. N'Diaye, J. Coraux, T. N. Plasa, C. Busse and T. Michely, *New. J. Phys.*, **10**(1), 1–16 (2008).

[42] J. M. Wofford, S. Nie, K. F. McCarty, N. C. Bartelt and O. D. Dubon, *Nano Lett.*, **10**, 4890–4896 (2010).

[43] L. Gao, J. R. Guest and N. P. Guisinger, *Nano Lett.*, **10**, 3512–3516 (2010).

[44] R. M. Jacobberger and M. S. Arnold, *Chem. Mater.*, **25**, 871–877 (2013).

[45] M. Losurdo, M. M. Giangregorio, P. Capezzuto and G. Bruno, *Phys. Chem. Chem. Phys.*, **13**(46), 20836–20843 (2011).

[46] L. Tao, J. Lee, H. Chou, M. Holt, R. S. Ruoff and D. Akinwande, *ACS Nano*, **6**(3), 2319–2325 (2012).

[47] A. W. Robertson and J. H. Warner, *Nano Lett.*, **11**(3), 1182–1189 (2011).

[48] P. Y. Huang, C. S. Ruiz-Vargas, A. M. van der Zande, W. S. Whitney, M. P. Levendorf, J. W. Kevek, S. Garg, J. S. Alden, C. J. Hustedt, Y. Zhu, J. Park, P. L. McEuen and D. A. Muller, *Nature*, **469**(7330), 389–392 (2011).

[49] D. Geng, B. Wu, Y. Guo, L. Huang, Y. Xue, J. Chen, G. Yu, L. Jiang, W. Hu and Y. Liu, *Proc. Nat. Aca. Sci. USA*, **109**(21), 7992–7996 (2012).

[50] Y. A. Wu, Y. Fan, S. Speller, G. L. Creeth, J. T. Sadowski, K. He, A. W. Robertson, C. S. Allen and J. H. Warner, *ACS Nano*, **6**(6), 5010–5017 (2012).

[51] T. Wu, X. Zhang, Q. Yuan, J. Xue, G. Lu, Z. Liu, H. Wang, H. Wang, F. Ding, Q. Yu, X. Xie and M. Jiang, *Nature Mater.*, **15**(1), 43–47 (2016).

[52] Z. Sun, Z. Yan, J. Yao, E. Beitler, Y. Zhu and J. M. Tour, *Nature*, **468**(7323), 549–552 (2010).

[53] G. Ruan, Z. Sun, Z. Peng and J. M. Tour, *ACS Nano*, **5**(9), 7601–7607 (2011).

[54] Y. Lee, S. Bae, H. Jang, S. Jang, S.-E. Zhu, S. H. Sim, Y. I. Song, B. H. Hong and J.-H. Ahn, *Nano Lett.*, **10**(2), 490–493 (2010).

[55] A. Ambrosi and M. Pumera, *Nanoscale*, **6**(1), 472–476 (2014).

[56] G. Lupina, J. Kitzmann, I. Costina, M. Lukosius, C. Wenger, A. Wolff, S. Vaziri, M. Östling, I. Pasternak, A. Krajewska, W. Strupinski, S. Kataria, A. Gahoi, M. C. Lemme, G. Ruhl, G. Zoth, O. Luxemhofer and W. Mehr, *ACS Nano*, **9**(5), 4776–4785 (2015).

[57] L. Gao, G.-X. Ni, Y. Liu, B. Liu, A. H. Castro-Neto and K. P. Loh, *Nature*, **505**(7482), 190–194 (2014).

[58] F. Banhart, J. Kotakoski and A. V. Krasheninnikov, *ACS Nano*, **5**(1), 25–41 (2011).

[59] J. W. Suk, A. Kitt, C. W. Magnuson, Y. Hao, S. Ahmed, J. An, A. K. Swan, B. B. Goldberg and R. S. Ruoff, *ACS Nano*, **5**(9), 6916–6924 (2011).

[60] R. M. Tromp and J. B. Hannon, *Phys. Rev. Lett.*, **102**(10), 106104 (2009).

[61] J. Hass, J. E. Millán-Otoya, P. N. First and E. H. Conrad, *Phys. Rev. B*, **78**(20), 205424 (2008).

[62] U. Starke and C. Riedl, *J. Phys. Cond. Mat.*, **21**(13), 134016 (2009).

[63] S. Bae, H. Kim, Y. Lee, Z. Xu, J.-S. P. ad Y. Zheng, J. B. ad T. Lei, H. R. Kim, Y. Song, Y.-J. Kim, K. S. Kim, B. Özyilmaz, J.-H. Ahn and B. H. H. anf S. Iijima, *Nature Nanotechnol.*, **5**(8), 574–578 (2010).

[64] F. Mittendorfer, A. Garhofer, J. Redinger, J. Klimeš, J. Harl and G. Kresse, *Phys. Rev. B*, **84**(20), 201401 (2011).

[65] P. Sutter, J.-I. Flege and E. A. Sutter, *Nature Mater.*, **7**(5), 406–411 (2008).

[66] Y. Pan, H. G. Zhang, D. X. Shi, J. T. Sun, S. X. Du, F. Liu and H. J. Gao, *Adv. Mater.*, **21**(27), 2777 (2009).

[67] P. Sutter, J. T. Sadowski and E. Sutter, *Phys. Rev. B*, **80**(24), 245411 (2009).

[68] J. Wintterlin and M.-L. Bocquet, *Surf. Sci.*, **603**(10-12), 1841–1841 (2009).

[69] A. T. N'Diaye, S. Bleikamp, P. J. Feibelman and T. Michely, *Phys. Rev. Lett.*, **97**(21), 1–4 (2006).

[70] I. Pletikosić, M. Kralj, P. Pervan, R. Brako, J. Coraux, A. T. N'Diaye, C. Busse and T. Michely, *Phys. Rev. Lett.*, **102**(5), 056808 (2009).

[71] S. Y. Zhou, G.-H. Gweon, A. V. Fedorov, P. N. First, W. A. de Heer, D.-H. Lee, F. Guinea, A. H. C. Neto and A. Lanzara, *Nature Mater.*, **6**(10), 770–775 (2007).

[72] I. Meric, M. Y. Han, A. F. Young, B. Ozyilmaz, P. Kim and K. L. Shepard, *Nature Nanotech.*, **3**(11), 654–659 (2008).

[73] J. Kedsierski, P.-L. Hsu, P. Healey, P. W. Wyatta, C. L. Keast, M. Sprinkle, C. Berger and W. A. deHeer, *IEEE Trans, Elec. Dev.*, **55**(8), 2078–2085 (2008).

[74] G. K. Williamson and C. Baker, *Phil. Mag.*, **6**(62), 313–314 (1961).

[75] A. V. Karasheninnikov, K. Nordlund, M. Sirviö, E. Salonen and J. Keinonen, *Phys. Rev. B*, **63**(24), 245405 (2001).

[76] A. Hashimoto, K. Suenaga, A. Gloter, K. Urita and S. Iijima, *Nature*, **430**(7002), 870–873 (2004).

[77] Q. Chen, A. W. Robertson, K. He, C. Gong, E. Yoon, G.-D. Lee and J. H. Warner, *ACS Nano*, **9**(8) (2015).

[78] A. K. Stone and D. J. Wales, *Chem. Phys. Lett.*, **128**(5-6), 501–503 (1986).

[79] J. H. Warner, M. H. Rümmeli, L. Ge, T. Gemming, B. Montanari, M. N. Harrison, B. Büchner and G. A. D. Briggs, *Nature Nanotechnol.*, **4**(8), 500–504 (2009).

[80] H. A. Jahn and E. Teller, *Proc. Royal Soc. A*, **161**(905), 220–235 (1937).

[81] E. Cockayne, *Phys. Rev. B*, **85**(12), 125409 (2012).

[82] J. C. Meyer, C. Kisielowski, R. Erni, M. D. Rossell, M. F. Crommie and A. Zettl, *Nano Lett.*, **8**(11), 3582–3586 (2008).

[83] Y. Kim, J. Ihm, E. Yoon and G.-D. Lee, *Phys. Rev. B*, **84**(7), 075445 (2011).

[84] A. W. Robertson and J. H. Warner, *Nanoscale*, **5**(1), 4079–4093 (2013).

[85] A. W. Robertson, G.-D. Lee, K. He, E. Yoon, A. I. Kirkland and J. H. Warner, *Nano Lett.*, **14**(7), 3972–3980 (2014).

[86] A. W. Robertson, G.-D. Lee, K. He, E. Yoon, K. A and J. H. Warner, *Nano Lett.*, **14**(3), 1634–1642 (2014).

[87] L. Li, S. Reich and J. Robertson, *Phys. Rev. B*, **72**(18), 184109 (2005).

[88] A. Cortijo and M. A. H. Vozmediano, *Nuclear Phys. B*, **763**(3), 293–308 (2007).

[89] M. Sammalkorpi, A. Krasheninnikov, A. Kuronen, K. Nordlund and K. Kaski, *Phys. Rev. B*, **70**(24), 245416 (2004).

[90] A. Zandiatashbar, G.-H. Lee, S. J. An, S. Lee, N. Mathew, M. Terrones, T. Hayashi, C. R. Picu, J. Hone and N. Koratkar, *Nature Comm.*, **5**, 3186 (2014).

[91] T. O. Wehling, A. V. Balatsky, M. I. Katsnelson, A. I. Lichtenstein, K. Scharnberg and R. Wiesendanger, *Phys. Rev. B*, **75**(12), 125425 (2007).

[92] N. Jung, N. Kim, S. Jockusch, N. J. Turro, P. Kim and L. Brus, *Nano Lett.*, **9**(12), 4133–4137 (2009).

[93] F. Schedin, A. K. Geim, S. V. Morozov, E. W. Hill, P. Blake, M. I. Katsnelson and K. S. Novoselov, *Nature Mater.*, **6**(9), 652–655 (2007).

[94] S. Stankovich, D. A. Dikin, G. H. B. Dommett, K. M. Kohlhaas, E. J. Zimney, E. A. Stach, R. D. Piner, S. T. Nguyen and R. S. Ruoff, *Nature*, **442**(7100), 282–286 (2006).

[95] Y. Ma, Y. Dai, M. Guo, C. Niu and B. Huang, *Nanoscale*, **3**(9), 3883–3887 (2011).

[96] Y. Shi, W. Zhou, A.-Y. Lu, W. Fang, Y.-H. Lee, A. L. Hsu, S. M. Kim, K. K. K. abd H. Y. Yang, L.-J. Li, J.-C. Idrobo and J. Kong, *Nano Lett.*, **12**(6), 2784–2791 (2012).

[97] K.-J. Huang, L. Wang, J. Ling and Y.-M. Liu, *Sensor Actuat. B-Chem.*, **178**, 671–677 (2013).

[98] S. P. Koenig, N. G. Boddeti, M. L. Dunn and J. S. Bunch, *Nature Nanotechnol.*, **6**(9), 543–546 (2011).

[99] T. Yoon, W. C. Shin, T. Y. Kim, J. H. Mun, T.-S. Kim and B. J. Cho, *Nano Lett.*, **12**(1), 1448 (2012).

[100] B. Guo, Q. Liu, E. Chen, H. Zhu, L. Fan and J. R. Gong, *Nano Lett.*, **10**, 4975–4980 (2010).

[101] F. Rose, A. Debray, P. Martin, H. Fujita and H. Kawakatsu, *Nanotechnol.*, **17**(20), 5192–5200 (2006).

Chapter 2

Experimental Techniques

This chapter gives an introduction to the experimental techniques used to measure the data presented in this thesis. An overview of the theoretical background of each technique is provided and the use of each technique for the study of graphene is also discussed.

2.1 Introduction

When studying the properties of materials, large differences can be observed between bulk behaviour and that at the surface. These differences become far more pronounced when observing nanostructures, as the ratio of surface to bulk atoms is vastly increased. The two-dimensional nature of graphene can be seen as the limiting case, where each atom can be considered as lying on the surface. Therefore, the use of surface sensitive techniques that probe the uppermost layers of materials are of great value.

The use of low energy electrons epitomises this surface sensitivity due to their short inelastic mean free path (IMFP) [1]. This prevents the electrons from penetrating deeper than the first few layers of the material, resulting in all information gained from elastic scattering corresponding to the surface atoms. Consequently, techniques such as low energy electron diffraction (LEED) and electron back-scatter diffraction (EBSD), can provide clear crystallographic information of the first few atomic layers. In the case of graphene grown on various substrates, this can reveal both the graphene crystal structure and that of the surface it is grown upon. Whilst these electron diffraction techniques can provide excellent information on the structure of the surface, further data on electronic structure or elemental composition is not provided. At this point, spectroscopic measurements, which probe the electronic structure of materials, are required. For example, Auger electron spectroscopy (AES), Raman spectroscopy (RS) and scanning tunnelling spectroscopy (STS) can be used to provide complimentary information on elemental composition, film quality and thickness, and local electronic structure respectively.

With the crystallographic and electronic structure, as well as further information on quality, thickness and elemental composition obtainable using the techniques described above, all that remains is to make real-space observations of the structures that form on the surface. Techniques suggested above are unable to provide this information. Therefore, imaging techniques such as scanning tunnelling microscopy (STM) and scanning electron microscopy (SEM) provide direct evidence of surface morphology and allow specific areas of interest on the surface to be studied in great detail. This becomes particularly important when observing small isolated structures, such as graphene islands and defects, at which point other measurements can only provide data averaged over a large area. Therefore, it can be concluded that in order to fully study graphene and indeed other nanostructures, a combination of multiple surface sensitive techniques should be employed.

In this chapter, the experimental techniques used to obtain the data presented in this thesis are described. Focus is placed on the theory behind each technique and its specific application to studying graphene. The technical details of the instruments and methodology are discussed in Chapter 3.

2.2   Auger Electron Spectroscopy

In the early 1920s Lise Meitner (1922) and Pierre Auger (1925) [2] independently discovered that the ionisation of electrons from the core level of an atom, arising from the absorption of photons, released electrons with energies independent of the incident energy. These electrons have been subsequently referred to as Auger electrons and since then AES has become a standard of modern surface science research, due to the specificity of the transitions to the elements present [3], and the improvement in UHV display systems [4–6]. The emission of Auger electrons can be described as a process involving multiple steps, although it is in fact a single coherent quantum process (Fig. 2.1). An incident high energy particle beam (normally electrons) ionises a core electron, producing a core hole. An electron in a higher level fills this hole as the atom relaxes. This releases energy which is transferred, in a radiation-less process, to another electron in a higher level, which is then also ionised. As a result the energy of the Auger electron is independent of the incoming beam and is characteristic of the element. Furthermore, due to the short IMFP, Auger electrons are only detected from the outermost few layers of a material, as those from deeper layers have a significantly higher probability of being inelastically scattered. This results in a surface sensitive technique. The energy of the Auger electron, from an element with atomic number Z involving transitions between levels W, X and Y, can be described by:

$$E_{WXY} = E_W(Z) - E_X(Z + \Delta) - E_Y(Z + \Delta) - \Phi_A \; , \tag{2.1}$$

where E_W, E_X and E_Y are the energies of the levels from which: the core hole is emitted, an electron relaxes to fill the core hole and from which the Auger electron is emitted [7]. Φ_A is the work function of the analyser and Δ reflects the decrease in core-hole screening of the nucleus, which can be regarded as an effective increase in the atomic number. The notation used to categorise these transitions comes from the labelling of atomic shells corresponding to the principal quantum numbers i.e. K, L,

M, N etc. correspond to $n = 1,2,3,4$ etc. A further number is then used to indicate the electronic angular momentum of the level, based on the orbital quantum number *l*, spin quantum number *s* and total angular momentum *j*, where $j = l + s$. The process is shown diagrammatically in figure 2.1. The elements hydrogen and helium cannot be directly detected by AES since they have fewer than 3 electrons [7, 8]. Conversely elements with larger numbers of electrons will have more transitions available, consequently their spectra will show a series of peaks corresponding to the same element. In the case of carbon, the Auger transition is often referred to as a *KVV* transition. The letter '*V*' is used to indicate that the *L* shell is in fact the valence shell of the atom. This occurs in carbon due to only the *K* and *L* shells being occupied. This results in only one Auger transition being possible and hence a single peak associated with C that can be observed at 271 eV (Fig. 2.2).
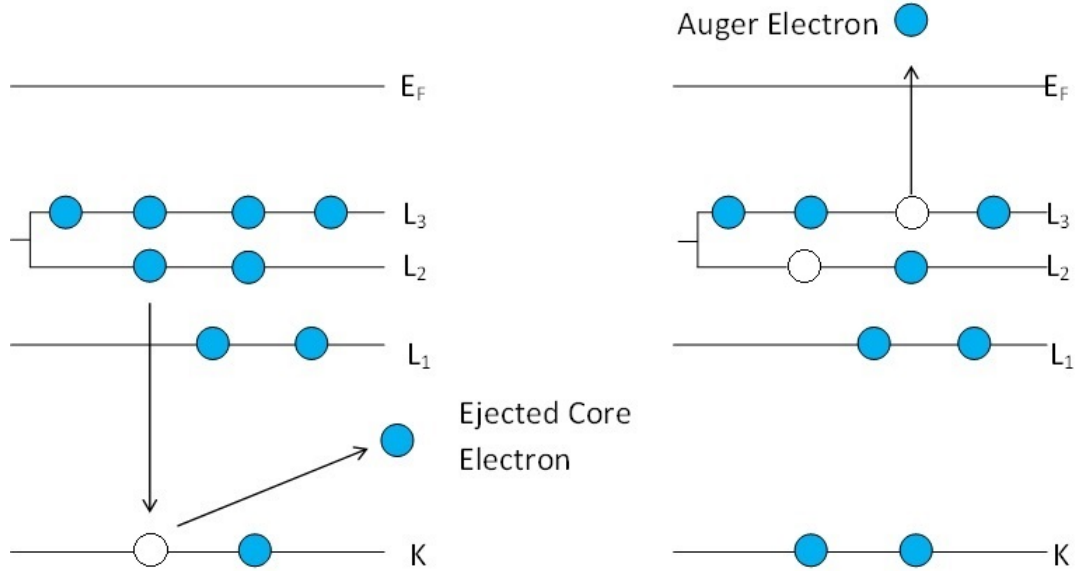
Figure 2.1: Schematic diagram showing a *KLL* Auger transition: the production of a core hole followed by the relaxation of an electron from the L_2 shell and the emission of an Auger electron from the L_3 shell.

It is important to note that for elements with higher atomic numbers, fewer Auger electrons are observed due to the competing process of X-ray fluorescence (XRF), which occurs when the electron decays into the core hole. In the case of XRF the energy is transferred to a photon rather than another electron. This processes occur with probabilities [9]:

$$P_{\mathrm{XRF}} = (1 + \alpha Z^{-4})^{-1} \tag{2.2}$$

$$P_{\mathrm{Auger}} = 1 - P_{\mathrm{XRF}} \, , \tag{2.3}$$

where Z is the atomic number of the element and α is a constant dependent on

the shell from which the electron is ionised. As a result the probability of an Auger electron being produced is the complement of photon emission probability (equation 2.3), and due to the dependence on Z is much more likely to occur for elements with smaller atomic numbers.
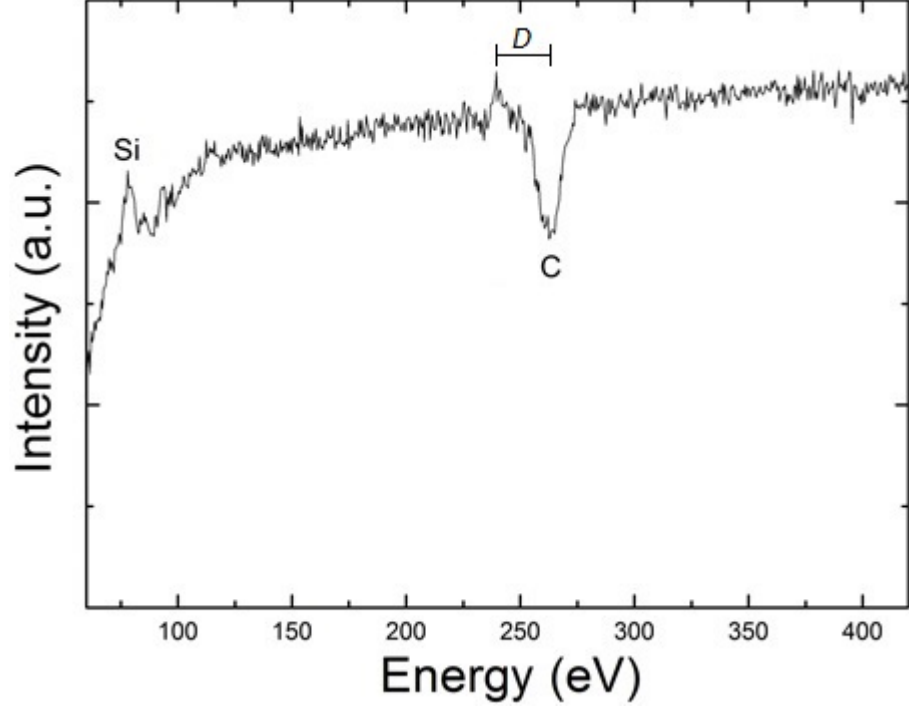
Figure 2.2: Differentiated AES spectrum obtained from graphene grown on SiC(0001). Silicon and Carbon peaks are clearly visible. A separation in energy (D) can be observed between the upper and lower C peak excursion.

Auger electron spectra have a strong background of backscattered electrons from the incident beam as well as secondary electrons released during irradiation. These secondary electrons can produce Auger electrons themselves if enough energy is available. In order to clearly observe Auger peaks the spectra are differentiated with respect to energy which enables much easier identification of the elements present. Furthermore, peak shape and relative intensity are now also identifiable allowing for further information to be extracted. For example the carbon peak visible in figure 2.2 exhibits an upper and lower excursion with a large separation in energy (D) of ~23 eV. This corresponds to carbon with a high proportion of sp^2 hybridisation, indicating the presence of graphitic carbon [10]. Conversely peaks showing smaller gaps between upper and lower excursions (not shown) would indicate the presence of non-graphitic carbon allotropes; for example a value of $D = 14.2$ eV would correspond to the presence of diamond [10].

Determination of film thickness is possible through the Auger yield (I_i, peak to

peak intensity) from individual layers and elemental sensitivity factors (S_i) using equation 2.4 [11]:

$$X_i = \frac{I_i/S_id_i}{\sum_\alpha I_\alpha/S_\alpha d_\alpha} \; , \tag{2.4}$$

in which X_i is the atomic concentration of element i, d_i is a scaling factor related to the lock in amplifier sensitivity (l_i) and primary beam current (I_p) by $d_i = l_iI_p$. Calibration curves based on these atomic concentrations can be produced, relating the number of layers in a film to the ratio of the Auger peaks for each element present allowing quick thickness determination. An example can be seen in a study by Luxmi *et al.* showing how the number of graphene monolayers grown on the surface of SiC(0001) can be calculated by this method [12].

2.3 Low Energy Electron Diffraction

The first use of LEED as a means to study the surface of materials was reported in 1927 by Davisson and Germer. A beam of electrons was focussed onto a Ni(111) surface and the dependence of scattered electron intensity on diffraction angle was measured [13]. Despite this first success, LEED did not become widespread until the 1960s, due to insufficient technology to produce a beam of focussed electrons, as well as a lack of systems to produce ultra high vacuum (UHV) conditions in which surfaces could be cleaned and maintained. Since this time LEED has become a standard technique for determining the long range order of a surface.

A typical LEED system consists of a means to produce and focus a beam of monoenergetic electrons to a small spot size. Most electron guns produce electrons via thermionic emission. This requires a filament that can be heated to a high enough temperature to emit a significant number of electrons. Most filaments are made of either of tungsten (W) or lanthanum hexa-boride (LaB_6). Tungsten is chosen for its extremely high melting temperature allowing for increased stability and lifetime. Despite its fragility and high price LaB_6 is often favoured however, due to its significantly lower work function that allows it to thermionically emit at lower temperatures. As a result the spread in energy of the electrons produced is much lower due to its dependence on temperature and this results in a more focussed beam. The electrons produced are focussed by a set of lenses to a spot

size of ~ 1 μm. Electrons incident on the surface of interest may be backscattered and therefore pass through a set of retarding grids (Fig. 2.3). These grids filter out inelastically backscattered electrons to leave elastically scattered electrons that are then accelerated to a phosphor screen, on which the diffraction pattern can be observed.
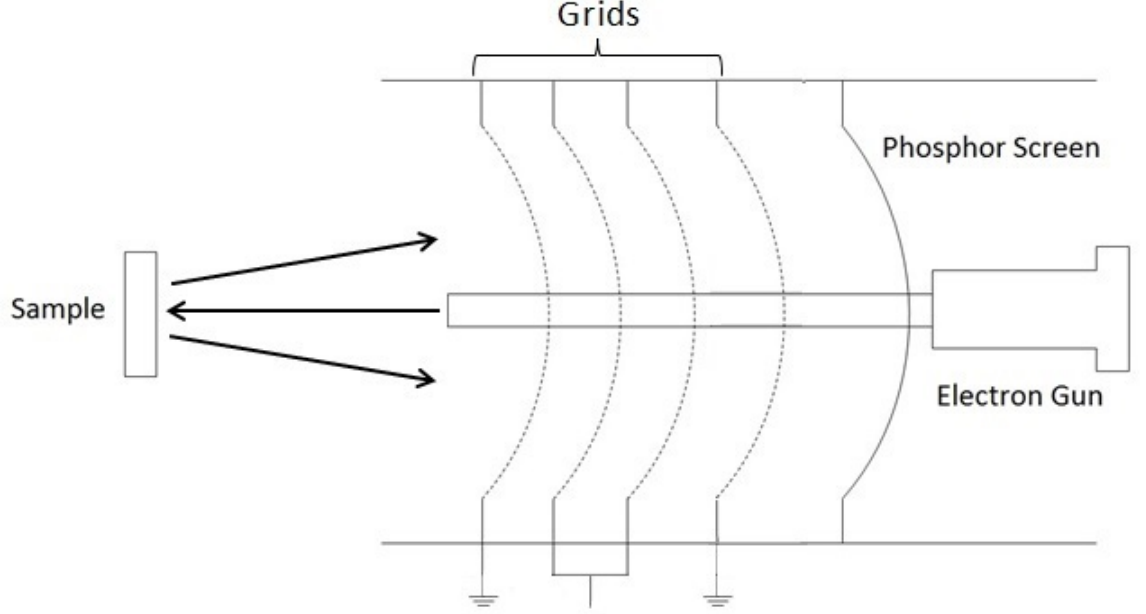
Figure 2.3: Schemaic diagram of a basic LEED apparatus. Three retarding grids filter out inelastically scattered electrons. Elastically scattered electrons strike the screen to produce diffraction spots. Based on [14].

Diffraction of electrons from a crystal surface forms a pattern that reflects the symmetries present. Much like the diffraction of X-rays, in order for a spot to be produced the conditions for Bragg diffraction must be satisfied:

$$\lambda = 2d\sin\theta \tag{2.5}$$

, where λ is the wavelength of the incident electrons, θ is the diffraction angle and d is the spacing between the atomic planes in the crystal which can be written in terms of the lattice constant a and the Miller indices h, k and l for a cubic system:

$$d = \frac{a}{\sqrt{h^2 + k^2 + l^2}} \qquad ; \qquad d = \frac{a}{\sqrt{h^2 + k^2}} \ , \tag{2.6}$$

however, in the case of LEED which probes the surface of a material, satisfying the diffraction conditions becomes simpler in comparison to those for a 3D bulk crystal. This is a result of the truncation of the real space lattice, which extends the reciprocal lattice points into rods which are normal to the surface. By constructing the Ewald

sphere it is clear that a diffraction spot will be observable at each point where a reciprocal lattice rod intersects its surface (Fig. 2.4). Furthermore by changing the energy of the incident beam the density of spots can be adjusted, as this adjusts the Ewald sphere radius and hence the number of lattice rods that intersect the surface. Therefore, the description of the surface net is also simplified, as seen in equation 2.6 (right) for a simple square surface mesh.
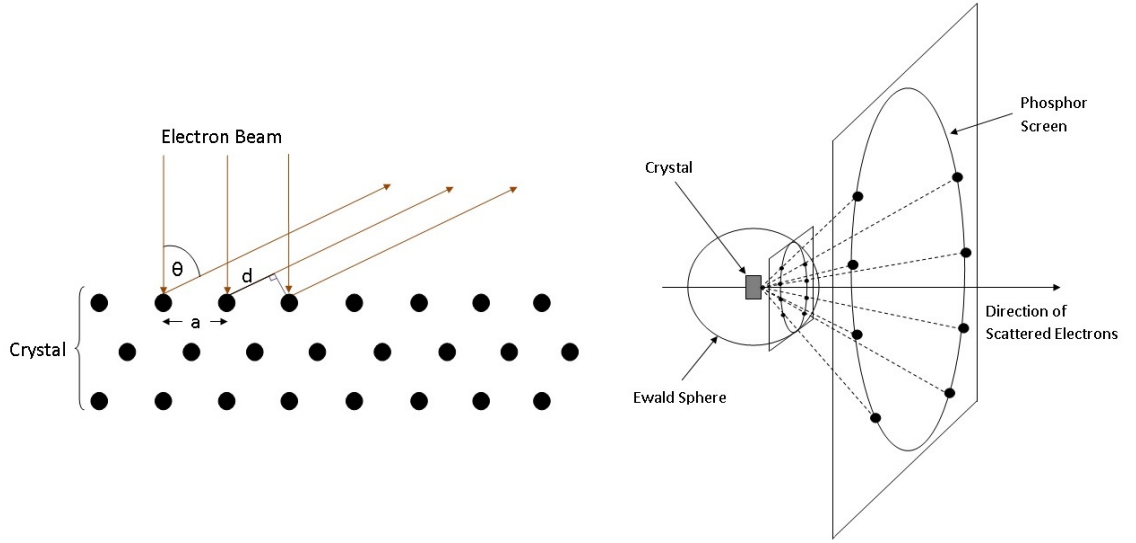
Figure 2.4: (left) Schematic diagram of the diffraction of an electron beam incident on the surface of a crystal. (Right) Construction of the Ewald sphere and the formation of spots on a LEED phosphor screen.

As discussed earlier, LEED is a highly surface sensitive technique, this is due to the short IMFP of electrons in the energy range of 50-500 eV, which results in significant attenuation of diffracted electrons from planes deeper than 5-10 Å, hence the pattern obtained will reflect only the long range order of the outermost few layers. An example can be seen in figure 2.5, in which graphitic layers have been grown on SiC(0001). Graphene (1×1) spots are clearly visible showing the characteristic hexagonal pattern indicative of the graphene lattice, spots defining smaller hexagons corresponding to a $(6\sqrt{3} \times 6\sqrt{3})R30°$ surface reconstruction are also apparent [15]; the smaller spacing in the LEED pattern is the result of a larger periodicity in real space, and hence a smaller size in reciprocal space. Spots corresponding to the hexagonal SiC(0001) substrate become visible with increased energy, demonstrating that layers a little deeper than the surface can still be observed via this technique.

Since the first few layers contribute to the diffraction pattern observed, LEED can be used as a method for determining the thickness of films through careful measurement of the change in intensity of spots with respect to the energy of incoming

electrons; this technique is known as LEED-IV, due to it's production of curves of spot intensity (I) against voltage (V). By measuring the intensity of a spot in comparison to spots from other structures, for example graphene (1×1) to ($6\sqrt{3}$) $R30°$ reconstruction spots, and comparing the results to those obtained from films of known thickness, a rough estimate of the number of layers in a film, can be obtained [16], assuming a complete and uniform coverage. This technique can be taken further by using spot tracking codes, allowing for improved data collection, which can then be compared with theoretically produced variations of intensity determined via dynamical scattering theory, for different surface structures [17]. Simple thickness estimates from LEED-IV are reported in this thesis, however detailed surface structure studies are not undertaken.
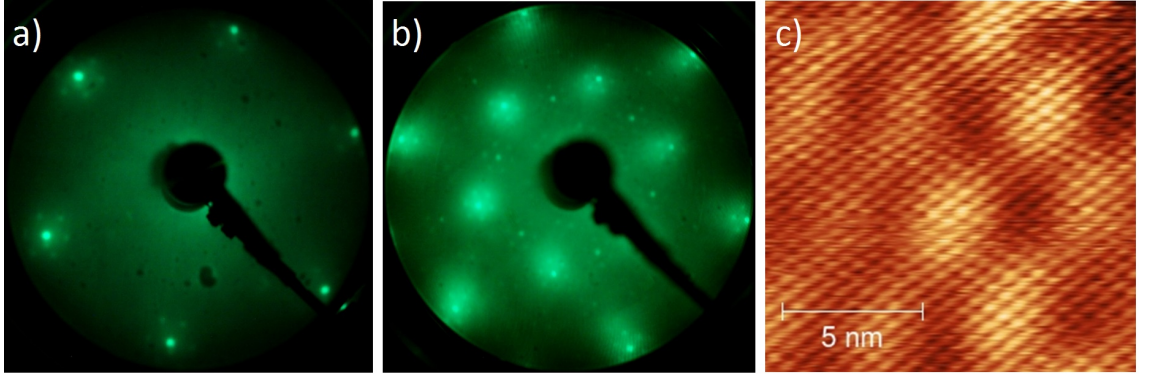
Figure 2.5: a) LEED pattern showing graphene (1×1) spots and ($6\sqrt{3} \times 6\sqrt{3})R30°$ reconstruction spots. b) LEED pattern showing graphene and SiC (1×1) spots and reconstruction spots. c) STM image of the graphene lattice and reconstruction corresponding to the (1×1) and ($6\sqrt{3} \times 6\sqrt{3})R30°$ LEED spots.

2.4   Raman Spectroscopy

The Raman effect was first observed in 1928 by Raman and Krishnan [18] and Raman spectroscopy has since become a widely used analytical tool. The Raman effect can be observed when light is focused on a material and the wavelength of scattered photons is measured. The incident photons scatter off the material and the radiation collected will be either the same wavelength, known as Rayleigh scattering, or have a slightly positively or negatively shifted wavelength. These small shifts in wavelength are due to the Raman effect and can be described as the scattering of photons through a 'virtual state' (Fig. 2.6) [19]. A positive shift in wavelength occurs by the transfer of a quanta of vibrational energy from the incident photon to a lattice phonon exciting it to a higher vibrational state; this is known as Stokes

scattering. Equally, a quanta of energy may be transferred from a lattice phonon in an excited vibrational state, to the incident photon, resulting in a shorter emitted wavelength, known as anti-Stokes scattering. As a result, the shifts in wavelength observed are highly dependent on the material's vibrational energy level structure.
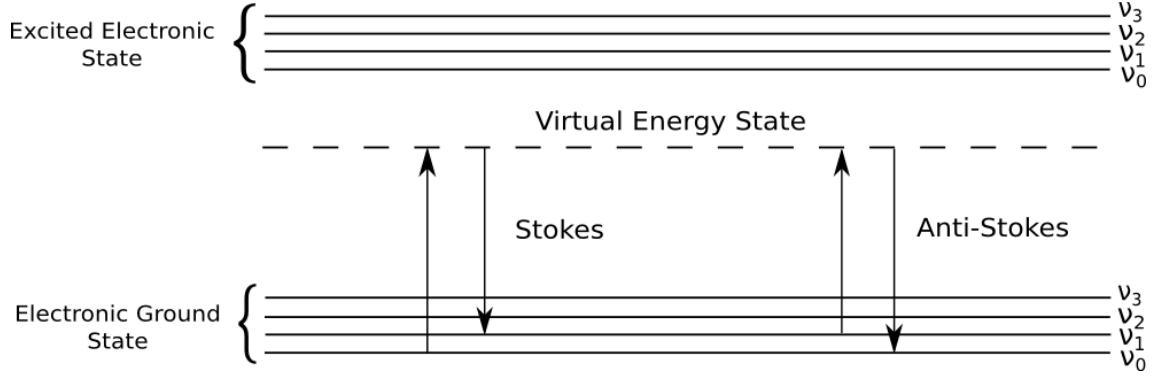
Figure 2.6: Energy level diagram showing showing Stokes and anti-Stokes Raman scattering occurring via a virtual state, where ν_0, ν_1, ν_2 and ν_3 are the ground and first 3 excited vibrational energy states respectively.

When considering Raman spectroscopy of graphene, three main peaks are often observed (Fig. 2.7). These peaks are referred to as the D, G and $2D$ (sometimes G') bands [20]. In order to understand the origin of these peaks the graphene phonon dispersion must be considered. The graphene unit cell consists of two carbon atoms, which can be labelled A and B, located at inequivalent sites. Since there are three degrees of translational freedom per atom, the graphene phonon dispersion relation has six branches, four of which oscillate within the graphene plane, denoted by (i) and two which oscillate out of plane, denoted by (o). Further categorisation results from the relative displacement of atoms with respect to the direction of propagation. Modes that oscillate along the direction of propagation are referred to as longitudinal (L) modes, whilst oscillations perpendicular to this direction are denoted as transverse (T) modes. Finally, if oscillations of the two atoms are in phase the phonon is classed as an acoustic mode (A), whilst out of phase vibrations result in optical phonons (O). As such, the phonons in graphene have a phonon dispersion consisting of iLO, iLA, iTO, iTA, oTO and oTA branches.

The G band at ~ 1582 cm^{-1}, is a doubly degenerate, first order Raman transition in which an incident photon inelastically scatters off an iTO or iLO phonon at the Brillouin zone centre, and is then collected without further interaction (Fig. 2.8(a)). In contrast, the D and $2D$ peaks originate from double resonance (DR) processes. Resonance enhanced scattering differs from first order Raman scattering, in that as the incident photon energy is close to that of an electronic transition
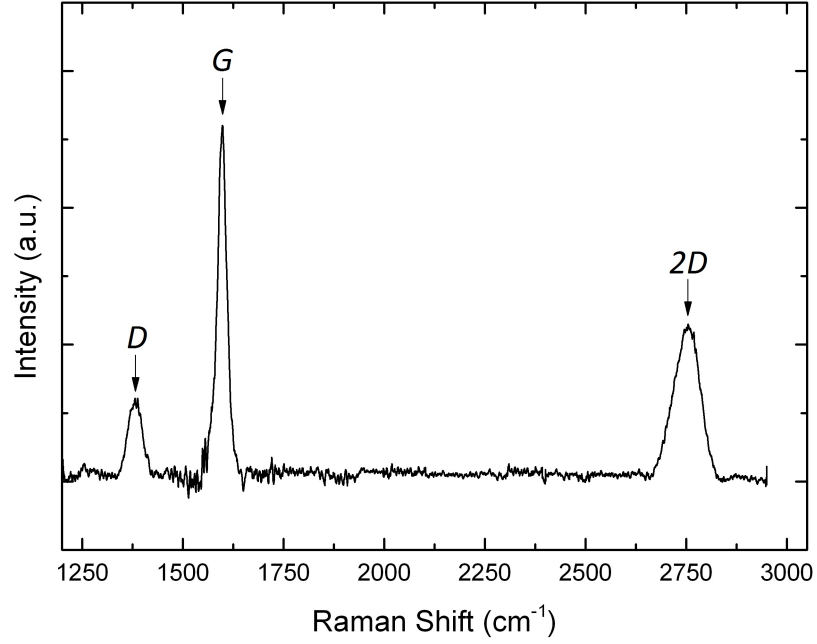
Figure 2.7: Typical Raman spectrum obtained from FLG grown on SiC(0001). Three clear peaks referred to as the D, G and $2D$ bands are clearly visible.

of the material, the photon scatters via a real, rather than 'virtual' energy state, significantly increasing the intensity of the Raman signal. For the $2D$ peak, this involves the incident photon scattering inelastically from an iTO phonon close to a graphene K-point and inelastically scattering a second time from another iTO phonon at a symmetry inequivalent Dirac point (labelled K')(Fig. 2.8(b)). Finally, the D band differs further in that the DR process requires a defect from which the photon elastically scatters, this is then followed by an inelastic scatter off an iTO phonon (Fig. 2.8(c)).
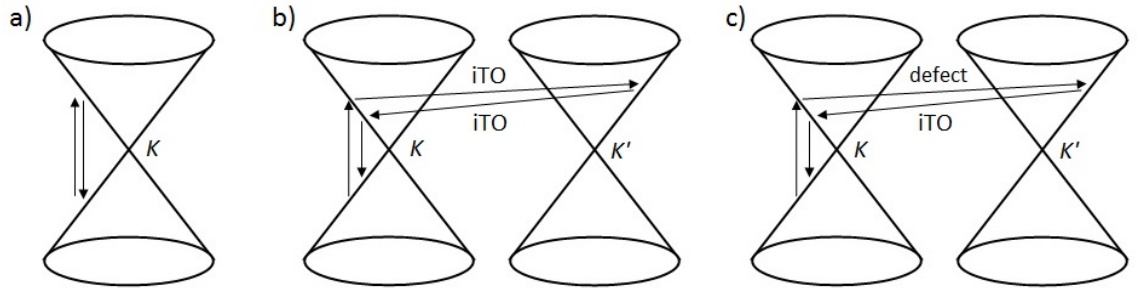
Figure 2.8: (a) G band first order Raman Scattering process from an iLO or iTO phonon mode. (b) $2D$ band DR process, inelastic scattering occurs from two iTO phonons at different Dirac points K and K'. (c) D band DR process, elastic scattering occurs off a defect site at K followed by inelastic scattering off an iTO phonon at a K'.

As a result of the significantly different processes which produce the D, $2D$ and G

bands, a large amount of information can be inferred from their relative intensities. For example, by studying the ratio of $2D$ to G peaks, an estimate of the thickness of the graphene present on the surface can be obtained, as the relative abundances of two and three dimensional graphite phases significantly affect the Raman lineshape [21]. Furthermore, when studying graphene grown on SiC, the attenuation of the Raman signal from the substrate can also provide a graphene thickness estimate [22]. This is due to changes in the number of layers resulting in differences in the resonant scattering processes and subsequent changes in Raman peak shape and intensity [23]. Furthermore, the D band also provides valuable information on graphene quality. Due to the requirement for elastic scattering from a defect site, the relative intensity of the D peak at 1350 cm^{-1} compared with that of the G band, can be used to approximate the level of disorder present on the surface [24,25]. Further information can be obtained from weaker peaks, such as the D' band at 1620 cm^{-1}, however their analysis is beyond the scope of this thesis.

2.5 Scanning Electron Microscopy

2.5.1 Imaging

First invented in 1938 [27] and further developed in the 1950s [28–30] the scanning electron microscope (SEM) has become a highly effective tool for imaging surfaces in many different scientific fields [31,32]. SEM probes the surface of a material with a beam of medium energy (1-50 kV) electrons [33]. The interaction of the beam with the material produces a number of signals which can be measured to produce a pixel within the image of the surface at that point. The beam is rastered back and forth to build up a complete image of the surface. The arrangement of the magnetic lenses can be seen in figure 2.9, in which the electron beam passes into the column and is concentrated, via a condenser lens. The beam then passes into an objective lens which focusses the incident beam into a precise probe of diameter, d. The magnetic lenses produce a rotationally symmetric magnetic field which the electron beam passes through. This causes electrons travelling through the magnetic field to feel a force allowing them to be carefully directed by small changes in the magnetic field to form a highly focussed beam.

In theory this allows for a minimum probe size of 5 nm [26], however in practice a number of imaging aberrations significantly increase this value. Both spherical
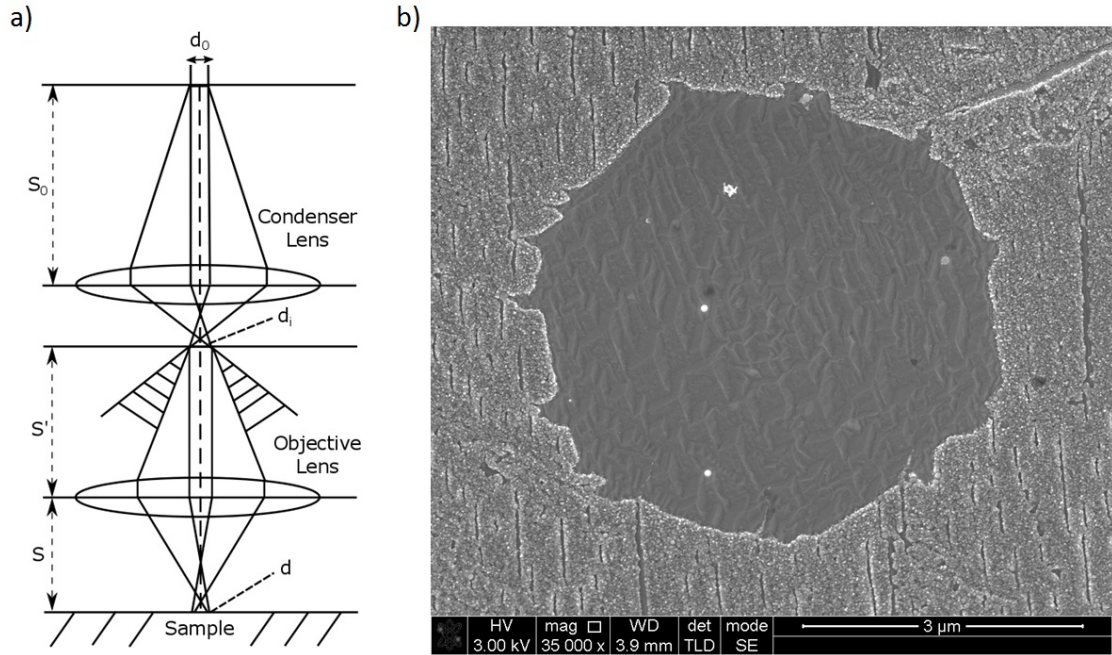
Figure 2.9: (a) Schematic diagram of ray traces in a typical SEM, ray divergence is exaggerated for clarity. Adapted from reference [26]. (b) SEM image showing 3D contrast of a graphene flake grown on Cu foil. Cu facets can be observed protruding from the surface under the graphene, whilst the graphene flake appears indented compared to the surrounding layer of oxidation.

aberrations, caused by electrons travelling further out from the optical axis being focussed significantly more than those closer to it; and chromatic aberrations, produced by slight differences in electron energy or variations in the magnetic field creating different focal points, act to blur the image. Slight asymmetries in the magnetic lenses can also cause astigmatism, however, with careful adjustment these limitations can be accommodated to ensure that a clear image is obtained. Despite these limiting factors, SEMs provide a substantially higher level of magnification than optical microscopes, accompanied by excellent depth of focus, as seen in figure 2.9(b). This is the consequence of the beam geometry which ensures a large depth ($\sim$2 μm), in comparison to the probe size ($\sim$5 nm), remains in reasonable focus around the area of optimal imaging.

As discussed above, in order to produce an image the electron beam is focussed on the surface and the signals from various electron-material interactions are measured. The region within the material where the beam interacts is known as the interaction volume (Fig. 2.10). This volume depends on a number of factors including the beam energy, spot size, angle of incidence and the material. The main SEM imaging methods involve the collection of secondary electrons (SE) and backscat-

tered electrons (BSE) which, as figure 2.10 indicates, allows a detailed image to be built up based on the interaction of electrons within the first 2 μm of the material surface. Secondary electrons are produced via inelastic collisions within the material, specifically with weakly bound electrons which may be ejected. The ejected electrons typically have an energy of $E \leq 50$ eV, meaning that those produced close to the surface will have enough energy to overcome the work function of 2-6 eV, escape the material and be measured [33]. Secondary electrons produced at lower depths are subject to further scattering from atomic nuclei and electrons and can recombine with the holes also produced by the electron beam, resulting in a significantly lower probability of escape from the material. This causes the signal produced by secondary electrons to be highly surface sensitive and ideal for imaging graphene domains on Cu substrates.
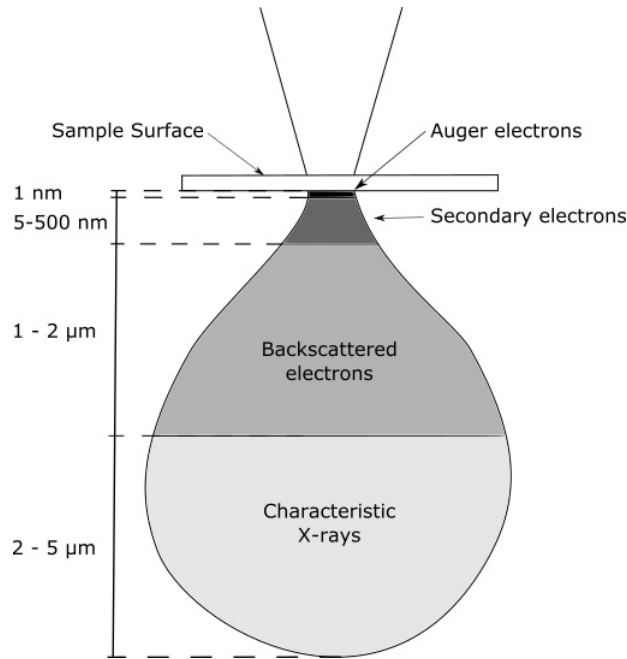
Figure 2.10: Schematic diagram of the interaction volume for electrons incident on a material. The penetration of electrons to different depths produces different imaging signals. Adapted from references [33, 34].

In contrast to the interactions which produce SE, elastic scattering events are far more probable. Electrons are generally either Rutherford scattered, resulting in large changes in direction, or perform multiple scattering in which a large number of small angle deviations occur. These scattering events and subsequent changes in direction can lead to electrons returning to the surface, where they escape and are measured. Small changes occur in the energy of the back scattered electrons due to inelastic collisions during their route through the material; this produces a signal from the BS electrons that is dependent on the path taken. The depth to which

the beam of electrons can penetrate is strongly dependent on the materials atomic number (Z), with larger Z materials producing significantly more scattering near the surface and therefore a higher BSE signal, whilst lower Z materials have larger penetration depths, at which point electrons are considerably less likely to escape [35, 36]. As such, BSE gives excellent contrast based on the different elements present. The diffraction of BSEs can also provide further information about the materials present, as discussed in section 2.5.2. Further signals such as Auger electrons and characteristic x-rays are also produced by the incident electron beam however, these will not be discussed further as they are not used within this thesis for the imaging of graphene.

2.5.2 Electron Back-Scatter Diffraction

As discussed above, BSEs are produced when electrons from the SEM probe scatter from atoms on and near the surface of a sample and are subsequently measured. Although BSEs are often used for elemental and topographic contrast images, they can also provide crystallographic information about the sample. This technique is referred to as electron backscatter diffraction (EBSD). EBSD allows for the micro-crystal structure of a sample to be identified by measuring BSEs that exit at, or close to, the Bragg diffraction angle. The diffraction of electrons produces Kikuchi lines, on a phosphor screen, which reflect the crystal phase of the substrate (Fig. 2.11) [37]. Therefore, with prior knowledge of the sample material the crystal phase close to the surface can be identified. Furthermore, by rastering across the surface and obtaining the diffraction pattern at each point a complete map of crystal orientations can be built up (Fig. 2.11(b) and (c)). Pole figures can also be constructed for each point post crystal mapping to show the different contributions to diffraction at each point on the surface, this reveals further micro-crystal structure that may be present below the surface. For graphene growth on Cu this technique allows crystal structure below individual domains to be identified, such that the effect of substrate structure on growth can be easily studied [38].

2.6 Scanning Tunnelling Microscopy

Since its first use by Binning *et al.* [39] to observe the (1×2) surface of a Au(110) crystal, in 1982, scanning tunnelling microscopy (STM) has become one of the most
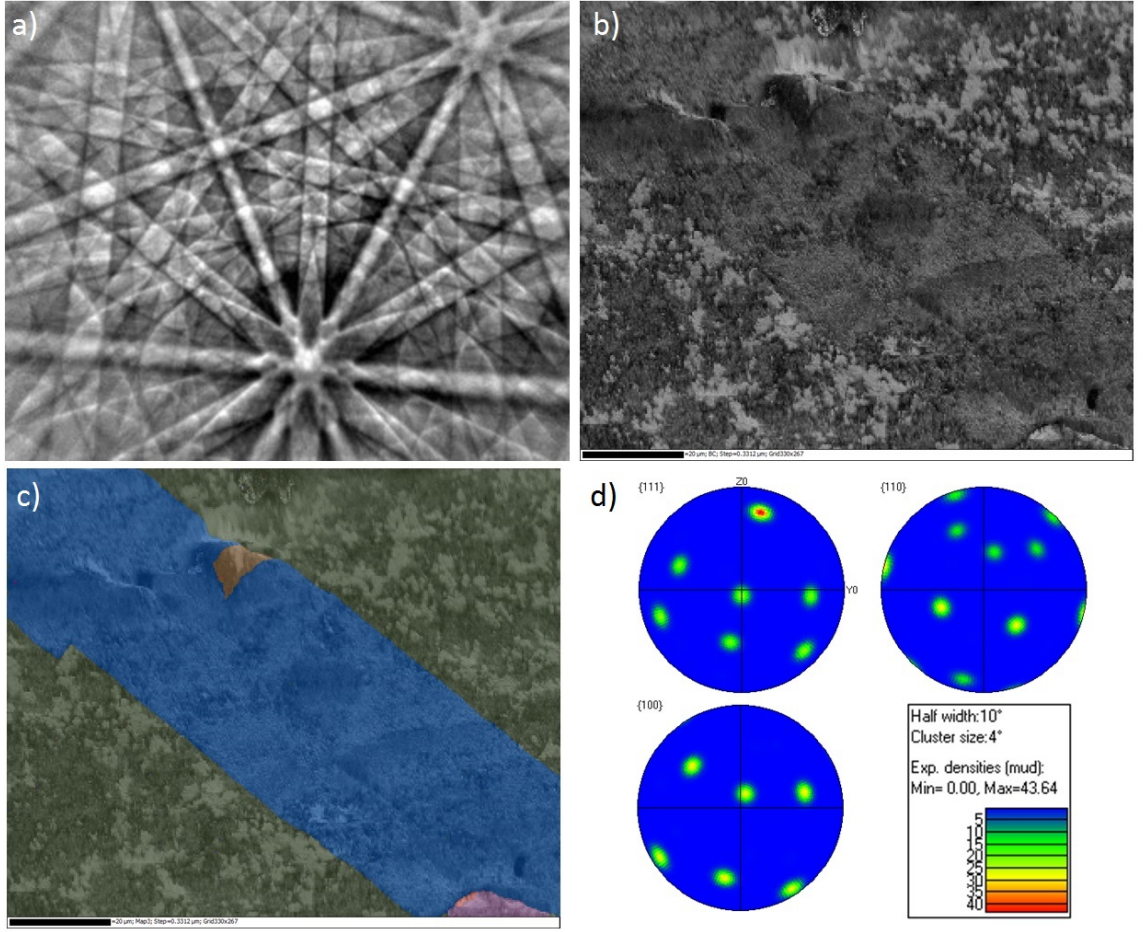
Figure 2.11: (a) Kikuchi diffraction lines obtained from a Cu foil at beam energy E = 20 keV. (b) Standard SEM image of a Cu foil after graphene growth, taken at E = 30 keV. (c) EBSD crystal orientation map overlayed onto the SEM image in part (b) showing four different Cu faces. (d) Pole figures obtained from a point in the dark green area of the image (c) showing the relative contributions from Cu(111), (110) and (100) faces.

effective and widely used surface science techniques. An STM system consists of an atomically sharp metal tip controlled by a piezo-tube allowing for movement sensitivity of the order 10^{-4} Å (Fig. 2.12). The tip is lowered to within a few Ångströms of the surface at which point the respective wavefunctions of the tip and the surface overlap and electrons can quantum mechanically tunnel across the potential barrier. As tunnelling occurs simultaneously from the tip to the surface and vice versa, a bias voltage is applied to produce a net current in which electrons close to the Fermi energy of the negatively biased tip (sample), tunnel to unoccupied states in the positively charged sample (tip). This current has been found to depend exponentially on the tip-surface spacing [40], hence small changes in separation (the tunnelling barrier width), result in large changes in the current. This can be seen

in equation 2.7, in which $I(E)$ is the tunnel current; L is the tip-surface spacing; m is the electron mass; ϕ is the material workfunction and $\hbar$ is the reduced Plancks constant. By rastering back and forth an image of the surface can be produced.
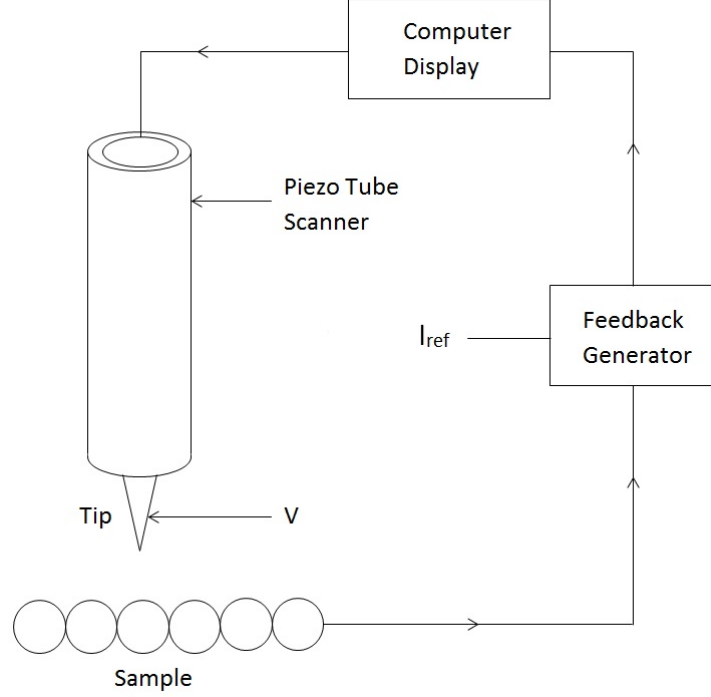
Figure 2.12: Schematic diagram of an STM. The tunnel current measured through the sample acts as a feedback loop, controlling the z distance to prevent tip crashing.

$$I(E) \propto |\Psi(z)|^2 = |\Psi(0)|^2 \; e^{-2\kappa L} \tag{2.7}$$

$$I(E) \propto e^{-2L\sqrt{2m\phi/\hbar^2}} \; . \tag{2.8}$$

The topographic image obtained is not a true description of the physical surface, but rather a mapping of the local density of states (LDOS). As a result, precautions are required when interpreting data as many factors can affect the LDOS other than the atomic/molecular structure of the surface. Furthermore, changes to the tunnelling current may occur due to various interactions with the surface and hence the height of features observed may not reflect the true surface morphology. For example, insulating material adsorbed to the surface will appear as a pit like structure despite physically protruding from the surface. Finally, the dimensions of the STM tip itself can significantly modify the image obtained, considerably reducing lateral resolution. This is a result of the STM profile being the convolution of the tip and the surface feature, an example can be seen in Fig. 2.13. This issue can be overcome through

careful calibration on a known surface structure such as a step edge. If the step is assumed to be a discontinuity, then deconvolution of the step line profile can allow the tip shape to be extracted. Alternatively, an approximate tip radius may be obtained via equation 2.9 [41], in which R_{eff} is the effective tip radius; L is the apparent width of the step; and h is the height of the step:

$$R_{\text{eff}} = (L^2 + h^2)/2h \ .$$
(2.9)
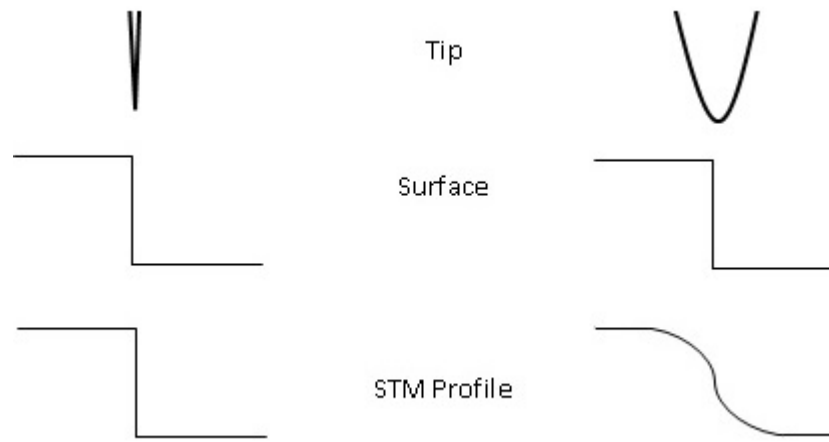
Figure 2.13: The effect of tip sharpness on STM line profiles. An atomically sharp tip is shown on the left and a rounded tip on the right.

Two different imaging modes can be used to obtain STM images: Constant current and constant height. Constant current mode causes the tip to track the height of the sample maintaining a constant spacing between the tip and the surface whilst scanning. This mode allows for rough surfaces to be imaged effectively, whilst preventing damage to the tip through collisions with protrusions. This is achieved via a feedback loop that allows for continued height adjustment at each point. This mode of imaging requires a longer scan time due to constant vertical adjustments made by the piezo. An image is produced by tracking the movement of the tip. In contrast, in constant height mode the vertical piezo positioning does not change. By measuring the changes in current at each point an image is produced. This method allows for images to be obtained faster, however, smooth sample surfaces are required to prevent collisions between the tip and the surface and subsequent damage to both.

2.7 Scanning Tunnelling Spectroscopy

Although predominantly used for imaging, the STM can also provide information on electronic structure through the technique scanning tunnelling spectroscopy (STS). The implementation of this technique was in fact one of the main motivations for the production of the first STM by Binning *et al.*, however tunnelling spectroscopy's origins date back much further, to the use of metal-insulator-metal (MIM) junctions which showed that the amplitude of electron transfer, also known as the tunnelling matrix element M was directly related to the wavefunctions of the materials at their respective surfaces, when at a set separation determined by the insulating layer [39, 42, 43]. This results in M being described by a surface integral, mapping the separation of the two materials:

$$M = \frac{\hbar}{2m} \int_{z=z_0} \left(\chi^* \frac{\partial \psi}{\partial z} - \psi \frac{\partial \chi^*}{\partial z} \right) dS \ , \tag{2.10}$$

in which the two material wavefunctions are ψ and χ, the separation distance is z and m is electron mass. This leads to the probability (w) of tunnelling from state ψ to state χ being described by:

$$w = \frac{2\pi}{\hbar} |M|^2 \delta(E_\psi - E_\chi) \ , \tag{2.11}$$

where the delta function ensures tunnelling can only occur between equal energy states.

The MIM junction approach is analogous to the STM based technique as the tip and sample provide the metal/conducting electrodes whilst the gap between the tip and surface provides an easily controllable insulating layer. As such, the results from these experiments are comparable to STS. Taking this into account, the tunnelling current between the tip and sample surface, or vice-versa, can be obtained by summing over the states of both the tip and sample from which tunnelling will occur:

$$I = \frac{4\pi e}{\hbar} \int_{-\infty}^{\infty} [f(E_F - eV + \epsilon) - f(E_F + \epsilon)] \times \rho_s(E_F - eV + \epsilon) \rho_T(E_F + \epsilon) |M|^2 d\epsilon \ , \tag{2.12}$$

where $f(E_F\text{-}eV + \epsilon)$ and $f(E_F + \epsilon)$ are the Fermi distribution functions of the tip and sample, whilst ρ_s and ρ_T are the DOS of the sample and tip respectively. This can be significantly simplified when the tip-surface distance is fixed, by switching the STM feedback loop off, ensuring that M changes insignificantly during spectroscopic

measurement. Furthermore, if the energy resolution is large compared with $K_\mathrm{B}T$, the Fermi distribution functions can be assumed to be steps. This results in the tunnel current being directly proportional to the DOS ρ_s and ρ_T:

$$I \propto \int_0^{eV} \rho_s(E_F - eV + \epsilon)\rho_T(E_F + \epsilon)d\epsilon \ . \tag{2.13}$$

With prior knowledge of a constant reproducible tip DOS, the dynamic tunnelling conductance is directly proportional the sample DOS [43]:

$$\frac{dI}{dV} \propto \rho_s(E_F - eV + \epsilon) \ . \tag{2.14}$$

Having attained the expected DOS of a sample, any changes observed in specific areas can then be assigned to tunnelling into localised states.

Due to the sensitive nature of STS measurement, a large number of factors need to be taken into account when analysing spectra. The first of these is the state of the STM tip. As indicated earlier due to the spectrum's dependence on the DOS of both the sample and tip, the requirement of a stable and reproducible tip DOS is vital. As this is challenging to maintain throughout the course of an experiment without highly specialised tip treatments [44], differences in subsequent scans may be used to determine if spontaneous tip restructuring has occurred. By taking spectra on a clear area of the sample before movement to an area of interest and then following with a further measurement on a clear region; should the first and final spectra look identical then the differences observed on the area of interest can be assumed to be due to the differences in the LDOS of the sample, rather than tip reconstruction. Other factors also play a large role in the shape of tunnelling spectra, specifically the tip surface spacing has been found to significantly affect resolution [45]. This is due to the tip breaking the symmetry of the surface and creating a localised state, which results in a loss in energy resolution the closer the tip is to the surface, broadening the sample DOS features as the tip-surface separation becomes smaller. This can be accounted for by setting the tip-surface spacing to a larger distance to ensure energy resolution is maintained. Finally, temperature also has a large effect on spectroscopic resolution, as the energy distribution of the tip will have a spread of $2K_\mathrm{B}T$. This combined with the sample also having a energy distribution spread of $2K_\mathrm{B}T$ will result in a total variation of $4K_\mathrm{B}T$, or 0.104 eV at room temperature. Therefore, when analysing spectra, features smaller in width than this value will be the result of noise rather than real peaks in the LDOS. This limit on energy resolution can be improved by lowering the temperature during measurement to

reduce the energy distribution spread [46].
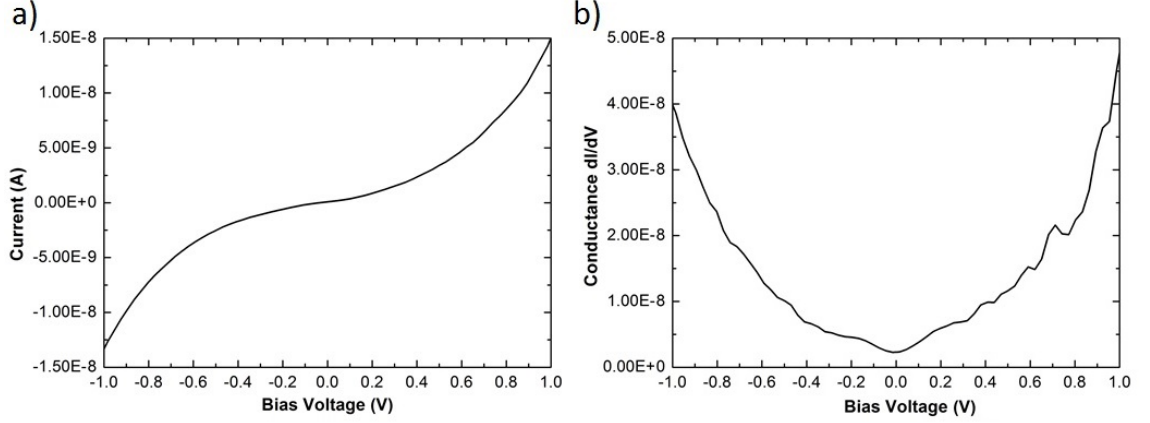
Figure 2.14: (a) *I-V* curve obtained from an area of pristine graphite lattice. (b) Resultant spectra from the differentiation of the *I-V* curve in (a) showing the parabolic graphite DOS.

Figure 2.14(a) shows a typical *I-V* curve obtained on a pristine area of HOPG, which exhibits a roughly cubic behaviour with tunnelling from the sample to the tip observed at negative biases, whilst positive biases result in tunnelling from the tip to the sample. Differentiation of the *I-V* curve produces the parabolic DOS expected for graphite, in which the number of states close to the Fermi level ($V = 0$) drops to a minimum, but non-zero value, characteristic of semi-metallic behaviour (Fig. 2.14(b)). Therefore, any features observed that break the symmetry of the graphite spectra around this point are the result of differences in the LDOS at that point compared with the DOS of the pristine lattice. In contrast, ML graphene typically shows a symmetric linear electronic dispersion with exactly zero density of states at the Fermi level [47]. However, when observing few-layer (FL) graphene on SiC, the combination of multiple graphene layers and the insulating substrate results in a band gap opening at the K-point [48]. This results in the obtained STS spectrum showing similarities to typical graphite spectra. As such, when taking tunnelling spectra of areas of interest on graphene, non symmetric features and shifts in the DOS can once again be assigned to local electronic effects.

2.8   Summary

In summary, the theory behind the various experimental techniques utilised in this thesis along with their specific advantages and potential limitations was discussed.

Further information regarding the use of each technique on each graphene-substrate system is provided in the relevant chapter.

2.9   References

[1] H. Lüth, *Solid Surfaces, Interfaces and thin Films*, Springer (2001).

[2] P. Auger, *J. Phys. Radium*, **6**, 205–208 (1925).

[3] J. J. Lander, *Phys. Rev.*, **91**(6), 1382–1387 (1953).

[4] L. N. Tharp and E. J. Scheibner, *J. Appl. Phys.*, **38**(8), 3320 (1967).

[5] R. E. Weber and W. T. Peria, *J. Appl. Phys.*, **38**(11), 4355–4358 (1967).

[6] P. W. Palmberg and T. N. Rhodin, *J. Appl. Phys.*, **39**(5), 2425–2432 (1968).

[7] J. C. Vickerman, *Surface Analysis*, Guildford: John Wiley and Sons (1998).

[8] D. Briggs and M. P. Seah, *Practical Surface Analysis*, Chichester: Wiley (1990).

[9] H. E. Bishop and J. C. Rivére, *J. Appl. Phys.*, **40**(4), 1740–1744 (1969).

[10] J. C. Lascovich, R. Giorgi and S. Scaglione, *Appl. Surf. Sci.*, **47**(1), 17–21 (1991).

[11] S. Mroczkowski and D. Lichtman, *Surf. Sci.*, **131**(1), 159–166 (1983).

[12] S. N. Luxmie, P. J. Fisher, R. M. Feenstra, G. Gu and Y. Sun, *J. Elec. Mater.*, **38**(6), 718–724 (2008).

[13] C. Davisson and L. H. Germer, *Phys. Rev.*, **30**(6), 705–740 (1927).

[14] Omicron Nanotechnology, *Auger Electron Spectroscopy with Four-Grid SPEC-TALEED* (2000).

[15] W. A. de Heer, C. Berger, X. Wu, P. N. First, E. H. Conrad, X. Li, T. Li, M. Sprinkle, J. Hass, M. L. Sadowski, M. Potemski and G. Martinez, *Solid State Commun.*, **143**(1-2), 92–100 (2007).

[16] C. Riedl, A. A. Zakharov and U. Starke, *Appl. Phys. Lett.*, **93**(3), 033106 (2008).

[17] G. Xu, X.-Q. Shi, R. Q. Zhang, W. W. Pai, H. T. Jeng and M. A. V. Hove, *Phys. Rev. B*, **86**(7), 1–7 (2012).

[18] C. V. Raman and K. S. Krishnan, *Nature*, **121**(3048), 501–502 (1928).

[19] M. D. Levenson and S. S. Kano, *Non-linear Laser Spectroscopy*, Academic Press Inc. (1988).

[20] L. M. Malard, M. A. Pimenta, G. Dresselhaus and M. S. Dresselhaus, *Phys. Reports*, **473**(5-6), 51–87 (2009).

[21] L. G. Cançado, K. Takai, T. Enoki, M. Endo, Y. A. Kim, H. Mizusaki, N. L. Speziali, A. Jorio and M. A. Pimenta, *Carbon*, **46**(2), 272–275 (2008).

[22] S. Shivaraman, M. V. S. Chandrashekhar, J. J. Boeckl and M. G. Spencer, *J. Elec. Mater.*, **38**(6), 725–730 (2009).

[23] A. C. Ferrari, J. C. Meyer, V. Scardaci, C. Casiraghi, M. Lazzeri, F. Mauri, S. Piscanec, D. Jiang, K. S. Novoselov, S. Roth and A. K. Geim, *Phys. Rev. Lett.*, **97**(18), 187401 (2006).

[24] M. M. Lucchese, F. Stavale, E. H. Martins, Ferreira, C. Vilani, M. V. O. Moutinho, R. B. Capaz, C. Achete and A. Jorio, *Carbon*, **48**(5), 1592–1597 (2010).

[25] A. C. Ferrari and D. M. Basko, *Nature Nanotechnol.*, **8**(4), 235–246 (2013).

[26] J. I. Goldstein and H. Yakowitz, *Practical scanning electron microscopy*, Plenum Press (1975).

[27] M. V. Ardenne, *Z. Phys.*, **109**, 553–572 (1938).

[28] P. McMullan, *Advances in Imaging and Electron Physics*, **133**(1381), 59–91 (2004).

[29] K. C. A. Smith and C. W. Oatley, *Brit. J. Appl. Phys.*, **6**, 391–399 (1955).

[30] E. M. S. et al., *J. Appl. Phys.*, **19**(11), 118–126 (1957).

[31] Y. Chen, J. Tarchitzky, J. Brouwer, J. Morin and A. Banin, *Soil Sci.*, **130**(1), 49–55 (1980).

[32] Q. Cheng, J. Tang, J. Ma, H. Zhang, N. Shinya and L.-C. Qin, *Carbon*, **49**(9), 2917–2925 (2011).

[33] J. I. Goldstein, D. E. Newbury, P. Echlin, D. C. Joy, C. Fiori and E. Lifshin, *Scanning Electron Microscopy and X-ray Microanalysis*, Plenum Press (1981).

[34] T. E. Everhart, R. F. Herzog, M. S. Change and W. J. DeVore, *Proc. 6th Intl. Conf. on X-ray Optics and microanalysis*, Tokyo Press (1972).

[35] P. Duncumb and P. K. Shields, *Bti. J. Appl. Phys.*, **14**, 626–634 (1963).

[36] K. Murata, T. Matsukawa and R. Shimizu, *Jap. J. Appl. Phys.*, **10**(6), 678–686 (1971).

[37] H. Wilman, *Proc. Phys. Soc.*, **60**(340), 341–360 (1948).

[38] J. D. Wood, S. W. Schmucker, A. S. Lyons, E. Pop and J. W. Lyding, *Nano Lett.*, **11**(11), 4547–4554 (2011).

[39] G. Binning, H. Rohrer, C. Gerber and E. Weibel, *Phys. Rev. Lett.*, **49**(1), 57–61 (1982).

[40] G. Binning, H. Rohrer, C. Gerber and E. Weibel, *Appl. Phys. Lett.*, **40**(2), 178–180 (1982).

[41] L. P. Biró, J. Gyulai, P. Lambin, J. B. Nagy, S. Lazarescu, G. I. Mark, A. Fonseca, P. R. Surhán, Z. Szekeres, P. A. Thiry and A. A. Lucas, *Carbon*, **36**(5), 689–696 (1998).

[42] J. Bardeen, *Phys. Rev. Lett.*, **6**(2), 57–59 (1961).

[43] C. J. Chen, *Introduction to Scanning Tunneling Microscopy*, Oxford University Press (1993).

[44] R. M. Feenstra, J. A. Stroscio and A. P. Fein, *Surf. Sci.*, **181**(1-2), 295–306 (1987).

[45] P. Avouris and I. W. Lyo, *Surf. Sci.*, **242**(1-3), 1–11 (1991).

[46] T. Matsui, H. Kambara, Y. Niimi, K. Tagami, M. Tsukada and H. Fukuyama, *Phys. Rev. Lett.*, **94**(22), 226403 (2005).

[47] X. Li, W. Cai, J. An, S. Kim, J. Nah, D. Yang, R. Piner, A. Velamakanni, I. Jung, E. Tutuc, S. K. Banerjee, L. Colombo and R. S. Ruoff, *Science*, **324**(5932), 1312–1314 (2009).

[48] S. Y. Zhou, G.-H. Gweon, A. V. Fedorov, P. N. First, W. A. de Heer, D.-H. Lee, F. Guinea, A. H. C. Neto and A. Lanzara, *Nature Mater.*, **6**(10), 770–775 (2007).

Chapter 3

Experimental Methods and Instrumentation

In this chapter, the equipment and sample preparation techniques used to obtain the data presented in this thesis are described. STM tip production methods are also outlined.

3.1   Instrumentation

3.1.1   JIPELEC Rapid Thermal Processor, Newcastle University, UK
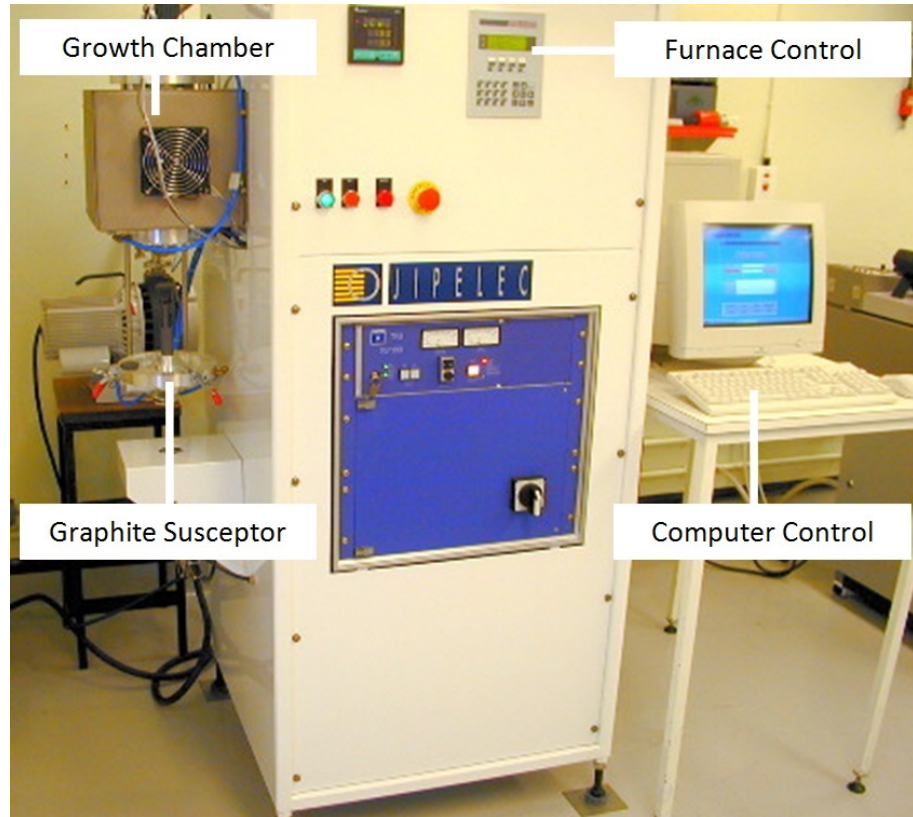
Figure 3.1: Upgraded JIPELEC rapid thermal processor at Newcastle Univesity. Key components of the system are labelled.

The graphene samples measured in Chapters 4, 5 and 6 were produced in an upgraded JIPELEC rapid thermal processor specifically modified for the controlled sublimation of Si from SiC wafers [1,2]. The furnace utilises radio frequency (RF) inductive heating of a graphite susceptor, allowing for temperatures as high as 2000 °C to be obtained. A helical coil produces a rapidly oscillating electromagnetic field which in turn induces eddy currents within the graphite susceptor. The high resistance of the graphite results in significant resistive heating of the susceptor. Used in conjunction with an optical pyrometer-controlled feedback system, the high degree of control over the heating mechanism results in a number of advantages, such as highly tunable heating and cooling ramp rates, up to 15 C°/s and excellent heating stability and uniformity, with temperatures fixed to within ±2 C° of their specified

values. Different growth atmospheres may be produced through gas inlets controlled via internal mass flow controllers. Heating was programmable via the front mounted control panel, allowing for simple heating cycles. However, for more complete control, heating and atmospheric conditions were set via the computer control allowing for programmed "recipes" to be written and implemented, fixing all aspects of the growth process.

3.1.2 Omicron Nanotechnology UHV VT-SPM System, Durham University, UK
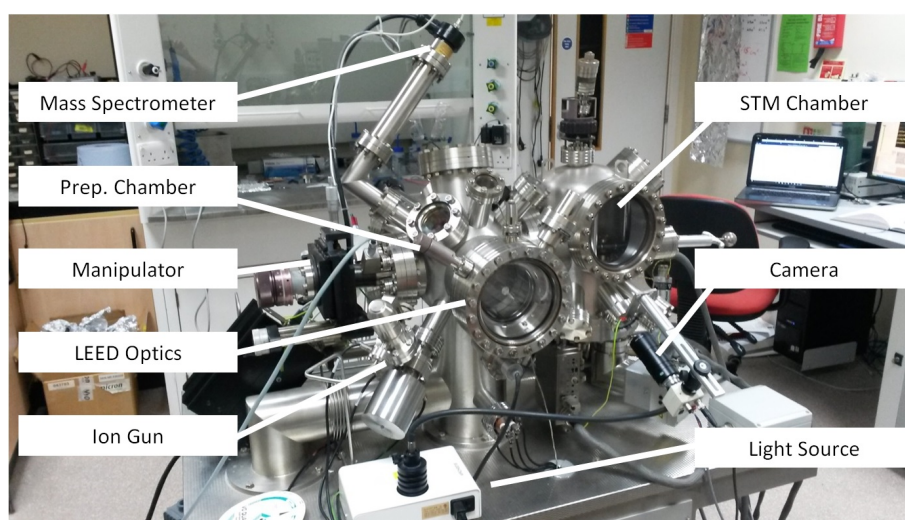
Figure 3.2: UHV VT-SPM system in the Department of Physics, Durham University. Various components of the system are labelled.

The majority of measurements were conducted at Durham University using an Omicron Nanotechnology ultra-high vacuum (UHV) variable temperature scanning probe microscope (VT-SPM) system. The system consists of a fast entry load lock (FEL), a preparation chamber and an STM analysis chamber. The presence of the FEL allows for easy transfer of samples from atmospheric pressure to UHV without the requirement of breaking vacuum. In order to maintain the vacuum at a base pressure of 5×10^{-10} mbar, a rotary backed turbo pump and ion pump run continuously; titanium sublimation pumps (TSP) also run intermittently to further reduce the pressure. A quadrupole mass spectrometer is also present to determine the residual gases present in the system or determine the composition of gas mixtures introduced into the system via a leak valve and gas handling line. The preparation chamber also allows for further sample processing and other measurement techniques

to be employed. The preparation chamber is fitted with a SPECTA-LEED optics and electron gun allowing low energy electron diffraction (LEED) and Auger electron spectroscopy (AES) to be performed. Furthermore, a Ag evaporation source and an Ar^+ ion gun are also present such that silver deposition and ion bombardment may be conducted. Finally, the sample can be manoeuvred into position for each technique via a manipulator with XYZ and rotational motion. Graphene samples are mounted on Omicron sample holders, which consist of a tantalum spade base with the sample held in place by a small tantalum strip. The high melting points of the sample plates allow for effective heating of samples via the resistive heating mechanism in the manipulator.

VT-SPM

STM measurements performed in all research Chapters were carried out using the VT-SPM system under UHV conditions. All STM images were obtained in constant current mode, using either manually cut Pt-Ir tips or etched tungsten tips as outlined in section 3.2.3. The VT-SPM is capable of atomic force microscopy (AFM), magnetic force microscopy (MFM) and STM with a temperature range of 25K to 750K possible via the combination of a liquid helium cryostat and a specialised heating sample holder using a ceramic boron-nitride heater.

The SPM consists of a single scanner tube on which the tip holder is mounted; the scanner is capable of a maximum of 12 μm $\times$ 12 μm with a maximum z travelling distance of 1.5 μm [3]. The scanner tube consists of a tube of a metallised lead zirconate titanate (PZT) ceramic which has been processed to produce a permanent electrical polarisation. This results in the tube exhibiting a strong piezoelectric effect [4]. The exterior of the tube is split into four quadrants which can have bipolar symmetric voltages applied to induce a torque. The torque produced leads to a bending of the piezoelectric tube resulting in the deflection of the STM tip. This high precision movement allows for a z resolution of better than 0.01 nm [3]. However, in order for this level or resolution to be obtained, vibration dampening is required to prevent damage to the STM tip; this is attained via suspension of the system by four soft springs which act as a vibration decoupling system. Any vibrations of the system are reduced using an eddy current damping mechanism which significantly reduces movement of the STM base plate. In order to reduce the level of electrical noise from the system, when obtaining images, the measured tunnelling current is preamplified and converted to a voltage. This produces an augmented signal which

is processed via the SPM control unit, along with the feedback loop, to ensure that a constant tunnelling current is maintained as the tip scans across the sample.

Manual control over the STM tip, including positioning and approaching is performed using the Matrix software [5]. Furthermore, all scan settings such as bias voltage, tunnel current and scan size are also controllable via the Matrix user interface, allowing for careful regulation over all aspects of imaging. The Matrix software also allows for scanning tunnelling spectroscopy (STS) experiments to be performed with both single point spectroscopy and spectroscopic mapping settings. Similarly to imaging, all settings can be controlled within the Matrix user interface to control multiple aspects of the STS scan, such as the start and ending voltages, raster time and resolution. STS spectra produced are then processed and converted to allow for further analysis.

LEED

The LEED patterns obtained in Chapters 4 and 5 were produced using the SPECTA-LEED optics and taken at normal incidence. Electrons were produced by a LaB_6 filament with 1.23 A of current, producing a beam with a controllable energy range of 50 eV to 300 eV, though for other techniques, significantly higher beam energies are obtainable [6]. The LEED optics are encased in Mu-metal shielding with three tungsten retarding grids and one phosphor grid which focus and produce a clear LEED pattern from the diffracted electrons. The patterns obtained were then recorded externally using a tripod stabilised, Canon EOS 1100D-SLR camera using a 20 second exposure. All measurements were performed in a blacked out lab to ensure a clear pattern could be observed on the phosphor screen. All LEED patterns were filtered to remove traces of red light produced by the LEED control box.

AES

Auger spectra reported in Chapters 4 and 5 were obtained using the SPECTA-LEED optics and taken at normal incidence. As with LEED, electrons were produced by a LaB_6 filament by a current of 1.23 A. However, significantly higher beam energies of 2-3 keV are required to obtain the necessary signal to noise ratio required for Auger analysis. Auger electrons produced are captured by the retarding grids and converted into a voltage signals which are amplified and processed before being

transferred to the DATAuger data acquisition software [7, 8]. Auger scan parameters are also set via the DATAuger software allowing for control over start and end energies, dwell time, energy step and the number of scans. Optimisation of signals obtained can be achieved via the use of the fast scan mode to identify known peaks and set sensitivity levels and time constants. For measurements of graphene, optimisation was performed on the graphitic carbon peak at 271 eV.

Ion Bombardment

The ion bombardment performed in Chapter 6 in the UHV VT-SPM system used an Omicron ISE 5 ion gun and controller [9]. When bombarding a sample Ar gas was released into the chamber via a pinhole leak valve to allow precise control over chamber pressure. A pressure of 7.5×10^{-5} mbar was required in the chamber to produce a high enough concentration in the ion gun gas cell for ion production under the low incident beam energies needed. A voltage is applied between the gas cell anode and cathode to initiate a discharge. A magnetic field is applied longitudinally through the source region ensuring that electrons produced during the discharge follow a spiral path in the discharge volume, resulting in significantly more ion production [10]. Ar^+ ions are then removed from the gas cell via an aperture in the cathode plate. The ions proceed through a flight tube which focuses and adjusts the resultant beam. The ion dose (equation 3.1) can be closely controlled via internal measurement of the sample current and control over the beam energy and focus via the external controls. This allows dosage to be calculated as:

$$D(\mu C) = I_{\text{sample}}(\mu A) \times t(s) \ , \tag{3.1}$$

where D, I_{sample} and t, are the ion dose, sample current and bombardment time respectively. A starting beam energy of 2 keV is often used to commence ion production with a moderate focus often required. With a constant stable sample current, the beam energy and focus can be reduced to produce lower energy ions ideal for creating single defects in carbon nanostructures [11]. During the beam optimisation process, to prevent any unintended damage to the material, the sample is oriented away from the beam. To control the dose the sample is then quickly oriented normal to the beam direction for a short period of time and then rotated back to its original position.

Ag Deposition

Silver deposition was performed in the course of Chapter 7 achieved using an evaporation source consisting of a W filament wrapped in 99.99% purity Ag wire. The filament was formed at a temperature of 970 °C by passing a current of 12.2 A through the W wire. A large current was required for forming due to the large numbers of parallel circuits caused by the Ag wire prior to melting. Upon forming, a lower current of 7.9 A was passed through the filament to sublimate small doses of silver. The level of deposition was controlled by the period of time the filament was heated to the optimal deposition temperature, with longer periods resulting in thicker Ag layers.

3.1.3 Horiba Jobin Yvon LabRAM-HR Raman System, Newcastle University, UK
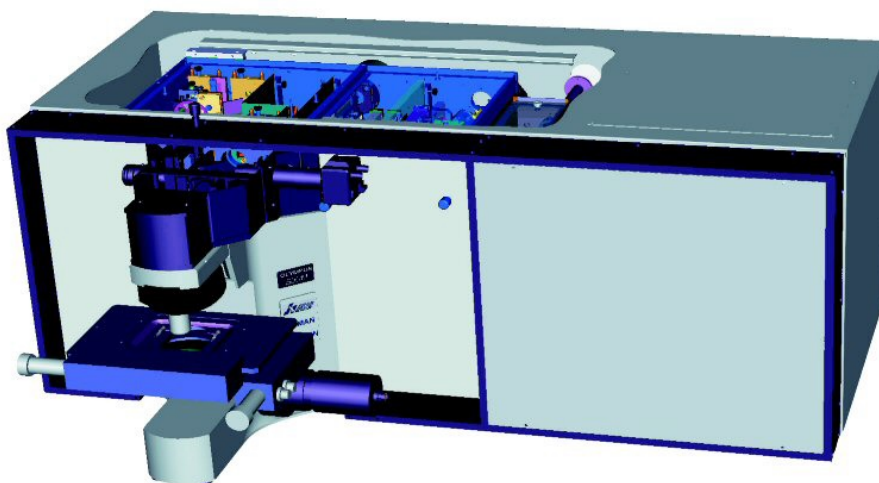
Figure 3.3: Cut-away diagram of the Horiba Jobin Yvon Raman Spectrometer at Newcastle University. [12]

The Raman Spectroscopy (RS) data presented in Chapter 4 were taken with a Horiba Jobin Yvon LabRAM High Resolution (HR) Raman Spectrometer at the University of Newcastle. The system consists of a 514.5 nm Ar^+ ion laser excitation source, a standard optical microscope, an internal optics system and the spectrometer itself, which includes a monochromator, photomultiplier, photon counter and recorder [12]. Samples required no special preparation.

The laser excitation source provides a coherent beam of monochromatic light

which is then focussed by the optical microscope, using a combination of the LabRAM software and four adjustable stems, onto the sample with a spot size of 700 nm. The beam excites the selected area of the surface resulting in a small proportion of the light being inelastically scattered. Scattered light was then collected and focussed by the internal optics onto the monochromator, via a notch filter which removes all elastically scattered light. This significantly reduces the noise on spectra allowing for the weaker Raman signals to be observed. The monochromated light is then amplified by the photomultiplier and counted and recorded to produce the Raman spectrum.

3.1.4   FEI Helios Nanolab 600, Durham University, UK
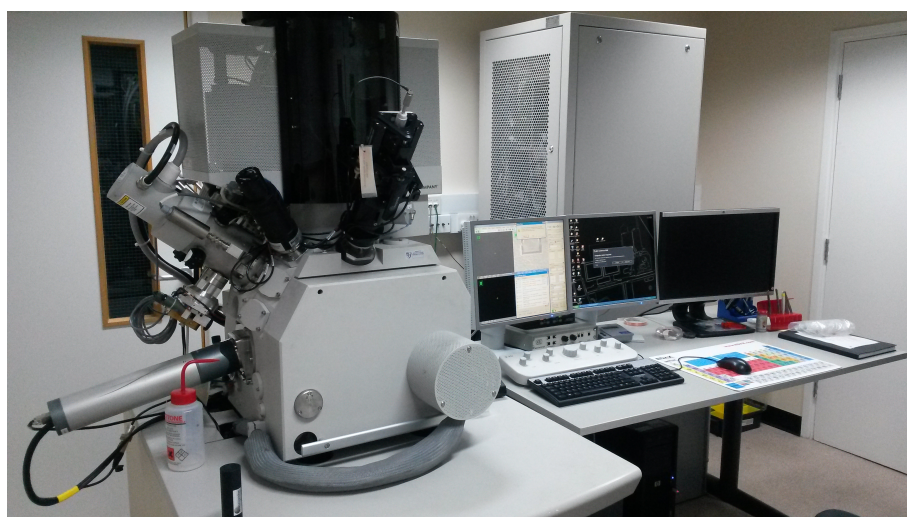
Figure 3.4: The FEI Helios Nanolab 600 SEM in the Department of Physics, Durham University.

Imaging

Scanning electron microscopy (SEM) performed in Chapter 7 was conducted using an FEI Helios Nanolab 600 dual beam system operating in SEM mode. Standard imaging of graphene grown on Cu was performed with a primary electron energy of 3-5 keV. Samples were mounted on specialised sample pucks, with graphene on Cu foils requiring no further sample preparation. Samples grown on evaporated Cu on SiO_2 required further preparation via a combination of silver paint and Cu tape to create a conductive path from the surface to the sample puck, this was due to the

insulating nature of the substrate preventing a sample current being measured.

The SEM contains a Schottky electron source, which produces electrons when heated at high temperatures via thermionic emission and an electric field induced at the source tip. An Elstar electron column directs and focusses the beam of electrons to a maximum resolution of 1.6 nm, onto the high precision 5-axis stage, which is capable of 360° rotation and XYZ translation, as well as 70° tilting. Finally, Elstar in-lens secondary electron (SE) and back-scatter electron (BSE) detectors as well as an Everhart-Thornley SE detector collect the signal from the sample to produce the image observed. Fine adjustments to imaging, and aberration correction are performed using a manual user interface (MUI) whilst the Helios NanoLab software allows complete control over the beam energy, sample positioning and detectors, with a choice of BSE and SE imaging modes possible.

Whilst imaging graphene on Cu substrates, preliminary focussing was performed at the edges of samples as the SEM was found to deposit material on the surface when imaging at high resolution (Fig. 3.5); the material corresponds to cracked hydrocarbons from the residual gases in the chamber. Once high resolution images were obtained, imaging was moved to a new area to avoid the now contaminated imaged area.
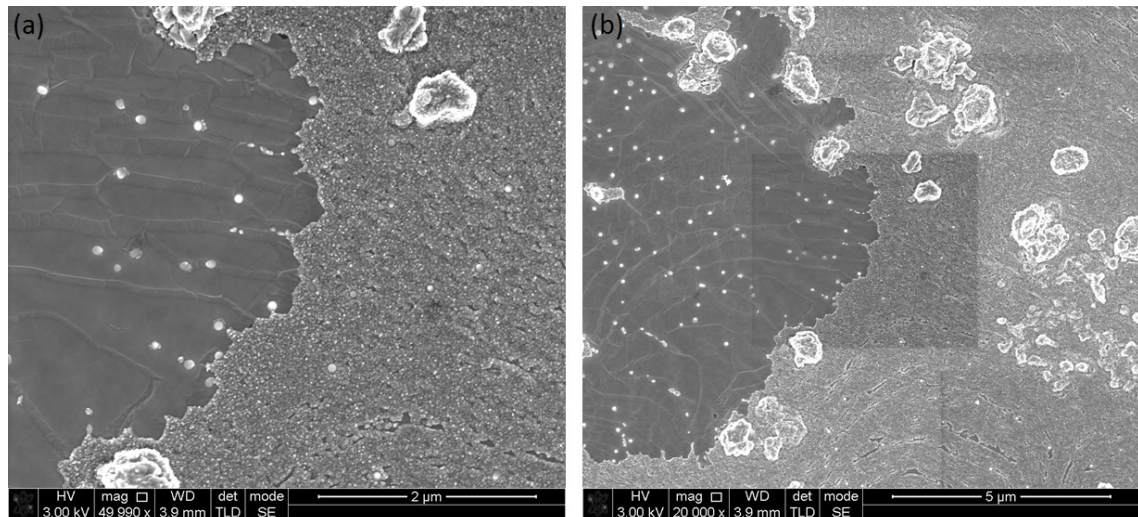
Figure 3.5: (a) SEM image of the edge of a graphene island grown on Cu foil. (b) Zoomed out image showing a dark rectangle of deposited material, caused by the electron beam, where image (a) was obtained.

EBSD

The crystallographic maps produced by Electron Back Scatter Diffraction (EBSD) in Chapter 7 were also obtained using the FEI Helios Nanolab 600 FIB SEM at Durham University. Samples were again placed on specialised pucks, however an alternate, angled stage was required. A specialised EBSD detector was brought into close proximity of the sample in order to collect an increased backscatter signal. Expected elemental crystallographic phases are selected prior to EBSD imaging to allow for easier identification of crystal orientations. A fast scan image is then obtained via the standard imaging technique, outlined above, and the EBSD patterns observed. A background is then obtained and subtracted to significantly reduce noise, improving the quality of the EBSD map. The electron beam then scans slowly across the surface of the sample in a raster pattern, with the backscattered electrons being collected via the EBSD detector, producing a crystallographic map of the surface. Further analysis of the EBSD maps was performed using the Mambo and Tango [13] programs to identify which crystal phases are present.

3.1.5 Hot-Wall Graphene Growth System, Durham University, UK
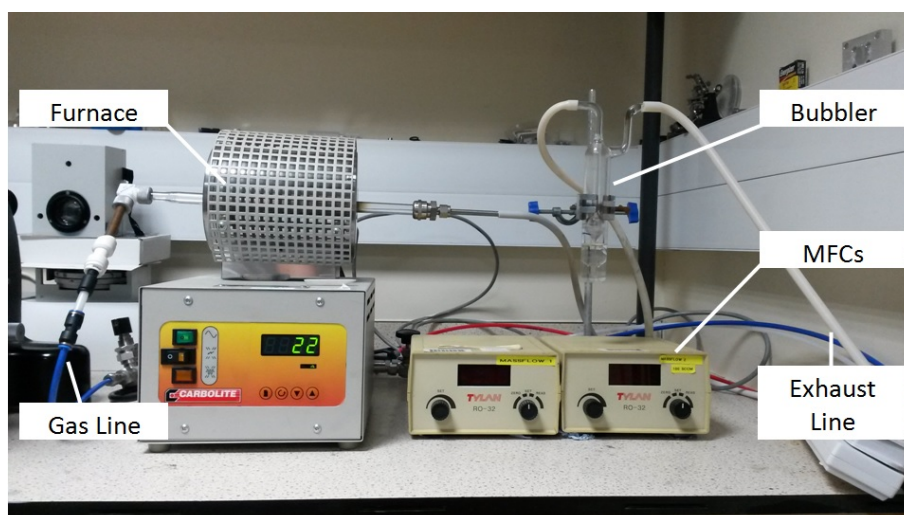
Figure 3.6: The home-built hot-wall graphene growth system in the Department of Physics, Durham University. Various components are labelled; full gas lines and MFC components are not visible.

The majority of the graphene grown on Cu substrates measured in Chapter 7

were produced in a home built hot-wall graphene growth system (Fig. 3.6). The system consists of a small Carbolite furnace with a 10 mm diameter quartz tube in which the sample is placed during growth. Growth temperature, ramp rate and cooling rate were all controllable via the furnace front control. A gas line connecting cylinders of 5% H_2/Ar and CH_4 was connected to one end of the quartz tube, whilst the other end is connected to a gas bubbler filled with oil to prevent atmospheric gasses entering the system from the exhaust direction. Gas flow was controlled by two Tylan RO-32 mass flow controllers (MFC), which ensure a consistent gas concentration inside the tube. On/off valves were also placed between the MFCs and the furnace to prevent any leakage of gases into the tube when not required. Gas is controllably let into the tube during heating, growth and cooling steps to produce graphene.

3.1.6 Cold-Wall Graphene Growth System, Durham University, UK

Further graphene samples in Chapter 7 were produced in a home built cold-wall graphene growth system (Fig. 3.7). The system consists of a bell jar enclosed main chamber attached to a rotary backed turbo pump operating at a base pressure of 1×10^{-6} mbar. The heating mechanism used comprises of electrical feed-throughs attached to two large Cu arms supporting a suspended graphite slab. A large current of 30 A was put through the slab causing resistive heating. Cu substrates were placed on top of the graphite slab to heat conductively, whilst a thermocouple was attached to the underside of the graphite to determine the temperature of the heater. 5% H_2/Ar and CH_4 gases, from cylinders, were controllably introduced to the system via Vacuum General Ultraflo MFCs.

3.2 Sample Preparation

3.2.1 Graphene Growth on SiC

The graphene samples used in the studies described in Chapters 4, 5 and 6 were prepared on 4H-SiC and 6H-SiC semi-insulating wafers, with zero off-cut angle and resistivity of $>10^9$ Ωcm, purchased from Cree, Inc. [14] and TankeBlue Semiconduc-
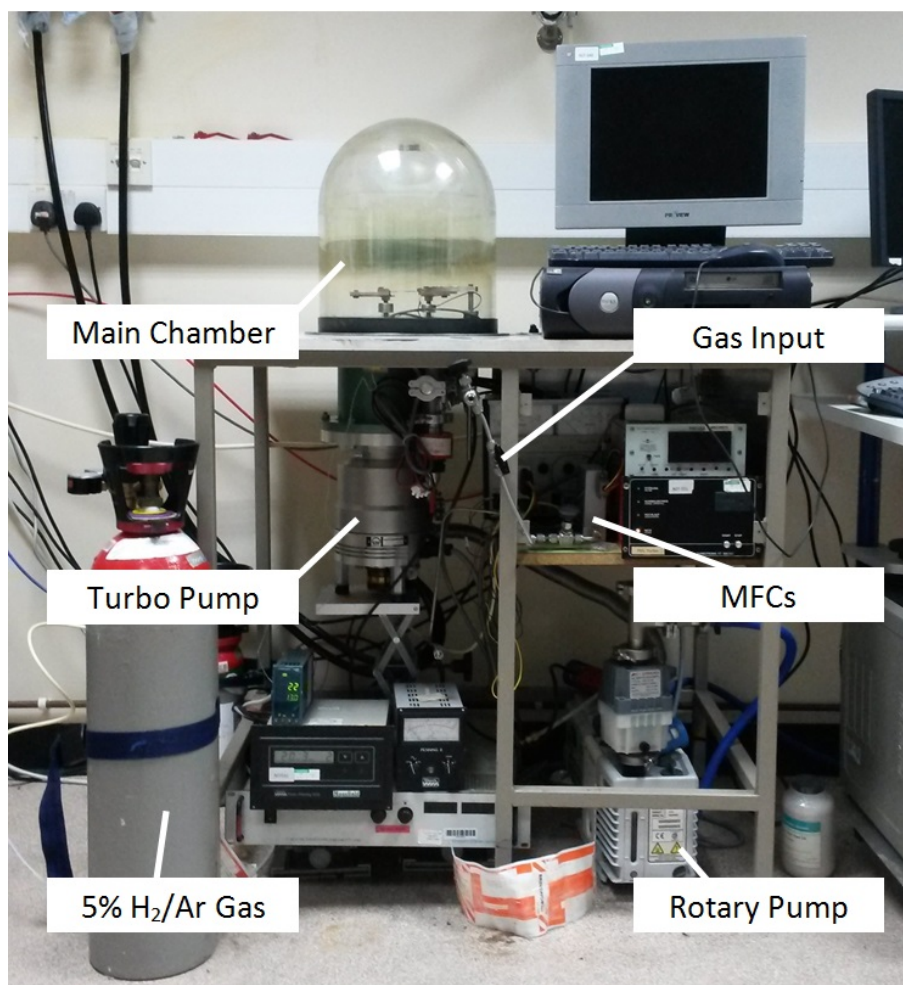
Figure 3.7: The home-built cold-wall graphene growth system. Various components have been labelled.

tor Co. Ltd [15] respectively. All substrates were prepared using acetone, piranha and RCA chemical treatments to remove all contaminants from the surface. Wafers were diced into 7×7 mm^2 segments for use in the rapid thermal reactor. The substrates were then subjected to high temperature etching at 1500 °C in 5% H_2/Ar forming gas followed by heating at 1200 °C to reconstruct the substrate surface ready for graphene growth [1]. Further details of the graphene growth are outlined in Chapter 4.

3.2.2 Graphene Growth on Cu

The graphene samples in Chapter 7 were grown on 99.9% purity, 0.2 mm copper foils (Advent Research Materials Ltd). A consistent cleaning method was implemented

to ensure any changes observed due to different growth methods were not caused by sample contamination pre-growth. Cu foils were cut into 10×5 mm^2 segments and were sonicated for 10 minutes in isopropyl alcohol (IPA), to remove surface contamination. This was followed by a further sonication for 10 minutes in acetic acid, which removed CuO from the surface, giving a clean growth surface. Cleaned Cu substrates were then blown dry in a N$_2$ flow before quickly being introduced to one of the two growth systems, as discussed above. An alternate method of Cu substrate preparation was also implemented in Chapter 7. 300 nm of Cu was evaporated onto 10×5 mm^2 SiO$_2$ wafer segments. Evaporation was performed in a shuttered high vacuum system using 99.99% purity copper pellets with a Al$_2$O$_3$ coated tungsten crucible. High precision of Cu thickness was achieved via the use of a quartz crystal micro-balance. Substrates produced by this method were then subjected to the same cleaning method outlined above.

3.2.3   STM Tip Production
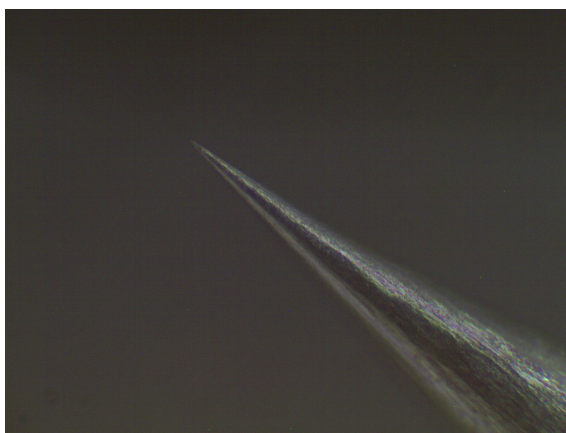
Figure 3.8: $50\times$ Magnification optical microscopy image of a W tip produced by electrochemical etching.

Pt-Ir tips were produced simply, through careful cutting of Pt-Ir wire ensuring the cutting implement is retracted away from the new tip in order to produce an atomically sharp point. Tungsten tips were produced via electro-chemical etching. W wire acting as a cathode was submerged in a solution of NaOH and distilled water (8 g:100 ml). A circular graphite anode is also submerged in the solution; the circular anode is used to prevent uneven etching. Applying a voltage of 4 V caused the tungsten wire to be etched at the surface of the solution. After prolonged (10-15 minutes) etching the wire breaks leaving two atomically sharp tips; an example

of an etched W tip can be seen in Fig. 3.8. All tips and holders were handled as minimally as possible, with gloves used at all times to ensure contamination was kept to a minimum. STM tips were introduced to the UHV system within 5 minutes of production to also keep atmospheric contamination to a minimum.

3.3   Summary

In this chapter the technical information regarding the various experimental systems implemented in this thesis is presented. Details of both SiC and Cu sample preparation and STM tip production is also provided.

3.4   References

[1] T. Hopf, K. V. Vassilevski, E. Escobedo-Cousin, P. J. King, N. G. Wright, A. G. O'Neill, A. B. Horsfall, J. P. Goss, G. H. Wells and M. R. C. Hunt, *J. Appl. Phys.*, **116**(15), 15404 (2014).

[2] For more information on the JIPELEC Rapid Thermal Processor see, *http://thesemcogroup.com/rtp-rta.*

[3] Omicron Nanotechnology, *The VT AFM User's Guide & Service Manual* (2004).

[4] C. J. Chen, *Introduction to Scanning Tunneling Microscopy*, Oxford University Press (1993).

[5] Omicron Nanotechnology, *MATRIX Application Manual SPM* (2012).

[6] Omicron Nanotechnology, *SPECTALEED Optics and Electron Gun User's Guide* (1999).

[7] Omicron Nanotechnology, *Auger Electron Spectroscopy with Four-Grid SPEC-TALEED* (2000).

[8] Omicron Nanotechnology, *DATAuger Software Manual* (2000).

[9] For more information on Ion Gun Technical Data see, *http://www.scientaomicron.com/en/products/ise-5-/technical-data.*

[10] Omicron Nanotechnology, *ISE 5 Sputter Ion Source User's Guide* (1999).

[11] M. M. Ugeda, D. Fernádez-Torre, I. Brihuega, P. Pou, A. J. Martínez-Galera, R. Pérez and J. M. Gómez-Rodríguez, *Phys. Rev. Lett.*, **107**(11), 116803 (2011).

[12] HORIBA Jobin Yvon, *LabRAM HR, Software and Hardware user guide* (2010).

[13] For more information on the MAMBO and TANGO EBSD post processing programs see, *http://www.oxford-instruments.com/products/microanalysis/ebsd/ebsd-post-processing-software.*

[14] For more information on wafer specifications see, *http://www.cree.com.*

[15] For more information on wafer specifications see, *http://www.tankeblue.com/product.*

Chapter 4

Optimisation of Graphene Growth on SiC(0001)

This chapter describes experiments performed to optimise the growth of graphene on SiC(0001) in-vacuo at high temperatures. A complete exploration of growth temperature, growth time and cooling rate is presented. Growth on trenched SiC substrates produced by photolithography is also investigated. Finally, a facile method for removing large scale contamination from graphene samples is also described.

4.1   Introduction

Since the first isolation of graphene in 2004, a huge amount of interest has been shown in its extraordinary electrical, thermal and mechanical properties [1]. As a result, a large number of potential applications have been proposed, including use as field effect transistors (FETs) [2], transparent electrodes [3] and biological sensors [4]. As outlined in Chapter 1, there are a large number of different methods that have been employed to produce high quality graphene, from mechanical exfoliation [1] to chemical vapour deposition (CVD) [5], however it is growth from SiC(0001) substrates, via Si sublimation, that shows some of the greatest promise for the realisation of graphene electronics [6]. The high quality and single crystallographic orientation of graphene grown on this substrate combined with pre-adhesion to a semi-insulating substrate with high thermal conductivity, negating the need for potentially damaging transfer processes, make this method ideal for device fabrication. Furthermore, unlike isolated layers, graphene grown on SiC exhibits a bandgap, which is desirable for its use in FETs as it allows significantly larger on/off ratios to be obtained [7].

The growth of graphene from SiC proceeds via the controlled sublimation of Si atoms at elevated temperatures, leaving a carbon rich surface which then forms single or few-layer graphene (FLG) upon cooling. However, the quality of the graphene produced is highly dependent on the growth conditions. The large variance in graphene produced due to different parameters has been well documented in previous work [8–12], therefore complete control over the growth conditions is required. Previous studies have predominantly produced graphene at temperatures of $\sim$1500 °C with short growth times [8, 13, 14]. However, earlier work suggested that higher temperature growth will result in higher quality films [15, 16]. Furthermore, it is also suggested that longer growth times may act to mediate growth, leading to more continuous graphene layers [16], whilst the cooling rate after growth has seen no investigation at all. Therefore, a full optimisation of the growth of graphene on SiC(0001) substrates at elevated temperatures is still required.

A different route to electronic applications is through controlling the dimensions of graphene sheets on the nanoscale. Fabrication of graphene nano-ribbons (GNRs) presents an effective route for manipulating graphene's excellent electronic properties, as careful control of ribbon width can enable a tailoring of the bandgap. By reducing graphene from a 2D to a 1D material, via "cutting" it into strips, 1D confinement states form [17]. This results in an energy gap opening which is inversely

proportional to the ribbon width [17–20]. The ability to move from a zero band gap to a finite band gap semiconductor by reducing GNR width, provides an excellent means to produce building blocks for a variety of applications in electronics. Further manipulation can be performed upon production of these GNRs via functionalisation allowing even tighter control over the electronic structure [21]. The attraction of this route towards graphene based electronics has resulted in a number of different methods being employed to produce GNRs, from lithography of mechanically exfoliated flakes [19] to chemically unzipping single and multi-walled carbon nanotubes via hydrogenation or oxidation [22–24], and even via specialised CVD [25]. These methods have been found to be effective at producing large quantities of GNRs, however for device production ribbons also require a high level of alignment. Sinitskii *et al.* produced arrays by unidirectional painting of GNR dispersions, however this method can cause damage to the GNRs and difficulties are found with reproducibility [26]. An alternative method using graphene grown on SiC combined with lithographic methods can produce highly ordered arrays, which show good electronic properties with excellent reproducibility [27,28]. Perhaps the most effective method comes from pre-patterning of SiC, from which GNRs can then be grown. Sprinkle *et al.* have shown this to be a highly effective method producing GNR-FETS via selective growth on lithographically produced crystal facets [29]. However, simpler pre-patterning approaches requiring less strict crystal orientations have not been attempted, which could lead to easier scalability in graphene device production.

In order to take advantage of its excellent electronic properties, high quality graphene, be it produced through growth from SiC [11, 14, 30] or via CVD based methods [5, 31, 32], it must be kept free of contamination. It has been shown that the presence of contamination on the graphene surface has a considerable effect on electronic behaviour. In particular, charged impurities cause significant issues, as electron transport suffers greatly due to scattering off the areas of inhomogeneous charge density at these points [5, 14, 33], whilst larger scale contamination has been shown to alter the electronic characteristics of entire graphene films due to doping [34]. As well as changing the electronic properties of films, graphene's mechanical properties are also affected. The wettability of graphene was found to degrade significantly upon contamination due to long exposure to atmosphere [35]. In addition to atmospheric contamination, impurities can originate from many different sources. The process used to transfer CVD grown graphene has been found to introduce high concentrations of metallic contamination, altering its electrochemical properties [36–38]. Furthermore, material can be deposited onto the graphene surface from electron beam filaments associated with device production or even char-

acterisation techniques [34]. In particular, it is these sources that are often more problematic due the contamination often being deposited over large areas, rather than as individually adsorbed molecules. Unlike atmospheric contamination, these impurities are often metallic and bond much more strongly to the surface preventing their removal via annealing [39, 40].

With contamination occurring from a wide variety of sources, which are often unavoidable, effective cleaning methods are required. As a result of this need a number of different cleaning methods have been reported. These methods vary from mechanical "sweeping" with the tip of an atomic force microscope (AFM) [41, 42], the use of sacrificial metal layers [43], application of high currents [44] and high temperature annealing under vacuum [39, 40]. These methods were found to be appropriate for removing small concentrations of contaminants from the surface, but for larger scale contamination a different approach is required.

For the work reported in this chapter, multilayer graphene was grown via Si sublimation from 6H and 4H-SiC(0001) substrates in high vacuum, under various different growth conditions. Growth temperature, growth time and cooling time were each varied independently to determine the optimum conditions for producing graphene on the SiC(0001) substrates. Samples were characterised by Auger electron spectroscopy (AES), low energy electron diffraction (LEED), Raman spectroscopy (RS) and scanning tunnelling microscopy (STM). The aim is to determine the ideal method for producing the highest quality graphene reproducibly, which can be used for electronic devices such as FETs. Furthermore, this characterisation provides a thorough analysis of the graphene samples used in the studies reported in subsequent chapters. The optimised method was then implemented on the "nano-trenched" substrates to determine whether graphene nano-ribbon arrays can be produced via this simple process. Finally, a facile technique for removing large scale metal contamination from graphene samples is introduced to allow for the cleaning and reuse of graphene grown on SiC(0001).

4.2   Experimental

Epitaxial graphene (EG) films were grown on the Si terminated face of commercial 6H and 4H-SiC substrates in the upgraded commercial rapid thermal processor at Newcastle University as described in Chapter 3. Substrates were preprepared using

Acetone, Piranha and RCA chemical treatments to remove contamination. This was followed by high temperature etching at 1500 °C in 5% H_2/Ar forming gas and a 20 minute heating step at 1200 °C under high vacuum ($\sim 2 \times 10^{-5}$ Torr) to reconstruct the surface [45]. Graphene samples were grown, still under high vacuum, at temperatures of 1700 °C, 1775 °C, 1850 °C and 1900 °C; with growth times between 1 minute and 90 minutes and cooling times of 2, 30 or 90 minutes. Graphene was also grown on patterned SiC substrates. These patterned samples were prepared via a standard photolithographic patterning technique, using plasma etching in a SF_6/O_2 gas mixture to produce lines 75 nm in height and 1.5 μm in width with a separation of 5 μm. The "standard" technique (see below) of high temperature etching and 4 minute growth at 1775 °C was then employed. All samples were characterised shortly after growth with RS to determine thickness and quality of the EG films. Thickness was determined by measuring the full width at half maximum (FWHM) of the graphene *2D* peak found at 2767 cm^{-1}, whilst an estimation of the quality of the film was obtained from the height of the *D* peak observed at approximately 1380 cm^{-1} (Fig. 4.1). All RS measurements were carried out at room temperature and ambient pressure.
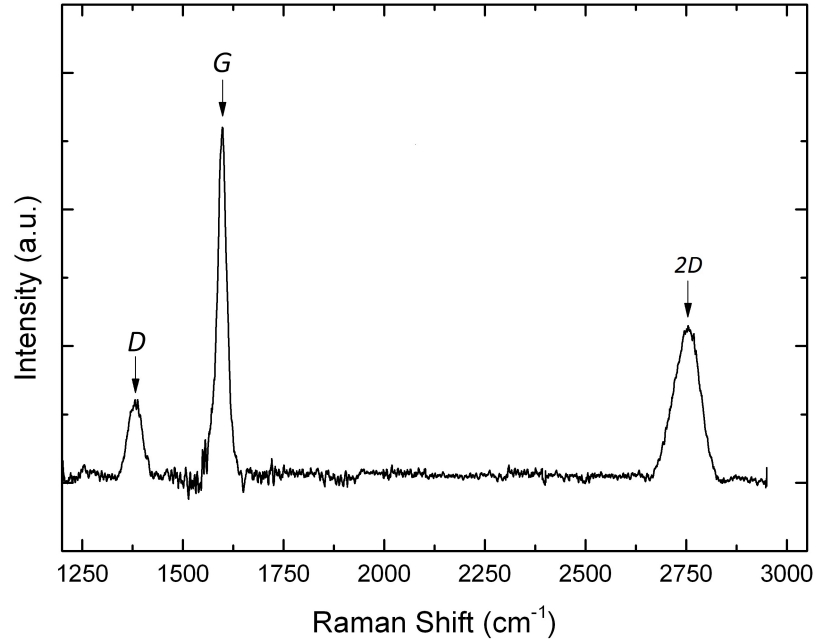
Figure 4.1: Raman spectrum of graphene grown on SiC(0001). The spectrum shows clear peaks at $\sim$1380 cm^{-1}, $\sim$1580 cm^{-1} and $\sim$2750 cm^{-1} corresponding to the *D*, *G* and *2D* peaks of few layer graphene.

All further sample analysis was conducted in the UHV-SPM system at Durham University, outlined in Chapter 3. Samples were annealed for a short time *in-situ* at 400 K to remove any contamination from exposure to atmosphere between

growth and transfer to the UHV system. The primary investigative technique was scanning tunnelling microscopy. Pt-Ir tips were commonly used for larger scale images (~ 1 μm^2), whilst W tips were used for higher resolution images (<100 nm^2) due to increased stability at the atomic scale (Fig. 4.2). All STM images were obtained at room temperature and are presented unprocessed apart from plane subtraction to remove sample tilt.
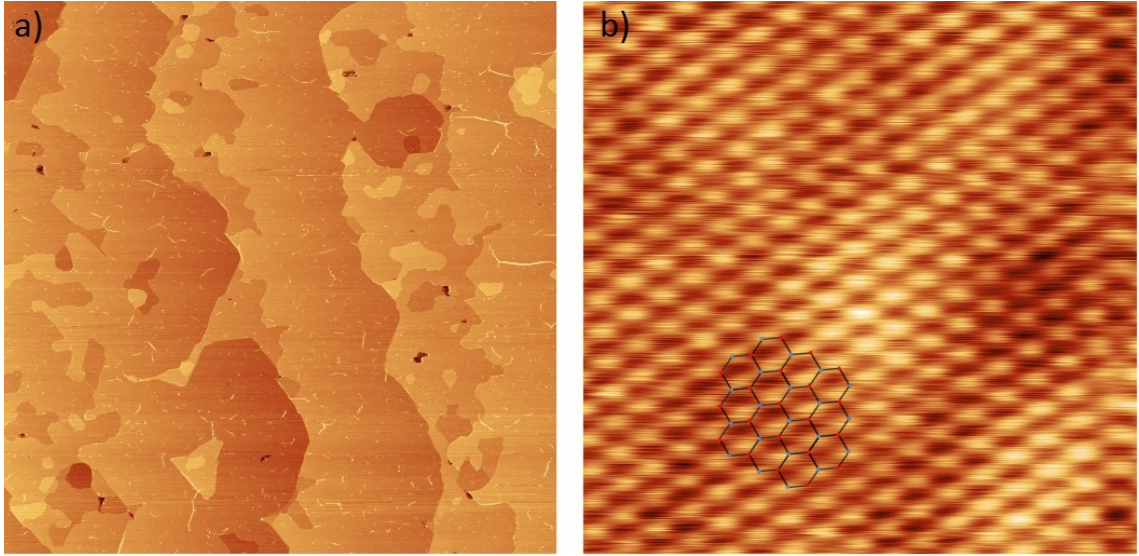
Figure 4.2: STM images taken with different tips. a) Typical 1 μm^2 image of FLG taken using a Pt-Ir tip (V_{bias}=1.2 V, I=0.8 nA). b) Typical 4 nm^2 atomic resolution image of FLG taken using a W tip. The graphene lattice is overlayed on the image (V_{bias}=200 mV, I=2.0 nA).

LEED and AES measurements were performed using the SPECTALEED optics and electron gun of the UHV-SPM system. LEED patterns were obtained at beam energies between 60 eV and 250 eV using a stabilised Canon Digital SLR camera. LEED pattern images presented are filtered to remove red background light to improve contrast but are otherwise unprocessed. AES was carried out at incident beam energies of 2 keV and 2.5 keV and a sample current of ~ 20 μA. The number of graphene layers was also estimated from AES spectra, using the ratio of the carbon *KLL* and silicon *LMM* peaks. This is used in conjunction with a calibration curve produced from the C and Si relative elemental sensitivity factors which takes into account the electron yield from each individual graphene layer compared with the SiC substrate as discussed in Chapter 2 [46, 47].

Silver contamination was deposited onto graphene films (grown for 60 minutes at 1775 °C) via resistive heating of a tungsten filament, wrapped in 99.99% Ag wire (Agar Scientific), to ~ 960 °C. Evaporation was performed at a chamber pressure

of 5×10^{-8}mbar for 10 minutes, to produce thick Ag layers, and for 30 seconds to produce films with low thickness and coverage. Adventitious contamination was also produced by the electron beam used during AES measurements. Typical measurement times resulted in exposure to the electron beam for 1.25 hours. The elemental composition of this contamination is unknown, however a likely candidate material is LaB_6 from the electron gun filament. After contamination, commercially available Scotch Magic Tape was applied to the sample surface and then peeled away as shown in figure 4.3. STM and AES was performed, as described above, prior to contamination, after deposition and after contamination removal to determine film thickness and any change in the quality of graphene as a result of the cleaning process.
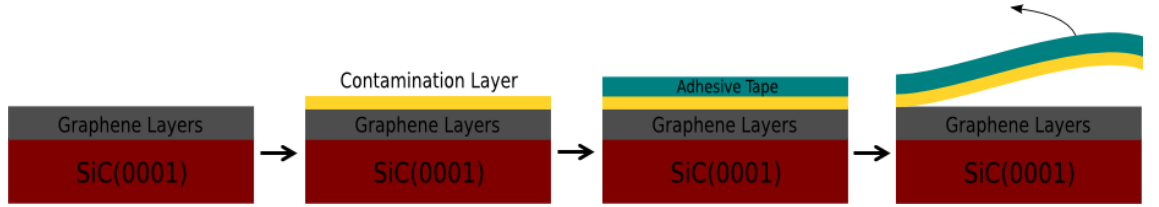
Figure 4.3: Experimental process of contamination deposition followed by removal by adhesive tape. [48]

4.3 Results and Discussion

4.3.1 Graphene Growth: Temperature Dependence

Figure 4.4 shows STM images of graphene grown on SiC(0001) at various growth temperatures. At the lowest growth temperature of 1700 °C, Fig. 4.4(a), large graphene terraces separated by rough edged steps corresponding to three SiC bilayers ($\sim$7.5 Å) are clearly visible. Graphene terraces spreading outward from steps appear rough with large numbers of small islands forming. Furthermore, small pitted areas are visible all across the surface with a concentration of $\sim30/\mu m^2$. The origin of this roughened surface most likely arises due to kinetic limitations on graphene growth brought about by the lower growth temperature. At lower temperatures, graphene nuclei are more stable and less able to overcome the energy barriers found at defect sites and step edges. This results in a large number of nucleation sites from which islands grow [49]. This combined with a short growth time of 4 minutes results in many smaller islands and incomplete graphene layers. Therefore it is probable

that small pit formation occurs due to secondary and tertiary graphene layer growth before a complete monolayer forms below.

At the higher temperature of 1775 °C, Fig. 4.4(b), large graphene terraces separated by irregular SiC and graphene step edges are again clearly visible. Small graphene islands are again prevalent on the surface forming at steps away from larger graphene terraces, again most likely due to the 4 minute growth time. Island size appears marginally increased in comparison to growth at 1700 °C combined with a reduced concentration. This is to be expected, as the higher growth temperature allows graphene nuclei to be significantly more mobile. This is due to enough energy being available for graphene islands to overcome energy barriers found at defect sites and step edges that would pin them at lower temperatures. This results in graphene islands diffusing across the surface, joining the growth of larger terraces or other small islands and producing a more complete, higher quality graphene layer. Despite the increased quality observed, small pitted areas are still visible under higher temperature growth conditions, at a concentration of $15\pm1/\mu\text{m}^2$. This indicates that second, and in some areas third, layer growth still begins before a complete monolayer forms, leaving small gaps in the subsequent upper layers [13]. Alternatively it should be noted that the dark spots attributed to small pitting of the surface may be insulating contamination on the surface, however with the origin of possible contamination unknown, this explanation is less plausible. Furthermore, larger pits are also observable on the surface of samples grown at 1775 °C (Fig. 4.4(b) bottom left corner). Much less common than the smaller pits at $1\pm1/\mu\text{m}^2$, these larger holes extend to the SiC buffer layer much further below. These large pits show many similarities with those observed by Hannon *et al.* during the etch phase of SiC surface preparation, in which the preprepared $(\sqrt{3} \times \sqrt{3})$ structure retreats non-homogeneously from step edges as $(6\sqrt{3} \times 6\sqrt{3})$ buffer layer islands nucleate [13]. At higher temperatures the continued etching of the substrate would result in the large pits observed. The formation of these large etch pits at higher temperatures has a negative effect on the transport properties of the graphene film as well as preventing effective device production [50]. This counteracts the improved quality of the film observed at higher temperatures.

Upon a further increase in growth temperature to 1850 °C, graphene terraces appear more uniform, with smoother edges. A reduction in the number of small islands, in comparison to samples grown at lower temperatures can also be observed (Fig. 4.4(c)). Small island formation appears to be a constant feature of graphene films produced from a short growth time of 4 minutes, having been observed on
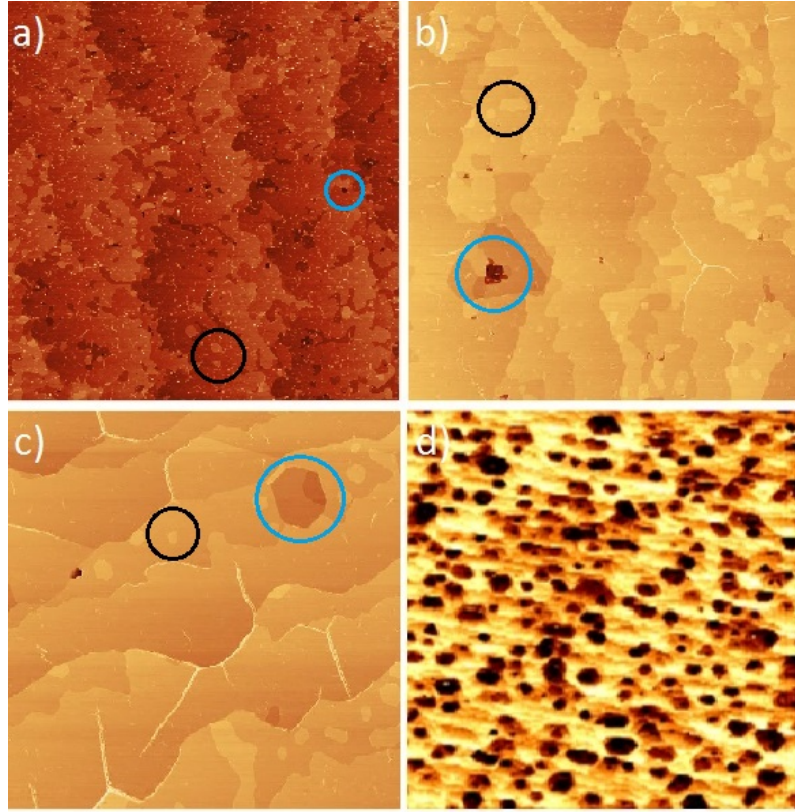
Figure 4.4: 1 μm^2 STM images of graphene on SiC(0001) grown for 4 minutes at different growth temperatures a) 1700 °C (V_{bias}=1.0 V, I=0.6 nA) b) 1775 °C (V_{bias}=1.2 V, I=0.8 nA) c) 1850 °C (V_{bias}=1.1 V, I=0.5 nA). Small islands (black circles) and pits (blue circles) can be observed on all samples. (d) 10 μm^2 AFM image of graphene grown on SiC(0001) grown at 1900 °C.

samples grown at all temperatures, with only small changes in island concentration apparent. The smaller concentration observed at 1850 °C can again be explained by the increase in growth temperature allowing for nuclei to be more mobile on the surface and hence merge with larger graphene terraces with more regularity. Further indication of increased quality as a result of the higher temperature can be seen in the reduction of small pits on the surface, with an average concentration of $1\pm1/\mu$m^2. This is likely caused by the increased energy available to graphene nuclei at this temperature, which allows islands to traverse the energy barriers found at step edges. This ensures complete lower layers form before next layer growth proceeds. Despite the decrease in small pitting, larger pits are again visible as a result of the higher temperature growth step (Fig. 4.4(c) top right). Further increases in temperature to 1900 °C were found to further exacerbate the issue of etch pits with an unacceptable surface morphology being produced [45]. Atomic force microscopy (AFM) images obtained by Hopf *et al.* (Fig. 4.4(d)) show an increased concentration of large, deep pits of $180\pm10/10$ μm^2 with an average size of $\sim$70000 nm^2 covering

13±1 % of the surface.
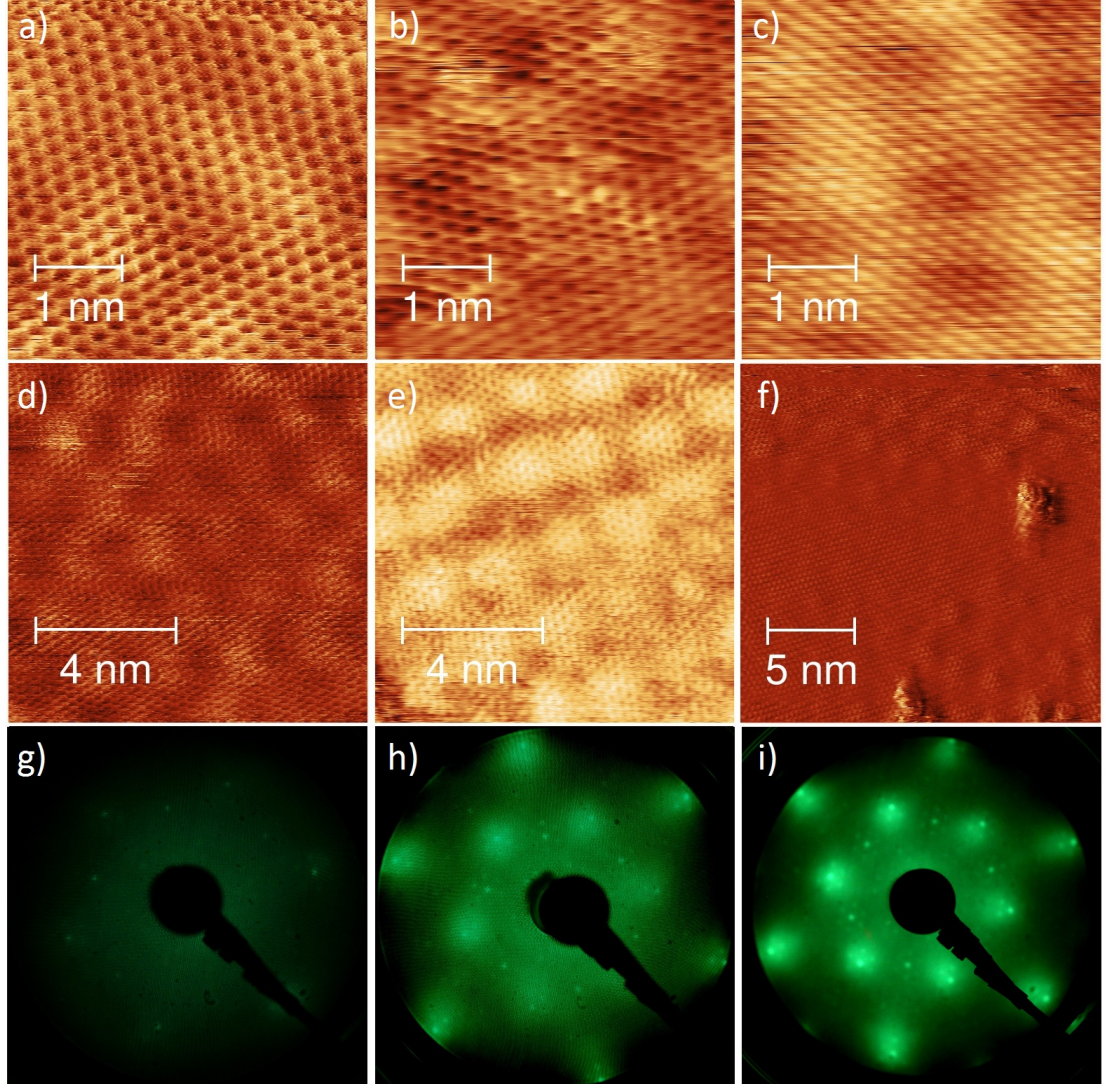
Figure 4.5: From left to right, graphene samples grown at 1700 °C, 1775 °C and 1850 °C. 4 nm^2 images a) (V_{bias}=0.5 V, I=2.0 nA), b) (V_{bias}=0.2 V, I=2.1 nA) and c) (V_{bias}=-0.7 V, I=1.1 nA) show the pristine hexagonal graphene lattice. Images d) (V_{bias}=0.6 V, I=1.8 nA), e) (V_{bias}=-0.4 V, I=1.7 nA) and f) (V_{bias}=0.9 V, I=0.6 nA) show the $(6\sqrt{3} \times 6\sqrt{3})R30°$ reconstruction associated with buffer layer between the SiC substrate and graphene layers. LEED images g), h) and i) taken at 100.5 eV, 165.2 eV and 171.0 eV respectively, show both graphene and SiC (1×1) spots as well as $(6\sqrt{3}\times6\sqrt{3})R30°$ reconstruction spots.

At smaller scales the hexagonal graphene lattice becomes visible. Figures 4.5 (a)-(c) show the graphene lattice as measured on samples grown at 1700 °C, 1775 °C and 1850 °C respectively. Despite significant differences between samples at larger scales due to variation in temperature all images show the hexagonal arrangement of carbon atoms, although a contrast inversion is observed in (c) due to the use of negative tip

biases, indicating areas of pristine graphene form at all growth temperatures studied, with minimal intrinsic defects. Furthermore, the lattice exhibits small differences in height of 0.27Å [51]. Larger scan sizes show these height differences are periodic in nature and correspond to the $(6\sqrt{3} \times 6\sqrt{3})R30°$ reconstruction of the SiC substrate, which remains intact at the interface between the bulk SiC and the first graphene layer (Fig. 4.5 (d)-(f)) [52]. This is supported by LEED patterns (Fig. 4.5 (g)-(i)) which show clear graphene and SiC (1 × 1) spots as well as $(6\sqrt{3} \times 6\sqrt{3})R30°$ reconstruction spots, indicating that pristine graphene is present on a large scale over all samples. The presence of a single set of graphene spots, indicates Bernal stacked FLG is produced, rather than turbostratic or rhombohedral [53]. Furthermore, the presence of the $6\sqrt{3}$ reconstruction pattern, both in LEED and STM indicates an upper limit of 4 ML on the thickness of graphene produced at all temperatures. This is due to a reduction of ∼50% in the corrugation amplitude observed for each successive graphene layer that grows [54]. LEED-IV measurements by Riedl *et al.* have supported this, showing that peak intensities are significantly reduced by graphene layers indicating a strong attenuation of signals from the buffer layer, or alternatively that the signal only comes from a small area of the surface [55].

Figure 1.7 (a), (b) and (c) show the Auger spectra obtained from the samples grown at 1700 °C, 1775 °C and 1850 °C respectively. All spectra show clear peaks at 271 eV and 92 eV corresponding to carbon and silicon. The carbon line shape of an upward excursion followed by a plateau and a large negative excursion is indicative of sp^2 hybridisation [56]. This further confirms the presence of high quality graphene on all samples. The silicon peaks observed show only small variance in height with respect to the carbon peaks at different growth temperatures, suggesting thickness is fairly consistent across all samples. Measuring the ratio of carbon to silicon peaks, thicknesses of 2.4±0.8 ML, 2.1±0.6 ML and 2.0±0.5 ML were obtained from spectra a), b) and c) respectively. The lack of change in the thickness measured on samples grown at different temperatures indicates that that the growth temperature does not strongly affect the rate at which layers form, with variation instead occurring in the homogeneity of the graphene. These results are supported by the STM images shown in figure 4.4, in which many small islands and pits are observe in comparison to growth at higher temperatures, which exhibit smooth homogenous terraces with fewer islands and pits.

Figure 4.7 shows Raman spectra obtained from the graphene samples. Three peaks are clearly observable from the graphene samples grown at all temperatures. The G and $2D$ peaks at ∼1560 cm^{-1} and ∼2750 cm^{-1} respectively, indicate the
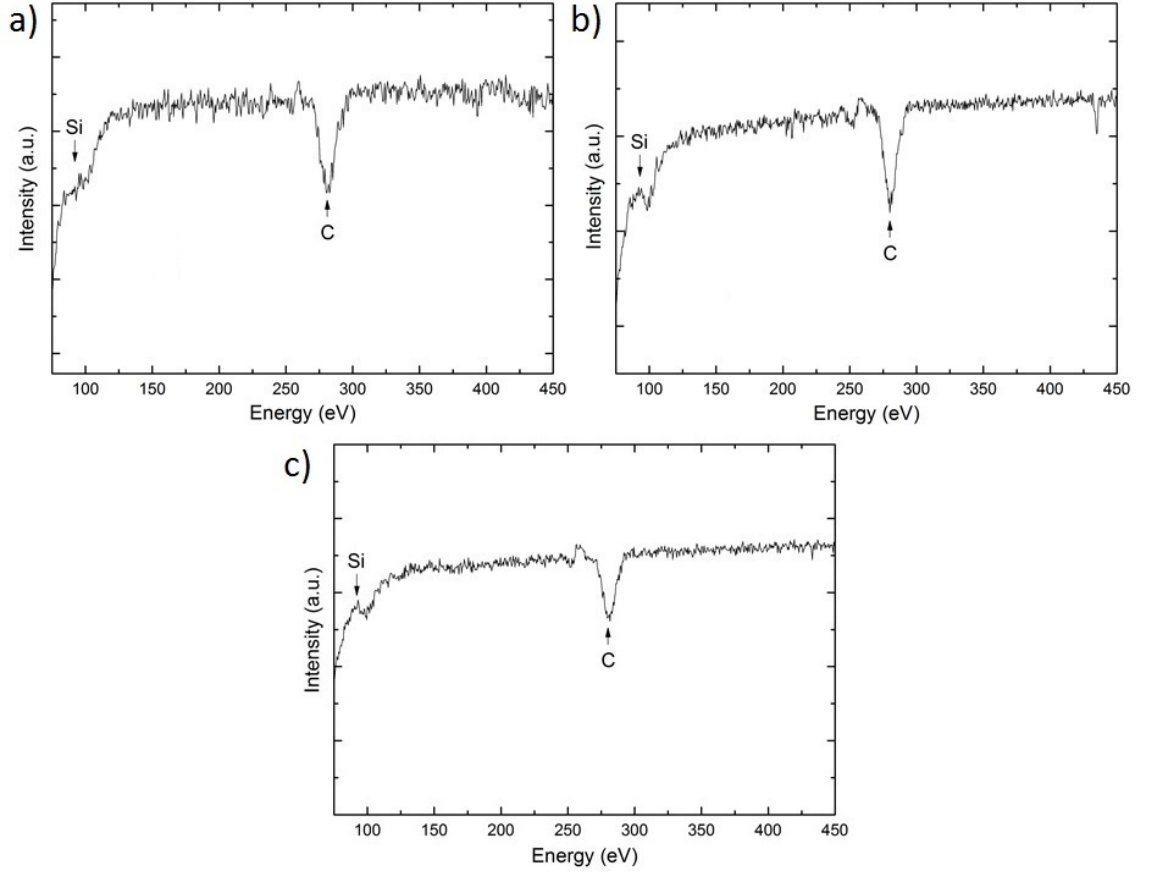
Figure 4.6: Auger spectra of graphene grown on SiC(0001) at a) 1700 °C, b) 1775 °C c) 1850 °C. Spectra a) and b) were obtained at a beam energy $E_0 = 2.0$ keV, whilst spectra c) was obtained at $E_0 = 2.5$ keV.

presence of graphene, whilst a peak is also observed at ~ 1380 cm^{-1}, the D peak, which is associated with the defects. What becomes immediately obvious is that the intensity of the D peak drops rapidly, with increasing growth temperature. This supports the STM, LEED and AES results outlined above, that a higher growth temperature produces higher quality graphene films on SiC. Furthermore, the FWHM of the $2D$ peak always falls in the range of 65-75 cm^{-1} giving an estimated thickness of 2-3 ML for all samples [57], corroborating the estimates obtained from AES. Hence, the growth temperature has only a small effect on the thickness of the graphene produced via Si sublimation.

In summary, the temperature at which graphene is grown on SiC(0001) has a significant effect on the quality of the film produced. Lower temperatures were found to result in many small islands, partial layer growth and higher defect density, which can be attributed to kinetic limitations. Higher temperatures resulted in larger areas of pristine graphene with few isolated small islands, though increasing
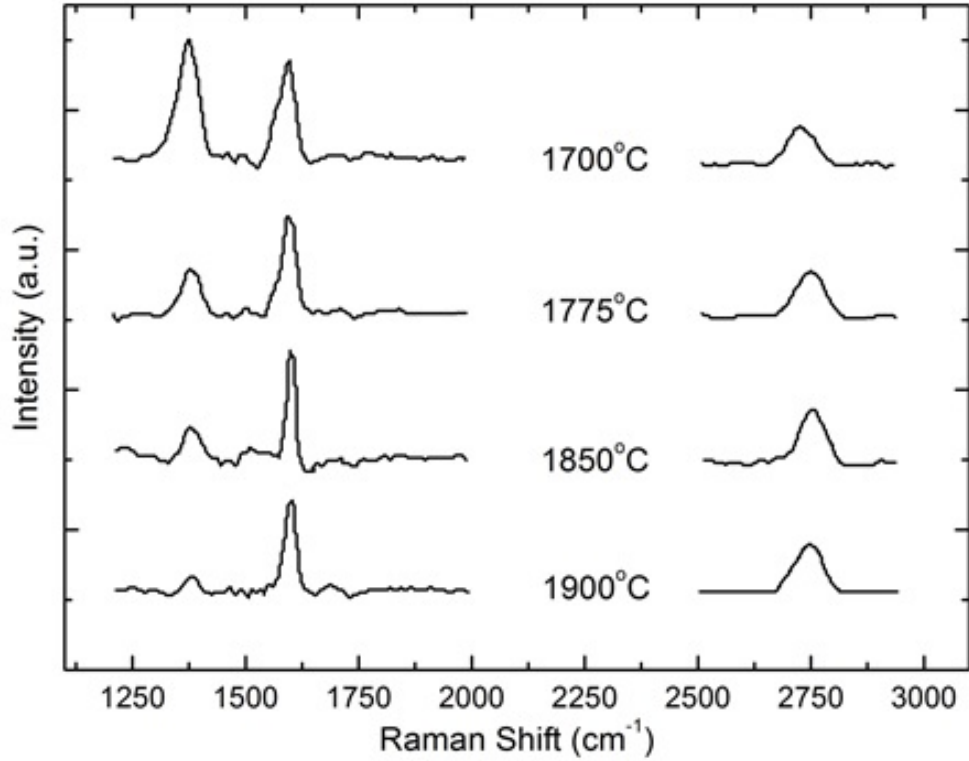
Figure 4.7: Raman spectra of graphene grown at various temperatures. All spectra show clear G and $2D$ peaks at $\sim$1580 cm^{-1} and $\sim$2750 cm^{-1}. The D peak at $\sim$1380 cm^{-1}, associated with defects, decreases in intensity with increasing growth temperature.

the growth temperature too much resulted in an unacceptable surface morphology. Despite differences at larger scales, pristine graphene was observed on all samples with long range ordering present. AES and RS determined that the number of graphene layers does not change significantly based on the growth temperature, remaining at $\sim$2 ML. However, these results in conjunction with STM images suggest that the homogeneity of graphene layers produced is reduced with decreasing temperature. Therefore, in order to produce the best quality graphene a higher growth temperature of 1850 °C is recommended.

4.3.2 Graphene Growth: Growth Time

Figure 4.8 shows graphene grown at 1775 °C for (a) 4 minutes and (b) 60 minutes. As discussed earlier, in section 4.3.1, graphene grown at 1775 °C for 4 minutes exhibits large terraces separated by three SiC bi-layer steps. A high concentration of small islands ($40\pm7/\mu$m^2) can be observed on larger graphene terraces, towards the edges of steps. Furthermore, small pits that descend to the buffer layer are again

visible across the surface. In samples grown for 60 minutes significant changes can be observed. The graphene still exhibits large terraces separated by multiple SiC bilayer steps, but the number of small islands drops significantly to $9\pm1/\mu m^2$ with an increased average area of 0.004 ± 0.001 μm^2, compared with 0.001 ± 0.001 μm^2 seen previously. Furthermore, small pits are no longer observed at all. These improvements are more pronounced than those observed for an increase in growth temperature to 1850 °C, for which the number of small pits was also found to decrease (Section 4.3.1). As this process appears to be kinetically limited, as seen by the higher quality of graphene grown at higher temperatures, these improvements are likely the result of the increased time at elevated temperatures, which allows Ostwald ripening to occur for a longer period allowing terraces and larger islands to grow further at the expense of more smaller islands. Although the lower temperature will reduce the mobility of carbon atoms on the surface slowing the ripening process, the increased growth time significantly increases the probability of diffusing atoms encountering terraces and large islands. This results in the substantially more uniform graphene layers absent of pits observed; this is further supported by the reduction in small islands. A further noticeable difference between samples is in the pleat defects that cover the surface, with significant increases in length and height observed with the increased growth time, much like with the increased growth temperature (Fig. 4.4), indicating that the dimensions of pleat defects may provide a qualitative measure of the quality of the graphene sample, this will be discussed further in Chapter 5.
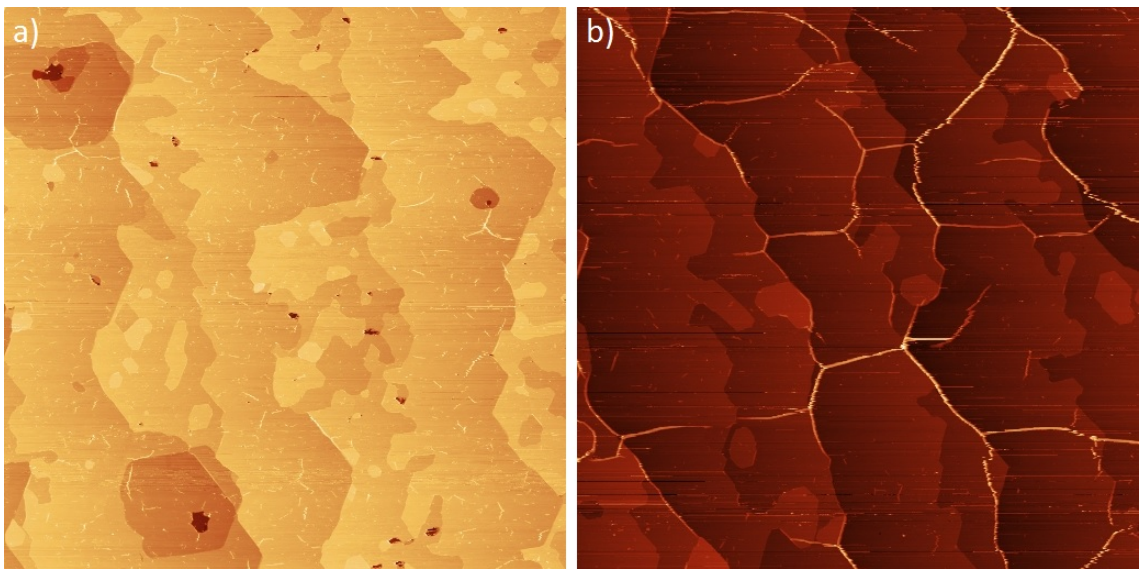
Figure 4.8: 1 μm^2 STM images of FLG grown on SiC(0001) at 1775 °C for (a) 4 minutes (V_{bias}=1.2 V, I=0.8 nA) and (b) 60 minutes (V_{bias}=2.2 V, I=0.3 nA).

Raman measurements were performed on samples produced at a large range of growth times to obtain a quantitative measurement of the quality of samples grown (Fig. 4.9). All samples show clear G and $2D$ peaks at $\sim$1580 cm^{-1} and $\sim$2750 cm^{-1} respectively, which remain fairly constant with changing growth time. However, there is a significant change in the relative intensity of the D peak at 1380 cm^{-1} as growth time is increased. At the lowest growth phase time, the ratio of the intensity of G to D peaks (I_D/I_G) is at 1.05, indicating that the graphene grown is of low quality. Although STM images were not obtained for graphene grown for this length of time, based on those obtained for the slightly longer growth time of 4 minutes, it can be surmised that the high intensity of the D peak is the result of a high concentration of small graphene nuclei. As the growth time employed is so short, carbon atoms are unable to diffuse significantly far across the surface and combine with graphene terraces or larger islands. This results in a large number of small isolated graphene islands that provide step edges which, along with any intrinsic lattice defects present, will contribute to an increase in the Raman D peak. As growth time is increased, the intensity of the defect Raman peak can be seen to decrease quite significantly. After an increase in growth time of three minutes the I_D/I_G peak ratio drops to 0.74. Although the I_D/I_G ratio is still high, the reduction observed in comparison to growth for 1 minute is considerable, indicating a significant increase in sample quality. STM images (Fig. 4.8), despite showing a high concentration of small graphene islands, also show large pristine graphene terraces. This indicates that graphene islands grow very rapidly during the first few minutes of growth, resulting in a larger surface area covered with pristine graphene and fewer step edges.

Upon further increases in growth time, the quality of the graphene produced continues to improve. A I_D/I_G ratio of 0.29 obtained after 20 minutes indicates a further significant increase in quality in comparison to growth at 4 and 1 minutes respectively. The sharp rise in quality is most likely the result of the continued growth and mobility of graphene nuclei on the surface; as the growth phase proceeds the graphene islands grow and combine with others to form a more complete graphene layer. Further increases in growth time appear to show a continued rise in graphene quality, however the rate of improvement slows quite considerably. After a growth time of 60 minutes the I_D/I_G ratio measured shows a small decrease with respect to growth for 20 minutes. An increase to 90 minutes growth time also provides only a minor improvement in quality, though it should be noted the I_D/I_G of 0.17 is comparable with that obtained by other groups [58]. The apparent exponential decay (Fig. 4.10) in the I_D/I_G ratio with increasing growth time suggests that as
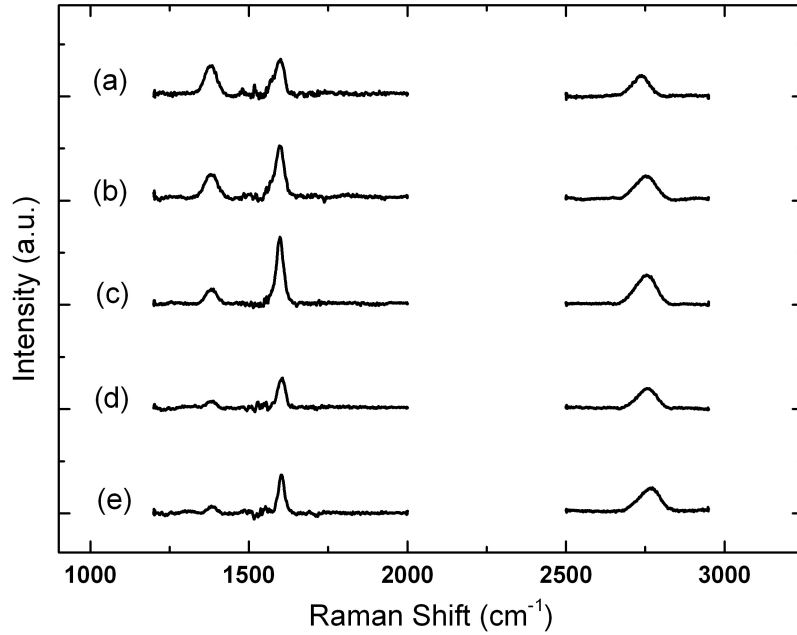
Figure 4.9: Raman spectra of graphene grown at 1775 °C for (a) 1 minute, (b) 4 minutes, (c) 20 minutes , (d) 60 minutes and (e) 90 minutes. The D peak at $\sim$1380 cm^{-1} drops in relative intensity as the growth time is increased.

growth proceeds, the graphene produced tends toward its optimum quality for this growth method.

The reduced rate at which the I_D/I_G ratio improves is most likely the result of the reduction in the number of graphene islands, brought about by their merging into a complete graphene layer on the surface over longer time scales. STM images obtained from samples with a growth time of 60 minutes, are consistent with this picture showing significantly fewer small graphene islands in comparison to shorter growth times (Fig. 4.8). Though STM images were not obtained from samples grown for 90 minutes, it can be assumed, based on the I_D/I_G ratio obtained, that few small islands remain on the surface after this length of time, and are incorporated into larger terraces that cover the vast majority of the surface. Further increases in growth time are likely to result in diminishing returns in terms of the quality of the graphene layer, and may even result in a degradation of properties due to multiple layer growth. Therefore, in order to produce the highest quality graphene via this method it is recommended that an extended growth time of 60-90 minutes is used.

With the quality of graphene appearing to increase, although slowly, with longer growth times, consideration should be given as to whether the thickness of the samples grown for extended periods also increases. As graphene's excellent properties
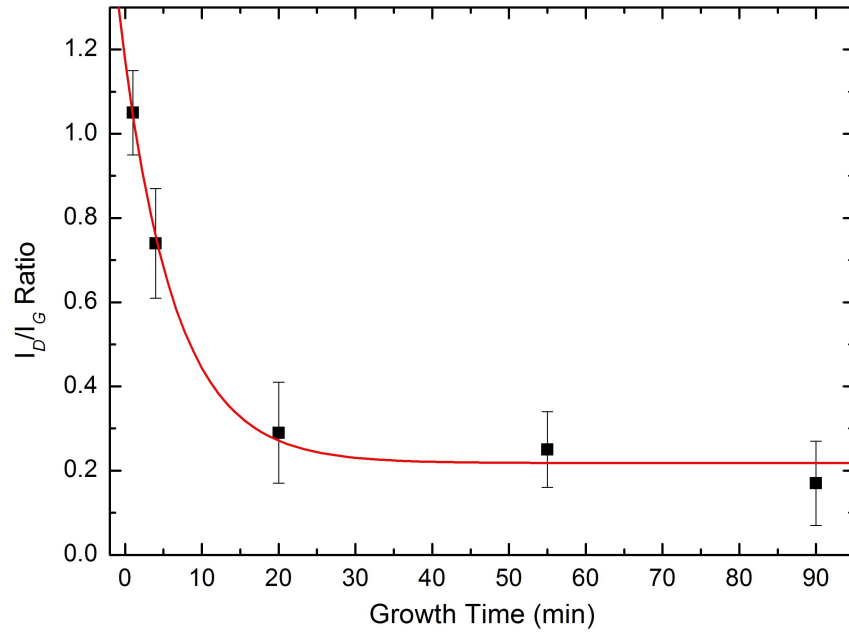
Figure 4.10: Exponential decay of the I_D/I_G ratio with increasing growth time as a result of improved film quality.

arise from its 2D nature, maintaining the 1-3 ML thickness is paramount for many device applications. Figure 4.11 shows Auger spectra obtained for graphene grown for (a) 4 minutes and (b) 60 minutes. Both spectra show clear peaks at 92 eV and 271 eV as before. Measurement of the ratio of C to Si peaks provides an estimate of 2.1 ML and 2.0 ML for growth for 4 minutes and 60 minutes respectively. The invariance of thickness observed between samples grown for short and long times indicates that new layers did not begin to form in the latter stages of longer growth cycles. Therefore, it can be suggested that growth predominantly proceeds via the continuous diffusion of carbon atoms across the surface. As the concentration of carbon from which graphene layers can form is limited by what is available in the first few SiC layers, extended growth will be self-limiting. As growth time increases, redistribution of carbon on the surface becomes more favourable than further thermal decomposition, due to the presence of the initial graphene layers. Smaller graphene islands will therefore gradually shrink as their carbon atoms diffuse to larger terraces, resulting in more uniform graphene layers forming over longer growth steps.

In conclusion, graphene was grown on SiC(0001) at 1775 °C at several growth times. Samples were characterised by RS and STM to determine their quality. It was found that samples grown for a shorter lengths of times (1-4 minutes) were lower in quality than those grown for longer periods (20-90 minutes). Samples with shorter growth exhibited high concentrations of small islands and high I_D/I_G Raman peak
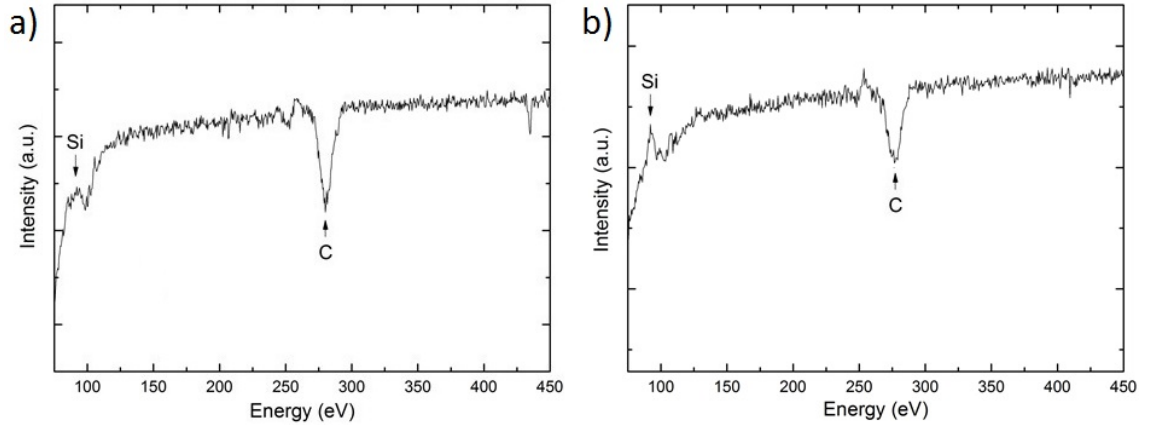
Figure 4.11: Auger spectra of FLG grown on SiC(0001) at 1775 °C for (a) 4 minutes and (b) 60 minutes obtained at primary beam energies of $E_0 = 2.0$ keV and $E_0 = 2.5$ keV respectively.

ratios indicating poor quality. With increased growth time, more complete graphene layers were observed with a significant reduction in the number of small graphene islands. A large drop in the I_D/I_G ratio was observed with longer growth steps (20-90 minutes) in comparison to short growth phases (1-4 minutes), indicating a substantial increase in graphene quality. Although, the quality of graphene was found to consistently improve as growth time increased, the rate of improvement slows quite significantly after 20 minutes. Finally, estimates of the thickness of graphene grown for 4 minutes and 60 minutes were made using AES, which indicated no significant changes with growth time. As a result, a growth time of 60 to 90 minutes is suggested to produce high quality graphene that is suitable for electronic purposes.

4.3.3 Graphene Growth: Cooling Rate Dependence

Figure 4.12 shows FLG grown on SiC(0001) with various post growth cooling rates. At a cooling time of 2 minutes (Fig. 4.12(a)), large terraces of high quality graphene can be observed on the surface. However, small circular agglomerations of material can also be observed, adsorbed to the surface (Note these should not be confused with the elongated pleat defects which are visible, meeting at 120° on the surface). This material is attributed to contamination deposited on the surface during sample production, as this material has not previously been observed on graphene grown by this method. Furthermore, the possibility of these agglomerations being regions of increased reactivity, such as lattice defects, was ruled out by high resolution STM
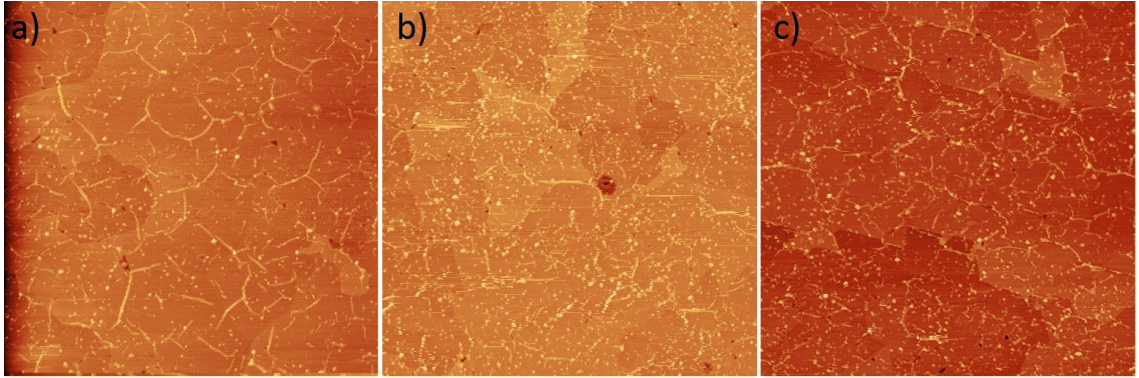
Figure 4.12: STM images of graphene grown on SiC(0001) at 1775 °C for 60 minutes with a post growth cooling time of a) 2 minutes (V_{bias}=-2.4 V, I=0.6 nA), b) 30 minutes (V_{bias}=-0.8 V, I=0.7 nA) and c) 90 minutes (V_{bias}=1.8 V, I=1.2 nA).

images which showed no Friedel oscillations, indicating the material sits on top of the lattice without causing significant changes to the surround electronic structure. The origin of this deposited material is unknown and at low concentrations the elemental composition cannot be determined by AES. Figure 4.12(b) shows graphene grown with a longer cooling time of 30 minutes. As with the shorter cooling time, graphene is once again visible on the surface. Negligible change is observed in the quality of the graphene as a result of the slower cooling rate, with terraces forming of the same shape and extent. However, what becomes immediately apparent is the concentration of contamination has increased. With a 2 minute cooling step, contamination was found to cover 2.5±0.4% of the surface. With the increase in cooling time to 30 minutes the percentage coverage of contamination increased to 3.7±0.3%. Upon a further increase in cooling time to 90 minutes (Fig. 4.12(c)) the coverage also increased to 4.1±0.5%, with no change in the underlying graphene quality.

Therefore, graphene grown via this method appears insensitive to the cooling rate, with no differences observed over the 2-90 minute range. Despite the lack of change in graphene quality, increases in surface contamination were observed at slower cooling rates, with significantly more adsorbed material observed after a 90 minute cooling step compared to 2 minutes. The origin of this contamination is unknown, however, a possible source may be the graphite heater which will desorb material, at high temperatures, that has collected whilst it is exposed to the atmosphere. Furthermore, the heater itself may degrade during the hydrogen etching phase of the process, resulting in the material observed. Another possible source of contamination are the walls of the growth chamber, which upon heating, will desorb material which can then be deposited on the surface. As the cooling time increases,

the length of time at which the sample heater and chamber are at a higher temperature is extended. This allows more time for contamination to desorb into the local atmosphere and eventually results in a higher concentration of contamination on the graphene surface itself. It is not currently possible to discern which of these possible sources the contamination originates with the techniques available, however the experiment outlined in Chapter 8 could be employed to provide a solution.

In conclusion, it was found that the quality of graphene grown on SiC(0001) substrates is invariant to the cooling rate employed after growth. However, the concentration of contamination on the surface increased significantly as cooling time was extended, firstly from 2 minutes to 30 minutes and then further to 90 minutes. The source of this contamination cannot be determined at this time, however possible sources include the graphite heater and chamber walls. Therefore, to produce the best quality graphene a short cooling time should be employed to keep surface contamination to a minimum.

4.3.4   Growth on Patterned Surfaces

Figure 4.13(a) shows graphene grown on a patterned SiC(0001) substrate consisting of flat ridges separated by trenches. Sharp contrast is observed between the low trenches and protruding ridges. LEED patterns obtained from these samples (Fig. 4.13(b)) show graphene (1×1) spots, indicating that single orientation graphene has been grown on the surface as observed for the non-patterned surface (section 4.3.1). However, unlike growth observed on unpatterned samples no Si (1×1) or $(6\sqrt{3} \times 6\sqrt{3})R30°$ reconstruction spots are observed, suggesting that >4 graphene MLs have been grown, resulting in complete attenuation of electrons from the buffer layer and SiC substrate; or that there is no long range order in the buffer layer or SiC substrate. The diffuse nature of the graphene (1×1) spots observed indicates that the graphene is significantly less ordered than that seen on pristine SiC surfaces [59]. Hence the suggestion that the substrate and buffer layer present no long range order is most likely correct.

Upon imaging with STM the state of the surface becomes clear. Whereas samples grown on unpatterned SiC show large, pristine graphene terraces separated by distinct steps, with some smaller islands, patterned samples show neither terraces or steps at larger scales (Fig. 4.13(c)). What is observed instead are large rough areas which exhibit significant damage in the form of etch pits. A wide variation in the size
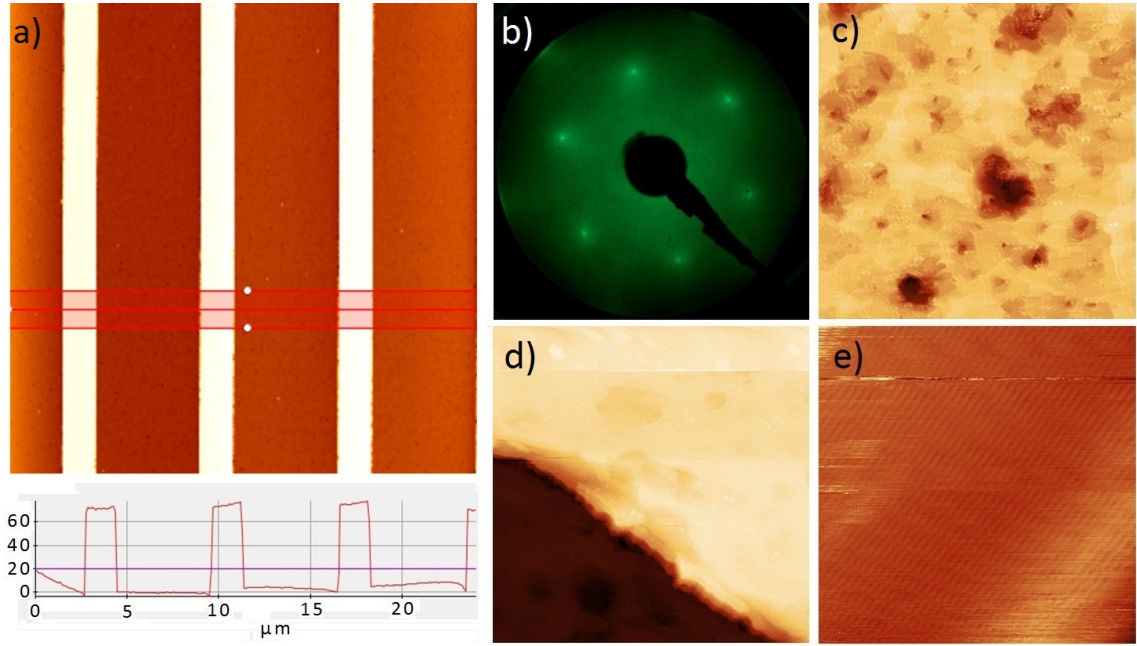
Figure 4.13: (a) 25 μm^2 AFM image of graphene grown on a patterned SiC(0001) substrate. 2 μm ridges appear bright white separated by $\sim$6 μm trenches. Below: Line profile shown by the red lines on the above AFM image. (b) LEED pattern obtained at E=135.8 eV showing graphene (1 × 1) spots. (c) 1 μm^2 STM image of graphene grown on the patterned SiC surface showing large etch pits and damaged areas (V$_{bias}$=2.0 V, I=0.5 nA). (d) 1 μm^2 image showing graphene growth both on pillars and in trenches, both areas show significant damage (V$_{bias}$=2.0 V, I=0.3 nA). (e) 10 μm^2 image showing the warped graphene lattice (V$_{bias}$=-0.6 V, I=1.7 nA).

of damaged areas can be observed. Larger, deeper pits, with an average diameter of 220±30 nm and depth of 12±2 nm, occur with a density $\sim$3/μm^2; whilst smaller indentations 4.7±2.0 nm in depth and 60±10 nm in diameter are observed more frequently at a density of $\sim$13/μm^2. The combination of these deep pits and small terraces gives a Root Mean Square (RMS) surface roughness of 2.0±0.2 nm. This roughness was found over the entire sample with both trenches and ridges showing deep and shallow etch pits (Fig. 4.13(d)). Damage is therefore unavoidably present both in areas where etching was desired and also on the areas intended to remain untouched. Upon imaging at higher resolution, the graphene lattice can be observed on the small flat areas found between etch pits. Although these areas appear flat at larger scan sizes, multiple undulations of 0.2±0.1 nm can be observed. At these points the lattice exhibits significant warping with the imaged bond length increased by up to 83% in some areas. As this is physically impossible, it is likely that this warping corresponds to Friedel oscillations caused by the highly defective surface, which supports the diffuse nature of the graphene LEED spots observed. Furthermore, no $(6\sqrt{3})R30°$ pattern is visible in these images, confirming that a pristine

graphene-SiC buffer layer does not form after growth on the plasma etched surface.

On unpatterned SiC surfaces the $(6\sqrt{3} \times 6\sqrt{3})R30°$ reconstruction buffer layer forms on the Si terminated face, during the anneal phase at 1200 °C [8]. This reconstruction provides the basis for high quality graphene to form on top. However, on substrates patterned by plasma etching, significant damage is caused to the surface, including regions intended to be left pristine. Unintended etching of ridges resulted in a more disordered SiC surface on which graphene was grown. Subsequently, upon annealing, the $(6\sqrt{3})R30°$ buffer layer that precedes graphene growth, cannot form. This is because decomposition to form the buffer layer occurs exclusively at SiC steps and the quality is highly dependent on its stability with respect to the surrounding SiC $\sqrt{3}$ phase [13]. The plasma etching process appears to destroy ordering on the substrate resulting in a defective surface without steps that provides little to no stability from which the carbon rich buffer layer can form. Despite the absence of this intermediary layer graphene is still able to form on the disordered surface. The presence of graphene indicates that despite the highly defective substrate, carbon is still able to diffuse across the flatter areas that remain on the surface. However, while the lack of the buffer layer does not seem to prevent the growth of graphene on a large scale, as shown by the long range order present in LEED patterns, the quality of graphene appears severely diminished. This has been seen to a lesser degree by Yu *et al.* who observed poor uniformity in graphene grown from defective SiC substrates [60]. The drop in the quality of the graphene will have a large effect on its electrical properties, which will consequently inhibit their use for nano-ribbon array devices. For example, the high defect density will result in multiple scattering centres resulting in significant drops in carrier mobilities [61]. Furthermore, the curvature seen even on the smoothest areas of graphene could introduce partial sp^3 hybridisation. Therefore, the method of plasma etching to pattern substrates prior to graphene growth is not suitable due to the significant damage caused.

In summary, plasma etching was employed to pattern trenches in SiC(0001) substrates on which graphene was then grown via controlled Si sublimation. Graphene was found to grow both in trenches and on the upper plateaus; However the quality was poor due to the significant damage caused to the SiC substrate by the etching process. As a result, the graphene produced is unsuitable for device purposes.
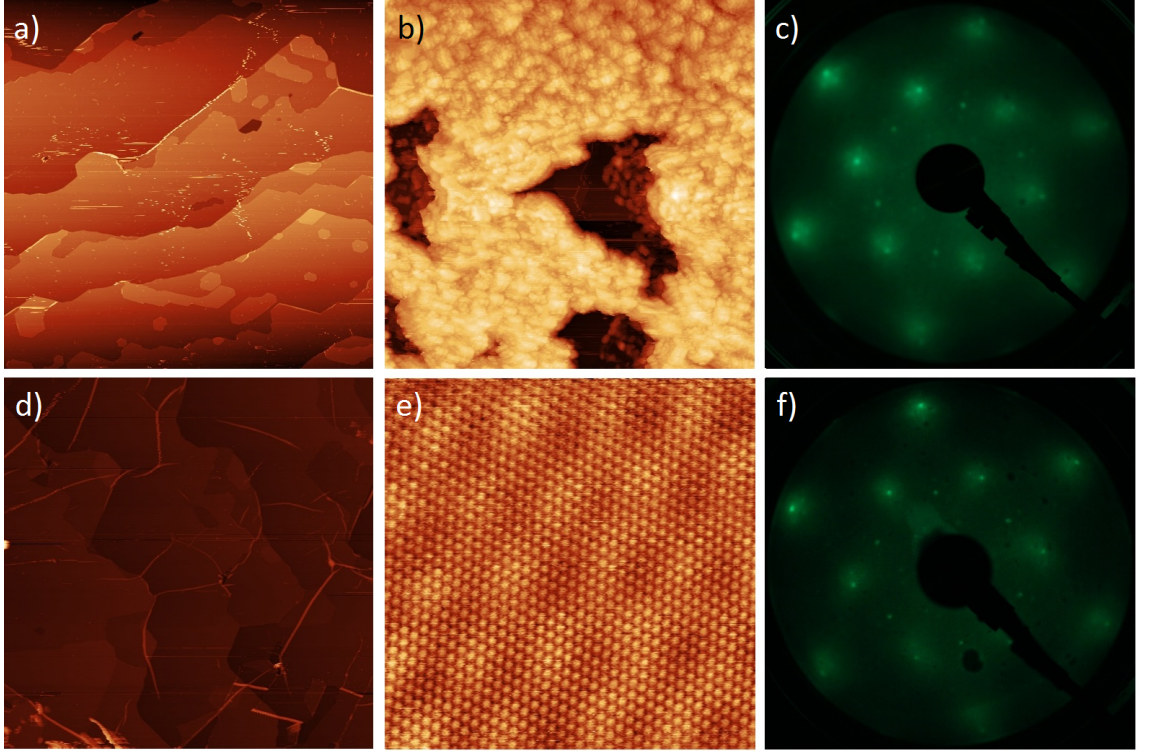
Figure 4.14: (a) 1 μm^2 STM image of uncontaminated graphene grown on SiC (V$_{bias}$=1.1 V, I=0.5 nA). (b) 1 μm^2 image of the graphene sample contaminated by evaporation of Ag (V$_{bias}$=2.2 V, I=0.4 nA). (c) LEED pattern of the graphene before contamination, at beam energy $E_0 = 180.2$ eV, showing graphene and SiC (1 $\times$ 1) and $(6\sqrt{3} \times 6\sqrt{3})R30°$ reconstruction spots. (d) 1 μm^2 of graphene after cleaning with adhesive tape (V$_{bias}$=2.0 V, I=0.3 nA). (e) 12 nm^2 atomic resolution image of the pristine graphene lattice and buffer layer reconstruction pattern, after contamination and cleaning (V$_{bias}$=-0.2 V, I=1.6 nA). (f) LEED pattern of the graphene after contamination and subsequent cleaning obtained at a beam energy $E_0 = 181.1$ eV, showing identical spots to those observed before contamination [48].

4.3.5 Contamination Deposition and Removal

Figure 4.14(a) shows large terraces of pristine graphene grown on SiC(0001) seperated by bilayer steps. Small graphene islands and pleat defects can also be clearly seen on the surface; pleat defects, the pale lines on the surface that form due to the difference in thermal expansion between the graphene layers and the substrate, appear fairly unstable as significant dragging by the STM tip is evident [58, 62]. The high quality of the graphene present is further shown by the LEED pattern obtained (Fig. 4.14(c)), which shows clear graphene and SiC (1 $\times$ 1) spots as well as the expected $(6\sqrt{3} \times 6\sqrt{3})R30°$ reconstruction spots indicative of excellent long range ordering on the surface and the layers below. Silver was chosen as a model contaminant that could be easily deposited upon the surface. After 10 minutes of Ag

deposition a thick layer can be observed (Fig. 4.14(b)) with some small clear areas where graphene can be observed below. The silver layer was found to be ~14 nm in thickness with a RMS roughness of 1.4 nm. The non-uniformity and thickness of the Ag layer allows it to effectively simulate unwanted contamination caused by uncontrolled deposition.

Figure 4.14(d) shows the graphene surface after cleaning with adhesive tape. What immediately becomes apparent is that 99.5% of the deposited Ag has been removed from the surface, as pristine graphene terraces are now once again visible, with only one small area appearing to contain any silver contamination. Upon further imaging on multiple areas of the surface, the residual silver was found to be an isolated occurrence. What is also evident is that the cleaning process causes very little damage to the graphene, with only a small number of areas present in which tiny graphene flakes appear to have been pulled up from the surface. The only significant difference observed between the graphene before and after contamination and cleaning are in the pleat defects visible on the surface. Before contamination the pleat defects observed were highly mobile on the surface, being dragged by the STM tip to step edges. After cleaning these pleats are now significantly more stable showing no indications of dragging by the STM tip. Furthermore, the concentration of pleats also increased from $13\pm3/\mu\text{m}^2$ to $19\pm3/\mu\text{m}^2$. Pleat dimensions were also significantly different with average pleat length and height increasing by 81 ± 9 nm and 0.2 ± 0.1 nm respectively, whilst width decreased by 1.7 ± 0.4 nm (Fig. 4.15). Moreover, the total variation in all dimensions substantially increased after the cleaning process. These differences in pleat defects are likely to occur due to the cleaning method pulling the graphene on the surface up to a small degree whilst removing the contamination. This leads to pre-existing pleat defects increasing in size whilst also creating new ones. The changes observed in pleat defects may indicate that the graphene layers adhere less strongly than before contamination due to the strain applied by the cleaning process [62]. However, these changes to the pleats may instead be metastable and may revert to their previous dimensions upon heating.

Despite the changes observed in pleat defects, upon imaging at higher resolution the pristine graphene lattice can be clearly observed with a negligible defect concentration (Fig. 4.14(e)). Furthermore, the $(6\sqrt{3})R30°$ buffer layer is also clearly visible indicating that the quality of the buffer layer also remains excellent despite the strain put on the film during the cleaning procedure. The quality is further confirmed by the LEED pattern obtained which shows no differences compared with
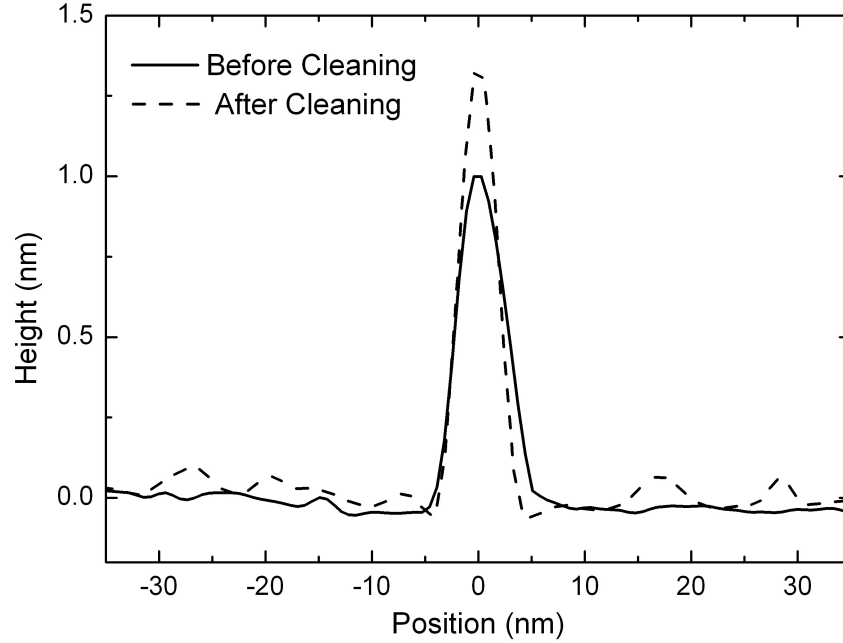
Figure 4.15: Cross section height profile of typical pleat defects before and after contamination removal. After cleaning pleats are generally taller and narrower than those measured before contamination [48].

that obtained before contamination and cleaning, with graphene, SiC (1 × 1) and buffer layer reconstruction spots all clearly visible (Fig. 4.14(f)). The long range ordering of the graphene is therefore unaffected by the cleaning method.

In order to explain how this method can be used to remove large scale contamination, whilst leaving the graphene in pristine condition, it is suggested that the Ag contamination adheres weakly to the surface. This is to be expected due to its inert nature, which consequently has prevented the growth of graphene on Ag substrates until the study by Kiraly *et al.* produced dendritic islands on a Ag(111) single crystal [63]. In contrast, graphene adheres very strongly to SiC in comparison to other substrates due to the buffer layer formation (see Chapter 5) [62,64,65]. As a result, when the adhesive tape is applied to the contaminated sample, the silver contamination adheres to it to a much stronger degree than it does to the graphene layers below. Therefore, upon peeling away from the surface the contamination is removed along with it; the graphene layers however, being much more strongly adhered to the surface, are not pulled away by the tape. It can be surmised that in areas that are still free of contamination after deposition, the tape may adhere more strongly to the uppermost layer than the graphene adheres to the substrate. As a result we would expect to see a high defect concentration in these areas; however this was not observed. We propose that the tape adheres primarily to the raised

asperities offered by the contamination on the surface rather than conforming to the surface. Due to the high flexibility and mechanical strength of graphene [66], it is likely that adhesion over a large area is required to delaminate and/or damage the uppermost graphene layer. As a result, the concentration of defects produced by the cleaning method remains low. The small areas where contamination does remain after the cleaning process are likely the result of defects in the graphene layer below. Defective areas in the graphene lattice, present prior to deposition, produce reactive sites at which the Ag contamination can adhere much more strongly, preventing its removal via mechanical peeling [61]. It can be speculated that a more reactive metal contaminant than Ag, such as Ni which binds more strongly to the surface would result in significantly more damage [67].
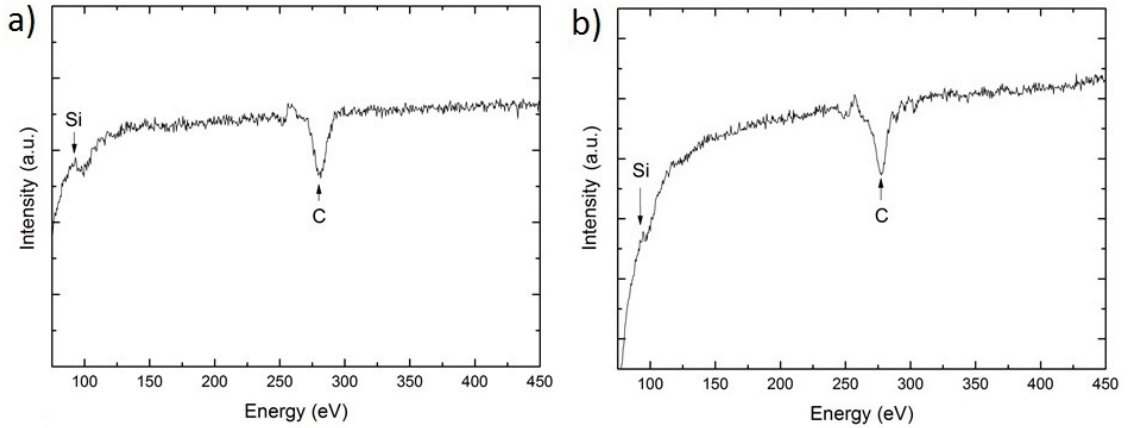
Figure 4.16: Auger spectra of graphene on SiC(0001) taken (a) before contamination with Ag and (b) after contamination and cleaning. Silicon and carbon peaks are visible in both spectra at 92 eV and 271 eV. [48]

With the silver contamination removed from the surface and a pristine graphene surface observed below, an alternative mechanism must be considered. As the graphene observed after cleaning is of an excellent quality and only minute amounts of contamination are visible, it is possible that during the process, both the silver and the uppermost graphene layer it is adhered to are removed by the adhesive tape. This process would show many similarities to the original production of isolated graphene in which cleaving highly oriented pyrolytic graphite (HOPG) multiple times produced large graphene single crystals [1]. To rule out this alternative mechanism AES was used to determine if any change in the graphene layer thickness was seen after the cleaning process was employed. Figure 4.16(a) shows the AES spectrum obtained before contamination; clear peaks corresponding to Si and C can be observed at 92 eV and 271 eV respectively. Based on the C:Si peak ratio an estimate of 3±1 graphene layers was obtained for the thickness of the film. After

the contamination and cleaning of the graphene sample the AES spectrum once again showed clear Si and graphitic carbon peaks, from which a C:Si ratio indicated a thickness of 3±1 strongly suggesting that the cleaning method only removes the contaminant layer, leaving all graphene layers intact. This is further supported by STM images taken after repetition of the deposition and cleaning process, which showed the expected multiple layers of graphene present. Had a layer of graphene been removed from the surface after each iteration, it would be expected that only the graphitic buffer layer would be observed following two repetitions. Therefore, it can be concluded that the cleaning process only removes the contamination from the surface, leaving all graphene layers in excellent condition.
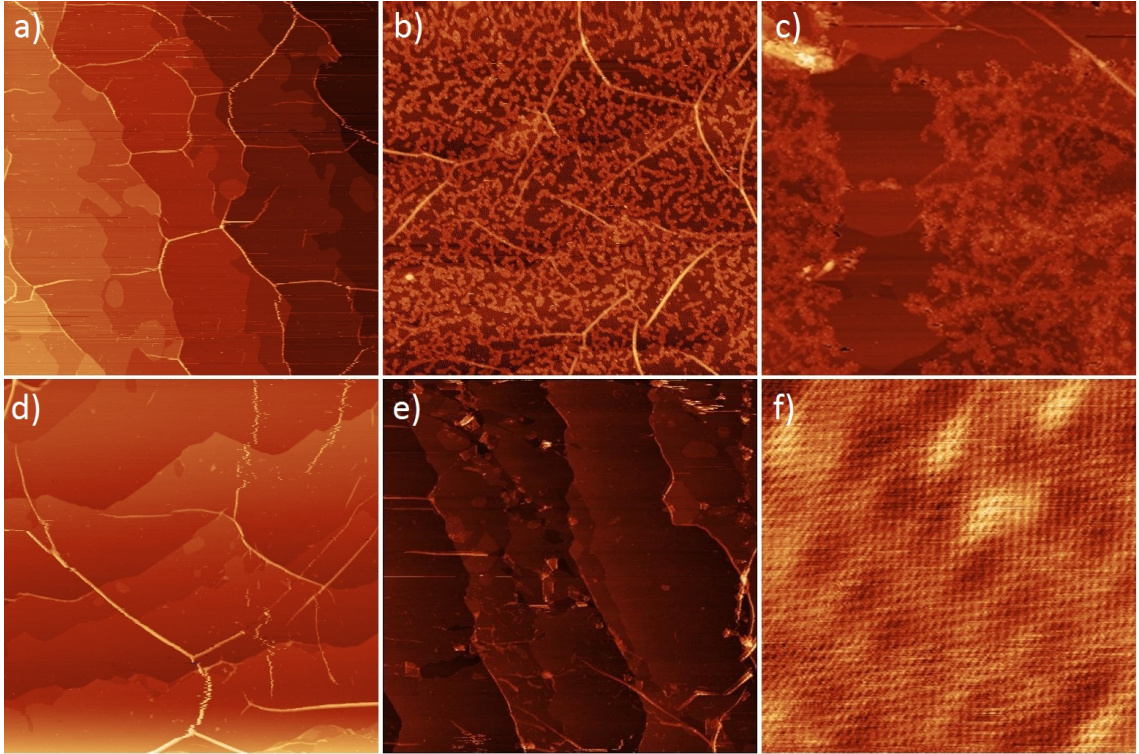
Figure 4.17: (a) 1 μm^2 STM images of graphene grown on SiC taken before contamination (V_{bias}=1.9 V, I=0.3 nA) and (b) after contamination from an electron gun (V_{bias}=1.0 V, I=0.7 nA). (c) 500 nm^2 image of thin Ag contamination deposited on graphene grown on SiC, showing similarities to that observed in (b) (V_{bias}=2.0 V, I=0.5 nA). (d) 1 μm^2 image of the graphene-SiC sample in (b) after cleaning (V_{bias}=0.7 V, I=0.4 nA). (e) 1 μm^2 image of graphene after multiple cleaning cycles (V_{bias}=0.4 V, I=0.3 nA) (f) 12 nm^2 image of an area of pristine graphene lattice that remains after multiple cleaning cycles (V_{bias}=0.5 V, I=1.6 nA).

The method has been shown to be effective at removing thick layers of metallic contamination, with minimal damage to the graphene layers below, however, often contaminant layers will be thin with only partial coverage of the surface. Figure 4.17(a) shows graphene grown on SiC(0001) before any contamination has been de-

posited on the surface. As observed previously, long terraces of graphene with small isolated islands and pleat defects are clearly visible. However, after AES was performed on the sample, a thin layer of material can now be observed covering $\sim$46% of the surface with a thickness of $\sim$1.2 nm (Fig. 4.17(b)). Unlike after the purpose-fully deposited silver the large graphene terraces and pleat defects are still visible. In fact, pleat defects appear to be much more stable, likely due to the contamination pinning them in place, preventing them from being dragged by the STM tip. The most likely source of this contamination is the LaB_6 electron gun filament, which after prolonged use can degrade, depositing material during emission. In previous studies of graphene grown on SiC, similar images have been obtained, but with lower coverages which attribute this material to roughened graphene, caused by hydrogen etching [47]. However, no indication of this roughening is observed before AES measurement is conducted, and furthermore, the level of deposition shows similarities to low coverages of surface contamination (Fig. 4.17(c)).

Having deposited contamination on the surface via AES, adhesive tape was once again applied and removed to see whether thin layers of an unknown contamination could also be removed by the same method. Figure 4.17(d) shows the graphene sample after the cleaning process. As seen before for samples with thick layers of contamination, >99% of the deposited material is removed, with the clear graphene terraces once again visible on the surface. The pleat defects again show increased length and height compared to before contamination as expected due to the slight pulling up of the graphene layers during cleaning. Additionally, the amount of damage observed is reduced compared to that observed upon samples which were heavily contaminated and subsequently cleaned. This is most likely due to the reduced thickness of the contaminant layer, resulting in fewer areas where contamination is strongly adhered at reactive sites at which graphene flakes will be pulled up with the contamination. As with the thicker deposited Ag layer, the contamination adheres strongly to the adhesive tape and upon peeling is removed, whilst the graphene, which is adhered very strongly to the SiC substrate is left unaffected [62,68].

Despite seeing reduced damage to the uppermost graphene layer from removing thin contaminant layers, after multiple cycles the level of damage becomes much more significant. Figure 4.17(e) shows the graphene sample after contamination and cleaning three times; the long terraces remain intact with some small graphene islands still clearly visible. However, large numbers of holes in the topmost graphene layer can be observed with small graphene flakes littering the surface. Furthermore, the number of pleat defects present is reduced to a large degree, with those that

remain being dragged to step edges. This indicates that the top layer of graphene has been pulled up in enough areas that the pleat defects, which are the predominant means of strain release brought on by the difference in thermal expansion between the graphene and the substrate, are no longer required to release the strain on the system [58]. The larger extent of this damage is likely a result of the uppermost layer being partially delaminated with each cleaning cycle, resulting in more weak points being produced each time, which upon further contamination removal will result in tearing of the graphene sheet. This process would compound with each cleaning cycle, eventually resulting in small graphene flakes being removed from the surface completely. Although significant damage is observed at larger scales, the hexagonal graphene lattice remains pristine over the majority of the surface, suggesting that damage occurs predominantly at the edges of graphene layers rather than on flat areas, most likely due to the stronger bonding of contamination at these points (Fig. 4.17(f)). However, despite large areas of pristine graphene lattice still present after cleaning multiple times, the level of damage after several cycles would drastically reduce its viability for electronic devices.

In summary, a facile technique to remove metal contamination from graphene grown on SiC(0001) is presented. Ag contamination was deposited and subsequently removed via the application of adhesive tape and by subsequently peeling it away. The method was found to remove >99% of deposited contamination, causing minimal damage to the sample in the process. The method was found to be effective at removing contamination at many different thicknesses. Material previously thought to be roughened graphene caused by hydrogen etching was found to most likely be contamination from the filament of an electron gun deposited during AES measurements [47]. This material was also removable by the technique discussed. Atomic resolution images found that the graphene lattice remains in pristine condition even after multiple cleaning cycles. However, cleaning more than three times was found to cause significant damage, with graphene flakes being pulled up from the surface. The method discussed presents a low cost and effective way of removing contamination from graphene samples grown on SiC, allowing for their reuse for electronic or experimental purposes.

4.4 Conclusions

In this chapter, graphene was grown on SiC(0001) substrates at different growth temperatures, for different lengths of time, followed by different cooling rates. Samples were then characterised via STM, LEED, RS and AES to determine the optimum conditions for growth of graphene. Though graphene has been grown on SiC(0001) before, previous reports involved lower temperatures, and a complete optimisation of the growth process was not undertaken. From the results obtained here, we are able to report the optimum conditions at which graphene can be grown on SiC(0001). Fully characterised samples grown under these ideal conditions were then utilised in the work reported in Chapters 5 and 6 of this thesis. Additionally to growth optimisation, graphene was grown on patterned SiC(0001) samples as a potential method to produce nano-ribbon arrays. However, the damage caused by etching prevented the formation of graphene of an acceptable quality. Finally, a cleaning method was developed to remove large scale contamination from the graphene surface. Various cleaning methods have been previously reported, however, they are not appropriate for large scale contamination removal. Our cleaning method allows for the easy reuse of graphene samples for further study or electronic purposes.

Graphene samples were grown at various growth temperatures for 4 minutes to observe how temperature affects the formation of graphene on SiC(0001). At growth temperatures of 1700 °C and 1775 °C, the graphene grew in rough edged terraces with high concentrations of small islands. Growth at 1850 °C produced large pristine graphene terraces with a significant reduction in the number of small islands. Despite the observed improvements in graphene quality with increasing temperature, further increases above 1850 °C were found to produce an unacceptable surface morphology due to the formation of large etch pits. Continued etching of the substrate is most likely the cause of the pits observed. Characterisation via AES indicated that the thickness of the graphene grown is fairly constant across all growth temperatures, with slight increases at lower temperatures. Finally, RS provided a quantitive measure of the quality of the graphene produced via the relative intensity of the D peak associated with defects. This peak was found to decrease in intensity with respect to the G and $2D$ peaks as growth temperature was increased, confirming that higher quality graphene is produced at higher growth temperatures. Therefore, it can be concluded that to produce the highest quality graphene via the sublimation of Si from SiC(0001) method a temperature of 1850 °C should be implemented during short growth phases.

Although growth temperature plays a large part in the quality of graphene produced, the length of the growth phase is also highly significant. Graphene was grown on SiC(0001) at 1775 °C for various different growth times. STM images obtained of graphene grown for 4 minutes showed high concentrations of small islands and pits, most likely due to graphene nuclei forming in the earliest stages of growth. In contrast, graphene grown at 1775 °C for 60 minutes exhibits considerably more uniform graphene with a significant drop in the number of small graphene islands and negligible small pits. The higher quality observed, despite being at a lower temperature than that suggested by earlier temperature dependence measurements, indicates that growth time plays a key role in the production of complete graphene layers. RS measurements over a larger range of graphene growth times further support this, as the I_D/I_G ratio observed was found to drop significantly as growth phase was lengthened. Therefore, we suggest a longer growth phase of 60-90 minutes should be used to produce the highest quality graphene which is suitable for electronic applications.

Following the growth phase, cooling rate was also varied for samples grown at 1775 °C. No significant difference was observed in the morphology of graphene between samples produced with a cooling time of 2, 30 and 90 minutes, indicating cooling rate does not affect the quality of graphene grown via this method. However, the level of contamination on the samples was found to increase significantly as cooling time was increased. The origin of this contamination is unknown, however potential sources are the graphite heater and chamber walls, that remain hotter for longer periods allowing for material to desorb and be deposited on the surface. An alternative source may be the SiC wafer as Si sublimation is likely to continue during the cooling phase, which may result in their subsequent readsorbtion to the graphene surface. In conclusion, although the graphene produced is not affected by the cooling rate, in order to keep contamination of the surface at a minimum a fast cooling rate should be implemented.

Having optimised the growth of graphene on SiC(0001), substrates were trenched via photolithography, prior to growth, as a method to produce graphene nanoribbons. Graphene was found to form both on the upper and lower plateaus. However, the quality of the graphene produced was low due to the significant damage caused to the substrate by the lithography process. The damage caused was found to prevent the formation of the buffer layer, which is a prerequisite for high quality graphene formation. As such, this method is currently not suitable for producing graphene nanoribbon arrays. Should the amount of damage to upper areas of the substrate be

reduced via a more accurate lithography, graphene nanoribbons may be produced by this method.

Finally, a method for large area contamination removal from graphene samples grown on SiC(0001) is presented. It was found that the method was able to remove greater than 99% of silver contamination that had been deposited on the surface, leaving pristine graphene below. The method was capable of removing both thick and thinner layers of of full and partial coverage, with negligible damage to the graphene below, or complete graphene layer removal. Contamination was also found to be deposited during LEED and AES measurements, most likely from the electron gun filament. This deposited material showed many similarities with "roughened" graphene reported by a previous group, however the cleaning method was also capable of removing this contamination, allowing for the reuse of graphene samples for further study.

4.5   References

[1] K. S. Novoselov, A. K. Geim, S. V. Morozov, D. Jiang, Y. Zhang, S. V. Dubonos, I. V. Grigorieva and A. A. Firsov, *Science*, **306**(5696), 666–669 (2004).

[2] F. Schwierz, *Nature Nanotechnol.*, **5**(7), 487–496 (2010).

[3] F. Schedin, A. K. Geim, S. V. Morozov, E. W. Hill, P. Blake, M. I. Katsnelson and K. S. Novoselov, *Nature Mater.*, **6**(9), 652–655 (2007).

[4] K. S. Kim, Y. Zhao, H. Jang, S. Y. Lee, J. M. Kim, K. S. Kim, J. Ahn, P. Kim, J. Choi and B. H. Hong, *Nature*, **457**(7230), 706–710 (2009).

[5] X. Li, W. Cai, J. An, S. Kim, J. Nah, D. Yang, R. Piner, A. Velamakanni, I. Jung, E. Tutuc, S. K. Banerjee, L. Colombo and R. S. Ruoff, *Science*, **324**(5932), 1312–1314 (2009).

[6] C. Berger, Z. Song, X. Li, X. Wu, N. Brown, C. Naud, D. Mayou, T. Li, J. Hass, A. N. Marchenkov, E. H. Conrad, P. N. First and W. A. de Heer, *Science*, **312**(5777), 1191–1196 (2006).

[7] S. Y. Zhou, G.-H. Gweon, A. V. Fedorov, P. N. First, W. A. de Heer, D.-H. Lee, F. Guinea, A. H. C. Neto and A. Lanzara, *Nature Mater.*, **6**(10), 770–775 (2007).

[8] C. Riedl and U. Starke, *Phys. Rev. B*, **76**(24), 245406 (2007).

[9] J. Hass, J. E. Millán-Otoya, P. N. First and E. H. Conrad, *Phys. Rev. B*, **78**(20), 205424 (2008).

[10] J. Hass, W. A. de Heer and E. H. Conrad, *J. Phys.: Condens. Matter*, **20**(32), 323202 (2008).

[11] R. M. Tromp and J. B. Hannon, *Phys. Rev. Lett.*, **102**(10), 106104 (2009).

[12] X. Hao, Y.-F. Chen, P.-J. Li, Z.-G. Wang, J.-B. Liu, J.-R. He, R. Fan, J.-R. Sun, W.-L. Zhang and Y.-R. Li, *Chinese Phys. B*, **21**(4), 046801 (2012).

[13] J. B. Hannon and R. M. Tromp, *Phys. Rev. B*, **77**(24), 241404 (2008).

[14] W. A. de Heer, C. Berger, X. Wu, P. N. First, E. H. Conrad, X. Li, T. Li, M. Sprinkle, J. Hass, M. L. Sadowski, M. Potemski and G. Martinez, *Solid State Commun.*, **143**(1-2), 92–100 (2007).

[15] W. Dangchao, Z. Yuming, Z. Yimen, L. Tianmin, G. Hui, W. Yuehu, T. Xiaoyan and W. Hang, *J. Semicond.*, **32**(11), 113003 (2011).

[16] M. L. Bolen, S. E. Harison, L. B. Biedermann and M. A. Capano, *Phys. Rev. B*, **80**(11), 115433 (2009).

[17] P. Avouris, *Nano Lett.*, **10**(11), 4285–4294 (2010).

[18] M. Y. Han, B. Özyilmaz, Y. Zhang and P. Kim, *Phys. Rev. Lett.*, **98**(20), 206805 (2007).

[19] Z. Chen, Y.-M. Lin, M. J. Rooks and P. Avouris, *Physica E*, **40**(2), 228–232 (2007).

[20] K. Wakabayashi, Y. Takane, M. Yamamoto and M. Sigrist, *New J. Phys.*, **11**, 095016 (2009).

[21] T. B. Martins, R. H. Miwa, A. J. R. da Silva and A. Fazzio, *Phys. Rev. Lett.*, **98**(19), 196803 (2007).

[22] X. Li, X. Wang, L. Zhang, S. Lee and H. Dai, *Science*, **319**(5867), 1229–1232 (2008).

[23] D. B. Kosynkin, A. L. Higginbotham, A. Sinitskii, J. R. Lomeda, A. Dimiev, B. K. Price and J. M. Tour, *Nature*, **458**(7240), 872–876 (2009).

[24] L. Tsetseris and S. T. Pantelides, *Appl. Phys. Lett.*, **99**(14), 143119 (2011).

[25] J. Campos-Delgado, J. M. Romo-Herrera, X. Jia, D. A. Cullen, H. Muramatsu, Y. A. Kim, T. Hayashi, Z. Ren, D. J. Smith, Y. Okuno, T. Ohba, H. Kanoh, K. Kaneko, M. Endo, H. Terrones, M. S. Dresslehaus and M. Terrones, *Nano Lett.*, **8**(9), 2773–2778 (2008).

[26] A. Sinitskii, A. Dimiev, D. V. Kosynkin and J. M. Tour, *ACS Nano*, **4**(9), 5405–5413 (2010).

[27] Y. Zhang, C. Hui, R. Sun, K. Li, K. He, X. Ma and F. Liu, *Nanotechnology*, **25**(13), 135301 (2014).

[28] W. S. Hwang, P. Zhao, K. Tahy, L. O. Nyakiti, V. D. Wheeler, R. L. Myers-Ward, C. R. E. Jr., D. K. Gaskill, J. A. Robinson, W. Haensch, H. Xing, A. Seabaugh and D. Jena, *Appl. Phys. Lett. Mater.*, **3**(1), 011101 (2015).

[29] M. Sprinkle, M.Ruan, Y. Hu, J. Hankinson, M. Rubio-Roy, B. Zhang, X. Wu, C. Berger and W. A. de Heer, *Naure Nanotechnol.*, **5**(10), 727–731 (2010).

[30] T. Hopf, K. V. Vassilevski, E. Escobedo-Cousin, N. G. Wright, A. G. O'Neill, A. B. Horsfall, J. P. Goss, A. Barlow, G. H. Wells and M. R. C. Hunt, *Mater. Sci. Forum*, **778-780**, 1154–1157 (2014).

[31] P. Sutter, J. T. Sadowski and E. Sutter, *Phys. Rev. B*, **80**(24), 245411 (2009).

[32] A. T. N'Diaye, J. Coraux, T. N. Plasa, C. Busse and T. Michely, *New. J. Phys.*, **10**(1), 1–16 (2008).

[33] A. K. Geim and K. S. Novoselov, *Nature Mater.*, **6**(3), 183–191 (2007).

[34] Y. Dan, Y. Lu, N. J. Kybert, Z. Luo and A. T. C. Johnson, *Nano Lett.*, **9**(4), 1472–1475 (2009).

[35] Z. Li, Y. Wang, A. Kozbial, G. Shenoy, F. Zhou, R. McGinley, P. Ireland, B. Morganstein, A. Kunkel, S. P. Surwade, L. Li and H. Liu, *Nature Mater.*, **12**(10), 925–931 (2013).

[36] A. Ambrosi, C. K. Chua, B. Khezri, Z. Sofer, R. D. Webster and M. Pumera, *PNAS*, **109**(32), 12899–12904 (2012).

[37] A. Ambrosi and M. Pumera, *Nanoscale*, **6**(1), 472–476 (2014).

[38] G. Lupina, J. Kitzmann, I. Costina, M. Lukosius, C. Wenger, A. Wolff, S. Vaziri, M. Östling, I. Pasternak, A. Krajewska, W. Strupinski, S. Kataria, A. Gahoi, M. C. Lemme, G. Ruhl, G. Zoth, O. Luxemhofer and W. Mehr, *ACS Nano*, **9**(5), 4776–4785 (2015).

[39] Q. Cheng, J. Tang, J. Ma, H. Zhang, N. Shinya and L.-C. Qin, *Carbon*, **49**(9), 2917–2925 (2011).

[40] Z. H. Ni, H. M. Wang, Z. Q. Luo, Y. Y. Wang, T. Yu, Y. H. Wu and Z. X. Shen, *J. Raman Spectrosc.*, **41**(5), 479–483 (2009).

[41] N. Lindvall, A. Kalabukhov and A. Yurgens, *J. Appl. Phys.*, **111**(6), 064904 (2012).

[42] A. M. Goossens, V. E. Calado, A. Barreiro, K. Watanabe, T. Taniguchi and L. M. K. Vandersypen, *Appl. Phys. Lett.*, **100**(7), 073110 (2012).

[43] C. A. Joiner, T. Roy, Z. R. Hesabi, B. Chakrabarti and E. M. Vogel, *Appl. Phys. Lett.*, **104**(22), 223109 (2014).

[44] J. Moser, A. Barreiro and A. Bachtold, *Appl. Phys. Lett.*, **91**(16), 163513 (2007).

[45] T. Hopf, K. V. Vassilevski, E. Escobedo-Cousin, P. J. King, N. G. Wright, A. G. O'Neill, A. B. Horsfall, J. P. Goss, G. H. Wells and M. R. C. Hunt, *J. Appl. Phys.*, **116**(15), 15404 (2014).

[46] S. Mroczkowski and D. Lichtman, *Surf. Sci.*, **131**(1), 159–166 (1983).

[47] S. N. Luxmie, P. J. Fisher, R. M. Feenstra, G. Gu and Y. Sun, *J. Elec. Mater.*, **38**(6), 718–724 (2008).

[48] G. H. Wells, T. Hopf, K. V. Vassilevski, E. Escobedo-Cousin, A. G. O'Neill, A. B. Horsfall, J. P. Goss and M. R. C. Hunt, *J. Vac. Sci. Tech. B*, **33**(5), 051802 (2015).

[49] S. Tanaka, K. Morita and H. Hibino, *Phys. Rev. B*, **81**(4), 041406 (2010).

[50] A. Sandin, J. E. Rowe and D. B. Dougherty, *Surf. Sci.*, **611**, 25–31 (2013).

[51] A. Zugarramurdi, M. Debiossac, P. Lunca-Popa, A. J. Mayne, A. Momeni, A. G. Borisov, Z. Mu, P. Roncin and H. Khemliche, *Appl. Phys. Lett.*, **106**(10), 101902 (2015).

[52] J. Hass, J. E. Millán-Otoya, P. N. First and E. H. Conrad, *Phys. Rev. B*, **78**(20), 205424 (2008).

[53] A. W. Robertson and J. H. Warner, *Nano Lett.*, **11**(3), 1182–1189 (2011).

[54] J. R. Hass, *Structural characterisaztion of epitaxial graphene on silicon carbide*, Ph.D. thesis, School of Physics, Georgia Institute of Technology (2008).

[55] C. Riedl, A. A. Zakharov and U. Starke, *Appl. Phys. Lett.*, **93**(3), 033106 (2008).

[56] J. C. Lascovich, R. Giorgi and S. Scaglione, *Appl. Surf. Sci.*, **47**(1), 17–21 (1991).

[57] S. Shivaraman, M. V. S. Chandrashekhar, J. J. Boeckl and M. G. Spencer, *J. Elec. Mater.*, **38**(6), 725–730 (2009).

[58] W. A. de Heer, C. Berger, M. Ruan, M. Sprinkle, X. Li, Y. Hu, B. Zhang, J. Hankinson and E. Conrad, *Proc. Nat. Aca. Sci. U.S.A*, **108**(41), 16900–16905 (2011).

[59] H. Ibach, *Physics of surfaces and interfaces*, Springer, New York (2006).

[60] G. Yu, G. Li-Wei, L. Wei, H. Jiao, J. Yu-Ping, S. Wei, L. Zhi-Lin and W. Yi-Fei, *Chin. Phys. B*, **23**(8), 086501 (2014).

[61] F. Banhart, J. Kotakoski and A. V. Krasheninnikov, *ACS Nano*, **5**(1), 25–41 (2011).

[62] G. H. Wells, T. Hopf, K. V. Vassilevski, E. Escobedo-Cousin, N. G. Wright, A. B. Horsfall, J. P. Goss, A. G. O'Neill and M. R. C. Hunt, *Appl. Phys. Lett.*, **105**(19), 193109 (2014).

[63] B. Kiraly, E. V. Iski, A. J. Mannix, B. L. Fisher, M. C. Hersam and N. P. Guisinger, *Nature Commun.*, **4**(2804), 1–7 (2013).

[64] S. P. Koenig, N. G. Boddeti, M. L. Dunn and J. S. Bunch, *Nature Nanotechnol.*, **6**(9), 543–546 (2011).

[65] T. Yoon, W. C. Shin, T. Y. Kim, J. H. Mun, T.-S. Kim and B. J. Cho, *Nano Lett.*, **12**(1), 1448 (2012).

[66] C. Lee, X. Wei, J. W. Kysar and J. Hone, *Science*, **321**(5887), 385–388 (2008).

[67] J. Lahiri, T. S. Miller, A. J. Ross, L. Adamska, I. I. Oleynik and M. Batzill, *New J. Phys.*, **13**(2), 025001 (2011).

[68] A. Mattausch and O. Pankratov, *Phys.Rev. Lett.*, **99**(7), 076802 (2007).

Chapter 5

Pleat Formation and the Determination of the Adhesion Energy of Graphene on SiC

This chapter details an investigation of pleat defects formed under various growth conditions in graphene grown on SiC(0001). The length, height, width and orientation of pleats were measured by Scanning Tunnelling Microscopy (STM). Pleat heights and widths were used in conjunction with a continuum energy model to determine the adhesion energy of graphene on SiC(0001).

5.1   Introduction

As discussed in previous chapters, the high mechanical strength [1] and excellent electrical properties of graphene [2,3] make it an ideal candidate for future electronic devices. One avenue for this research is through formation of hetero-structures [4–6]. However, the influence of a substrate has a large effect on mechanical properties at the nanoscale [7], making a complete knowledge of graphene adhesion to different substrates vital. A number of different methods have been used to measure the adhesion energy of graphene on different materials, such as the creation and characterisation of pressurised blisters [8, 9], deformation by atomic force microscope (AFM) tips [10] and intercalation of nanoparticles [11, 12]. However, a simple technique to determine the adhesion of graphene on any substrate is still required. This solution may be provided by a commonly observed defect, the pleat.

A frequent feature on both epitaxially grown and transferred graphene, the pleat defect, also known a wrinkle, buckle or fold [13], occurs when graphene layers delaminate from the substrate due to various stresses in the film. These differ from the smaller ripples observed in both epitaxially grown and free-standing graphene, which arise from local interactions with the surface [14] and intrinsic thermal fluctuations [15] respectively. The mechanism for the formation of pleats on epitaxially grown films is attributed to the difference in thermal expansion between the graphene and the substrate [16,17]; whereas on transferred graphene, their formation is determined by the transfer method used and the surface morphology of the substrate [15]. Pleat defects have been observed on graphene grown on SiC [13, 18–24], Cu [25–27], Ni [28,29], Pt [17] and Ir [16,30], as well as graphene transferred to SiO_2 [15,31,32], indicating pleats are a universal feature of graphene adhered to surfaces. As a result, this defect has become of interest due to the increased chemical reactivity along raised delaminated areas and has even been proposed as a route towards producing large arrays of graphene nanoribbons based on preferential etching along the pleats [33, 34].

It has also been suggested that pleat formation acts to reduce the strain on epitaxially grown graphitic films, brought about by their elastic mismatch [35]. The strain and subsequent delamination is inherently linked to the interaction between the overlayer and the substrate. Consequently, the delamination is highly dependent on the adhesion energy. This has been explored theoretically by Zhang *et al.* who describe the formation of large pleat structures from the merging of smaller wrinkles, via the adhesion energy of the system and other, frictional, parameters [36]. It can

be inferred that by studying the interplay between pleat formation and the adhesive properties of graphene an effective adhesion energy can be determined through the measurement of key pleat parameters, such as height and width. Due to the presence of pleat defects on the large number of graphene-substrate systems mentioned above, such an analysis has the potential to provide substantial quantitative data on the adhesion of graphene films.

With pleat defects having been observed on many systems, their formation mechanism well known, and significant interest shown in their properties for technological purposes [37], one would expect the factors that determine pleat dimensions to have been identified. However, this is not the case and little is known about the physical parameters which result in pleat variance. In the case of graphene growth on SiC, studies by de Heer *et al.* and Hass *et al.* have quantified the heights and widths of pleat structures that form but focus predominantly on the quality of graphene growth making few comments on how pleats vary under different growth conditions [13, 19]. Furthermore, significant variation in the concentration of pleats can also be seen between different studies, with images obtained in some cases exhibiting large numbers of pleats [22,23] whilst others show little to no pleat formation [38,39]. To our knowledge, no work has sought to explain this disparity in pleat concentration which may result from a large number of factors, such as the graphene growth conditions or even the measurement techniques employed. Where no pleats are observed, it would be pertinent to consider whether pleats are stable on the surface or are they dragged out of the imaging frame via interaction with the experimental probe. Such effects are potentially important in studies using scanning probes, in which there can be significant interaction between probe and surface [22, 40]. The fact that studies via STM reported in the literature have not discussed issues with pleat stability [13] may indicate that pleat dragging is considered a hindrance, rather than a property which may reveal further information about the system.

When studying the pleat defects, their orientation may also reveal information about the graphene-substrate system, as orientational dependence may reflect the pleat formation process and reveal further information on the graphene substrate interaction. Despite this, very little has been reported on the orientation of pleats, even though their presence has been noted on all graphene-substrate systems. Work by N'Diaye *et al.* and Sutter *et al.* suggests that pleat defects will follow the step structure of the substrate, whilst a second set of pleats will form perpendicularly to ensure that both components of the biaxial strain on the film are relaxed [16, 17]. However, this is not clearly observable in the Low Energy Electron Microscopy

(LEEM) and STM data presented in these studies, with pleats often meeting at 120°, along with those junctions close to 90° often showing local distortions tending towards 120°. Therefore, although these studies show to a small degree, pleats forming roughly rectangular networks to reduce strain in the system, this behaviour is certainly not universal and may reflect the substrate-film interaction or result from a large step density [17, 41–43]. Previous imaging of graphene on SiC(0001), Cu and Ni has not exhibited the same pleat morphology observed on Pt(111) and Ir(111), but in fact shows pleats meeting at angles closer to 120°, with three way junctions much more common [21, 22, 24, 28, 44].

In this chapter, scanning tunnelling microscopy (STM) was used to observe pleat defects in graphene grown on SiC(0001). Samples were also characterised by Auger electron spectroscopy (AES) to obtain graphene film thickness, whilst low energy electron diffraction (LEED) was used to determine the high symmetry directions of the graphene lattice. A continuum energy model was developed that describes the buckling of epitaxially grown graphene films, which when combined with the experimentally obtained values for pleat height, width and film thickness allows the adhesion energy of graphene to a substrate to be obtained. This model was then applied to obtain the adhesion energy of graphene on SiC(0001). Variation in pleat defects as a result of changes in growth temperature and growth time was also measured. Finally, the effects of surface contamination and the introduction of defects were examined, to observe how external surface factors affected the stability of pleat defects.

5.2 Experimental

5.2.1 Sample Preparation

Few layer graphene samples (3±1 ML) were grown on SiC(0001) substrates (Tanke-blue Semiconductor Company Ltd.) at various temperatures and for different growth times in the rapid thermal processor, as outlined in Chapter 4 and reference [24]. The samples were then characterised via Raman spectroscopy (RS) followed by transfer to the ultra-high vacuum (UHV) system for further study by low energy electron diffraction (LEED), Auger electron spectroscopy (AES) and Scanning Tunnelling Microscopy (STM).
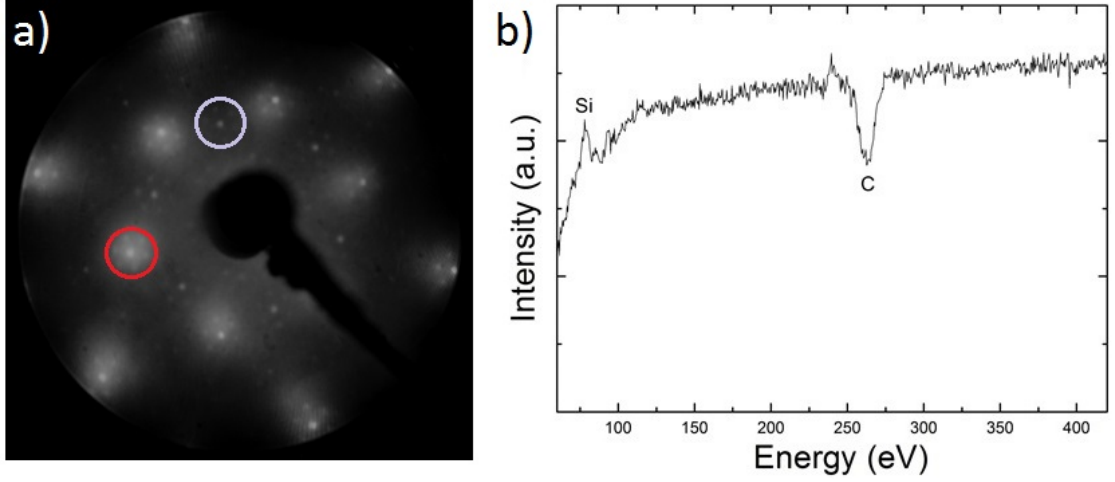
Figure 5.1: LEED pattern obtained at a primary beam energy of 116.5 eV showing graphene and SiC (1 × 1) spots (red and blue circles, respectively), and the ($6\sqrt{3}$ × $6\sqrt{3}$)$R30°$ buffer layer reconstruction. (b) Auger spectrum taken with a primary beam energy of 2.5 keV showing a strong silicon peak at 92 eV and a graphitic carbon peak at 271 eV. Film thickness is estimated to be 3±1 ML. [45]

Samples analysed with the continuum model were grown at 1775 °C for 60 minutes. Figure 5.1 shows the LEED pattern and an Auger spectrum obtained from a typical sample from which pleat heights and widths were obtained. The Si, C and surface reconstruction spots observed in the LEED pattern indicated that high quality graphene was present over large areas of the surface, with a maximum thickness of 4 ML [46]. The Auger spectrum exhibits well defined peaks at 92 eV and 271 eV corresponding to Si and C, indicating a thickness of three graphene monolayers (ML). Large scale STM images obtained were levelled via a mean plane subtraction, to allow cross-sectional pleat height profiles to be acquired. Furthermore, as pleat width is one of the key parameters in the model outlined below, images were required to contain at least one step edge from which to calibrate lateral width values by the method outlined in Chapter 2, eliminating the broadening associated with finite probe size.

5.2.2 Pleat Measurement

In order to obtain pleat width and height, line profiles obtained from STM images are fit to equation 5.1 using the non-linear least squares method.

$$Y = \frac{\delta}{2}\left(1 + cos\left(\frac{\pi}{b}X\right)\right) \quad , \quad -b \leq X \leq b \,, \tag{5.1}$$

where Y is the pleat height, δ is the maximum pleat height, b is the pleat half width and X is the position along the pleat length. As pleats are not always completely stable under imaging, they can be prone, on occasion, to dragging across the surface by the STM tip [45]. This phenomenon has been observed previously by Sun *et al.* [22], in which pleats were deliberately manipulated by a scanning probe, and new pleats created via interaction between the tip and the surface. When moved, pleats are often dragged to step edges where, due to the energy barrier associated with the step, they become pinned. A cross-sectional height profile of a pleat pinned at a step edge can be seen in figure 5.2(a), in comparison to one obtained on a flat terrace (b). Due to the uneven boundaries of the pleat, equation 5.1 cannot be fit to the profile, preventing an accurate measurement of the pleat width. Therefore, pleats observed at step edges are not used in the adhesion energy analysis.
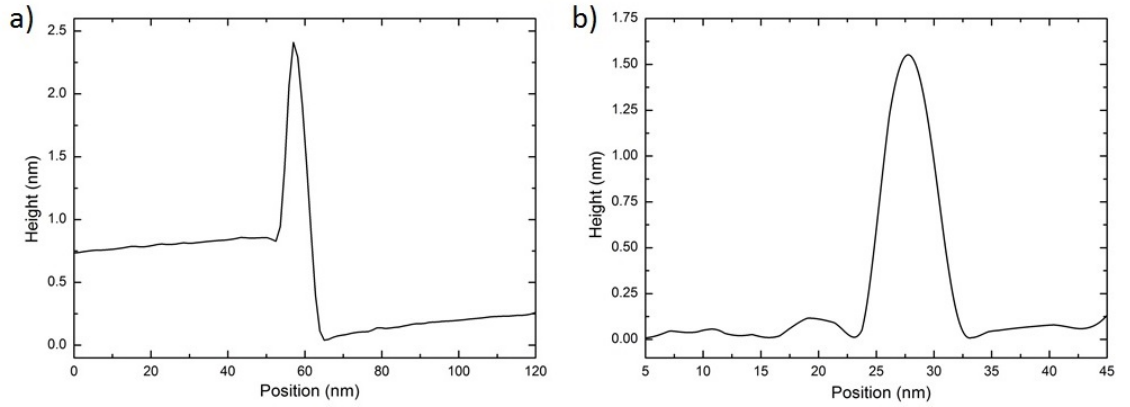
Figure 5.2: (a) Cross-sectional height profile obtained from a pleat pinned at a step edge. (b) Cross-sectional height profile from a pleat on a flat terrace.

With pleats inappropriate for measurement discounted, further care is required to ensure that derived values of height do not contain systematic errors or artefacts from the measurement process. Figure 5.3(a) shows a typical cross sectional pleat height profile. Arrows indicate small negative excursions at the edges of the pleat. Further investigation showed that these dips were not topographic, but were in fact the result of the STM feedback loop, where the large excursion in height of the pleat required smaller feedback values reducing its ability to follow the surface topography. Due to this poor tracking of the surface by the STM tip over these small areas, they appear lower in height. However, higher resolution images, not containing the upper excursion of the pleat, showed no depressions. Therefore, in order to obtain an accurate value for pleat width and height, the fitting employed removes these indentations, by subtracting an appropriate background (Fig. 5.3(b)).
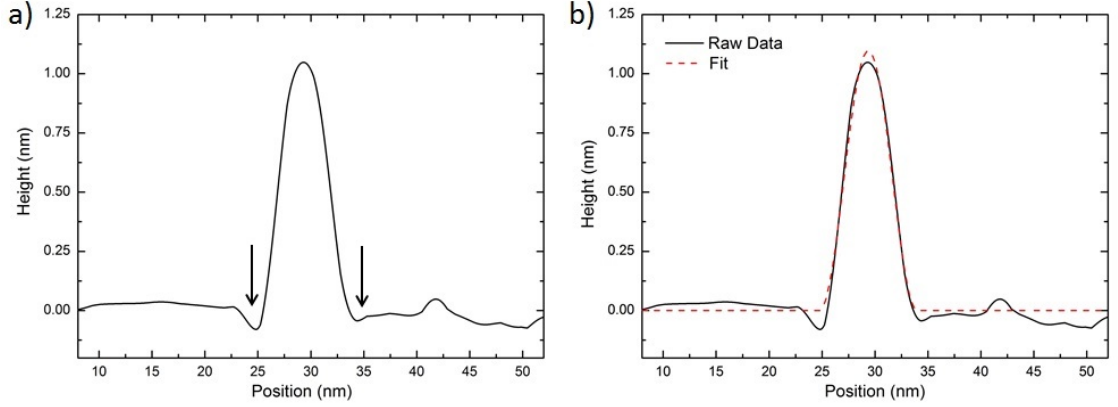
Figure 5.3: (a) Cross sectional pleat height profile, arrows indicate depressions in the STM image caused poor tracking of the surface. (b) Pleat profile in (a) fit using non-linear least squares method also applying a flat background outside the range of the pleat.

5.3 Results and Discussion

5.3.1 Continuum Energy Model

To obtain the adhesion energy, sometimes referred to as the energy release rate, of graphene grown on SiC(0001), a continuum energy model (based on an existing model used to describe buckling of Cr films on polyimide) was developed and implemented [47, 48]. As described previously, pleats are areas of graphene which have buckled upwards in order to reduce the stress on the system caused by the difference in thermal expansion between the SiC substrate and the graphene overlayer [13]. These long straight pleats can be described as Euler buckling modes, where the graphene layer is pinned, i.e. fully bonded to the substrate, either side of the pleat, with complete debonding from the surface along the pleat length, where vertical displacement occurs [49]. In order for this buckling to occur, the residual compression on the system must exceed the classical buckling stress for the clamped graphene area [50].

Prior to buckling, this system can be described as an infinitely deep isotropic substrate, due to the depth of the bulk material being many orders of magnitude larger than the overlayer thickness, with the graphene above under a membrane stress with the Euler bending stress $\sigma_{Y,crit}^m$ and Young's modulus E'_{film}:

$$\sigma_{Y,crit}^m = \frac{\pi^2 E'_{film}}{12} \left(\frac{h}{b}\right)^2 \tag{5.2}$$

$$E'_{film} = \frac{E_{film}}{1 - \nu_f^2} \, , \tag{5.3}$$

in which E_{film} is the standard Young's modulus of isolated graphene, ν_f is the Poisson ratio and b is the half buckle width. The values used for the Young's modulus and Poisson ratio were obtained from the studies by Lee *et al.* [1] and Scarpa *et al.* [51], in which E_{film} and ν_f were found to be 1.0 TPa and 0.165 respectively. The large Young's modulus observed, in comparison to other materials, is thought to arise from the strong C-C bonds present in graphene, and is similar to that of both graphite and carbon nanotubes [52–54]. Similarly, the Poisson ratio, is also fairly close to that observed for both graphite and carbon nanotubes and is indicative of graphene's extremely high intrinsic strength [1, 52, 55]. The critical compressive buckling strain, $\varepsilon_{Y,crit}^m$, can then be obtained as:

$$\varepsilon_{Y,crit}^m = \frac{\pi^2}{12} \left(\frac{h}{b} \right)^2 \, , \tag{5.4}$$

where h is the thickness of the graphene film. The height of the pleat at each point across its width, Y, can be described as a sinusoidal delamination much like the one dimensional blisters investigated by Hutchinson and Suo, which are pinned at their edges [48, 50]:

$$Y = \frac{\delta}{2} \left(1 + cos \left(\frac{\pi}{b} X \right) \right), -b \leq X \leq b \tag{5.5}$$

in which δ is the maximum pleat height. These pleats also have an associated length reduction due to buckling, Δ_{2b}, given by:

$$\Delta_{2b} = \frac{1}{2} \int_{-b}^{b} \left(\frac{dY}{dX} \right)^2 dX = \frac{\pi^2}{8} \frac{\delta^2}{b^2} b \tag{5.6}$$

In the previous system in which this model was applied, the Cr film buckled upwards with channel cracks forming on both sides at the base and apex of the buckle [47]. However, in the case of a graphene overlayer on SiC the pleats present no cracking during delamination, with the lattice continuous across the entirety of the buckle. The absence of cracks in this system, results in pleats being more accurately described by the model, due to cross-sectional height profiles modelled as films that remain continuous across the entirety of the buckle. By taking into account the reduction of the pleat width as a result of the delamination, Δ_{2b}, and the critical membrane buckling strain (equation 5.4) a total compressive shortening strain, ε_s,

may be described by:

$$\varepsilon_s = \varepsilon_{y,crit} + \frac{\pi^2}{16}\frac{\delta^2}{b^2}b \ , \tag{5.7}$$

which upon simplification and rearrangement this produces:

$$\frac{\varepsilon_s}{\varepsilon_{y,crit}} = 1 + \frac{3}{4}\left(\frac{\delta}{h}\right) \tag{5.8}$$

With the strain in the graphene membrane now found, the various energy contributions that lead to the stable pleat structure must be considered in order to obtain an expression that relates the adhesion energy to measurable experimental parameters. The strain energy within the buckle due to bending may be described as:

$$U_{2b,b} = \frac{1}{2}E'_{film}\frac{h^3}{12}\int_{-b}^{b}\left(\frac{d^2Y}{dX^2}\right)^2 dX = E'_{film}\frac{\pi^4}{8.12}\frac{\delta^2}{b^2}\frac{h^3}{b} \ , \tag{5.9}$$

plus the strain energy due to the membrane stress:

$$U_{2b,m} = 2bhE'_{film}\varepsilon^2_{y,crit} \ , \tag{5.10}$$

which when combined, produces the total strain energy within the buckle:

$$U_{2b} = bhE'_{film}\left(2\varepsilon_s\varepsilon_{y,crit} - \varepsilon^2_{y,crit}\right) \tag{5.11}$$

The strain energy remaining in the unbuckled region of the film, U_{B-2b}, can then be written as:

$$U_{B-2b} = (B - 2b)E'_{film}h\frac{\varepsilon^2_s}{2} \tag{5.12}$$

When combining equations 5.11 and 5.12 with the adhesion energy, $2b\Gamma$, the total potential energy of the system (TPE) may be written as:

$$TPE = U_{2b} + U_{B-2b} + 2b\Gamma \tag{5.13}$$

$$TPE = BhE'_{film}\frac{\varepsilon^2_s}{2} - 2bhE'_{film}\frac{(\varepsilon_s - \varepsilon_{y,crit})^2}{2} + 2b\Gamma \tag{5.14}$$

The dissipation of strain in the film can then be written in terms of the thermodynamic force, which is simply the TPE differentiated with respect to the half buckle width:

$$D_b = F\dot{b} = -\frac{\partial TPE}{\partial b}\dot{b} \tag{5.15}$$

$$F = hE'_{film}(\varepsilon_s^2 + 2\varepsilon_s\varepsilon_{y,crit} - 3\varepsilon_{y,crit}^2) - 2\Gamma \tag{5.16}$$

From these relations and by considering the equilibrium state in which pleats are stable upon the surface, $F = 0$, the adhesion energy, Γ, may be obtained as a function of the total compressive shortening strain and the critical compressive buckling strain:

$$\Gamma_{crit}^* = \frac{2\Gamma_{crit}}{hE'_{film}} = \varepsilon_s^2 + 2\varepsilon_s\varepsilon_{y,crit} - 3\varepsilon_{y,crit}^2 = \varepsilon_{y,crit}^2 \left(\frac{\varepsilon_s}{\varepsilon_{y,crit}} - 1\right)\left(\frac{\varepsilon_s}{\varepsilon_{y,crit}} + 3\right) \tag{5.17}$$

Inputting equation 5.8 into 5.17, followed by equation 5.4, gives the adhesion energy purely in terms of measurable parameters b, δ and h:

$$\left(\frac{\delta}{h}\right)^2 = \frac{4}{3}\frac{\Gamma^*}{\varepsilon_{y,crit}^2(\varepsilon_s/\varepsilon_{y,crit} + 3)} \quad , \tag{5.18}$$

which when rearranged produces:

$$\left(\frac{\delta}{h}\right)^2 \left(1 + \frac{3}{16}\left(\frac{\delta}{h}\right)^2\right) = \frac{\Gamma^*}{3\varepsilon_{y,crit}^2} \tag{5.19}$$

By inverting the equation above, a model from which the adhesion energy can be obtained is produced. It should be noted that in the original derivation of this model by Cordill *et al.* [47], a factor of $3/2$ is erroneously present, which has been corrected:

$$\sqrt{\frac{\delta}{h}}\left(1 + \frac{3}{16}\left(\frac{\delta}{h}\right)^2\right)^{\frac{1}{4}} = \frac{2}{\pi}(3\Gamma^*)^{\frac{1}{4}}\left(\frac{b}{h}\right) \tag{5.20}$$

$$\sqrt{\frac{\delta}{h}} = (2\alpha)^{\frac{1}{4}}\frac{b}{h}\left(1 + \sqrt{1 + \frac{3}{4}\alpha\left(\frac{b}{h}\right)^4}\right)^{-\frac{1}{4}} \quad , \tag{5.21}$$

with the parameter α defined as:

$$\alpha = 3\Gamma^*\left(\frac{2}{\pi}\right)^4 = \frac{6\Gamma}{hE'_{film}}\left(\frac{2}{\pi}\right)^4 \tag{5.22}$$

By plotting $\sqrt{(\delta/h)}$ against (b/h) and determining α the adhesion energy may then be produced as:

$$\Gamma = \frac{hE'_{film}\alpha}{6}\left(\frac{\pi}{2}\right)^4 \tag{5.23}$$

Figure 5.4 shows curves corresponding to different adhesion energies, produced

from the model in equation 5.21. Two potential pleat cross-sections are also shown in figure 5.4 to indicate the variance in pleat dimensions with increasing adhesion energy. Lower adhesion energies typically produce flatter more spread out buckles in comparison to higher adhesion energies.
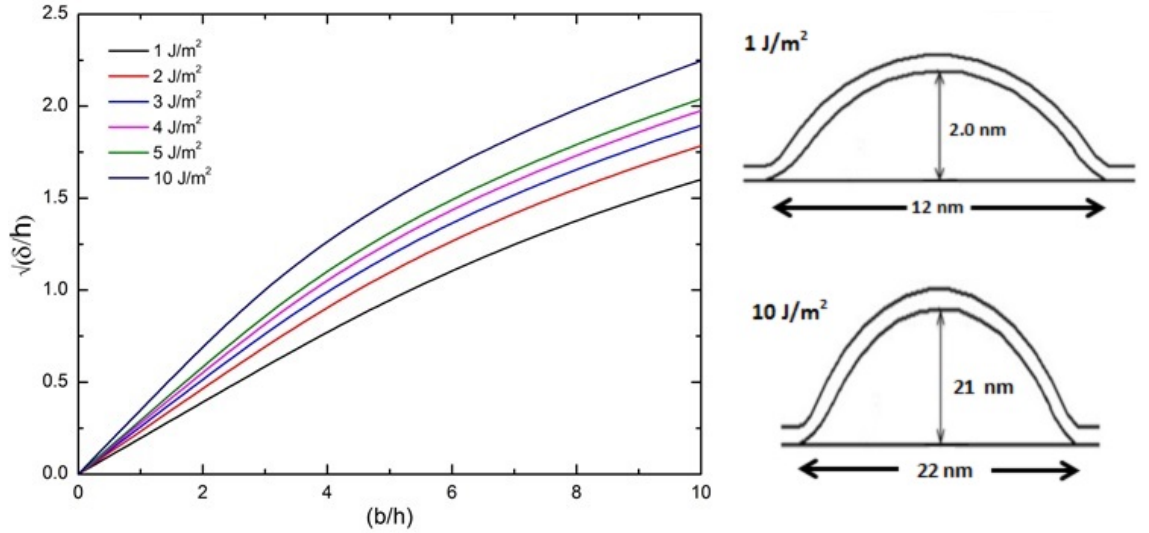
Figure 5.4: (Left) Parametric curves obtained from the model described by equation 5.21 for differing adhesion energies. (Right) Two possible pleat cross-sectional diagrams for 1 J/m^2 and 10 J/m^2 (not to scale).

5.3.2 Determination of the Adhesion Energy of Graphene on SiC(0001)

Figure 5.5 shows a typical STM image of graphene grown on SiC(0001). The sample shows large graphene terraces over several hundred nanometers in size, with the pristine hexagonal lattice visible at higher resolution (inset). Pleat defects are visible on the surface as pale lines intersecting at 120° angles to form an almost hexagonal network. This is due to the alignment of pleats preferentially along high symmetry directions, as will be discussed later. It can also be observed that pleat defects are not perfectly pinned to the surface and in some areas are dragged by the STM tip (Fig. 5.5, blue oval). These pleats are often dragged to steps where they become pinned, as discussed above. The vast majority of pleats observed are stable on the surface, forming on the large graphene terraces. Pleats were found to extend over 100 nm in length, crossing step edges in some regions.

The profile obtained from a pleat defect, indicated by the black line visible in figure 5.5 is shown in Figure 5.6. The model form of these pleats, as seen in equation
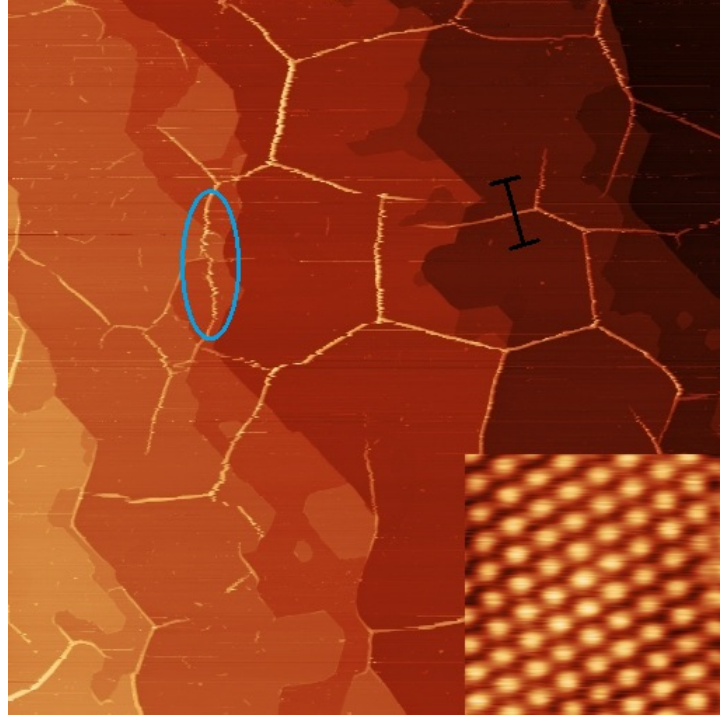
Figure 5.5: 1 μm^2 STM image of graphene grown on SiC(0001)(V$_\text{bias}$=1.9 V, I=0.3 nA). A hexagonal array of pleat defects is visible on the surface. A dragged pleat defect is visible (blue oval), a typical line profile across a pleat is also shown (black line). Atomic resolution of the graphene lattice is also observable (inset) (V$_\text{bias}$=0.2 V, I=1.9 nA) [45].

5.5, was fit to the experimentally obtained data via the non-linear least squares minimisation and results in a very close resemblance to the measured pleat defect. The pleat height and width were extracted via the fitting process and equation 5.21 used to obtain the corresponding α parameter and adhesion energy. Measurement of all the pleat defects on a sample and subsequently calculating their adhesion energies allows an average adhesion energy for the whole sample to be determined.

Figure 5.7 shows the pleat data, plotted alongside curves for various adhesion energies at a trilayer thickness (h=6.7Å). These results indicate an average adhesion energy of $3.0\pm^{1.6}_{1.0}$ J/m^2. This value is significantly higher than those previously determined on graphene grown on other substrates. For example, graphene grown on copper was found to have an adhesion energy of 0.72 J/m^2 [56], whilst graphene adhered to polydimethylsiloxane (PDMS) [10] and SiO$_2$ [8] exhibited adhesion energies of 0.176 J/m^2 and 0.45 J/m^2 respectively. This indicates that there is a significant variance in the adhesion energy on different substrates due to the film-substrate interaction. Koenig *et al.* found their value for the adhesion energy of graphene on SiO$_2$ to be very large with respect to other substrate-overlayer systems [57], which they attribute to the high flexibility of graphene allowing an almost liquid like confor-
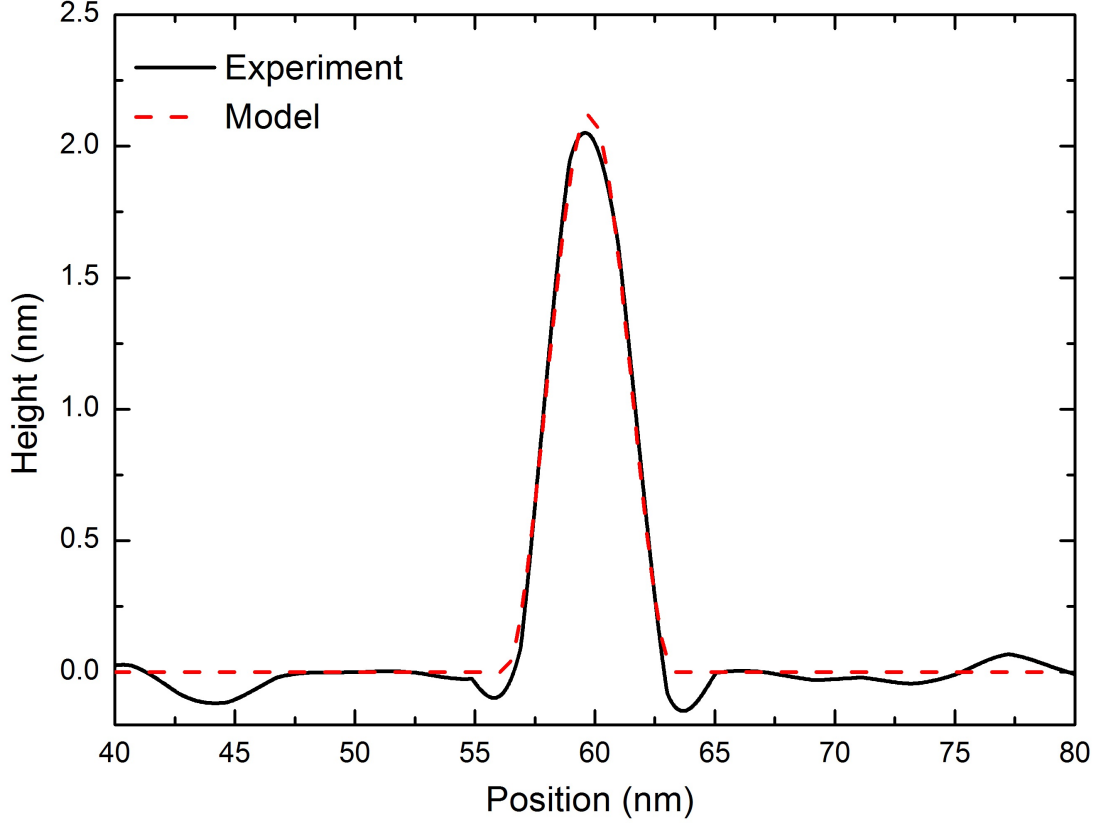
Figure 5.6: Cross-section height profile of a pleat as measured in figure 5.5 (black/solid); the pleat as treated by the continuum model outlined in Section 5.3.1 (red/dashed).

mation to the surface [8]. The adhesion energy of graphene on SiC(0001), at almost five times higher than that observed for graphene on copper, a predominantly Van der Waals type interaction [56], indicates a significantly different adhesion regime is in effect.

We believe that the value obtained for the adhesion energy of graphene on SiC is the result of the carbon rich buffer layer (see Chapter 1) delaminating from the surface in addition to the "free" graphene above. The formation of this intermediate layer, involves the formation of covalent bonds between carbon atoms in the buffer layer and the Si atoms in the substrate below [58]. This results in a far stronger adhesion than is seen in other graphene-substrate systems [35, 59]. Therefore, delamination of graphene from the surface in the form of pleats requires the breaking of these bonds. Previous theoretical work by Mattausch and Pankratov indicated that strong covalent bonding was present between the surface and the buffer layer, with weaker van der Waals bonding between subsequent graphene layers, resulting in a value of 2.3 J/m^2 for the graphene-SiC(0001) adhesion energy, supporting the value obtained here [59]. Furthermore, an experimental study on graphene exfoli-
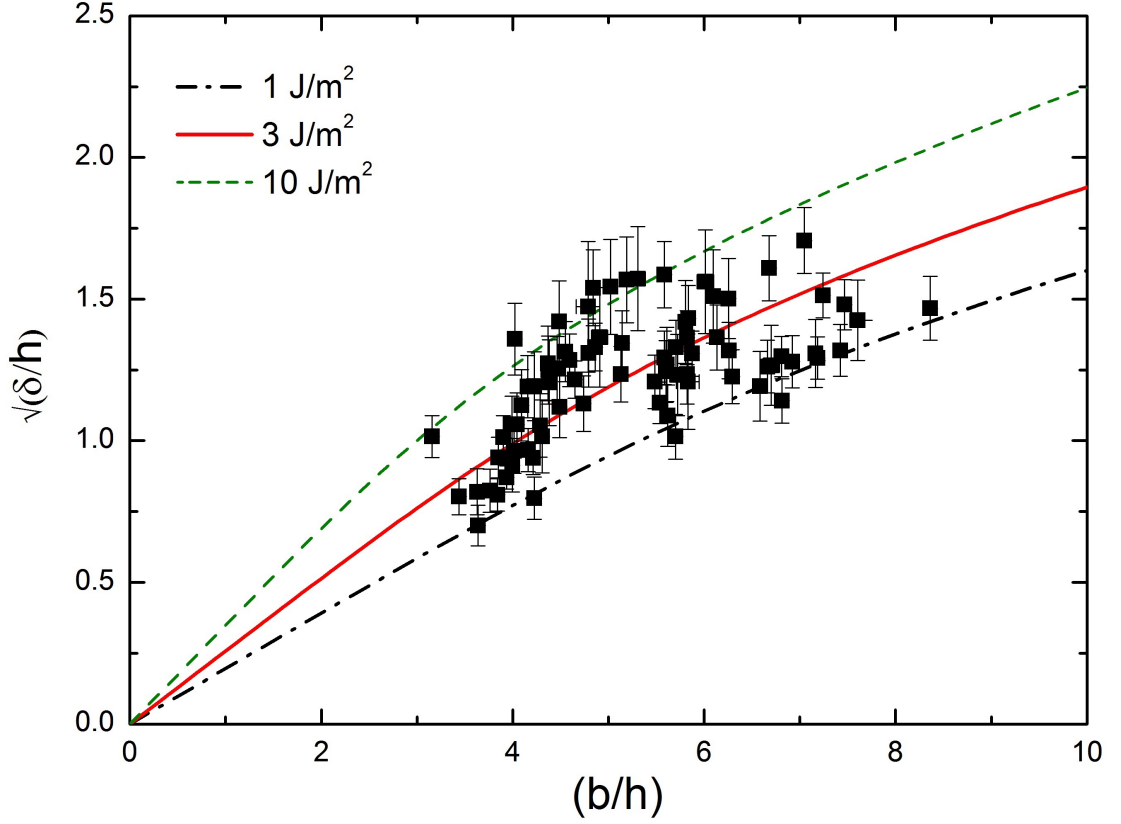
Figure 5.7: Pleat height and width data as described by the continuum energy model for a film thickness of 3 ML. Curves for adhesion energies of 1, 3 and 10 J/m^2 are shown to illustrate the average adhesion and upper and lower bounds.

ation from SiC, employing the deposition and subsequent peeling of metal layers, demonstrated that Cu, Pd and Au were unable to remove graphene from the surface due to weaker adhesion of graphene to these metals than to SiC, whereas Ni was capable of exfoliating 95% of the graphene layer [60]. With the graphene-Ni adhesion energy reported to be as high as 3.65 J/m^2, the smaller value of the graphene-SiC adhesion energy reported here is consistent with the observations of Kim *et al.* [60].

The spread in the data observed in figure 5.7 is the result of small variations in pleats, possibly caused by structural imperfections in the graphene lattice, such as defects. Such defects would affect the stability of pleats on the surface as discussed in section 5.3.5, and affect their formation and the adhesion energy. Furthermore, the data was compiled over multiple samples which, although grown using nominally identical conditions, may present minor differences in quality, or possibly variations in roughness, which have previously been shown to have an effect on adhesion [61].

In conclusion, the average adhesion energy of graphene on SiC(0001) can be

obtained via the measurement of pleat defects. A continuum energy model using the readily measurable parameters of pleat height and width was developed from which a value for the adhesion energy of $3.0\pm^{1.6}_{1.0}$ J/m^2 was obtained. This value, significantly larger than other graphene-substrate systems, is attributed to the buckling of the carbon rich buffer layer during pleat formation. Delamination of the buffer layer requires the breaking of covalent bonds between carbon atoms in the layer and Si atoms below. The model presented provides a simple method for determining the adhesion energy of graphene to a substrate that can, in principle, be adapted to any system in which pleat formation occurs.

5.3.3   Pleat Orientation
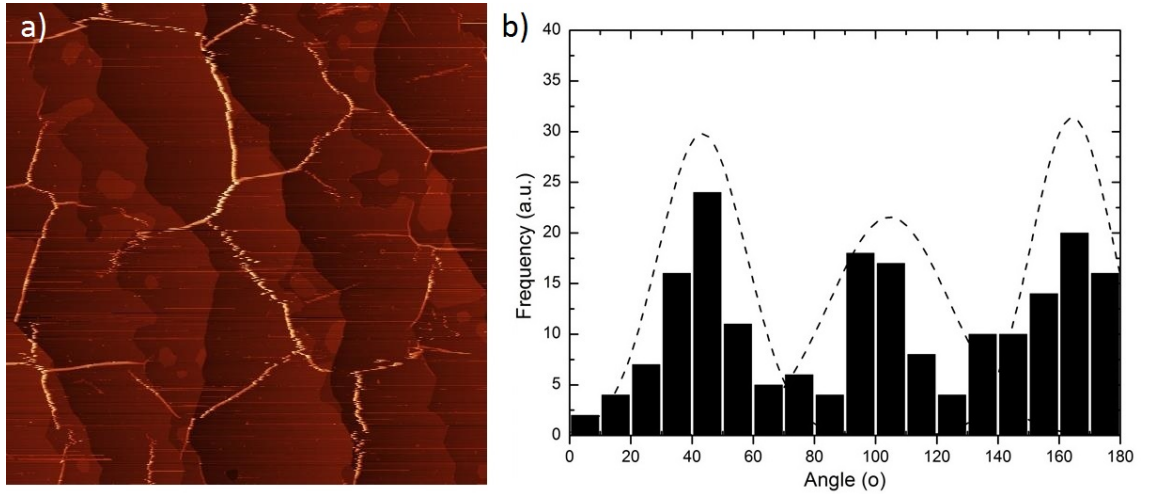
Figure 5.8: (a) 1 μm^2 STM image of graphene grown on SiC(0001) showing large terraces with a high concentration of pleat defects meeting at 120° angles on the surface (V_{bias}=2.2 V, I=0.2 nA). (b) Distribution of the orientation of pleat defects. Gaussian peaks were observed at 43°, 104° and 164° to vertical.

Figure 5.8(a) shows a typical STM image of graphene grown on SiC, consisting of straight edged terraces separated by SiC steps. Multiple pleat defects are visible on the surface, both at step edges and on terraces. These pleats appear to form an almost hexagonal network with the defects meeting at roughly 120° angles. This preferential orientation becomes more obvious upon measurement of the azimuthal angle of the pleats on the surface. The resultant histogram (Fig. 5.8(b)) presents three Gaussian peaks at 43±10°, 104±14° and 164±9°, indicating that pleats predominantly form along one of three directions, separated by 60°. Although a spread in pleat orientation is observed, the clear preference to align along one of three directions strongly suggests that their formation is dependent on, and therefore reflects,

the symmetry of the graphene lattice. Although pleat networks have been observed previously on many graphene-substrate systems [30, 62], many of which also show similar pleat intersections at 120° [29], no consistent orientational dependence across all systems has been reported. Sutter *et al.* suggest that the pleats that form on graphene on Pt(111) are in general perpendicular or parallel to each other in order to relieve the biaxial strain on the graphene film [17]. However, the data presented by Sutter *et al.* does not clearly show this behaviour, with many pleats exhibiting angles closer to 120°. While pleats reduce the biaxial strain on graphene grown on SiC, the three-fold symmetry observed indicates an alternative buckle formation mechanism.
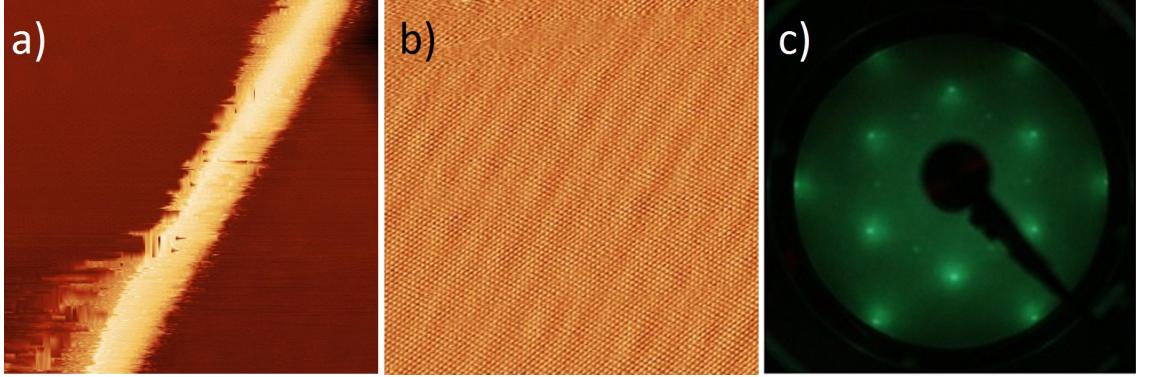
Figure 5.9: (a) 20 nm^2 STM image showing a pleat (top left) oriented parallel to a high symmetry direction of the graphene atomic lattice, taken at V_{bias}=0.8 V, I=1.2 nA. (b) STM current topograph showing the graphene lattice and buffer layer reconstruction close to the pleat in (a) (V_{bias}=0.8 V, I=1.3 nA). (c) LEED pattern obtained at a beam energy of $E_0 = 135.5$ eV showing graphene, SiC (1×1) spots and $(6\sqrt{3} \times 6\sqrt{3})R30°$ buffer layer spots.

Upon imaging at higher resolution it becomes clear that the orientation of pleats on graphene grown on SiC is related to the hexagonal nature of the substrate and buffer layer. This can be seen clearly in figure 5.9 which shows a pleat (a) that has formed parallel to a high symmetry direction of the buffer layer (b). The graphene lattice is also just discernible on the top of the pleat, with no warping visible, demonstrating that the lattice is continuous across the entire defect as expected [16, 63]. This alignment was confirmed to be consistent across the whole sample via LEED (Fig. 5.9(c)), which showed clear SiC and reconstruction spots. The orientation of the reconstruction and SiC(0001) substrate spots were in close agreement with the preferable pleat formation directions, with azimuthal angles measured to be 45±2°, 102±2° and 62±2°. This differs significantly from the work by N'Daiye *et al.* whose study of graphene on Ir(111) showed pleat formation predominantly perpendicular to the graphene atomic lattice, which itself is in registry with the substrate, rather

than at 30° observed here [16]. We propose that the preference to follow these high symmetry directions may result from the presence of the $(6\sqrt{3} \times 6\sqrt{3})R30°$ buffer layer as it plays a large role in the adhesion of graphene to SiC and hence may also result in the hexagonal buckling networks observed [45]. Although the true structure of the buffer layer is still under debate, it is well established that it is hexagonal with a high carbon concentration [64–66]. Under one of the proposed buffer layer structures, a combination of sp^2 and sp^3 hybridised carbon and Si tetramer adatoms, we suggest that buckling along the graphene high symmetry directions will result in the least number of bonds broken during the delamination process and is therefore more favourable [64]. As a buffer layer is not present in other graphene-substrate systems, such as on Pt(111), Ir(111) and Cu, it is likely that the preferential orientation of pleats with respect to the graphene lattice differs, although the 120° angle junctions persist.

With the pleats forming preferentially due to the presence of the buffer layer, a further question that must be addressed is why pleats meet at 120° angles, and 60° junctions are not observed at all. A potential solution was investigated by considering the energy required to form junctions at both 60° and 120° angles. An attempt to model this behaviour was performed by approximating a junction of two pleats as a single rod which is deformed to produce a parabolic bend. From this, an estimated value for the free energy per unit volume could be obtained. The free energy per unit volume was defined by

$$F = \frac{1}{2}Ea^2/R^2 \ , \tag{5.24}$$

n which E is the Young's modulus of the rod, a^2 is the rod cross section and R is the radius of curvature of the rod [67]. By assuming a parabolic bend of the form $Y = Ax^2$, and that only a small portion of the pleat actually bends to form the junction, the radius of curvature and consequently the free energy might be obtained. However, although the estimates obtained by this method showed a reduction in the free energy when the rod was bent at 120° compared to that obtained when bent at 60°, the values for the free energy were found to be of the order of a few eV/atom. Values this large would indicate the breaking of a large number of bonds at the pleat junction, which is highly unlikely given the continuous nature of the graphene lattice across the pleat. Therefore, a better model that can incorporate bond rotations is required to fully describe pleat junctions. Despite the failure of this model, the absence of 60° junctions would still suggest that forming at more acute angles is much more costly energetically. The configuration of three pleats at

120° is perfectly capable of relieving all components of the compressive strain on the film, whilst also minimising the number of broken bonds required for delamination.

To conclude, pleat defects were found to form along preferential orientations on the graphene surface. This resulted in pleats forming with 120° junctions between them. Furthermore, upon high resolution STM imaging it was found that pleats were aligned along high symmetry directions of the SiC substrate and buffer layer reconstruction; this was further confirmed by LEED. The preferential orientation is attributed to minimisation of the number of bonds that require breaking between the substrate and the carbon rich buffer layer. Finally, The formation of three-pleat junctions rather than six-pleat junctions, in keeping with the six-fold symmetry of the lattice is suggested to be more energetically favourable, whilst still providing complete compressive strain relief.

5.3.4 Pleat Variation
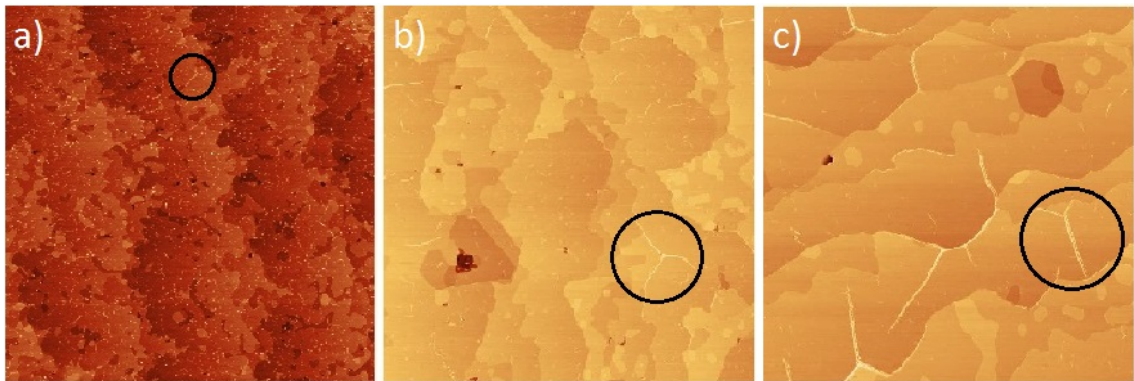
Figure 5.10: 1 μm^2 STM images of graphene grown on SiC(0001) at a) 1700 °C (V$_{bias}$=1.0 V, I=0.6 nA), b) 1775 °C (V$_{bias}$=1.2 V, I=0.8 nA) and c) 1850 °C (V$_{bias}$=1.1 V, I=0.5 nA). Pleat defects are circled in each image.

Figure 5.10(a) shows an STM image obtained from graphene grown at 1700 °C for four minutes on SiC(0001). The surface exhibits poor quality graphene with the large terraces covered in small pits and bounded by rough edged steps. A small number of pleats have formed on the surface, one of which has been circled in black. These pleats are fairly small in all dimensions with an average length, height and width of 33±6 nm, 0.8±0.1 nm and 6.0±0.5 nm respectively; this is combined with a fairly low concentration of 7±2/μm^2. The small dimensions and low pleat concentrations observed are in significant contrast to those seen in section 5.3.2 from a high quality graphene sample. A potential explanation for this is that the

quality of the sample is directly correlated with the growth temperature, as shown in Chapter 4 [24]. At low temperatures, a high concentration of pits and defects are present on the surface. Pleats will only form if the compression of the graphene layer, caused by the difference in thermal expansion, is of a sufficient level. The compressive strain is relieved in areas where the lattice is defective or pits exist as the lattice mismatch can be partially corrected at these points [68]. Therefore due to the low quality of the graphene, significantly less compression of the graphene layer occurs, and as such the formation of larger pleats is suppressed, resulting in only small pleat formation in low concentrations.

With an increase in the growth temperature to 1775 °C, STM images showed an increase in the quality of graphene with significantly smoother step structures and a reduction in pits and islands compared to growth at lower temperatures (Fig. 5.10(b)). A substantial change was also observed in the pleats that formed (black circle), with large increases in length, width and height, to 70$\pm$20 nm, 7.3$\pm$0.3 nm and 1.3$\pm$0.1 nm respectively, whilst the concentration of pleats also rises to 15$\pm$4/μm^2. Furthermore, pleats now exhibit an angular preference with multiple pleats meeting at 120° angles. The observed increase in pleat dimensions supports the explanation given above, that pleat formation is directly related to the quality of the graphene on which they form. Due to the lower defect and pit concentration on the surface, the strain in the graphene layer is larger; as a result pleat formation is required for its relief. The larger pleat dimensions allow a greater level of strain to be released over a larger area of the surface. Furthermore, the higher concentration of pleats also indicates that the predominant form of strain relief is now via buckling [47]. This indicates that the compression caused by the lattice mismatch is no longer being sufficiently corrected by the presence of intrinsic defects and pits.

Upon increasing the growth temperature further to 1850 °C, STM images indicate a further improvement in quality compared with lower temperatures, samples displaying much smoother steps and significantly lower defect and pit concentrations (Fig. 5.10(c)). This is again reflected in the pleat defects on the surface which show further increases in length, height and width with average values of 160$\pm$60 nm, 1.4$\pm$0.1 nm and 9.8$\pm$0.4 nm respectively. Once again the pleats clearly follow the high symmetry directions of the graphene lattice meeting at 120° angles, as expected on a high quality film. However, despite these significant increases, the concentration of pleats only rises slightly to 17$\pm$4/μm^2, this is most likely due to the strain over a larger area being more effectively released by the presence of larger, longer pleats rather than high concentrations of smaller ones. Consequently, although the

graphene quality has improved further, resulting in more strain on the film, higher concentrations of pleats are not required. It can be surmised that the size and extent of pleats on the surface can provide a quantitative representation of the quality of graphene produced, as higher growth temperature was found to lead to higher quality films, which in turn presents significantly longer, larger pleats. Furthermore, measurement of pleat concentration may indicate a point at which the level of intrinsic defects from growth do not affect the adhesion of the graphene film to the substrate.
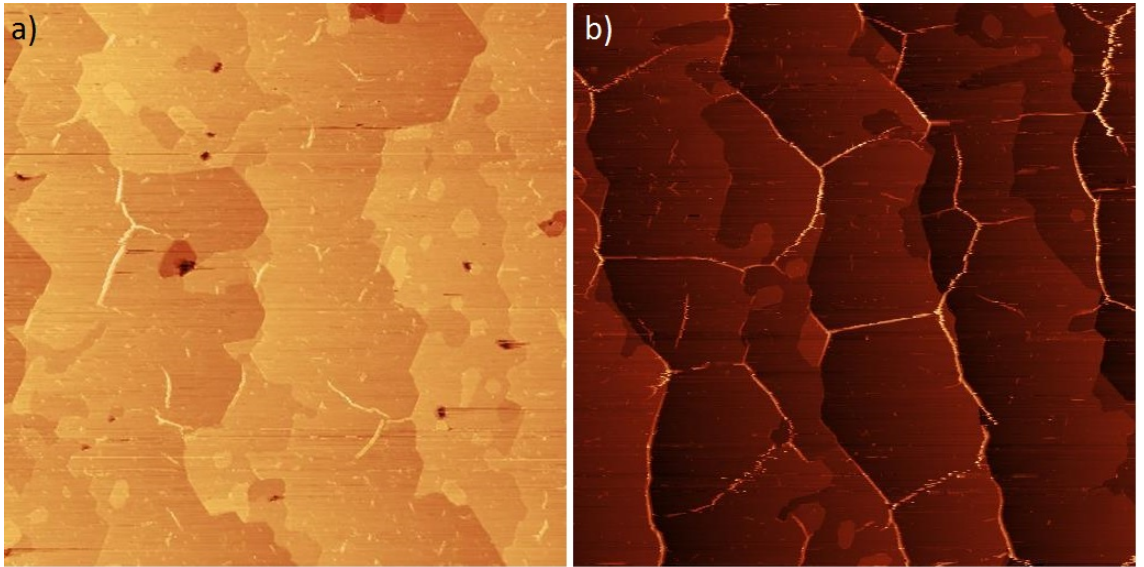
Figure 5.11: (a) 0.9 μm^2 STM image of graphene grown on SiC(0001) at 1775 °C for 4 minutes, taken at V_{bias}=1.2 V and I=0.8 nA. (b) 1 μm^2 image of graphene grown for 60 minutes, taken at V_{bias}=2.2 V and I=0.3 nA.

With higher growth temperature found to increase the size and number of pleats on the surface, associated with improvements in graphene quality, the effect of an increased growth time was also investigated to observe if further pleat variation was apparent. Figure 5.11 (a) and (b) show graphene grown for at 1775 °C for 4 and 60 minutes respectively. In comparison to growth for 4 minutes, 60 minute growth presents a much improved surface, with long straight terraces with high quality graphene clearly visible. The pleat defects on the surface show substantial growth, with all dimensions rising from those stated above for growth at 1775 °C for 4 minutes, to 1.8±0.2 nm, 8.6±0.2 nm and 140±50 nm for pleat height, width and length respectively. However, these values do not surpass those observed on growth at 1850 °C for 4 minutes. This indicates that the dimensions and formation of pleats are only linked to growth time via the fact that increased quality is obtained when growth is performed for longer periods. Therefore, the subsequent improvement in

quality determines the extent of pleat formation on the surface. This is further corroborated by the marginal increase in pleat concentration in comparison to growth at 1850 °C, $20\pm4/\mu m^2$ compared with $17\pm4/\mu m^2$, suggesting that despite widely differing growth times and temperatures, the level of pleat formation on the surface stays constant due to the similar quality of the graphene that is produced. Hence, it can be concluded that pleat formation is purely dependent on the condition of the graphene grown, rather than the individual growth parameters.

5.3.5 Pleat Stability and Pinning

Although pleats are generally stable on the surface, dragging by the tip may occur when imaging with STM. This is the result of the tip being unable to effectively track the surface over the pleats and interacting strongly with the pleat which it drags across the surface. This phenomenon has been previously observed by Sun *et al.* who were able to manipulate the pleats, referred to as ridges, and even create new ones [22]. Despite this apparent instability when encountering the STM tip, a number of factors have been observed that appear to increase the stability of pleats on the surface. These range from increased disordering of the surface caused by the production of defects, to the introduction of surface contamination. Furthermore, some areas, such as step edges, also provide points at which pleats become pinned.

Pleat Pinning due to Defects

Figure 5.12(a) shows a typical 1 μm^2 image of graphene grown on SiC(0001). The pleat defects observable on the surface exhibit significant dragging by the STM tip, with the vast majority being pulled laterally and becoming pinned at steps. The few pleats that remain on terraces, away from steps, are most commonly oriented parallel to the scan direction, as the larger "width" seen by the STM tip allows the feedback loop to more effectively track along its surface, preventing dragging. Pleats that have been pulled to steps adhere strongly at these points in comparison to on terraces and are no longer subject to being dragged by the tip. This indicates that steps pin the pleats in place. This is likely due to the presence of dangling bonds at steps, which as reactive sites result in increased bonding of the graphene layer at these points. Therefore, in these areas the tip is unable to provide enough force to move the pleat.
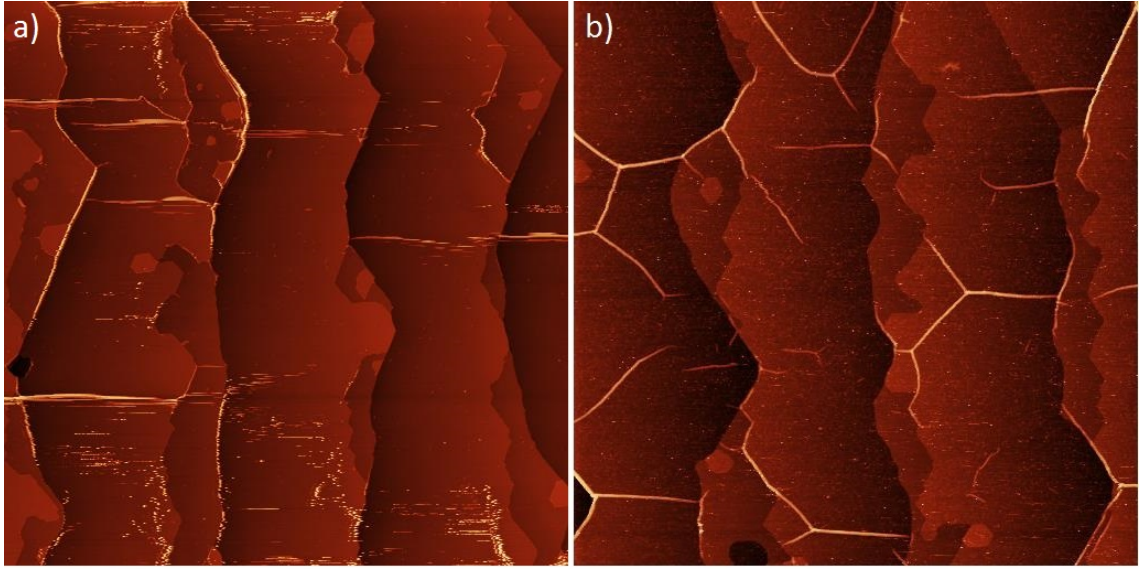
Figure 5.12: 1 μm^2 STM images of graphene grown on SiC(0001); (a) Before ion bombardment, taken at V$_{\text{bias}}$=0.7 V and I=0.6 nA. (b) After ion bombardment dose of 1.7 μC of Ar$^+$ ions at a beam energy of E=0.2 keV, taken at V$_{\text{bias}}$=1.6 V and I=0.6 nA.

In contrast to the pristine graphene surface, when a large concentration of defects are introduced to the system the stability of pleats is significantly altered. Figure 5.12(b) shows a 1 μm^2 image of graphene on SiC which has received a 1.7 μC dose of Ar$^+$ ions. A high concentration of defects can be observed on the sample, showing up as small pale dots. The presence of these point defects appears to have a large effect on the pleat defects present on the surface as they are considerably more stable than those previously observed on the non-defective graphene, with negligible dragging by the STM tip, even when imaging conditions were varied. Instead, pleat defects remain on terraces, meeting at 120°, with little difference observed between pleats predominantly parallel and perpendicular to the scan directions. This change in pleat behaviour during scanning can be explained as a result of the irradiation causing significant damage to the surface. When an ion interacts with the surface, it will collide with a carbon atom causing it to debond from its neighbours; the ion itself will either implant itself between the graphene layers or scatter away from the surface. The carbon atom will also either be ejected or remain on top of the lattice, resulting in a combination of vacancy, interstitial and adatom defects, as described previously [68]. Due to the dangling bonds left by the presence of defects, a large number of reactive sites are created on the surface [69]. As a result of these more reactive areas, pleat defects are more likely to be pinned to the surface, as the adhesion of the graphene layers to the substrate is increased by the presence of the dangling bonds [68]. This prevents the STM tip from delaminating the graphene

film adjacent to the original pleat position in order to drag it.

It is important to note that the effect of defects which have been introduced after growth and complete pleat formation is likely to differ greatly from that of defects produced intrinsically during the growth process. As seen above, the length, width and height of the pleats that form depends strongly on the quality of the graphene grown, with graphene with a high concentration of intrinsic defects resulting in formation of smaller pleats. This is in contrast to the situation when ion irradiation introduces point defects after growth which do not appear to perturb the size, shape or orientation of the pleats which have already formed. Should pleats/ridges be utilised for technological purposes [33], manipulation could be performed via the use of an STM tip followed by controlled ion bombardment to pin the resultant structures.

Pleat Pinning by Contamination
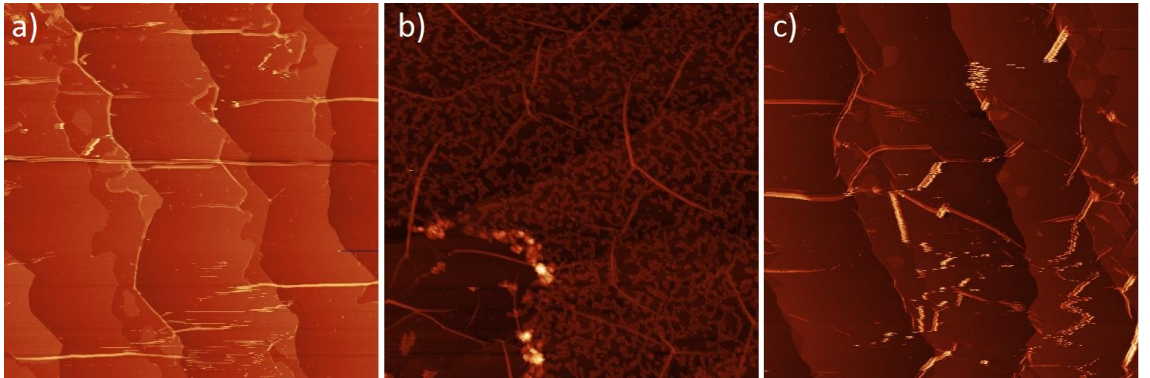
Figure 5.13: 1 μm^2 STM images of graphene grown on SiC(0001) (a) before contamination showing many pleats being dragged across the surface (V_{bias}=0.8 V, I=0.4 nA); (b) after contamination, showing many pleats now stable on the surface (V_{bias}=1.0 V, I=0.7 nA), and (c) After cleaning via the method outlined in Chapter 4, pleats are once again highly mobile on the surface and easily dragged (V_{bias}=0.4 V, I=0.3 nA).

Figure 5.13(a) again shows a typical 1 μm^2 STM image, on which significant pleat dragging has occurred. Once again pleats parallel to the scan direction are less affected, whilst perpendicularly oriented pleats have been dragged to steps. However, upon deposition of a thin layer of contamination, which covers ~50% of the surface at a thickness of 1.2 nm, the pleats are again significantly more stable (Fig. 5.13(b)). Even pleats that are only partially covered by contamination (bottom left corner) present significantly more resistance to dragging. However,

when contamination is removed from the surface, via the technique outlined in Chapter 4, pleats once again become mobile during scanning (Fig. 5.13(c)). This indicates that the presence of contamination on the surface pins pleats in place. This is perhaps unsurprising as the contamination creates an effective physical barrier between the STM tip and the pleat, reducing their interaction. This is combined with an apparent reduction in the pleat height caused by the presence of material on top, further reducing the probability of sufficiently strong tip-surface interaction, as pleats are no longer protruding significantly above their surroundings. As a result, the feedback loop is able to ensure the surface is effectively tracked. The stability of pleats only partially covered by contamination indicates this cannot be the complete explanation. We suggest that the partial coverage of a pleat pins that particular area of the defect; the uncovered part of the pleat also increases in stability due to a preference for the entire pleat to be dragged rather than the production of a sharp turning point or pleat division. This resistance to producing these sharp bends arises from the rigidity of the pleat along its primary axis, which is a result of graphene's high tensile strength [1], as well as the preference for pleat formation along high symmetry directions [45], as discussed in section 5.3.3. Therefore, even a small quantity of contamination may result in the pinning of pleats to the surface and the use of a thin layer of material could be employed to fix pleats in place for device applications.

5.4   Conclusions

In this chapter, a continuum energy model was developed to describe the formation of pleat defects on epitaxially grown graphene due to the differential thermal expansion of graphene with respect to the substrate. The model describes pleats as half-sinusoidal delaminations of the graphene film caused by the significant compressive strain. By taking into account the energy released in buckling to form pleats, the energy stored in the unbuckled areas of the graphene and the energy required to debond the film, an expression for the adhesion energy can be obtained. This expression contains the pleat parameters of height, width and film thickness, allowing its use of experimentally obtained data to determine a value for the adhesion energy of graphene to the substrate. In principle the model can be adapted to any graphene-substrate system on which pleat formation occurs, enabling the adhesion energy to be straightforwardly calculated. Therefore this model could provide highly useful information for the effective use of graphene layers in future electronic and

mechanical devices.

Graphene grown on SiC(0001) was measured via STM and AES to obtain pleat dimensions and the film thickness for use in the continuum energy model. The measured pleat profiles were fit using non-linear least squares to obtain heights and widths. Fitting the experimental data to the continuum energy model produced a value of $\Gamma = 3.0\pm_{1.0}^{1.6}$ J/m² for the adhesion energy of graphene on SiC. This result is significantly larger than values obtained on other graphene-substrate systems, such as graphene on Cu (0.72 J/m²) [56], on SiO_2 (0.45 J/m²) [8] or PDMS (0.176 J/m²) [9], which themselves are large in magnitude, compared to other materials, due to graphene's high degree of conformation to the surface. This very large adhesion energy is attributed to carbon rich buffer layer which forms between the substrate and the first true graphene layer. During pleat formation both the "free" graphene layers and the buffer layer delaminate from the surface; which requires the breaking of strong covalent bonds which have formed between the carbon atoms in the buffer layer and the uppermost Si atoms of the substrate. Therefore, the adhesion energy obtained reflects this strong graphene surface interaction.

Preferential orientation of pleat defects was observed on the surface with the majority of pleats forming at 120° angles to each other. High resolution images showed the graphene lattice was continuous across the pleats and the pleat directions coincide with the high symmetry directions of the buffer layer and substrate. The preferential formation along these directions is attributed to minimisation of the number of bonds between the substrate and the intermediary buffer layer that must be broken in order for delamination of the film to take place. This orientation preference is not seen in other systems like graphene on Pt(111) [17] and Ir(111) [70] which do not have intermediary layers between the substrate and first true graphene layer, therefore supporting the notion that the buffer layer determines the pleat orientation. Pleats were also observed meeting at 120° angles on the surface; a property also apparent on other graphene-substrate systems without intermediary buffer layer structures [17, 28, 70]. No six-fold pleat junctions were observed suggesting that three-way junctions are more energetically favourable. Simple modelling indicated that three-way pleat junctions reduced the free energy of the system more than six-way, but the energetics are unrealistic. The lack of observation of six-fold junctions indicates that meeting at 120° does, however, provide adequate strain release without requiring as much energy to form.

Pleat variation with respect to changes in growth conditions was also investi-

gated. Pleat length, height and width were all found to change significantly with changes in the graphene growth parameters. At the lower growth temperature of $T = 1700$ °C pleats were small in all dimensions, with average values of 33±6 nm, 0.8±0.1 nm and 6.0±0.5 nm for length height and width respectively, with a concentration of $7\pm2/\mu\text{m}^2$. This was attributed to the high concentration of pits and defects on the surface, as these areas will relieve the strain caused by the lattice mismatch, reducing the need for pleat formation. With increasing growth temperature, pleats were found to increase significantly in all dimensions, with higher concentrations also observed. The increased length and concentration, are attributed to the increase in graphene quality, which results in larger pristine graphene terraces, therefore requiring pleat formation to relieve the compressive strain. At the highest growth temperature investigated, 1850 °C, pleats again increased in width, length and height, but their concentration was not found to increase significantly, which suggests an optimum pleat concentration to reduce the strain on a high quality graphene film. Measurement of graphene grown for different lengths of time also showed similar results, with increases in pleat length and cross-section. Pleat concentration was found to be similar to that observed for higher temperature growth, indicating that once the graphene has reached a certain level of quality, regardless of the growth parameters used, a critical quantity of pleats is reached that can effectively release all the strain in the film. It can therefore be concluded that pleat formation is inextricably linked to the quality of the graphene film and measurement of pleat concentration can provide an effective metric for determining the standard of graphene produced.

Finally, the stability of pleats was also investigated, with the effects of surface contamination and defect introduction studied. Pleats can be easily dragged by the STM tip during imaging, most likely due to their significant height in comparison to the surrounding graphene. Pleats oriented perpendicular to the scan direction were found to be dragged to a much larger degree than those parallel, which is attributed to more effective tracking of the pleat along its length. Pleats were also found to adhere preferentially at steps when dragged, most likely due to the increased bonding of the graphene layer at these points effectively pinning the pleat. When point defects were introduced via ion bombardment a significant increase in the stability of the pleats, both parallel and perpendicular to the scan direction, was observed. This increased stability most likely arises from the dangling bonds produced at defects, which provide reactive sites at which pleats are pinned. A similar increase in pleat stability was observed upon the deposition of a layer of contamination on the surface. When contamination was present, pleat dragging

was once again significantly reduced. This reduction in dragging was also seen on pleats that were only partially covered by contamination. We suggest that the contamination acting as an over layer creates a physical barrier between the STM tip and the pleat, preventing dragging. Furthermore, in the areas where the pleat is only partially covered, the contamination induced stability is still present in the uncovered area of the pleat, this likely results from the preference for the entire pleat to be dragged rather than producing rotational movement of the pleat, which arises from graphene's high tensile strength [1]. To conclude, multiple methods can be employed to increase the stability of pleats on the surface of graphene grown on SiC(0001). Therefore, careful use of either defects or small concentrations of material may be used fix pleats in position for technological applications.

5.5   References

[1] C. Lee, X. Wei, J. W. Kysar and J. Hone, *Science*, **321**(5887), 385–388 (2008).

[2] A. K. Geim and K. S. Novoselov, *Nature Mater.*, **6**(3), 183–191 (2007).

[3] A. H. C. Neto, F. Guinea, N. M. R. Peres, K. S. Novoselov and A. K. Geim, *Rev. Mod. Phys.*, **81**(1), 109–162 (2009).

[4] Y. Ma, Y. Dai, M. Guo, C. Niu and B. Huang, *Nanoscale*, **3**(9), 3883–3887 (2011).

[5] Y. Shi, W. Zhou, A.-Y. Lu, W. Fang, Y.-H. Lee, A. L. Hsu, S. M. Kim, K. K. K. abd H. Y. Yang, L.-J. Li, J.-C. Idrobo and J. Kong, *Nano Lett.*, **12**(6), 2784–2791 (2012).

[6] K.-J. Huang, L. Wang, J. Ling and Y.-M. Liu, *Sensor Actuat. B-Chem.*, **178**, 671–677 (2013).

[7] J. S. Bunch and M. L. Dunn, *Solid State Commun.*, **152**, 1359–1364 (2012).

[8] S. P. Koenig, N. G. Boddeti, M. L. Dunn and J. S. Bunch, *Nature Nanotechnol.*, **6**(9), 543–546 (2011).

[9] Z. Cao, P. Wang, W. Gao, L. Tao, J. W. Suk, R. S. Ruoff, D. Akinwande, R. Huang and K. M. Liechti, *Carbon*, **69**, 390–400 (2014).

[10] S. Scharfenberg, N. Mansukhani, C. Chialvo, R. L. Weaver and N. Mason, *Appl. Phys. Lett.*, **100**(2), 021910 (2012).

[11] Z. Zong, C.-L. Chen, M. R. Dokmeci and K. Wan, *J. Appl. Phys.*, **107**(2), 026104 (2010).

[12] M. Yamamoto, O. Pierre-Louis, J. Huang, M. S. Fuhrer, T. L. Einstein and W. G. Cullen, *Phys. Rev. X*, **2**(4), 041018 (2012).

[13] W. A. de Heer, C. Berger, M. Ruan, M. Sprinkle, X. Li, Y. Hu, B. Zhang, J. Hankinson and E. Conrad, *Proc. Nat. Aca. Sci. U.S.A*, **108**(41), 16900–16905 (2011).

[14] F. Varchon, P. Mallet, J.-Y. Veuillen and L. Magaud, *Phys. Rev. B*, **77**(23), 235412 (2008).

[15] N. Liu, Z. Pan, L. Fu, C. Zhang, B. Dai and Z. Liu, *Nano Research*, **4**(10), 996–1004 (2011).

[16] A. T. N'Diaye, R. V. Gastel, A. J. MArtíez-Galera, J. Coraux, H. Hattab, D. Wall, F.-J. M. Z. Heringdorf, M. H. Hoegen, J. M. Gómez-Rodríguez, B. Poelsema, C. Busse and T. Michely, *N. J. Phys.*, **11**(11), 113056 (2009).

[17] P. Sutter, J. T. Sadowski and E. Sutter, *Phys. Rev. B*, **80**(24), 245411 (2009).

[18] W. A. de Heer, C. Berger, X. Wu, P. N. First, E. H. Conrad, X. Li, T. Li, M. Sprinkle, J. Hass, M. L. Sadowski, M. Potemski and G. Martinez, *Solid State Commun.*, **143**(1-2), 92–100 (2007).

[19] J. R. Hass, *Structural characterisaztion of epitaxial graphene on silicon carbide*, Ph.D. thesis, School of Physics, Georgia Institute of Technology (2008).

[20] X. Wu, Y. Hu, M. Ruan, N. K. Madiomanana, J. Hankinson, M. Sprinkle, C. Berger and W. A. de Heer, *Appl. Phys. Lett.*, **95**(22), 223108 (2009).

[21] S. N. Luxmie, P. J. Fisher, R. M. Feenstra, G. Gu and Y. Sun, *J. Elec. Mater.*, **38**(6), 718–724 (2008).

[22] G. F. Sun, J. F. Jia, Q. K. Xue and L. Li, *Nanotechnology*, **20**(35), 355701 (2009).

[23] G. Prakash, M. A. Capano, M. L. Bolen, D. Zemlyanov and R. G. Reifenberger, *Carbon*, **48**(9), 2383–2393 (2010).

[24] T. Hopf, K. V. Vassilevski, E. Escobedo-Cousin, N. G. Wright, A. G. O'Neill, A. B. Horsfall, J. P. Goss, A. Barlow, G. H. Wells and M. R. C. Hunt, *Mater. Sci. Forum*, **778-780**, 1154–1157 (2014).

[25] X. Li, W. Cai, J. An, S. Kim, J. Nah, D. Yang, R. Piner, A. Velamakanni, I. Jung, E. Tutuc, S. K. Banerjee, L. Colombo and R. S. Ruoff, *Science*, **324**(5932), 1312–1314 (2009).

[26] G. H. Han, F. Günes, J. J. Bae, E. S. Kim, S. J. Chae, H.-J. Shin, J.-Y. Choi, D. Pribat and Y. H. Lee, *Nano Lett.*, **11**(10), 4144–4148 (2011).

[27] Y. A. Wu, Y. Fan, S. Speller, G. L. Creeth, J. T. Sadowski, K. He, A. W. Robertson, C. S. Allen and J. H. Warner, *ACS Nano*, **6**(6), 5010–5017 (2012).

[28] S. Amini, J. Garay, G. Liu, A. A. Balandin and R. Abbaschian, *J. Appl. Phys.*, **108**(9), 094321 (2010).

[29] A. N. Obraztsov, E. A. Obraztsova, A. V. Tyurnina and A. A. Zolotukhin, *Carbon*, **45**(10), 2017–2021 (2007).

[30] E. Loginova, S. Nie, K. Thürmer, N. C. Bartelt and K. F. McCarty, *Phys. Rev. B*, **80**(8), 085430 (2009).

[31] D. Pandey, R. Reifenberger and R. Piner, *Surf. Sci.*, **602**(9), 1607–1613 (2008).

[32] K. Xu, P. Cao and J. R. Heath, *Nano Lett.*, **9**(12), 4446–51 (2009).

[33] Z. Pan, N. Liu, L. Fu and Z. Liu, *J. Am. Chem. Soc.*, **133**(44), 17578–81 (2011).

[34] B. Wang, Y. Zhang, H. Zhang, Z. Chen, X. Xie, Y. Sui, X. Li, G. Yu, L. Hu, Z. Jin and X. Liu, *Carbon*, **70**, 75–80 (2014).

[35] N. Ferralis, R. Maboudian and C. Carraro, *Phys. Rev. Lett.*, **101**(15), 156801 (2008).

[36] K. Zhang and M. Arroyo, *J. Appl. Phys.*, **113**(19), 193501 (2013).

[37] Y. Wang, R. Yang, Z. Shi, L. Zhang, D. Shi, E. Wag and G. Zhang, *ACS Nano*, **5**(5), 3645–3650 (2011).

[38] C. Riedl and U. Starke, *Phys. Rev. B*, **76**(24), 245406 (2007).

[39] M. L. Bolen, S. E. Harison, L. B. Biedermann and M. A. Capano, *Phys. Rev. B*, **80**(11), 115433 (2009).

[40] T. Hopf, K. V. Vassilevski, E. Escobedo-Cousin, P. J. King, N. G. Wright, A. G. O'Neill, A. B. Horsfall, J. P. Goss, G. H. Wells and M. R. C. Hunt, *J. Appl. Phys.*, **116**(15), 15404 (2014).

[41] J. Coraux, A. T. N'Diaye, C. Busse and T. Michely, *Nano Lett.*, **8**(2), 565–570 (2008).

[42] G. Imamura and K. Saiki, *J. Phys. Chem. C*, **115**(20), 10000–10005 (2011).

[43] J.-H. Gao, K. Sagisaka, M. Kitahara, M.-S. Xu, S. Miyamoto and D. Fukita, *Nanotechnology*, **23**(5), 055704 (2012).

[44] W. A. de Heer, C. Berger, X. Wu, M. Sprinkle, Y. Hu, M. Ruan, J. A. Stroscio, P. N. First, R. Haddon, B. Piot, C. Faugeras, M. Potemski and J.-S. Moon, *J. Phys. D: Appl. Phys.*, **43**(37), 18 (2010).

[45] G. H. Wells, T. Hopf, K. V. Vassilevski, E. Escobedo-Cousin, N. G. Wright, A. B. Horsfall, J. P. Goss, A. G. O'Neill and M. R. C. Hunt, *Appl. Phys. Lett.*, **105**(19), 193109 (2014).

[46] C. Riedl, A. A. Zakharov and U. Starke, *Appl. Phys. Lett.*, **93**(3), 033106 (2008).

[47] M. J. Cordill, F. D. Fischer, F. G. Rammerstorfer and G. Dehm, *Acta Mater.*, **58**(16), 5520–5531 (2010).

[48] H. Chai, C. D. Babcock and W. G. Knauss, *Int. J. Solid Structures*, **17**(11), 1069–1083 (1981).

[49] M.-W. Moon, *Acta Mater.*, **52**, 3151–3159 (2004).

[50] J. W. Hutchinson and Z. Suo, *Adv. Appl. Mech.*, volume 29 (1992).

[51] F. Scarpa, S. Adhikari and A. S. Phani, *Nanotechnology*, **20**(6), 065709 (2009).

[52] O. L. Blakslee, D. G. Proctor, E. J. Seldin, G. B. Spence and T. Weng, *J. Appl. Phys.*, **41**(8), 3373 (1970).

[53] A. Krishnan, E. Dujardin, T. W. Ebbesen, P. N. Yianilos and M. M. J. Treacy, *Phys. Rev. B*, **58**(20), 14013–14019 (1998).

[54] M.-F. Yu, O. Lourie, M. J. Dyer, K. Moloni, T. F. Kelly and R. S. Ruoff, *Science*, **287**(5453), 637–640 (2000).

[55] D. Sánchez-Portal, E. Artacho, J. M. Soler, A. Rubio and P. Ordejón, *Phys. Rev. B*, **59**(19), 12678–12688 (1999).

[56] T. Yoon, W. C. Shin, T. Y. Kim, J. H. Mun, T.-S. Kim and B. J. Cho, *Nano Lett.*, **12**(1), 1448 (2012).

[57] R. Maboudian and R. T. Howe, *J. Vac. Sci. Tech. B*, **15**(1), 1–20 (1997).

[58] J. Hass, J. E. Millán-Otoya, P. N. First and E. H. Conrad, *Phys. Rev. B*, **78**(20), 205424 (2008).

[59] A. Mattausch and O. Pankratov, *Phys.Rev. Lett.*, **99**(7), 076802 (2007).

[60] J. Kim, H. Park, J. B. Hannon, S. W. Bedell, K. Fogel, D. K. Sadana and C. Dimitrakopoulos, *Science*, **342**(6160), 833–6 (2013).

[61] W. Gao and R. Huang, *J. Phys. D: Appl. Phys.*, **44**(45), 452001 (2011).

[62] L. B. Biedermann, M. L. Bolen, M. A. Capano, D. Zemlyanov and R. G. Reifenberger, *Phys. Rev. B*, **79**(12), 125411 (2009).

[63] J. Hass, W. A. de Heer and E. H. Conrad, *J. Phys.: Condens. Matter*, **20**(32), 323202 (2008).

[64] J. Hass, J. E. Millán-Otoya, P. N. First and E. H. Conrad, *Phys. Rev. B*, **78**(20), 205424 (2008).

[65] G. M. Rutter, N. P. Guisinger, J. N. Crain, E. A. A. Jarvis, M. D. Stiles, T. Li, P. N. First and J. A. Stroscio, *Phys. Rev. B*, **76**(23), 235416 (2007).

[66] L. I. Johansson, F. Owman and P. Mårtenson, *Phys. Rev. B*, **53**(20), 13793–13802 (1996).

[67] L. D. Landau and E. M. Lifshitz, *Theory of Elasticity*, Pergamon Press, Oxford (1970).

[68] F. Banhart, J. Kotakoski and A. V. Krasheninnikov, *ACS Nano*, **5**(1), 25–41 (2011).

[69] M. M. Ugeda, D. Fernádez-Torre, I. Brihuega, P. Pou, A. J. Martínez-Galera, R. Pérez and J. M. Gómez-Rodríguez, *Phys. Rev. Lett.*, **107**(11), 116803 (2011).

[70] A. T. N'Diaye, J. Coraux, T. N. Plasa, C. Busse and T. Michely, *New. J. Phys.*, **10**(1), 1–16 (2008).

Chapter 6

Defects in Graphite and Graphene: Agglomeration and Alignment

This chapter discusses experiments in which point defects were introduced in graphene and graphite by ion irradiation. The migration and agglomeration of defects on both materials upon annealing was studied along with behaviour at step edges. STS experiments were performed to characterise the defects produced and determine their effects on the LDOS.

6.1 Introduction

The impact of defects on the mechanical and electronic properties of graphene has been the subject of significant recent interest [1, 2]. A large number of effects that arise from the presence of defects have been reported, such as significantly reduced carrier mobility due to scattering and drastic losses in intrinsic strength due to the reconstruction of the lattice [3–5]. However, the controlled introduction of defects presents an interesting avenue to engineer graphene at the nanoscale [6–8]. Such "defect engineering" has been carried out on other carbon materials with the predominant work in this area directed towards the ion irradiation of graphite, as a result of its potential use as a material in nuclear reactors [9]. It has also been demonstrated that new structures can be developed via energetic particle bombardment. For example, Ugarte was able to produce carbon onions via irradiation with an electron beam [10]. These structures could then be irradiated further to induce the formation of nanoscale diamond [11], indicating that such approaches provide a powerful technique for tailoring material properties. Defects induced in graphite became of further interest upon the observation that they were not fixed, but could migrate across the surface if sufficient energy was available [12], suggesting the removal of defects from large areas and a greater degree of control over defect concentration. Despite this large body of research and the observation of processes like defect migration, effects such as agglomeration and the conditions under which this occurs have not been studied fully.

The bulk of research into the ion irradiation of carbon nanostructures has since moved towards other allotropes such as fullerenes and nanotubes, in part due to the use of transmission electron microscopy (TEM) which can cause significant radiation damage to carbon nanostructures [12]. The similar structure of sp^2 bonded carbon in fullerenes and nanotubes provides information that is analogous to that which can be obtained from graphene [13, 14]. An example of such a similarity can be seen in how the mechanical strength of both nanotubes and graphene deteriorates with increasing defect density [5, 15, 16]. This loss in mechanical strength is characterised by the way in which these materials reconstruct in the presence of a defect in order to maintain the coherence of the lattice [6]. Therefore, although some differences between these structures will arise due to the presence of curvature, certain processes remain comparable.

The manipulation and engineering of graphene via the controlled input of defects has been achieved in a number of ways [1]: graphene doping via ion bombardment,

followed by filling vacancy defects with dopant atoms [17, 18] to electronic structure tuning via ion irradiation [19]. Furthermore, significant research has been performed using Transmission Electron Microscopy (TEM) in which divacancies and larger defect structures were produced with a high degree of precision [20, 21]. Studies via this method have also revealed the various structural transformations defects may pass through in order to reduce their free energy, whilst also demonstrating the localised strain caused by their presence [22–24]. These experimental results have been combined with theoretical work that revealed the rate at which monovacancies could hop on CVD grown graphene; a rate of one hop every 100-200 s, comparable to that observed in graphite [25, 26]. Further theoretical studies even suggest the possibility of induced magnetism due to vacancy and adatom introduction [27–29]. Despite advances in the study of defects on graphene, only a small body of work exists on the formation and effects of defect structures on graphene grown on SiC. Rutter *et al.* found that two main types of intrinsic defect were produced during the growth of graphene from SiC: lattice defects which produce significant scattering and subsurface irregularities which do not strongly affect the electronic structure [3]. However, of the different types of lattice defect, only the divacancy was investigated further [30]. As growth on SiC(0001) presents a potential route towards graphene electronics, understanding both the effects of both intrinsic and externally introduced defects is paramount.

Observation of local electronic structure may also provide information with which to further analyse the influence of defects on graphene's electronic properties [31,32]. As discussed in Chapter 1, the unique electronic structure of graphene arises from its pristine honeycomb lattice [33, 34], consequently lattice defects result in significant modification of this structure in their close proximity. A clear example of this can be observed in the case of mono-vacancies in graphene on Pt, in which a significant increase in the local density of states (LDOS) close to the Fermi level can be observed [35]. These results suggest that with the careful introduction of defects, the electronic structure of graphene may be engineered for technological purposes. Although the effects of defects on the electronic structure of other graphene substrate systems have been investigated [35], graphene on SiC(0001) has seen little research into the modification of its electronic structure due to the presence of defects [3]. This indicates that by determining the effects of different types of defect on the LDOS of graphene on SiC(0001), further engineering of graphene's electronic properties may be achieved.

In this chapter, highly oriented pyrolytic graphite (HOPG) and graphene grown

from SiC(0001) were bombarded by Ar^+ ions to produce defects. The HOPG samples were heated at various temperatures and the migration and subsequent level of defect agglomeration was observed via scanning tunnelling microscopy (STM). Scanning tunnelling spectroscopy (STS) was employed to characterise the defects and determine their effect on the LDOS. Furthermore, the alignment of defects was also quantified to observe whether, upon annealing, defects align along preferential directions. The intrinsic defects that form during graphene growth on SiC(0001) were also annealed at various temperatures, to observe whether defect migration or agglomeration occurred, which was followed by an identical study of the extrinsically introduced defects. STS was performed on both the intrinsic and extrinsic defects to determine what effects different types of defect have on graphene's local electronic structure. Finally, the alignment of defects on graphene is also studied to determine whether preferential directions along which defects migrate are observed. All the studies performed on graphene are compared to those on graphite to determine whether the defects that are produced on few-layer graphene (FLG) differ significantly in their properties to those observed on HOPG.

6.2 Experimental

6.2.1 Sample Preparation

Prior to ion bombardment and analysis, clean low defect density surfaces of HOPG and FLG were prepared. In order to produce a graphite surface with negligible intrinsic defects, a HOPG slab was cleaved by applying adhesive tape (Scotch Magic Tape) to the sample and carefully peeling away, also known as cleaving (Fig. 6.1). The cleaving process removes the uppermost graphite layers, which may contain extrinsic defects and contaminants, leaving a pristine graphite layer below [36]. The majority of the resulting surface is defect free, allowing for effective study of extrinsic defects. Once cleaved, the graphite sample was quickly introduced to the the UHV system outlined in Chapter 3 and heated at 400 K for 2 hours to remove atmospheric contamination from the surface, at which point the sample was then ready for imaging.

Few layer (3±1 ML) graphene samples were grown on 6H-SiC(0001) wafers via the method outlined in Chapter 4, for 60 minutes at 1775 °C. The samples were characterised via Raman spectroscopy (RS) and then transferred to the UHV-SPM
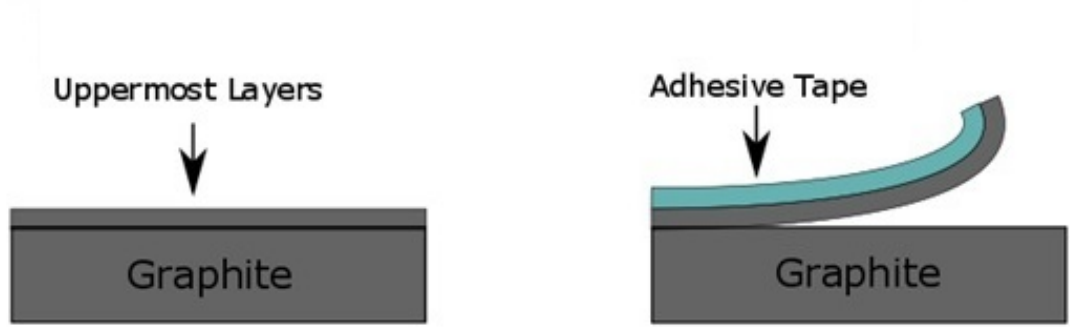
Figure 6.1: Schematic diagram of the graphite cleaving process. Adhesive tape is applied to the graphite surface and peeled away carefully to remove the upper most layers.

system where they were also heated at 400 K for 2 hours to remove atmospheric contamination. Samples were imaged before ion bombardment was carried out, to determine the quality of the surface and ensure that the level of intrinsic lattice defects was known prior to ion irradiation.

Ion bombardment of graphite and graphene samples was performed in the UHV-SPM system using the ion gun system outlined in Chapter 3. In order to obtain a suitable sample current, the pressure in the system was increased from a base pressure of 5×10^{-10} to 7.5×10^{-5} mbar by introducing 99.99 % purity Ar gas. Optimisation of the irradiation conditions was conducted by testing various beam energies and bombardment times on graphite until an acceptable defect density was obtained. An optimised sample current of 0.007 μA, measured from the reverse side of the sample holder was found to produce an appropriate defect density. A beam energy of $E_{beam} = 200$ eV was required to reduce the beam current and defect densities to an acceptable level [29]. Exposure times of 1 second were used in conjunction with the above conditions to produce the samples investigated in this chapter.

STM and STS

STM imaging was performed in the UHV-SPM system outlined in Chapter 3, images of graphite were typically obtained using Pt-Ir tips, both for larger (1 μm^2) scales and at atomic resolution. Images of graphene on SiC were obtained using Pt-Ir tips for larger scales, whilst W tips were employed for atomic resolution imaging, as seen in previous chapters. An exception to this was made prior to STS on graphene, where Pt-Ir tips were used at all scales to improve the quality of the tunnelling spectra obtained. Use of Pt-Ir tips was characterised by less noise, indicating a more

stable tip DOS. STS was performed in the UHV-SPM system using the VT-SPM at standard operating conditions. When acquiring spectra, samples were mounted in the usual manner and the STM tip brought into close proximity of the surface. When obtaining a single spectrum, imaging was performed until a typical image of $\sim$20 nm^2 was obtained containing both the pristine graphite/graphene lattice and also a feature, most commonly a defect, of interest. Having identified a clear area the scan size was reduced to $\sim$5 nm^2 and a spectrum taken. The smaller area used helps to maintain the tip position by reducing the drift during scanning, ensuring the tip remained on the area of pristine lattice over the course of data acquisition. Upon obtaining the spectrum from the clear area, the scan size was increased once more, such that the feature of interest could once more be identified. A spectrum was then obtained by zooming in on the feature. Finally, once the feature spectrum was obtained, a further spectrum from the original area was obtained to ensure that any changes between the STS from clean and defective areas originated from the surface feature and not by effects such as spontaneous tip restructuring.
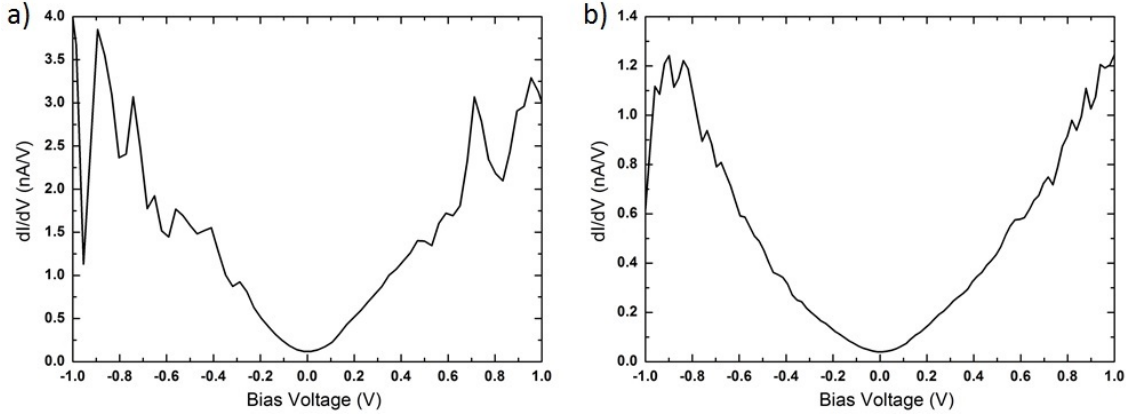
Figure 6.2: STS spectra obtained from a pristine graphite surface. (a) Average of 60 spectra, showing significant noise. (b) Average of 300 spectra showing significantly reduced noise as a result of the increased number of scans.

Spectra were obtained over a scan range of -1 V to +1 V with points taken in 0.01 V increments. The spectra were then differentiated to obtain the LDOS from the scanned area of the sample. A single spectrum was found to be very noisy, most likely due to thermal and electrical fluctuations, persisting even after averaging over tens of scans, as can be seen in figure 6.2(a). To reduce the noise to an acceptable level, spectra were averaged 300 to 500 times. This resulted in a far smoother line shape (Fig. 6.2(b)) from which real LDOS features could be identified. All spectra presented were obtained >10 times in different areas.

6.2.2   Image Processing and Data Analysis Methods
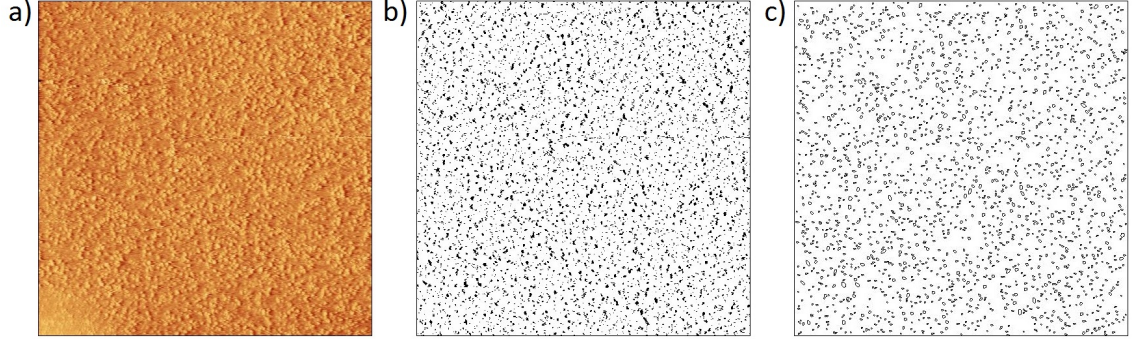
Figure 6.3:   (a) 200 nm^2 STM image of a highly defective graphite area (V_{bias}=1.4 V, I=0.7 nA). (b) Result of background subtraction and filtering of (a). (c) Result of particle analysis of (b), showing measured defect outlines.

In order to perform the analysis found in the Results and Discussion section of this chapter, pre-processing of the STM images was required. The images of defective graphite/graphene were first subjected to a typical background subtraction consisting of maximum and minimum filters, followed by a Gaussian blur. This ensured that larger surface features such steps, or large scale ripples do not contribute to the defect statistics. Background subtracted images were then further filtered to produce binary maps showing the points at which defects are present, this process can be seen in figures 6.3(a) and (b). Particle analysis was then performed on the fully filtered images to determine the concentration and size of defects on the surface (Fig. 6.3(c)).

Similarly, when studying the orientation of defects in sections 6.3.1 and 6.3.2, the same background subtraction and filters are used, however the final image is inverted to produce a map in which defects appear as white spots. To quantify the level of alignment of defects on the surface that might occur, the filtered image was then rotated through 180° and an intensity line profile along the vertical direction was produced at each degree increment. By summing the intensity profiles over the 180° rotation, a final profile of intensity against angle can be obtained (appendix B). An important point to note is that to remove the effects of the straight edges the largest circular area possible was cut out of the centre of the image. Although this involves removing information, by ensuring the image is rotationally symmetric, the intensity profiles are not skewed by the longer lengths presented by the diagonals of the image.

TRIM Simulation

Simulations of the ion bombardment of graphite and graphene were performed using the Transport of Ions through Matter (TRIM) package [37]. The package simulates the interaction of ions in various materials, allowing the tracking of both the incident ions and any atoms displaced by the bombardment. TRIM simulations of both graphite and graphene grown on SiC(0001) were performed. Ar^+ ions with an energy of 0.2 keV at normal incidence were chosen to mimic experimental conditions used. Graphite samples were simulated as 7 distinct graphite layers using the material properties provided. In the case of graphene grown on SiC(0001), due to limitations in the code, the graphene layers were treated as single layers of graphite. Furthermore, due to the lack of an exact structure for the carbon rich buffer layer, a compound layer of 2:1 carbon to silicon, with a density of 2.7 g/cm^3 was utilised [38]. 2 layers of true graphene and one buffer layer, were followed by four layers of SiC, the material parameters of which were supplied with the software. Simulations were performed using 10000 incident ions and data was collected on the range of ions within the material, the distribution of sputtered ions and the number of vacancies produced.

6.3   Results and Discussion

6.3.1   Graphite

Defect Agglomeration

Figure 6.4(a) shows a graphite surface after ion bombardment. Defective areas were observable, with a concentration of $1300\pm100/\mu m^2$ and an average size of 4 ± 3 nm^2, following an ion dose of 0.38 μC. The area of these defects would, at first, indicate that a large number of atoms are involved in the defect structure as the graphite unit cell area is significantly smaller at 0.051 nm^2, however it has long been known that the electronic effects of defect structures are of a much longer range due to charge enhancement, which increases the reactivity of the material over a large distance for a multi-atom defect [39]; this is particularly clear in the work by Hahn *et al.* in which few atom defects appear as bright hillocks [40]. Hence, the defects observed may correspond to the displacement of 2-3 atoms rather

than tens. Such long range effects are the result of electron scattering around the defect site, which produces Friedel oscillations that are apparent as a $\sqrt{3} \times \sqrt{3}$ superstructure [41]. The predominant defects produced during ion bombardment are most likely vacancies and adatoms/interstitials, as the incoming Ar^+ atoms have sufficient energy to remove carbon atoms from the lattice producing Frenkel defects [9, 42]. Based on the larger size of the bright areas, the defects observed are likely to be small agglomerations of defects and subsequently can be expected to be more stable. Despite the agglomerations being more clearly visible, it is also likely that single adatoms and vacancies are also present, however due to their significantly smaller migration energies they are unlikely to be observed, due to the large distances they can migrate over during the scan time [12]. Furthermore, due to the very fast diffusion of adatoms/interstitials even at room temperature, it is likely that a large proportion will encounter single vacancies and annihilate before they can be imaged, whilst the remainder will have encountered the pre-existing agglomerations or other interstitials to produce larger structures such as interstitial loops [12, 43].

Upon heating at 300 °C for four hours (Fig. 6.4(b)) defects can still be observed on the surface as small bright areas. The average size of defect agglomerations was found to be 7±4 nm² with a concentration of 900±90/μm². The large drop in the concentration of defects, combined with the increased area of those that remain, strongly suggests that the heating cycle has led to defect agglomeration. The larger agglomerations are expected to be stable to extremely high temperatures due to their high activation energies (for example the di-vacancy defect is predicted to have a migration energy of 7.0 eV and hence is stable to temperatures close to 2000 °C) [9, 44], it is therefore doubtful that these defects diffuse across the surface to result in the larger structures observed. It is likely that the increased agglomeration is the result of mono-vacancy defects diffusing across the surface which, upon encountering static defect agglomerations or other vacancies, will produce a significantly more stable structure resulting in the increased defect size observed. Following the jumping frequency model discussed by Banhart *et al.*:

$$n = n_0 e^{-\left(\frac{E_m}{kT} \right)} \ , \tag{6.1}$$

in which n is the jump frequency, E_m is the migration energy, n_0 is a pre-exponential factor, k is the Boltzmann constant and T is temperature), combined with a random walk trajectory, at a migration energy of $E_m = 1.0$ eV, vacancy defects will travel ~775 nm from their original position over 4 hours at 300 °C. In comparison to the average defect separation observed via STM imaging of 33.5 nm, the probability of a
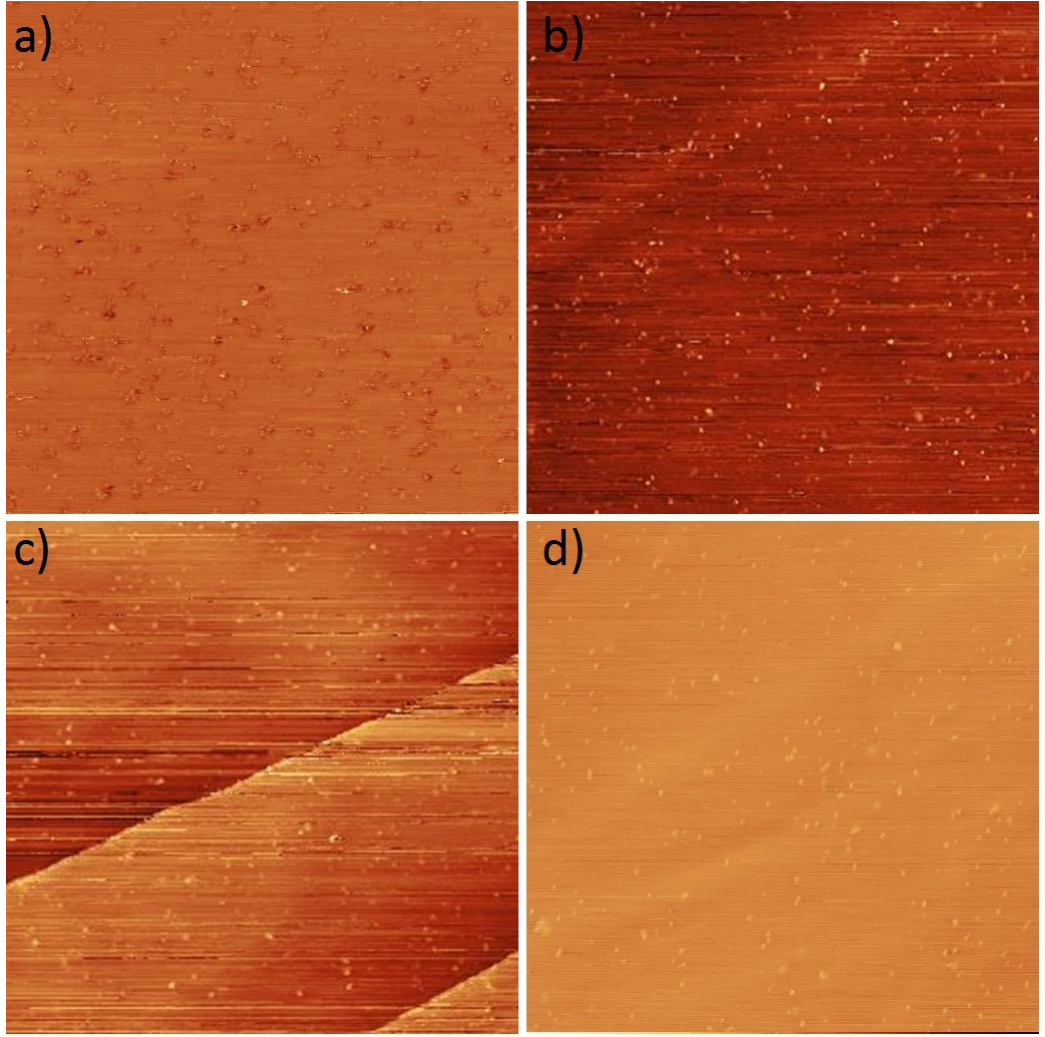
Figure 6.4: 300 nm^2 STM images of ion bombarded graphite taken (a) before annealing (V_{bias}=1.7 V, I=0.7 nA), (b) after annealing at 300 °C for 4 hours (V_{bias}=2.0 V, I=0.6 nA), (c) after annealing at 500 °C for 4 hours (V_{bias}=1.9 V, I=0.8 nA) and (d) after annealing at 750 °C for 4 hours (V_{bias}=1.6 V, I=0.7 nA).

vacancy encountering another defect during diffusion across the surface is very high. Di-interstitials may also contribute to defect agglomerations, however significant mobility of this defect does not occur until the graphite is annealed to temperatures exceeding 300 °C [45].

Upon increasing the anneal temperature to 500 °C (Fig. 6.4(c)) and annealing for four hours the defect density was found to remain fairly constant in comparison with heating at 300 °C, at 900 /μm^2 with the area of defects also remaining stable at 7±4 nm^2. The lack of change observed in the concentration and size of defects after annealing at 500 °C would indicate that the processes that drove defect agglomeration when heating at 300 °C applies at higher temperatures, but that fur-

ther growth in defect structures appears to be arrested upon reaching a critical size. This is most likely the result of the majority of smaller defects being incorporated rapidly into larger agglomerations which require significantly more energy to either become mobile as a whole or for smaller defects, such as interstitials, to desorb from them [12]. This is to be expected when taking into account the di-vacancy migration energy once again, which at this temperature produces a practically zero probability of hopping. It is possible that loops of three or more interstitials may be mobile at this temperature, but based on the lack of change in the defect structures observed, it is likely that this was not the case and that di-interstitial defects were able to diffuse to a substantial degree at 300 °C whilst larger interstitial loops remained static, resulting in the similar defect concentrations and sizes observed.

With a further increase in temperature to 750 °C for 4 hours the defect concentration was found to drop significantly to 640 $/\mu m^2$ combined with little increase in the average size of defect structures at 8±4 nm^2 (Fig. 6.4). The decrease in the number of defects indicates that further agglomeration or recombination occurs. The small increase in defect area suggests that the larger agglomerations are not diffusing and combining, consistent with their large migration energies. One possibility is that, agglomeration may be proceeding via an Ostwald ripening type mechanism in which defects made up of many vacancies or interstitials emit single defects which may then diffuse rapidly across the surface before combining with larger defect structures. A similar process has been proposed for interstitial loops, in which single interstitials are released, though this has not been observed directly via TEM, with an estimate that temperatures as high as 1000 K are required for this process to occur [12]. At 750 °C this mechanism may be more favourable resulting in the changes in defect size distribution observed.

Figure 6.5: 300 nm^2 STM images of Ar$^+$ ion irradiated graphite after annealing for 8 hours at (a) 300 °C (V$_{bias}$=1.3 V, I=0.8 nA), (b) 500 °C (V$_{bias}$=1.5 V, I=0.4 nA) and (c) 750 °C (V$_{bias}$=1.7 V, I=0.6 nA).

In order to observe whether the length of time at elevated temperatures affects the agglomeration and annihilation of defects, heating steps at 300 °C, 500 °C and 750 °C were also performed for 8 hours (Fig. 6.5). Upon heating for 8 hours at 300 °C similar results were observed to the shorter heating period previously used, with the average size of defects found to be 6±2 nm^2. The concentration of defects was however found to drop considerably to 560 /μm^2, which indicates that the distribution of defects rapidly reaches a steady state when heated to 300 °C, at which point further significant increases in size no longer occur. Therefore, a longer heating period does not result in further defect evolution as the majority of smaller defects such as mono-vacancies and adatoms may have already been incorporated into larger structures. The large drop in concentration, however, is possibly the result of remaining mono-vacancies and di-interstitials, which had yet to form stable agglomerations after annealing for 4 hours, now having sufficient time to agglomerate into larger structures, or alternatively annihilate [12]. The absence of an increase in the average defect size indicates that annihilation of remaining defects or even partial recombination at larger defect clusters restricts further growth in defect area.

Heating at 500 °C for 8 hours, much like heating to 300 °C for that time period, led to a defect size distribution of 5±3 nm^2 which differs negligibly to that observed after heating for 4 hours at the same temperature (Fig. 6.5(b)). Once again this indicates that once a critical defect size has been reached further growth is no longer preferable without significant further energy being available. Although an increase in the anneal temperature to 500 °C does provide greater energy to allow defects to migrate across the surface, the difference between annealing at 300 °C and 500 °C appears not to be significant enough to induce larger agglomeration of defects, even when annealing takes place for an extended period of time. The concentration of defects follows a similar behaviour to that seen with increased anneal time at 300 °C, in that a sharp drop in defect concentration to 550±30 /μm^2 occurs. The similarity between the results of defect concentration obtained at 300 °C and 500 °C, would suggest that there is little difference in the behaviour of defects between these temperatures. Therefore, the drop in concentration may be the result of further time at elevated temperatures allowing for more agglomeration and annihilation of the remaining vacancies and di-interstitials on the surface.

Annealing for 8 hours at 750 °C produced a small increase in defect size in comparison to annealing at 300 °C and 500 °C with an average defect area of 6±4 nm^2 found (Fig. 6.5(c)). The apparent defect size is the same to within error to that observed for annealing for 4 hours at the same temperature. The concentration of

defects was found to have been altered further by the extended high temperature annealing, with a significant drop to 230 ± 20 /μm^2. This strongly suggests that the increased anneal time at a high temperature results in increased defect agglomeration, and further vacancy-interstitial recombination, reducing defect concentration [42]. The longer anneal at 750 °C ensures that defects migrating across the surface are more likely to encounter others over the course of the anneal producing larger clusters and lower defect concentration.

The trends observed at longer anneal times appear to continue when the annealing time is extended further. Annealing at 750 °C for 24 hours produced a significantly larger average defect size of 10 ± 5 nm^2, although this was combined with a large size distribution. Furthermore, this increase in size is once again accompanied by a sharp drop in defect concentration to 190 /μm^2. The significantly higher defect area observed is evidence that agglomeration not only occurs readily at higher temperatures, but also that this clustering continues over longer time periods, indicating that defects continue to diffuse across the surface despite the expectation that the majority of single defects will have already clustered after shorter heating times. Therefore, two mechanisms are proposed here for the continued growth of defects over longer periods: (1) at high temperatures and long anneal times, larger defects such as interstitial loops are capable of diffusing. Due to the high migration energy of di-vacancies, it is likely that these remain stable on the surface and that any movement is therefore by large interstitial loops of 3-4 atoms, loops of > 4 may be too large for migration. However, no migration energy of large interstitial loops has been previously reported. (2) An Ostwald ripening type growth, as discussed above may occur, in which larger agglomerations continue to grow at the expense of smaller defects [12]. This is supported by the large size distribution observed after the longer anneal time, suggesting that some defects are shrinking whilst larger clusters grow. Banhart suggested that at higher temperatures single interstitials may be emitted by larger loops, which then migrate rapidly to combine with other defects [12]. However, Banhart was unable to observe this directly, suggesting that a higher temperature or significantly longer anneal time was required. By annealing the defective sample for very long periods the possibility of interstitial emission occurring to a measurable degree increases significantly, which could result in the observed changes to defects on the surface.
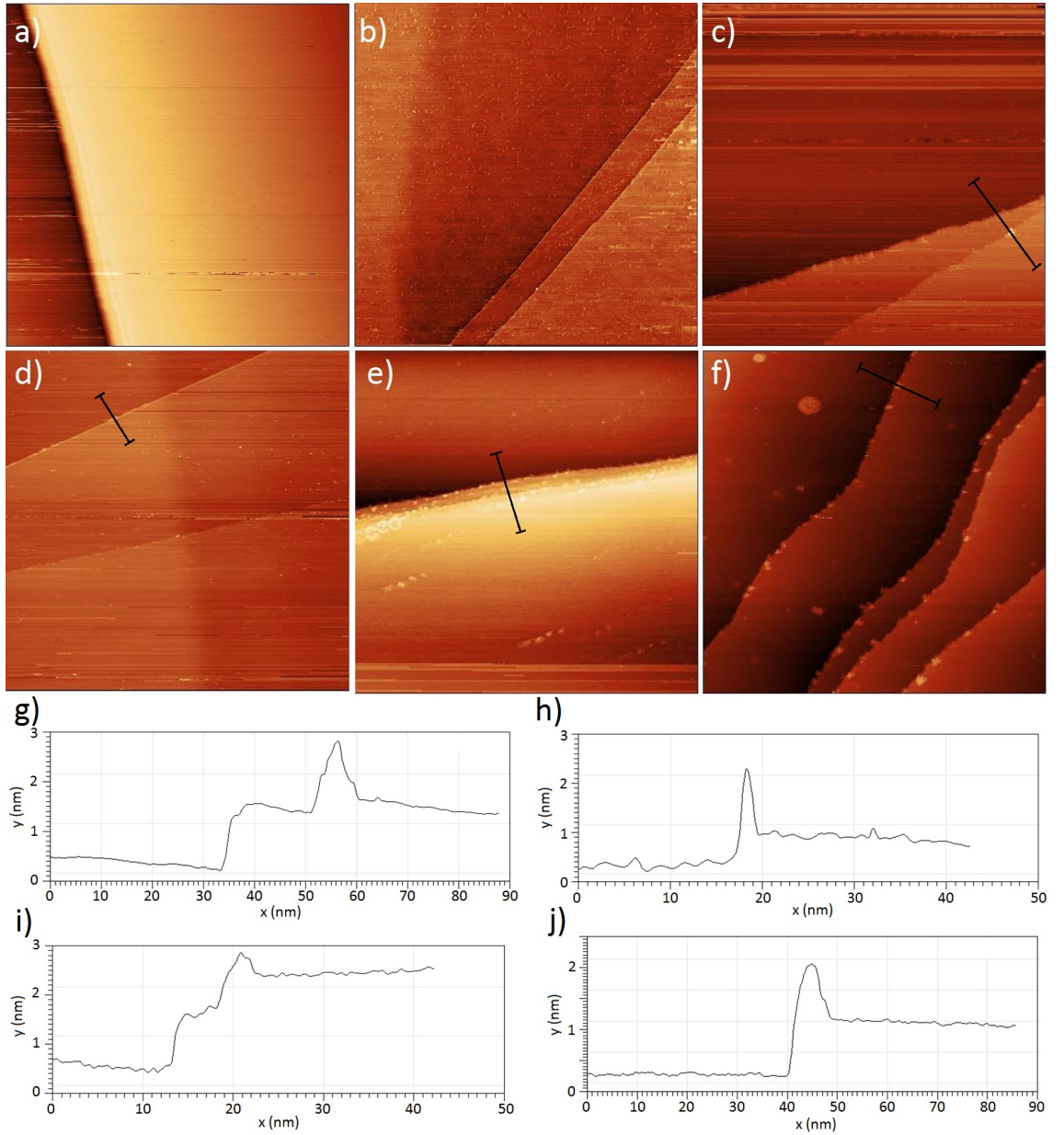
Figure 6.6: STM images of graphite steps (a) before ion bombardment (500 nm^2 V$_{bias}$=1.0 V, I=1.3 nA). (b) After bombardment (500 nm^2 V$_{bias}$=1.2 V, I=0.8 nA). (c) After annealing at 300 °C for 4 hours (300 nm^2 V$_{bias}$=1.3 V, I=0.8 nA). (d) After annealing for 4 hours at 500 °C (300 nm^2 V$_{bias}$=1.5 V, I=0.4 nA). (e) After annealing for 4 hours at 750 °C (300 nm^2 V$_{bias}$=1.7 V, I=0.8 nA). (f) After annealing for 24 hours at 750 °C (500 nm^2 V$_{bias}$=1.7 V, I=0.8 nA). Line profiles across defects at steps in (c), (d), (e) and (f) are shown in graphs (g), (h), (i) and (j) respectively.

The effects of defect agglomeration are clearly visible on graphite terraces as shown above, however, the introduction of these imperfections and their subsequent annealing also have a large effect on the steps. Figure 6.6(a) shows a pristine step on HOPG prior to ion bombardment, which is typically straight with little to no

roughness observed. Upon ion bombardment small changes in steps can be observed with edges appearing slightly brighter indicating an increased DOS and therefore defects are present along the majority of the length (Fig. 6.6(b)). At room temperature single adatoms and interstitials will likely diffuse rapidly across the surface as discussed above, some of which are also likely to contribute to the brightness observed at steps as the edges provide a sink at which dangling bonds may be satisfied through reconstruction. Upon annealing the defective graphite for 4 hours at 300 °C, a noticeable increase in the roughness of steps was observed, with the many protrusions and indentations, combined with a large number of clustered bright areas which are likely to be defect agglomerations (Fig. 6.6(c) and (g)). The unevenness of the steps after annealing can be attributed to the movement of the defects upon heating, with interstitials/adatoms and vacancies causing step growth and retraction respectively. Upon annealing the defective graphite at 500 °C for 4 hours little change is observed in the step morphology compared with that seen after annealing at 300 °C, with edges still appearing rough with some defect clustering (Fig. 6.6(d) and (h)). This suggests that, much like the behaviour seen on the graphite terraces, there is little difference in defect mobility between 300 °C and 500 °C.

Heating at 750 °C, unlike at 500 °C, showed further evolution in step morphology, with an additional increase in the roughness of the edges observed, as seen in figure 6.6(e). Furthermore, the number of bright areas at steps increased significantly from an average of one defect agglomeration every 21 ± 2 nm in step length after annealing at 300 °C to one agglomeration per 10 ± 2 nm, suggesting a large number of defect structures are trapped/nucleate at these boundaries. Furthermore, the size of these agglomerations at steps, in keeping with the behaviour on terraces, increased with the rise in temperature, from 3 ± 2 nm^2 to 5 ± 2 nm^2. To compare the concentration of defects at steps to that observed on flat terraces, a length of ±10 nm was taken along a step to produce an effective step area. The defect concentration at steps after annealing at 750 °C was found via this method to be an order of magnitude higher, at $5280/\mu$m^2, compared with the concentration on a flat terrace of 644 /μm^2, as determined above. This larger concentration was also observed on samples annealed at 300 °C, however the disparity between step and terrace was much less pronounced at $2400/\mu$m^2 to $890/\mu$m^2 respectively. This suggests that defect clustering occurs preferentially at step edges when the sample is raised to higher temperatures. It is likely that the step edges are acting as traps at which the larger defects which are mobile at higher temperatures are likely to become immobile. Furthermore, upon becoming pinned, unlike single atom defects such as vacancies and interstitials, these larger agglomerations are unlikely to result in step growth or loss.

Finally, after annealing for 24 hours at 750 °C, the behaviour observed with shorter anneal times is enhanced significantly, with a large number of defect clusters observed decorating the steps (Fig. 6.6(f) and (j)). The defect agglomerations appear to form on both the upper and lower edges of the step although a preference for the upper level was identified. Furthermore, in some places the step appears to grow outwards, whilst at others a loss of matter is observed, indicating that some interstitials and monovacancies are migrating to the steps and causing, both growth and recession of the step. It should be noted that these agglomerations show a number of similarities with decoration due to metal or contamination deposition at low coverage [46]. This can be ruled out as all measurements were performed under UHV conditions using a fully outgassed heater and ion gun, ensuring no contamination source was present. The concentration of defects along the step remains fairly constant in comparison with annealing at 750 °C, at one defect agglomeration per 11±2 nm, however the average defect size, much like on terraces, is significantly increased. It is thus clear that steps provide a region in which defect clustering is preferred, likely due to the energy barrier to further diffusion they provide. The defect structures will continue to grow at steps throughout longer anneals at high temperatures as larger defects such as interstitial loops migrate to the edge and add to pre-existing structures. This is combined with the gradual disappearance of smaller defects (e.g. Ostwald ripening), which results in the further roughening of the edge.

In conclusion, pristine HOPG was irradiated with Ar$^+$ ions of 200 eV energy and at doses of 0.38 μC, to produce defects. Samples were then annealed at various temperatures and times to observe defect evolution, both on terraces and at step edges. Defects were found to agglomerate on terraces after annealing at 300 °C for 4 hours, with practically identical results also observed after annealing at 500 °C for the same length of time. Increasing the temperature to 750 °C was found to produce significantly larger defect structures in comparison to annealing at lower temperatures. The respective levels of clustering were attributed to the migration of defects across the surface, with smaller defects such as di-interstitials and vacancies agglomerating significantly at the lower temperature anneals, whilst at higher temperatures, larger defect structure growth is likely to proceed at the expense of smaller defect structures via the emission of interstitials/vacancies. Similar results were observed when annealing was performed for longer periods, however small reductions in defect concentration were also observed at all temperatures, most likely the result of annihilation of vacancy-interstitial pairs due to increased anneal time. Annealing at 750 °C for 24 hours was found to produce significantly larger defect

agglomerations with a large size distribution also apparent. This suggests that Ost-wald ripening of defects is the most likely mechanism for further defect structure evolution. Finally, defect agglomerations were found to form considerably more at steps than on terraces, predominantly on the upper side of steps, most likely due to the increased diffusion barrier in these areas. The size of defect clusters followed a similar behaviour to those on terraces with increasing temperature, with significant increases being observed after annealing at 300 °C, 750 °C and after long anneals at 750 °C. This was attributed to larger defects such as interstitial loops migrating to steps where they become immobile.
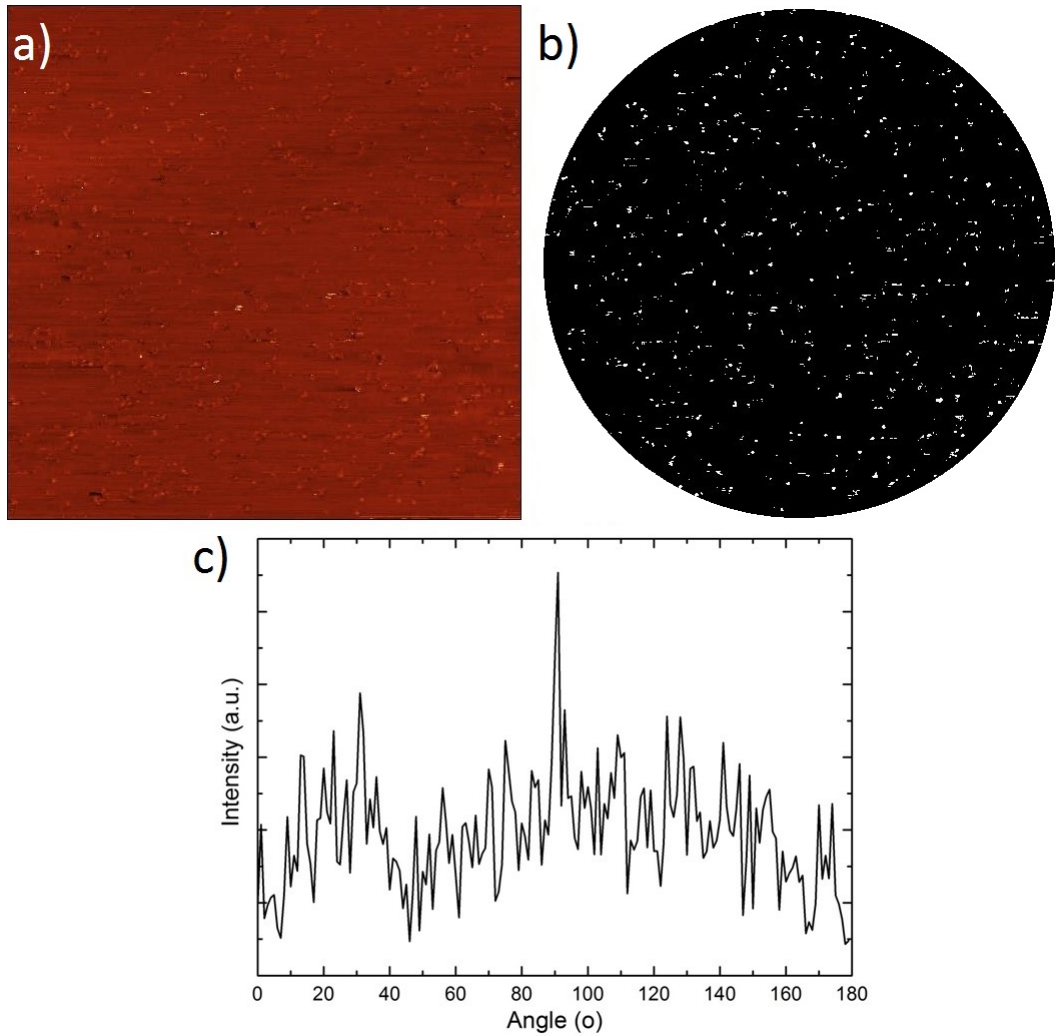
Defect Alignment

Figure 6.7: (a) 300 nm^2 STM image of graphite after ion bombardment, prior to annealing (V_{bias}=1.2 V, I=0.8 nA). (b) STM image in (a) after processing, defects appear as bright white spots. (c) Angular intensity distribution obtained from (b).

Figure 6.7(a) shows a typical graphite surface after Ar^+ bombardment to a dose of 0.38 μC. As previously seen, a defect concentration of 1300$\pm$200/μm^2 is observable as small bright regions on the surface. Image processing, as discussed in section 6.2.2 above, produced the circular intensity map in figure 6.7(b) in which defect structures appear as small white areas. By rotating (b) through 180° and summing the intensity profiles, the angular intensity distribution in figure 6.7(c) was obtained. The angular intensity distribution shows a single large peak exactly at 90° which corresponds to a single defect at the centre of the image and can therefore be neglected. No further significant features are present in the angular distribution, indicating no alignment of the extrinsic defects on the surface. This is to be expected as the divergence of the ion beam is large - indeed the beam is defocussed to cover the whole surface - therefore bombardment produces a homogeneous defect concentration on the length scales observed. At room temperature the majority of defects are stable and do not migrate significantly ensuring they remain in close proximity to their original sites [12].

Figure 6.8(a) and (c) show areas of the HOPG sample following an anneal for 24 hours at 750 °C. The defect density has dropped significantly as seen previously, as smaller defects combine to produce larger structures. Figure 6.8(b) and (d) show the angular intensity distributions obtained from 6.8(a) and (c) respectively, in which broad peaks in intensity can be observed. These peaks suggest that after annealing at high temperatures, during which defects migrate across the surface, agglomeration occurs preferentially along specific directions in the scanned region. Alignment was observed in the majority of areas scanned with 1$\pm$1 peaks/300 nm^2 scan area, however, no preferential alignment direction was observed over the whole sample, with peaks being observed at significantly different angles despite the separation between imaging areas being small (typically $\sim$300 nm). This suggests that the alignment observed is localised over areas of the order of hundreds of nm^2.

In order for defects to become pinned in certain regions the migration energy must be higher at these points than the energy available to the defect, even at raised temperatures [12]. This can typically occur when a defect encounters another defect to form a larger, more stable configuration that reduces the free energy of the structure. Therefore, for preferential agglomeration to occur over hundreds of nanometers, an extended defect structure may be present. In the case of HOPG, the obvious structures that could fill this role would be grain boundaries. In order to investigate this, the average graphite grain size is required. The method outlined by Tuinstra and Koenig was utilised, in which the relative ratio of D to G Raman
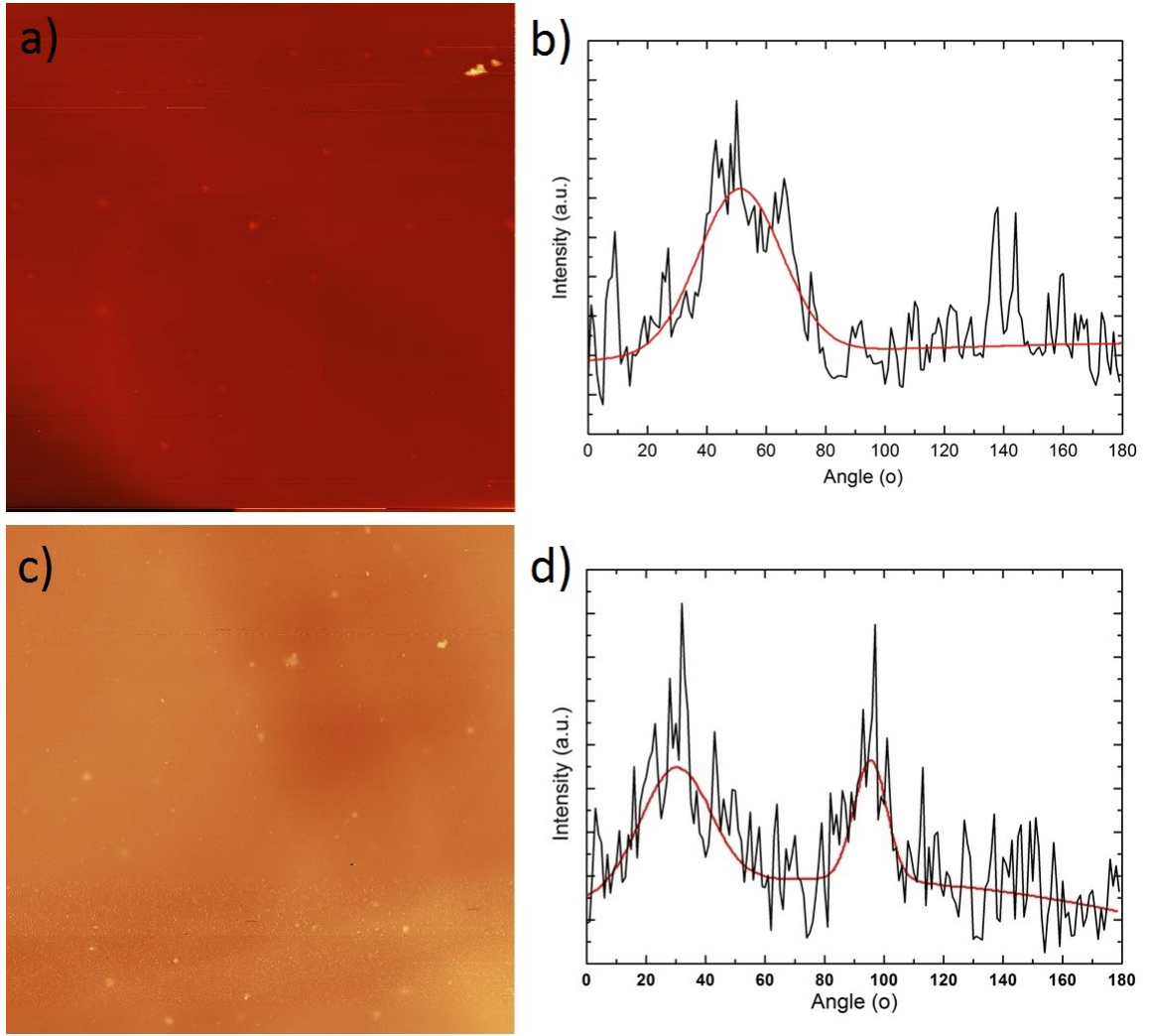
Figure 6.8: (a) 300 nm^2 STM image of HOPG after ion bombardment and annealing at 750 °C (V$_{bias}$=1.7 V, I=0.8 nA). (b) Angular intensity distribution obtained from (a). (c) Alternate 300 nm^2 area of bombarded graphite (V$_{bias}$=1.7 V, I=0.8 nA). (d) Angular intensity distribution obtained from (c).

peaks of the pristine graphite sample were measured [47]. The Raman spectrum obtained (Fig. 6.9) shows a high intensity G peak at 1575 cm^{-1} , with a very weak D peak at 1355 cm^{-1}. By comparing the relative intensities of the two peaks, an average crystallite size of 550±80 nm was determined. Comparing the image size of 300 nm^2 used to observe the alignment of defects, with the average grain size there is a high probability of at least one grain boundary being present in each imaged area, but there are unlikely to be multiple grains. This strongly suggests that when heated for an extended period of time, defects align along the boundaries between graphite grains.
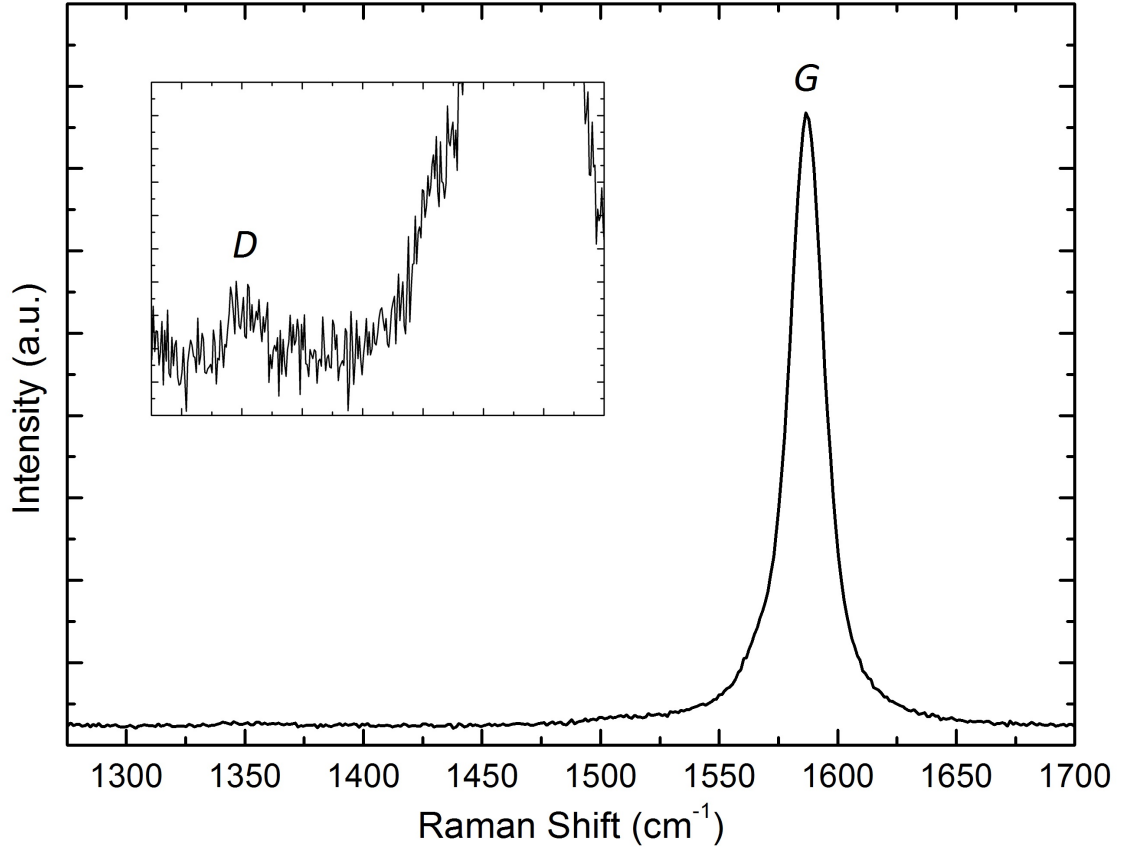
Figure 6.9: Raman spectrum obtained from HOPG showing the G peak at 1575 cm^{-1}. (inset) Close up of the D peak at 1335 cm^{-1}.

STS of Defects

Figure 6.10(a) shows an STM image of a defective graphite area in which, a single defect agglomeration, which appears bright compared to the surrounding pristine graphite lattice, much like those observed previously is boxed. An STS spectrum obtained from the defect in figure 6.10(a) shows the characteristic parabolic graphite LDOS within the bias voltage range of ± 0.7 V. However outside this range an asymmetry occurs in which the dynamic conductance drops off under negative bias, whilst at positive biases the "normal" graphite behaviour is observed (Fig. 6.10(a)). Similarly, the defect highlighted in figure 6.10(c) also shows this asymmetric behaviour in its STS spectrum with a reduction in the expected LDOS at ~ 0.5 V (Fig. 6.10(d)). However, in this case a further asymmetric feature is present at positive bias at ~ 1.0 V. The increase in the LDOS either side of the Fermi level suggests that the defect has caused a reconstruction of the graphite lattice. With no introduction of states at the Fermi level, no dangling bonds are likely to be present. This would indicate that either complete reconstruction of the surface has occurred at the de-
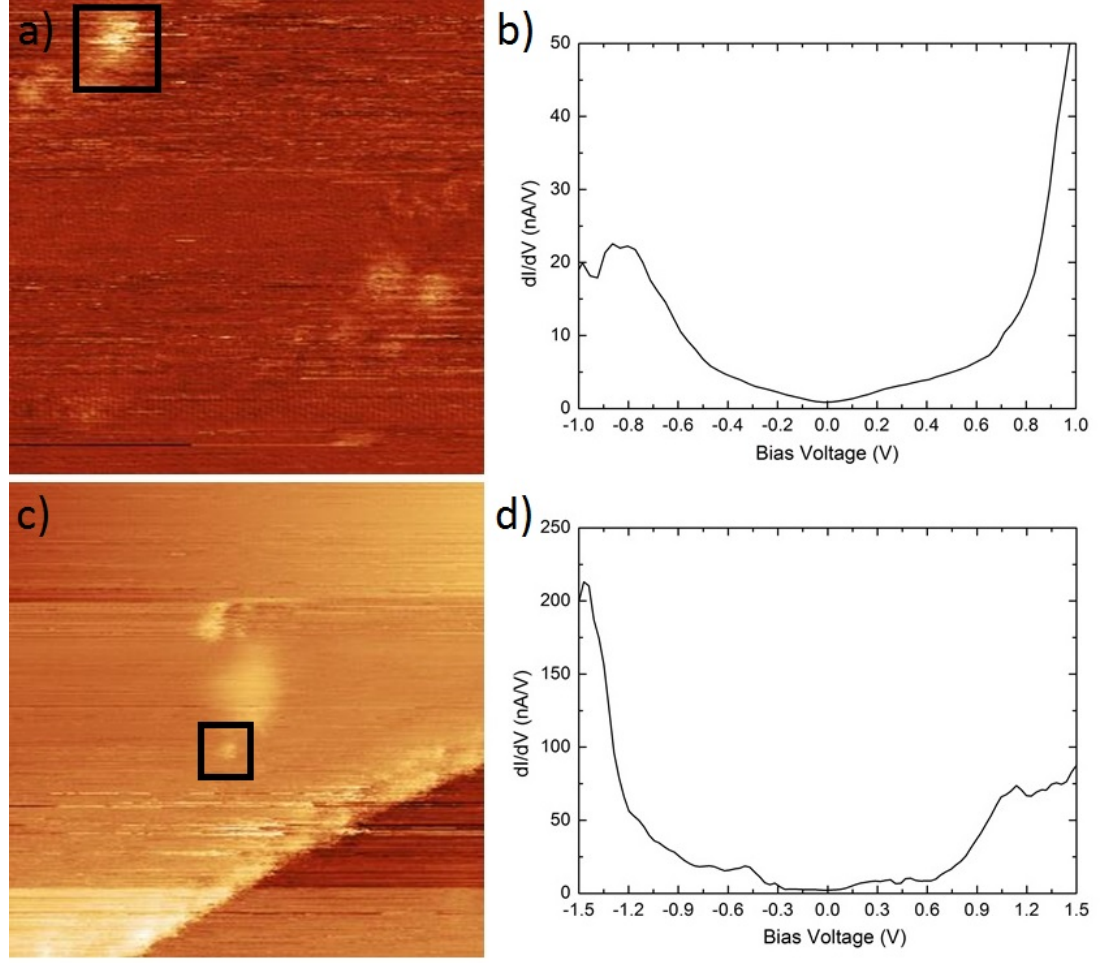
Figure 6.10: (a) 20 nm^2 STM image showing an area of both pristine and defective HOPG (V$_{bias}$=0.6 V, I=1.6 nA). (b) STS spectrum obtained from the defect boxed in (a). (c) 20 nm^2 Image showing another area on the HOPG sample containing both pristine regions and defect structures (V$_{bias}$=0.6 V, I=1.6 nA). (d) STS spectrum obtained from the defect agglomeration in (c).

fect site ensuring no dangling bonds remain, either through a combination of non six-membered rings, or through the saturation of dangling bonds via the binding of residual gas molecules present within the UHV system such as hydrogen or CO. Theoretical work performed by Bena *et al.* showed a similar shoulder in the simulated single particle DOS in the presence of an impurity indicating the saturation by impurities may be the cause of the increased local conductivity [48]. However, discrimination between these suggestions is beyond the scope of this study; a potential experiment to further investigate this is discussed in Chapter 8.

Figure 6.11 shows the second type of defect that was also observed, which despite showing the characteristic shape of the graphite LDOS, displays a significantly larger slope than that exhibited by the pristine graphite lattice. The considerably larger
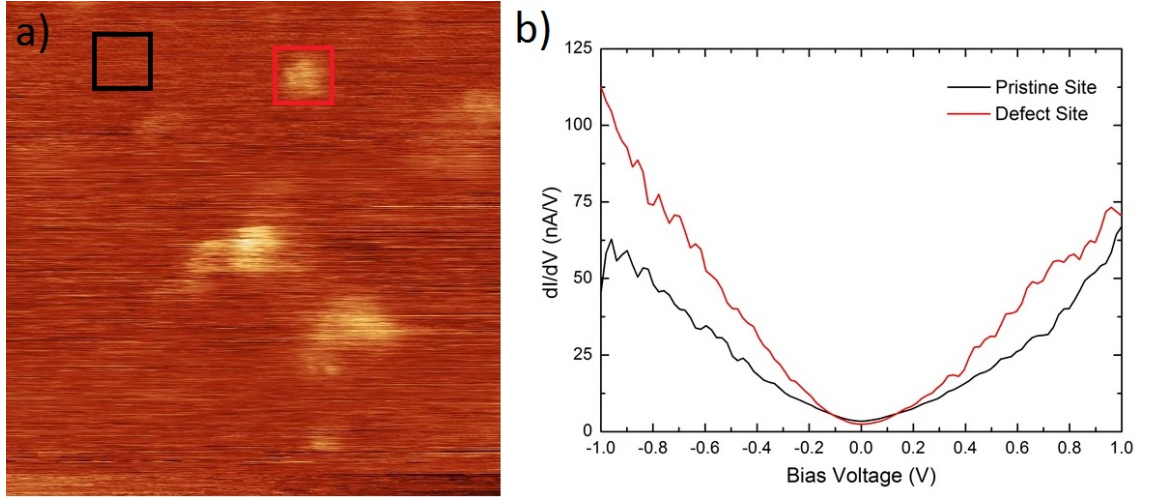
Figure 6.11: 20 nm^2 STM image of a defective area of graphite, clear (black) and defective (red) areas in which STS was obtained are shown (V_{bias}=0.5 V, I=1.8 nA). (b) STS obtained from the areas shown in (a).

conductance observed in close proximity to the Fermi level suggests an increase in the LDOS due to the presence of the defect structure. Once again the absence of states at E_F suggests that no dangling bonds remain after reconstruction of the graphite lattice around the defect site. This differs significantly to the STS spectra obtained by Hahn *et al.* in which mono-vacancies result in a large jump in conductance at the Fermi level [41]. Furthermore, narrow dips in the DOS brought about by unsaturated bonds are not observed, although these may be difficult to discern above the noise due to the relative lack of sensitivity at room temperature [49]. Again this indicates that either a reconstruction of the lattice or the binding of residual gas molecules. The increased LDOS of states close to the Fermi level shows a number of similarities with valence band ultra-violet photoemission spectroscopy (UPS) studies which showed significant increases in spectral intensity in this region. Schlögl suggested that the increased number of states in close proximity to the Fermi level arises from the defect converting the typical delocalised π electron states associated with the highly ordered graphite structure to a disordered state [50]. This results in an increase in the number of σ states at the expense of the usual π states. A further UPS study by Reinke *et al.* also shows a similar increase in intensity, however no suggestions are made as to its origin [51].

Similar behaviour is also observed in other graphitic carbon systems, particularly fullerenes. In C_{60}, when defects are introduced via ion-bombardment, at low enough energies to prevent complete deconstruction of the carbon cage an increase in intensity close to the Fermi level can once again be observed in UPS [51]. This

was attributed to the production of a structurally homogeneous surface layer as defect density in cages increased. A further study in which graphite was bombarded with neutrons showed similar results with a rapid linear increase in DOS outward from E_F [52]. The authors suggest that vacancy defects produced via bombardment modify the π band of graphite due to restructuring of the surface, resulting in the creation of new states. Due to similarities observed between the STS measurements and other studies, we propose that these particular defects are likely to be agglomerations made up predominantly of vacancies, which reconstruct the surface leaving no dangling bonds. However, the presence of interstitials or adatoms within these agglomerations can not be discounted.

6.3.2   Graphene on SiC(0001)

Defect Dynamics of Intrinsic Defects
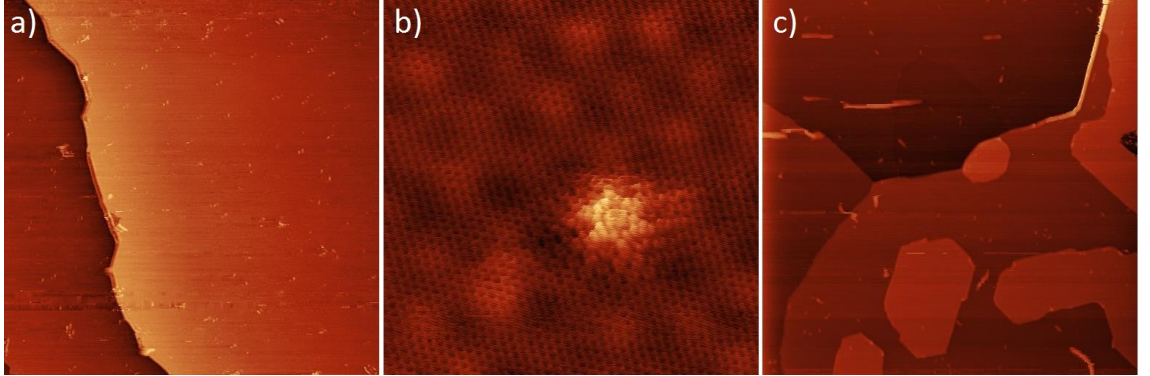
Figure 6.12: (a) 300 nm^2 STM image of graphene grown on SiC(0001) showing intrinsic defects (V$_{bias}$=1.7 V, I=0.6 nA). (b) 10 nm^2 image of a single "flower" defect structure. Atomic resolution of the graphene lattice, the $(6\sqrt{3} \times 6\sqrt{3})R30°$ reconstruction can also be observed, whilst a $(\sqrt{3} \times \sqrt{3})R30°$ reconstruction surrounds the defect (V$_{bias}$=1.2 V, I=1.1 nA). (c) 300 nm^2 image of graphene grown on SiC after annealing at 750 °C for 24 hours, showing no change in defect concentration (V$_{bias}$=1.9 V, I=0.5 nA).

Figure 6.12(a) shows a typical STM image of graphene grown on SiC(0001), in which two graphene terraces can be seen separated by a SiC bilayer step edge. A number of bright spots can also be observed on the surface corresponding to intrinsic defects produced during the growth process. These defects were produced at a concentration of 330$\pm$40 /μm^2 with an average size of 5$\pm$2 nm^2. Intrinsic defects were found to come in a number of forms, with shapes varying from triangular structures, most likely vacancy based V$_2$ 555-777 reconstructions, to larger defects that closely resembled 2-hexagon addimers [53, 54]. However, the most commonly

observed defect was a hexagonal defect, previously referred to in the literature as the flower defect, in which a stable symmetric configuration of 5 and 7 membered rings forms (Fig. 6.12(b)) [3,54]. These defects were found to remain static at room temperature, moving negligibly during imaging, whilst also showing no changes in structure, indicating a high level of stability. A warping of the surrounding graphene lattice was observed in close proximity to the defect with a larger $(\sqrt{3} \times \sqrt{3})R30°$ periodicity compared to the typical hexagonal lattice. This corresponds to quasi-particle scattering in the region of the defect, which is determined by the graphene electronic structure, resulting in scattering vectors a factor of $\sqrt{3}$ larger than the lattice vectors [3,39].

The graphene sample was heated first at 300 °C, followed by further heating at 500 °C and 750 °C for 8 hours, and finally for 24 hours at 750 °C with imaging performed between heating steps to observe any effects on the intrinsic defects present. For Images obtained of the graphene after the annealing steps at 300 °C and 500 °C no change was found in the defect concentration or average defect size with values of 300 ± 30 /μm^2 and 4 ± 2 nm^2, and 400 ± 30 /μm^2 and 4 ± 2 nm^2 obtained respectively. Additionally, no change was observed when the temperature was raised further to 750 °C with defect size and concentration remaining completely static. Annealing at 750 °C for 24 hours also showed no variation in the intrinsic defects despite the extended anneal time, with the concentration remaining identical to that observed before any heating was conducted (Fig. 6.12(c)); the final defect concentration remained at 320 ± 30/μm^2 with the size of defects also remaining constant at an average of 4 ± 2 nm^2.

Therefore, it can be concluded that the intrinsic defects that form during the growth of graphene on SiC(0001) at high temperatures are completely unaffected by temperatures up to 1000 K. This imperviousness likely arises from the conditions during which the defect forms, resulting in a significantly more stable defect structure. The graphene growth process (outlined in Chapters 3 and 4) is carried out at temperatures significantly higher ($\sim$1775 °C) than those used to probe defect dynamics. It is likely that these defect structures form during the cooling phase of the process, shortly after high quality graphene has been produced. During the growth of graphene from SiC(0001) Si atoms sublime from the surface leaving a carbon rich surface, however this process is not entirely homogeneous and significant diffusion of the carbon atoms on the surface occurs during cooling before complete graphene layers form [55,56]. As a result of this process, many structural features arise, including vacancy defects [57]. As the temperature remains high for a short while

after growth, these vacancies can migrate rapidly across the surface until they encounter graphene islands/steps and disappear or combine with other defects. Upon encountering other defects it is likely that a large degree of reconstruction will occur resulting in large stable defects with no dangling bonds, such as the production of non-six membered rings as seen above. As the temperature drops further, these defects become pinned and no further reconstruction occurs due to the significant energy requirements, for example Cockayne reports a total formation energy of 7.4 eV for the "flower" defect [54]. Therefore, subsequent movement or reconstruction of these defects is unlikely to be observed except at temperatures close to the growth temperature of 1775 °C.

Defect Agglomeration
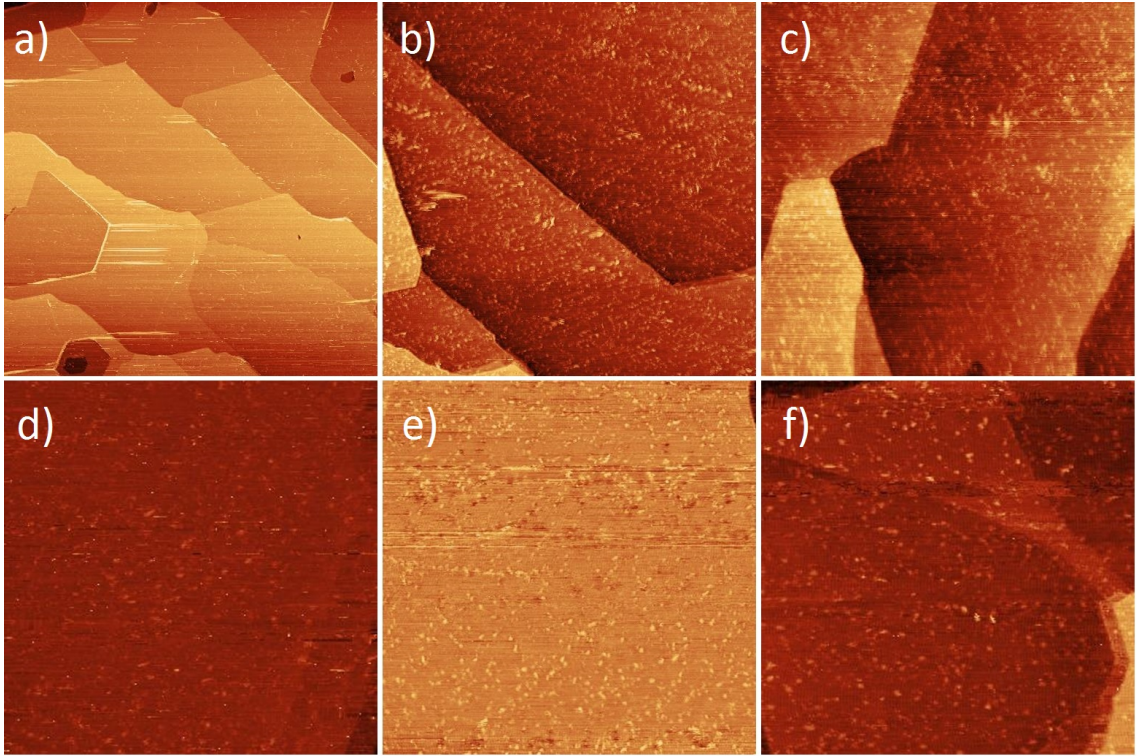
Figure 6.13: (a) 1 μm^2 STM image of graphene grown on SiC(0001) before ion bombardment (V_{bias}=1.9 V, I=1.0 nA). (b) 300 nm^2 image of graphene on SiC after ion bombardment (V_{bias}=1.4 V, I=1.0 nA). (c) 300 nm^2 image of the bombarded graphene sample after annealing for 4 hours at 300 °C (V_{bias}=1.9 V, I=0.9 nA). (d) 200 nm^2 image of defective graphene after annealing for 4 hours at 500 °C (V_{bias}=1.2 V, I=0.9 nA). (e) 250 nm^2 image of the bombarded sample after annealing for 4 hours at 750 °C (V_{bias}=1.4 V, I=1.2 nA). (f) 200 nm^2 image of graphene after annealing at 750 °C for 24 hours (V_{bias}=1.6 V, I=1.1 nA).

Figure 6.13(a) shows a typical image of graphene grown on SiC(0001), as ex-

pected large flat terraces with some small pleat defects and pit structures can be observed. The same sample can be seen in Fig. 6.13(b) after ion bombardment with a dose of 0.49 μC. As expected a large number of defects have been produced on the surface, apparent as bright regions compared with the pristine graphene. This dose was found to produce defects with an average size of 4$\pm$2 nm^2 with a concentration of 2100$\pm$100/μm^2. The size and concentration of defects is slightly higher than that observed on graphite, which can be attributed to slight variations in the ion dosage. Despite this slight increase, the concentration of extrinsic defects are still significantly smaller than those observed on graphite after any level of heating. Figure 6.13(c) shows the sample after annealing for four hours at 300 °C. The concentration of defects was found to drop to 1600$\pm$90/μm^2, however, the average defect size remained fairly constant at 4$\pm$2 nm^2. The drop in defect concentration can be explained in much the same way as in graphite, where the increase in temperature causes mono-vacancies and interstitials to migrate rapidly across the surface with recombination occurring when defects of opposite "type" collide, reducing the overall defect concentration.

The trend of decreasing defect concentration combined with no change in defect size continues when the anneal temperature is increased to 500 °C. Figure 6.13(d) shows the graphene sample after annealing at 500 °C, in which the defect concentration dropped, to 1300$\pm$80/μm^2, with the average defect size remaining similarly constant at 4$\pm$2 nm^2. This shows some similarities to the behaviour observed on graphite as the defect concentration, dropped to a lesser degree than observed for annealing at 300 °C. This would suggest that some recombination of smaller defects still occurs, quickly at first and then slowing as fewer small defects such as interstitials and monovacancies remain on the surface.

With further heating to 750 °C for four hours the defects present showed very little change from those observed after annealing at 500 °C (Fig. 6.13(e)). The defect concentration was found to remain stable at 1200$\pm$90/μm^2 with the average defect area also remaining static at 4$\pm$2 nm^2. This differs significantly from the behaviour observed on graphite, which displayed large decreases in defect concentration combined with significant defect agglomeration after annealing at 750 °C, explained by an Ostwald ripening mechanism leading to the loss of smaller defects to fuel the growth of larger ones. This evidently does not occur in graphene on SiC(0001), with increased defect stability being observed even when extending the anneal period to 24 hours at 750 °C. Figure 6.13(f) shows the defective graphene sample after this extended anneal time with the defect concentration remaining at

$1200\pm80/\mu\mathrm{m}^2$ with average defect size also remaining at 4 ± 2 nm^2.
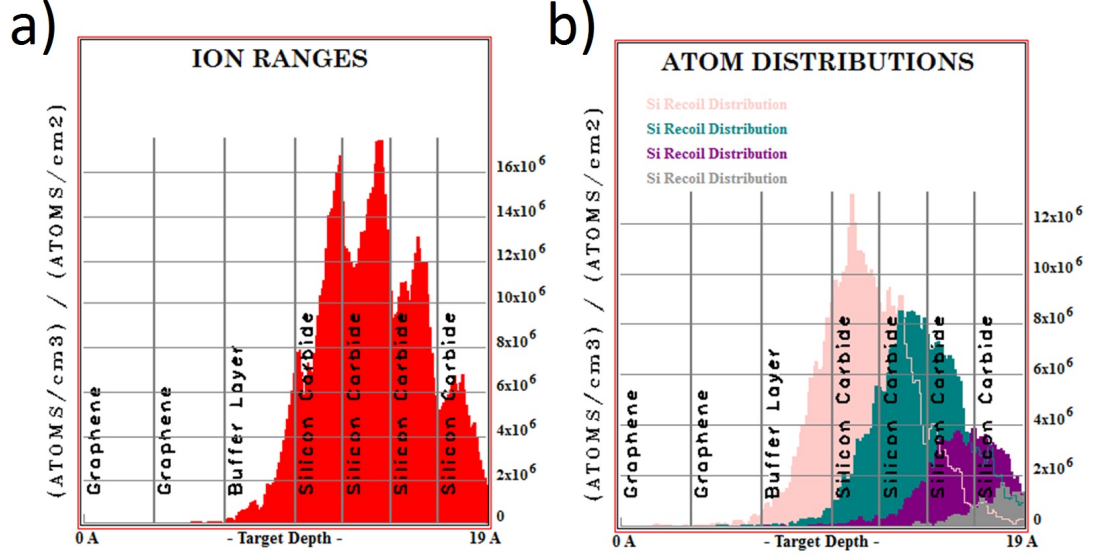
Figure 6.14: (a) Simulated ranges for Ar$^+$ ions incident on graphene grown on SiC(0001). (b) Simulated distribution of recoiling Si atoms in graphene on SiC after bombardment with 10000 Ar$^+$ ions. Si atoms from the buffer layer and first three SiC layers are coloured beige, green, purple and grey respectively.

The increased defect stability observed over all annealing temperatures indicates that defects produced in graphene on SiC(0001) behave differently to those in graphite. The mechanism by which defects remain static on the graphene surface, even at elevated temperatures is unknown. A number of possible explanations can be considered: The presence of Si in the substrate and buffer layer might suggest that during bombardment, Si atoms could be sputtered from these lower layers and bind at the defect sites above, increasing their stability. However, TRIM simulations indicate that despite ions penetrating to the depth of the buffer layer and SiC substrate (Fig. 6.14(a)) and sputtering occurring, Si atoms were not found to sputter outward to a significant degree, with the vast majority of displaced Si atoms being further embedded in the substrate. Therefore, with the concentration of back-sputtered Si low, the probability of intermixing at defect sites is small. An alternative explanation for increased defect stability is that there is an influence from the buffer layer. As seen in previous chapters, the buffer layer that forms between the SiC substrate and the first true graphene layer has a significant effect on the properties of the graphene film and a clear height modulation can be clearly observed as the $(6\sqrt{3}\times6\sqrt{3})R30°$ surface periodicity in STM and LEED. The presence of this Moiré pattern, and subsequent damage to it from ion bombardment, will have an effect on the energy landscape of the graphene layers above, possibly due to reorganisation from predominantly sp^2 bonding to sp^3, which may result in

the variation in defect stability observed. However, due to the depth of the buffer layer in the case of FLG, the effects of the changes in energy landscape on the layers above are likely to be strongly attenuated. When considering the increase in migration energy required to prevent the diffusion of both interstitials and vacancies at temperatures as high as 750 °C, estimated at $\sim$1.8 eV and $\sim$0.9 eV respectively via the model produced by Banhart *et al.* (equation 6.1), this would suggest that the presence of the damaged buffer layer is unlikely to be the cause for the increased stability observed [12,45]. Nevertheless, some regions may still see increased activation barriers, due some cross-linking between the layers.

A final possible explanation may come from the modification of the electronic structure of the graphene due to the presence of the buffer layer and SiC substrate. Such a modification may affect the way in which defects reconstruct on the surface, resulting in more stable configurations with significantly larger migrations energies. This may also support the unusual, but consistently observed, features in the STS of extrinsic defects in graphene on SiC(0001) (see below) in which resonance peaks can be seen in the conduction band of all spectra; such features are not observed in spectra obtained from defective graphite or intrinsic defects in graphene. However, without further measurements, this explanation is purely speculative.

With the agglomeration of defects on graphene terraces shown to be highly unfavourable due to the increased stability, it is perhaps unsurprising that this behaviour is also observed at step edges with no differences in concentration or defect size. This differs once again with graphite in which defects were observed to cluster preferentially at steps leading to large structures decorating the graphite edge, as seen above. Unlike on graphite, graphene layers are continuous across SiC steps, which most likely reduces the effectiveness of steps to act as defect sinks, as the increased reactivity presented by the step edge is diminished by the graphene shielding any dangling bonds. However, this is most likely a secondary effect as the lack of defect mobility on terraces would suggest that movement towards steps is suppressed, preventing agglomeration at these points.

Defect Alignment

Figure 6.15 shows the angular intensity distributions obtained from defective graphene grown on SiC(0001) before annealing (a), after annealing at 300 °C for four hours (b) and after annealing for twenty four hours at 750 °C. As expected, before any
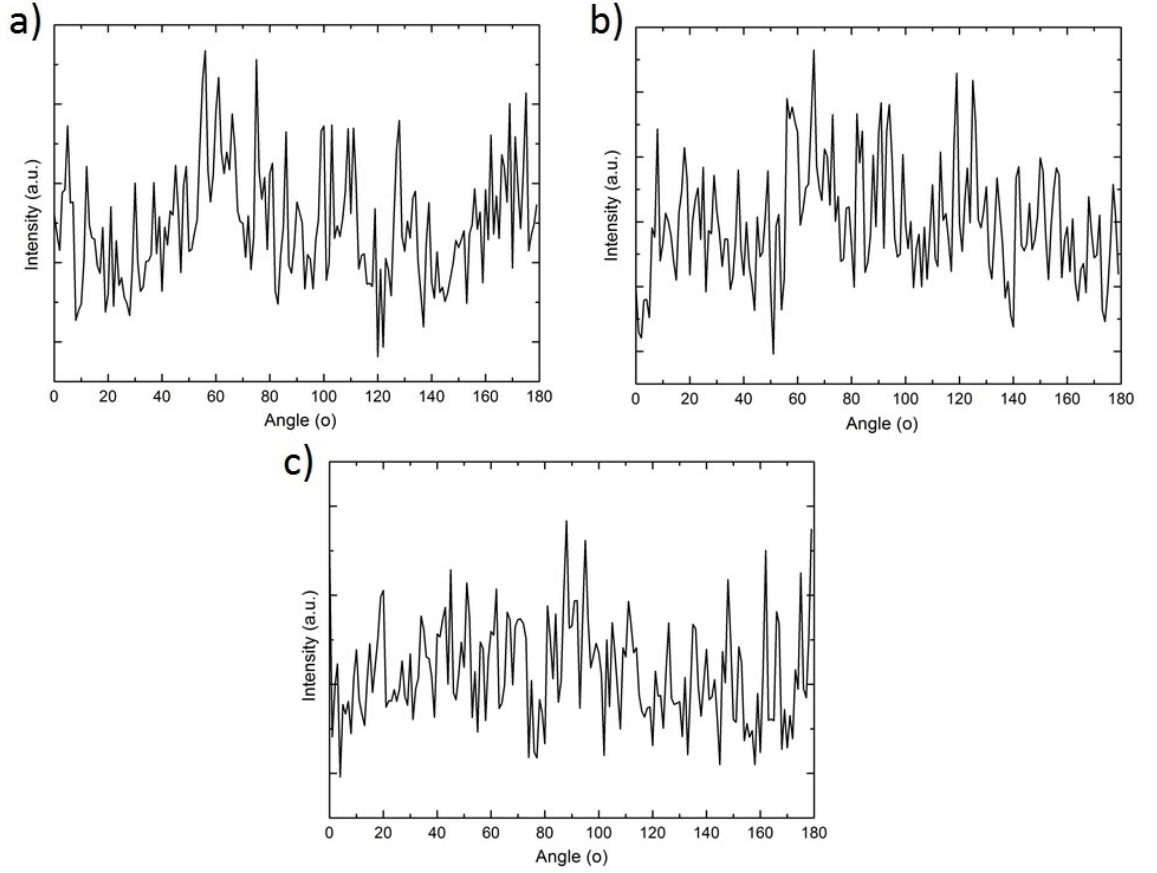
Figure 6.15: Angular intensity distributions produced from STM images of defective graphene on SiC(0001) (a) before annealing. (b) After annealing at 300 °C for 4 hours. (c) After annealing at 750 °C for 24 hours.

annealing was performed, the distribution shows no preferential alignment of defects, due to no significant mobility at room temperature, as is also seen in the case of graphite. After annealing at 300 °C for four hours, angular intensity profiles still show no clear peaks (Fig. 6.15(b)), indicating that no preferential alignment of defects has occurred over the course of the heating step. This is in keeping with the behaviour outlined above, in which no defect agglomeration was observed, suggesting that other than small amounts of recombination, defects are static on the surface. Further evidence supporting this can be seen in figure 6.15(c), in which the profile obtained after annealing at 750 °C for 24 hours again shows no clear preferential alignment of defects. This differs significantly from graphite in which clear alignment of defects can be observed, most likely due to clustering at grain boundaries.

It can be concluded therefore, that despite the many similarities in structure between FLG and graphite, significant differences are apparent in the behaviour of

extrinsic defects. This variation in behaviour is apparent in the relative stability of defects on the two surfaces upon annealing, with smaller defects on graphite observed to be highly mobile resulting in larger agglomerations. In contrast, defects in graphene grown on SiC(0001) were found to be significantly more stable, and remained static on the surface despite annealing for 24 hours at 750 °C. The source of the increased stability of defects is as yet unknown, however, possible explanations were discussed, and where appropriate, dismissed. Furthermore, on graphite, alignment of defects was observed upon annealing at high temperatures for long periods of time, whereas this was not observed on graphene, which is also attributed to the increased stability of defects on the surface.

STS of Defects

Figure 6.16(a) shows one of the two more common types of intrinsic defect that formed during the growth of graphene on SiC(0001). The pristine graphene lattice and $(6\sqrt{3} \times 6\sqrt{3})R30°$ reconstruction can be clearly observed in the background. Furthermore, the $(\sqrt{3} \times \sqrt{3})$ electronic distortion can also be observed in close proximity to the defect site [3]. The defect appears slightly elongated compared to some other defects suggesting a possible 2-hexagon dimer reconstruction, however, without higher resolution imaging, the exact defect nature is unknown [54]. STS spectra were obtained from both pristine areas and on the defect structure (Fig. 6.16). The STS spectrum acquired from the pristine regions of the graphene lattice show a point of minimal conductance at the Fermi level; contrary to the electronic structure of isolated graphene in which the conductance drops to exactly zero at the Dirac point, the spectrum exhibits a small conductance at E_F which is indicative of graphene grown on SiC [58]. Furthermore, the shape of the LDOS shows similarities with that observed for graphite rather than isolated graphene, exhibiting an approximately parabolic LDOS compared to the linear structure expected for graphene. This indicates that as the thickness of graphene reaches ∼3 ML the electronic structure resembles that of graphite strongly, though many of graphene's properties remain. It is important to note that the STS obtained from different areas of the $(6\sqrt{3})R30°$ reconstruction do not result in any significant change in the conductance obtained, as seen previously by Rutter *et al.* [3].

When studying the defect structure in figure 6.16(a), no increase in the LDOS is observed at the Fermi level indicating that, much like the defects in graphite discussed above, no dangling bonds remain which would result in increased conduc-
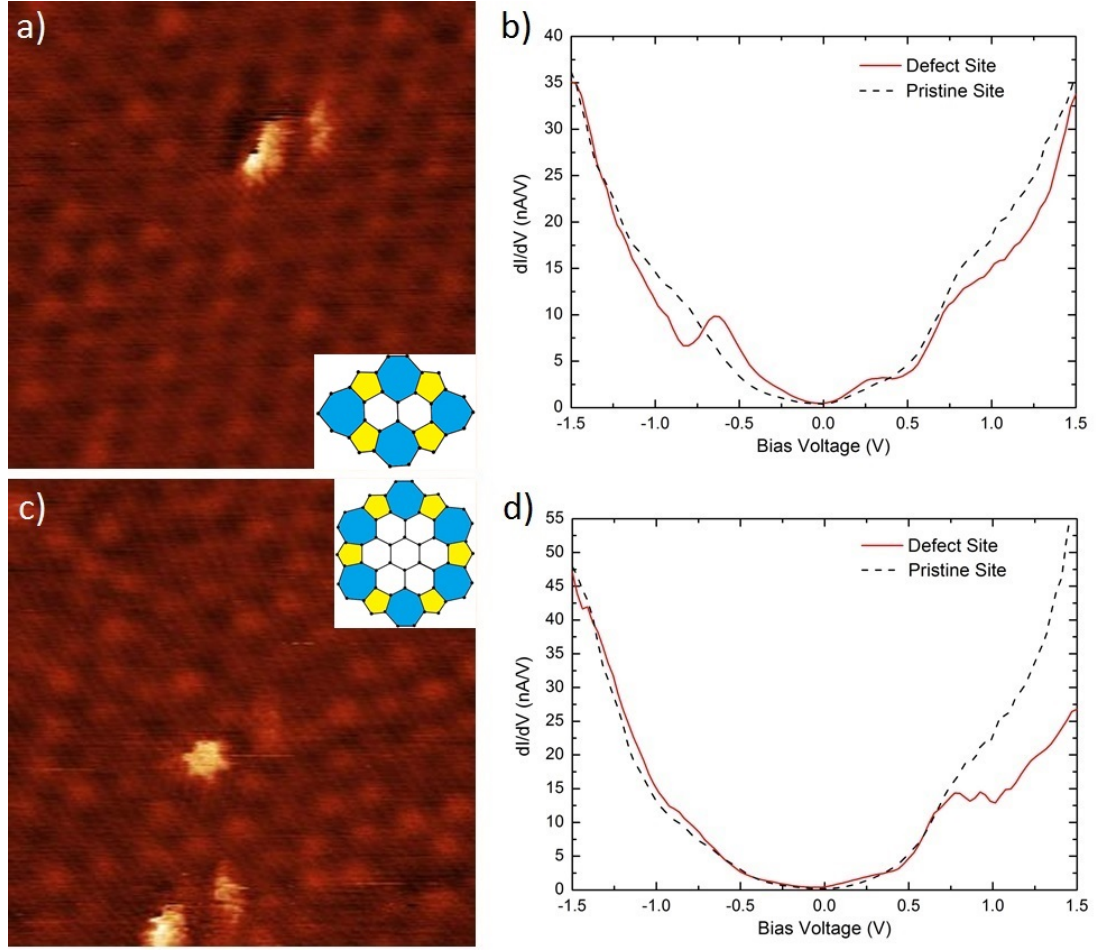
Figure 6.16: (a) 20 nm^2 STM image of an intrinsic long defect structure on graphene grown on SiC(0001), the surrounding pristine lattice also shows $(6\sqrt{3} \times 6\sqrt{3})R30°$ reconstruction (V_{bias}=0.6 V, I=1.6 nA). (Inset) Atomic model of 2-hexagon addimer. (b) STS Spectra obtained from the defect (red/whole) and pristine (black/dashed) sites in image (a). (c) 20 nm^2 image of a singular "flower" defect on graphene grown on SiC (V_{bias}=0.6 V, I=1.6 nA). (Inset) Atomic model of "flower" defect. (d) STS spectra from the "flower" defect (red/whole) and the pristine lattice observed in image (c).

tance [59]. Despite similarities with the spectra obtained for the pristine graphene site, a number of electronic features specific to the defect can be identified. Firstly, in close proximity to E_F the conductance rises sharply at negative voltage biases, whilst at positive biases an increase is also observed, but to a much smaller degree. The increased conduction observed mimics that seen from some of the extrinsic defects on graphite (see section 6.3.1), attributed predominantly to vacancies [52]. The increased LDOS close to the Fermi level was proposed to have arisen from the restructuring of the well ordered lattice into a more disordered state, resulting from the presence of the vacancy [50]. Due to the structural similarities between few-layer graphene and graphite, as discussed above, a comparable mechanism may be acting

here.

Despite these similarities, upon moving to larger biases both positive and negative, further features that were not typically observed on graphite arise. Firstly, a rise in the LDOS can be observed at ∼0.6 eV followed shortly after by a sudden drop (V_{bias} = 0.75 eV). This feature differs significantly from the usual graphene spectrum in which no such excursions are observed, indicating that states have been simultaneously introduced and removed by the presence of the defect. Although, this feature has not previously been observed experimentally, theoretical work by Wehling *et al.* has observed similar features arising due to the presence of impurities [60, 61]. Single impurities were found to produce a resonance in the LDOS within 1 V of the Dirac point. The subsequent drop in the LDOS shortly after this is proposed to result from the localisation of the impurity states on a different sublattice site to that of the impurity atom/molecule itself. The impurity site is proposed to produce a significant reduction in the LDOS, which may result in the lower excursion observed. Therefore, it is possible that these properties result from the production of a vacancy type defect during initial bombardment followed by residual impurity gases in the chamber such as H_2 or CO binding at these sites.

Contrary to the structure in figure 6.16(a), the "flower" defect observable in 6.16(c) shows significantly different properties. The STM image in figure 6.16(c) once again shows the graphene lattice with $(6\sqrt{3})R30°$ reconstruction with a single six-fold symmetric "flower" defect, which exhibits Friedel oscillations due to scattering. The STS spectra from this type of defect was found to closely resemble that from the pristine graphene lattice, especially at negative biases and with both spectra reaching a minima at the Fermi level (Fig. 6.16(d)). This close resemblance continues at positive biases up to ∼0.75 V at which point a significant drop off is observed in the defect DOS. This loss in conductivity suggests that the presence of the defect reduces the number of states available in the sample which electrons from the STM tip can tunnel into, whilst conversely tunnelling from the surface to the STM tip is unchanged. The suppression of empty states in the vicinity of the defect and with this particular reconstruction is only observed on graphene on SiC, which may suggest the substrate is involved in the loss in conductivity. However, without significant theoretical study firm conclusions cannot be drawn at this time.

Figure 6.17(a) shows an area of graphene grown on SiC(0001) after ion bombardment. Pristine regions of the graphene lattice remain after the bombardment whilst large defect structures also cover larger proportions of the surface. STS of
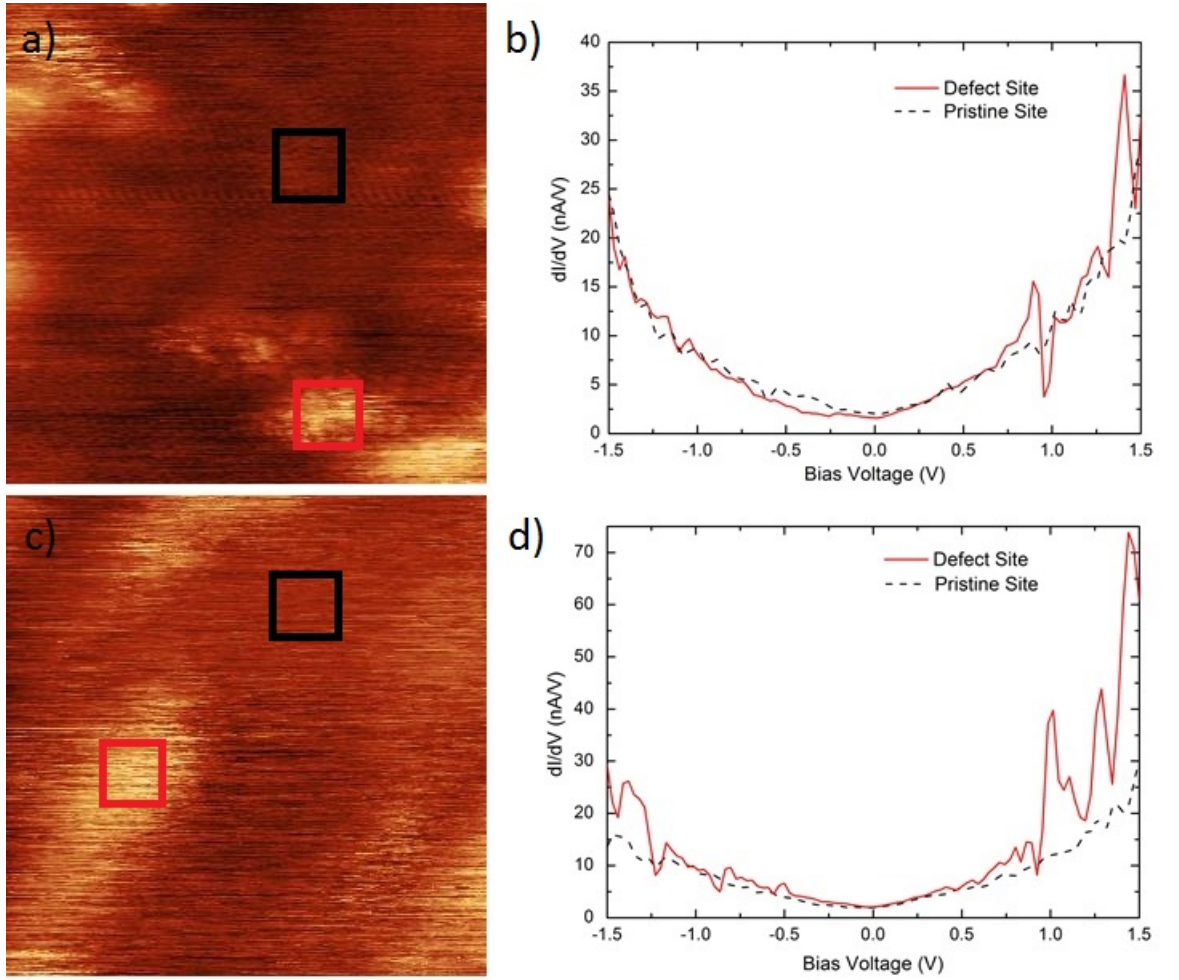
Figure 6.17: (a) 10 nm^2 STM image of graphene on SiC(0001) after ion bombardment, exhibiting both pristine and defective areas (V$_{bias}$=0.6 V, I=1.6 nA). (b) STS spectra obtained from pristine (black square) and defective (red square) regions of the bombarded graphene sample in (a). (c) 10 nm^2 image of a further area of the defective graphene sample (V$_{bias}$=0.6 V, I=1.6 nA). (d) STS spectra obtained from the pristine and defective areas of (c).

the pristine graphene regions (black rectangle) were found to produce identically shaped spectra to that seen before bombardment indicating that despite large areas of the lattice being damaged the LDOS in "clear" regions was not affected. STS obtained from defective areas however, showed significant modification compared to pristine regions. Although, the typical graphene spectra was followed quite closely at low biases (±0.5 V) with a parabolic dispersion and the expected minimum conductivity observed at the Fermi level, at larger biases new features can be observed (Fig. 6.17(b)). Specifically, at positive biases a resonance was regularly observed at ∼1.0 V, characterised by a sharp jump in conductivity followed by a rapid drop, thereafter returning to typical levels. A further resonance was also observed at larger positive biases, ∼1.4 eV. However at negative biases the spectra show no such fea-

tures and follows the pristine graphene spectrum closely. With the LDOS remaining close to zero at E_F, the presence of dangling bonds can once again be discounted with no new states observed at the Fermi level [62, 63].

Some similarities with a study by Ugeda *et al.* can be observed, whose simulations of di-vacancy defects on graphene produce STS spectra showing empty state resonances at ∼150 mV [30]. However, despite a similar shape being observed the resonance observed here is found significantly further from the Fermi level. Furthermore, larger defects appear to result in an amplification of the features observed in the smaller defects with the peaks in conductivity observed at positive biases increasing substantially in amplitude. Also, whereas intrinsic defects observed previously on graphene on SiC were found to come in multiple different forms, resulting in significantly different STS spectra, the defects produced via ion bombardment showed far less variation, with all spectra exhibiting sharp jumps in conductivity at positive biases, though with different levels of intensity. This indicates that the irradiation process predominantly forms defects with similar structures, at least electronically. This is perhaps surprising due to the possibility of sputtering Si from the substrate below, which would be expected to result in significantly different STS spectra to that of purely carbon reconstructions. The peaks in conductivity observed also show a number of similarities with those outlined by Lherbier *et al.* in their theoretical study, which produced resonant peaks in the conductance band of graphene due to the presence of Stone-Wales and 555-777 defects [64]. However, these simulations were conducted for a single layer of isolated graphene, rather than FLG on SiC, therefore, without atomic resolution of the defect structures is unknown whether similar defect structures and resultant DOSs are produced.

6.4   Conclusions

In this chapter, the results of irradiating graphite and graphene with low energy Ar^+ ions to produce extrinsic defects was reported. The defective samples were then heated at various temperatures and the evolution of the defects was observed. On graphite the defects were found to cluster significantly after annealing at 300 °C for four hours, whilst similar results were observed after annealing at 500 °C. Defect agglomeration at these temperatures was attributed to the migration of smaller defects such as mono-vacancies, adatoms and interstitials, which upon coming into contact with other larger more static defects, form clusters. The increased defect

structure size was found to occur in conjunction with a reduction in concentration, suggesting that recombination of vacancies and adatoms also occurs at elevated temperatures. Annealing at 750 °C was found to result in further agglomeration, with the average defect size found to be larger than that seen at lower temperatures. The further increase in defect cluster size may be attributed to Ostwald ripening, in which larger defects will grow at the expense of smaller ones, most likely through the emission of small defects such as interstitials and adatoms. Increased anneal time was not found to particularly affect defect size at 300 °C and 500 °C with no further growth observed in defects with increasing time. However, annealing for longer periods at 750 °C resulted in a substantial increase in defect size, with a significant drop in defect concentration compared with lower temperature anneals and shorter annealing times. These much larger defect structures support the notion that Ostwald ripening of defects is occurring. Finally, defects were found to cluster preferentially at step edges at all temperatures, which is assigned to the step providing an energy barrier to defect diffusion, pinning defects in place. Defect agglomeration at steps was found to follow similar behaviour to that observed on terraces, with the average defect size increasing after annealing at 300 °C and 750 °C.

Defects were also found to align on the graphite surface; angular distributions obtained from defective regions show 1 ± 1 peaks per 300 nm^2 scan area, suggesting preferential immobilisation at certain regions. The alignment observed is attributed to the migration of defects and their subsequent clustering at grain boundaries. As defective regions of the graphite lattice, grain boundaries pose a significant barrier to further diffusion, with a high probability that defects that encounter these boundaries agglomerate with existing non six-membered rings to produce stable defect configurations. RS was used to determine the average graphite grain size of the HOPG used. A grain size of 550 ± 80 nm was determined, suggesting that at least one grain boundary is likely to be present in the typical 300 nm^2 images, further supporting the idea that defects become pinned once encountering a boundary, leading to alignment.

STS performed on bombarded graphite showed that defect agglomerations produced significant changes to the LDOS. These modifications were separable into two distinct categories; asymmetric increases in the LDOS in both valence and conduction bands and a symmetric increase in the LDOS in close proximity to the Fermi energy. The changes observed in the STS spectra are likely to result from the reconstruction of the lattice in proximity of the defect, whilst the lack of states observed at E_F suggested that no dangling bonds remained. The asymmetries observed in

some spectra are tentatively assigned to the binding of H_2 or CO to dangling bonds, but complete lattice reconstruction via the formation of non six-memebered rings is not ruled out. The second category of defects are proposed to consist predominantly of vacancies which modify the graphite π band resulting in the creation of new states. The presence of adatoms and interstitials within these agglomerations is not ruled out, however, previous theoretical studies support the notion that vacancies are likely to produce the STS spectra with similar features.

Intrinsic defects on graphene grown on SiC(0001) prior to ion bombardment were also investigated upon annealing. Intrinsic defects were not found to migrate at any of the annealing temperatures investigated. The significant stability presented by these defects is attributed to their formation at much higher temperatures during the growth, which allows for larger stable configurations to form. The defects observed vary in size and shape, however two types of structure occur more commonly, an elongated defect with a possible 2-hexagon dimer reconstruction, and the hexagonally symmetric "flower" defect. STS spectra on elongated defects showed increases in the LDOS in close proximity to the Fermi level with resonance peaks also visible at negative biases. This feature shared some similarities with the defects observed on graphite, thereby suggesting a similar structure predominantly made up of vacancies, lending weight to the proposed 2-hexagon dimer reconstruction reported elsewhere [54]. Conversely "flower" defects were found to result in a suppression of the empty graphene states in its vicinity. The cause for this suppression was not determined, as this defect has not been observed on other graphene-substrate systems and the SiC substrate may play a role in the reduced conductivity in these defect areas.

Extrinsic defects on graphene were found to differ significantly from those produced in graphite, with significantly increased stability observed. Defects were not found to move, even upon annealing to temperatures up to 750 °C for 24 hours. Defect concentration was found to drop upon annealing at all temperatures, with the rate of decrease found to slow after longer periods at high temperatures, which is attributed to the recombination of vacancy-interstitial pairs upon annealing. The reason for the decreased mobility of defects on the surface remains unknown. Possible explanations of Si incorporation into defects, changes to the surface energy landscape due to damage to the buffer layer and modifications to the electronic structure were outlined and critically appraised. Also in contrast to graphite, no alignment or agglomeration at steps was observed in graphene, attributed to the lack of defect mobility.

Finally, STS performed on extrinsic defects contrasted the results observed for both graphite extrinsic and graphene intrinsic defects, with all spectra exhibiting resonance peaks at positive voltage biases. Once again no significant increase in states was observed at the Fermi level, however the spectra showed some similarities with previous studies on graphene which observed similar peaks in conductivity in proximity to Stone-Wales and 555-777 defects. Despite this evidence, significant further theoretical and experimental work is required to further determine the nature of these defect agglomerations.

6.5   References

[1] A. Hashimoto, K. Suenaga, A. Gloter, K. Urita and S. Iijima, *Nature*, **430**(7002), 870–873 (2004).

[2] E. Loginova, S. Nie, K. Thürmer, N. C. Bartelt and K. F. McCarty, *Phys. Rev. B*, **80**(8), 085430 (2009).

[3] G. M. Rutter, N. P. Guisinger, J. N. Crain, E. A. A. Jarvis, M. D. Stiles, T. Li, P. N. First and J. A. Stroscio, *Phys. Rev. B*, **76**(23), 235416 (2007).

[4] N. King, Q. Xue, C. Ling, T. Z. M. Shan, X. Zhou and Z. Jiao, *RSC Adv.*, **2**(24), 9124–9129 (2012).

[5] A. Zandiatashbar, G.-H. Lee, S. J. An, S. Lee, N. Mathew, M. Terrones, T. Hayashi, C. R. Picu, J. Hone and N. Koratkar, *Nature Comm.*, **5**, 3186 (2014).

[6] A. V. Krasheninnikov and F. Banhart, *Nature Mater.*, **6**(10), 723–733 (2007).

[7] M. T. Lusk, D. T. Wu and L. D. Carr, *Phys. Rev. B*, **81**(15), 155444 (2008).

[8] M. T. Lusk and L. D. Carr, *Phys. Rev. Lett.*, **100**(17), 175503 (2010).

[9] R. H. Telling and M. I. Heggie, *Philos. Mag.*, **87**(31), 4797–4846 (2007).

[10] D. Ugarte, *Nature*, **359**(6397), 707–709 (1992).

[11] F. Banhart and P. M. Ajayan, *Nature*, **382**(6590), 433–435 (1996).

[12] F. Banhart, *Rep. Prog. Phys.*, **62**(8), 1181–1221 (1999).

[13] H. W. Kroto, J. R. Heath, S. C. O'Brien, R. F. Curl and R. E. Smalley, *Nature*, **318**(6042), 162–163 (1985).

[14] S. Iijima, *Nature*, **354**(6348), 56–58 (1991).

[15] M. Sammalkorpi, A. Krasheninnikov, A. Kuronen, K. Nordlund and K. Kaski, *Phys. Rev. B*, **70**(24), 245416 (2004).

[16] B. Peng, M. Locascio, P. Zapol, S. Li, S. L. Mielke, G. C. Schatz and H. D. Espinosa, *Nature Nanotechnol.*, **3**(10), 626–631 (2008).

[17] B. Guo, Q. Liu, E. Chen, H. Zhu, L. Fan and J. R. Gong, *Nano Lett.*, **10**, 4975–4980 (2010).

[18] H. Wang, Q. Wang, Y. Cheng, K. Li, Y. Yao, Q. Zhang, C. DOng, P. Wang, U. Schwingenögl, W. Yang and X. X. Zhang, *Nano Lett.*, **12**(1), 141–144 (2012).

[19] L. Tapasztó, G. Dobrik, P. Nemes-Incze, G. Vertesy, P. Lambin and L. P. Biró, *Phys. Rev. B*, **78**(23), 233407 (2008).

[20] A. W. Robertson, C. S. Allen, Y. A. Wu, K. He, J. Olivier, J. Neethling, A. I. Kirkland and J. H. Warner, *Nature Comm.*, **3**(1144), 1–7 (2012).

[21] A. W. Robertson and J. H. Warner, *Nanoscale*, **5**, 4079–4093 (2013).

[22] A. W. Robertson, G.-D. Lee, K. He, E. Yoon, K. A and J. H. Warner, *Nano Lett.*, **14**(3), 1634–1642 (2014).

[23] A. W. Robertson, G.-D. Lee, K. He, E. Yoon, A. I. Kirkland and J. H. Warner, *Nano Lett.*, **14**(7), 3972–3980 (2014).

[24] Q. Chen, A. W. Robertson, K. He, C. Gong, E. Yoon, G.-D. Lee and J. H. Warner, *ACS Nano*, **9**(8) (2015).

[25] P. A. Thrower and R. M. Mayer, *Physica Sta. Sol. A*, **47**(1), 11–37 (1978).

[26] J. D. Wadey, A. Markevich, A. Robertson, J. Warner and A. I. K. E. Besley, *Chem. Phys. Lett.*, **648**, 161–165 (2016).

[27] P. Lehtinen, A. S. Foster, A. Ayuela, A. Krasheninnikov, K. Nordlund and R. Nieminen, *Phys. Rev. Lett.*, **91**(1), 017202 (2003).

[28] O. V. Yazyev, *Rep. Prog. Phys.*, **73**(5), 056501 (2010).

[29] O. V. Yazyev, I. Tavernelli, U. Rothlisberger and L. Helm, *Phys. Rev. B*, **75**(11), 1–5 (2007).

[30] M. M. Ugeda, I. Briuega, F. Hiebel, P. Mallet, J.-Y. Veuillen, J. M. Gómez-Rodríguez and F. Ynduráin, *Phys. Rev. B*, **85**(12), 121402 (2012).

[31] Y. Kobayashi, K. Kusakabe, K.-I. Fukui and T. Enoki, *Physica E*, **34**(1-2), 678–681 (2006).

[32] T. Matsui, H. Kambara, Y. Niimi, K. Tagami, M. Tsukada and H. Fukuyama, *Phys. Rev. Lett.*, **94**(22), 226403 (2005).

[33] K. I. Bolotin, K. J. Sikes, Z. Jiang, M. Kilma, G. Fudenberg, J. Jone, P. Kim and H. L. Stormer, *Solid State Comm.*, **146**(9-10), 351–355 (2008).

[34] S. V. Morozov, K. S. Novoselov, M. I. Katsnelson, F. Schedin, D. C. Elias, J. A. Jaszczak and A. K. Geim, *Phys. Rev. Lett.*, **100**(1), 016602 (2008).

[35] M. M. Ugeda, D. Fernádez-Torre, I. Brihuega, P. Pou, A. J. Martínez-Galera, R. Pérez and J. M. Gómez-Rodríguez, *Phys. Rev. Lett.*, **107**(11), 116803 (2011).

[36] H. C. A. J. Bard, *Langmuir*, **7**(6), 1143–1153 (1991).

[37] J. F. Ziegler, Transport of ions in matter (2013).

[38] J. Hass, J. E. Millán-Otoya, P. N. First and E. H. Conrad, *Phys. Rev. B*, **78**(20), 205424 (2008).

[39] H. A. Mizes and J. S. Foster, *Science*, **244**(4904), 559–562 (1989).

[40] J. R. Hahn and H. Kang, *Phys. Rev. B*, **53**(4), 1725–1728 (1996).

[41] J. R. Hahn and H. Kang, *Phys. Rev. B*, **60**(8), 6007–6017 (1999).

[42] C. P. Ewels, R. H. Telling, A. A. El-Barbary and M. I. Heggie, *Phys. Rev. Lett.*, **91**(2), 025505 (2003).

[43] L. M. Brown, A. Kelly and R. M. Mayer, *Philos. Mag.*, **19**(160), 721–741 (1969).

[44] A. A. El-Barbary, R. H. Telling, C. P. Ewels, M. I. Heggie and P. R. Briddon, *Phys. Rev. B*, **68**(14), 144107 (2003).

[45] K. Niwase, *Phys. Rev. B*, **52**(15), 785–798 (1995).

[46] P. Y. Huang, C. S. Ruiz-Vargas, A. M. van der Zande, W. S. Whitney, M. P. Levendorf, J. W. Kevek, S. Garg, J. S. Alden, C. J. Hustedt, Y. Zhu, J. Park, P. L. McEuen and D. A. Muller, *Nature*, **469**(7330), 389–392 (2011).

[47] F. Tuinstra and J. L. Koenig, *J. Chem. Phys.*, **53**(3), 1126–1130 (1970).

[48] C. Bena, *Phys. Rev. Lett.*, **100**(7), 076601 (2008).

[49] T. Kostyrko, M. Bartkowiak and G. D. Mahan, *Phys. Rev. B*, **60**(15), 10735–10738 (1999).

[50] R. Schlögl, *Surf. Sci.*, **189-190**, 861–872 (1987).

[51] P. Reinke and P. Oelhafen, *J. Chem. Phys.*, **116**(22), 9850–9855 (2002).

[52] H. Fukutani, A. Yamada, K. Yagi, S. Ooe, K. Higashiyama, H. Kato and T. Iwata, *J. Phys. Soc. Jap.*, **59**(9), 3089–3092 (1990).

[53] D. Orlikowski, M. B. Naqrdelli, J. Bernholc and C. Roland, *Phys. Rev. Lett.*, **83**(20), 4132–4135 (1999).

[54] E. Cockayne, *Phys. Rev. B*, **85**(12), 125409 (2012).

[55] W. A. de Heer, C. Berger, X. Wu, P. N. First, E. H. Conrad, X. Li, T. Li, M. Sprinkle, J. Hass, M. L. Sadowski, M. Potemski and G. Martinez, *Solid State Commun.*, **143**(1-2), 92–100 (2007).

[56] T. Hopf, K. V. Vassilevski, E. Escobedo-Cousin, N. G. Wright, A. G. O'Neill, A. B. Horsfall, J. P. Goss, A. Barlow, G. H. Wells and M. R. C. Hunt, *Mater. Sci. Forum*, **778-780**, 1154–1157 (2014).

[57] M. L. Bolen, S. E. Harison, L. B. Biedermann and M. A. Capano, *Phys. Rev. B*, **80**(11), 115433 (2009).

[58] S. Y. Zhou, G.-H. Gweon, A. V. Fedorov, P. N. First, W. A. de Heer, D.-H. Lee, F. Guinea, A. H. C. Neto and A. Lanzara, *Nature Mater.*, **6**(10), 770–775 (2007).

[59] V. M. Pereira, F. Guinea, J. M. B. L. dos Santos, N. M. R. Peres and A. H. C. Neto, *Phys. Rev. Lett.*, **96**(3), 27–30 (2006).

[60] T. O. Wehling, A. V. Balatsky, M. I. Katsnelson, A. I. Lichtenstein, K. Scharnberg and R. Wiesendanger, *Phys. Rev. B*, **75**(12), 125425 (2007).

[61] Y. V. Skrypnyk and V. M. Loktev, *Phys. Rev. B*, **73**(24), 241402 (2006).

[62] M. A. H. Vozmediano, M. P. López-Sancho, T. Stauber and F. Guinea, *Phys. Rev. B*, **72**(15), 155121 (2005).

[63] M. M. Ugeda, I. Brighuega, F. Guinea and J. M. Gómez-Rodríguez, *Phys. Rev. Lett.*, **104**(9), 096804 (2010).

[64] A. Lherbier, S. M.-M. Dubois, X. Declerck, Y.-M. Niquet, S. Roche and J.-C. Charlier, *Phys. Rev. B*, **86**(7), 075402 (2012).

Chapter 7

Hot and Cold Wall Graphene Growth on Cu Foils

This chapter describes initial experiments performed to optimise the growth of graphene via Hot-wall and Cold-wall CVD. A preliminary exploration of the effects of growth time and Cu substrate was performed. Graphene samples produced by both methods were studied with EBSD to determine the effect Cu surface orientation has on graphene formation.

7.1 Introduction

As discussed in Chapter 1, many different growth methods have been developed to produce high quality graphene. One such method, also outlined in Chapter 1, is Chemical Vapour Deposition (CVD) on metal substrates, particularly copper. First performed in 2009 by Li *et al.*, this method has since become the most commonly used approach to growing graphene [1]. As such, significant optimisation of each aspect of the growth process has also been performed, with in depth studies undertaken to determine the effects of the concentration of hydrogen in the local atmosphere [2], growth temperature [3], growth time [4,5], carbon precursor gas [6] and many other variables. This optimisation has resulted in the reproducible growth of high quality graphene in straight edged hexagonal domains with consistent orientations and negligible defect concentrations [4]. Consequently, a number of studies have now aimed to describe the growth kinetics of graphene on Cu, including the initial adsorption, dissociation and diffusion of carbon atoms on the surface [6,7]. However, the current models provide differing mechanisms for how graphene growth proceeds, indicating that thorough further discussion is required to confirm or disprove the current approaches.

It is known, however, that the growth of graphene on Cu substrates is highly dependent on the extent of the decomposition of the carbon precursor gas on the surface, as well as the subsequent diffusion of carbon atoms and nucleation to form islands [7,8]. During the CVD process, depending on a number of factors, particularly methane and hydrogen partial pressures, the Cu surface can become undersaturated, saturated or supersaturated [8]. In the first case, insufficient carbon decomposes on the surface resulting in no carbon nucleation. In contrast, when the surface is saturated, sufficient carbon is present on the surface leading to nucleation and graphene growth. In this situation, graphene islands of a finite size are produced, however, not enough carbon is present to form a complete layer. In the final case in which the surface becomes supersaturated, sufficient decomposition has occurred which leads to the production of a complete graphene monolayer. Careful optimisation of the growth parameters can therefore allow complete graphene films or isolated islands to be grown.

Although a large proportion of growth optimisation has focussed on the precursor gases and temperature conditions used, the Cu substrate was also found to be quite significant, with the crystal face upon which growth was performed found to result in very different graphene quality and growth rates [9,10]. Furthermore, the

presence of defects and other structures such as steps, were found to be associated with a large degree of variation in graphene growth dynamics, shape and thickness [4,11–15]. This has subsequently led to research into how to control the rate of nucleation on Cu substrates [16], with some methods even using liquid Cu surfaces as a means to eliminate grain boundaries and reduce nucleation density [17, 18]. These studies have predominantly focussed on which Cu faces lead to the highest quality graphene growth [3, 9, 15, 19, 20], however the effects of higher index faces and polycrystalline surfaces are not completely understood, suggesting that further research into these areas might provide valuable insights into the key factors that affect graphene growth.

The majority of the studies discussed above utilise a "hot-wall" growth method, in which the entire chamber is heated to the synthesis temperature, due to the simplicity of the experimental setup and the consistency of the graphene produced. However, this method can lead to increased contamination from material desorbing from the chamber walls, reducing the quality of the graphene produced. An alternative approach, which has been seen less in the literature [3, 21–23], is the use of highly localised heating, in which only the sample is raised to the growth temperature, whilst the rest of the chamber remains cool; this method is referred to as "cold-wall" growth. As the chamber walls remain cool, a significant potential source of contamination is removed, suggesting that further improvements in graphene quality might be achieved. Increased cleanliness is combined with significantly reduced processing times, as a result of the rapid sample cooling, leading to an increase in the rate at which graphene can be produced [24]. Such advantages suggest that growth via this method may provide a more industrially compatible process from which large scale graphene may be grown. Therefore, although some research has been conducted into the growth of graphene via cold-wall synthesis, a complete optimisation of the growth is still required, combined with detailed modelling of the kinetic process.

In this chapter, Scanning Electron Microscopy (SEM) was utilised to study graphene grown by hot-wall and cold-wall CVD methods for various growth times on Cu foils and evaporated Cu substrates. The samples produced by these methods were then studied with Electron Back-Scatter Diffraction to further investigate the effect Cu surface has on the quality of graphene.

7.2   Experimental

Graphene films were grown on 99.9% pure Cu foils 0.2 mm thick. The cleaning method is outlined in Chapter 3, in which Cu foils were cut and then chemically cleaned with isopropyl alcohol (IPA) followed by further cleaning with acetic acid. Figure 7.1 shows the substrate before (a) and following (b) the cleaning steps outlined. A significant colour difference can be observed, with the sample exhibiting the typical Cu colouring before cleaning followed by a pinkish tint afterwards indicating that the CuO on the surface has been successfully etched away. Rapid introduction to the growth systems helped minimise the level of oxidation and atmospheric contamination of the samples, though some exposure was unavoidable. Once introduced to the sample chambers, further sample preparation in the form of high temperature annealing in a 5% H_2/Ar_2 atmosphere was conducted. In the hot-wall growth system the annealing time, annealing temperature and gas flow were kept constant at 60 minutes, 1000 °C and 50 sccm respectively. The anneal in a hydrogen atmosphere for an extended period was found to smooth the surface significantly by further etching the Cu allowing for higher quality graphene to be grown. A similar approach was also taken for cleaning in the cold-wall growth system with an annealing step at 1000 °C for one hour implemented, this was combined with a 5% H_2/Ar_2 at a chamber pressure of 5.0 mbar. All samples were cooled naturally by switching off the heating mechanism, this led to a cooling step of 4 hours in the hot-wall system and 30 minutes by the cold-wall system.
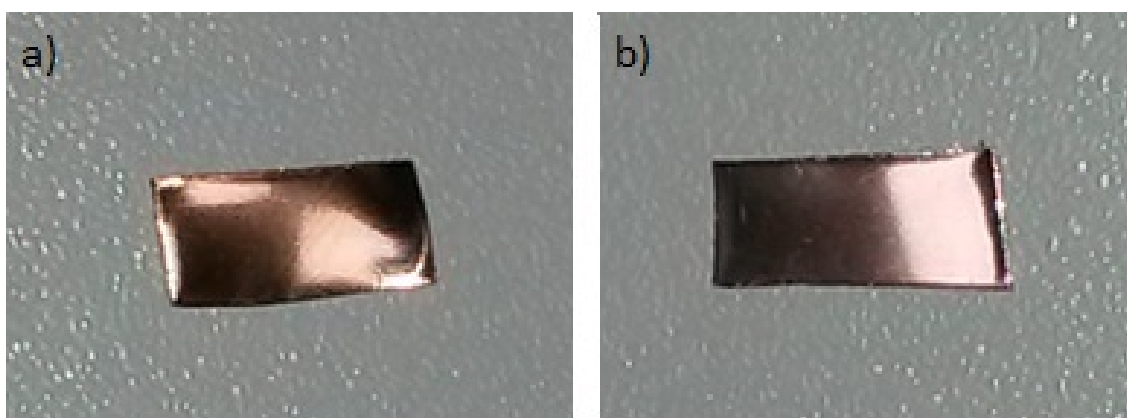

Figure 7.1: Cu substrates on which graphene was grown (a) before cleaning and (b) after cleaning.

Figure 7.2(a) shows an SEM image of graphene grown on a Cu sample, in which all regions appear identical, despite the presence of graphene on the surface. Therefore, in order to clearly discern the graphene islands which have grown from the

background of the Cu substrate, samples were annealed at 150 °C for 2 hours post-growth causing any areas uncovered by graphene to oxidise [25]. The oxidised Cu exhibits considerable roughness in comparison to the predominantly flat graphene islands, whilst also protruding significantly further from the surface, resulting in graphene islands appearing indented (Fig. 7.2(b)). Furthermore, the oxidation of the Cu substrate destroys the underlying step structure, whilst monolayer graphene formation on Cu preserves these steps, which can be clearly identified.
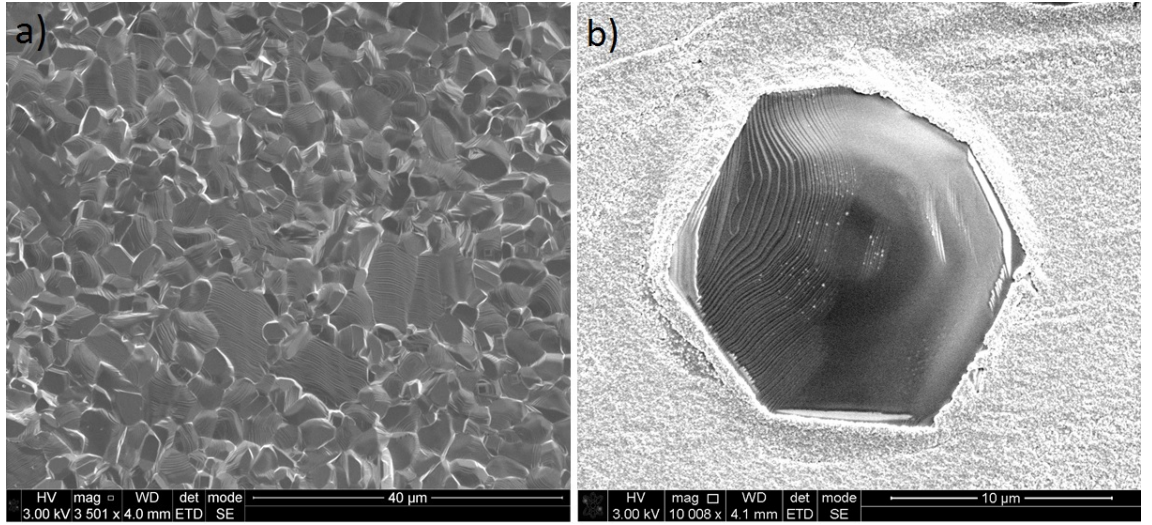
Figure 7.2: SEM images of graphene grown on Cu substrates (a) before annealing showing a grain like structure with no distinction between graphene and Cu at the surface. (b) After annealing showing a clear graphene island with Cu steps beneath surrounded by a significantly brighter area of CuO.

EBSD was performed on samples to identify the crystal structure of the Cu substrate beneath. A beam energy of E = 30 keV was used throughout to produce enough back-scattered electrons to obtain a significant Cu signal. Upon attaining an EBSD map of the surface, analysis was performed using the Tango software to determine the crystal face on which various graphene domains formed. However, some of the maps produced are slightly incomplete with small areas producing an insufficient signal to allow crystal structure to be identified. This often occurs in areas of significant height variation, due to the raised regions preventing back-scattered electrons from reaching the detector. At these points blank areas are produced in the EBSD maps, in cases where these areas are minor some extrapolation has been conducted which estimates the crystal structure at these points based on the surrounding crystal orientations. This allows a complete crystallographic map of the surface to be produced.

7.3 Results and Discussion

7.3.1 Hot-Wall Graphene Growth on Cu Foils
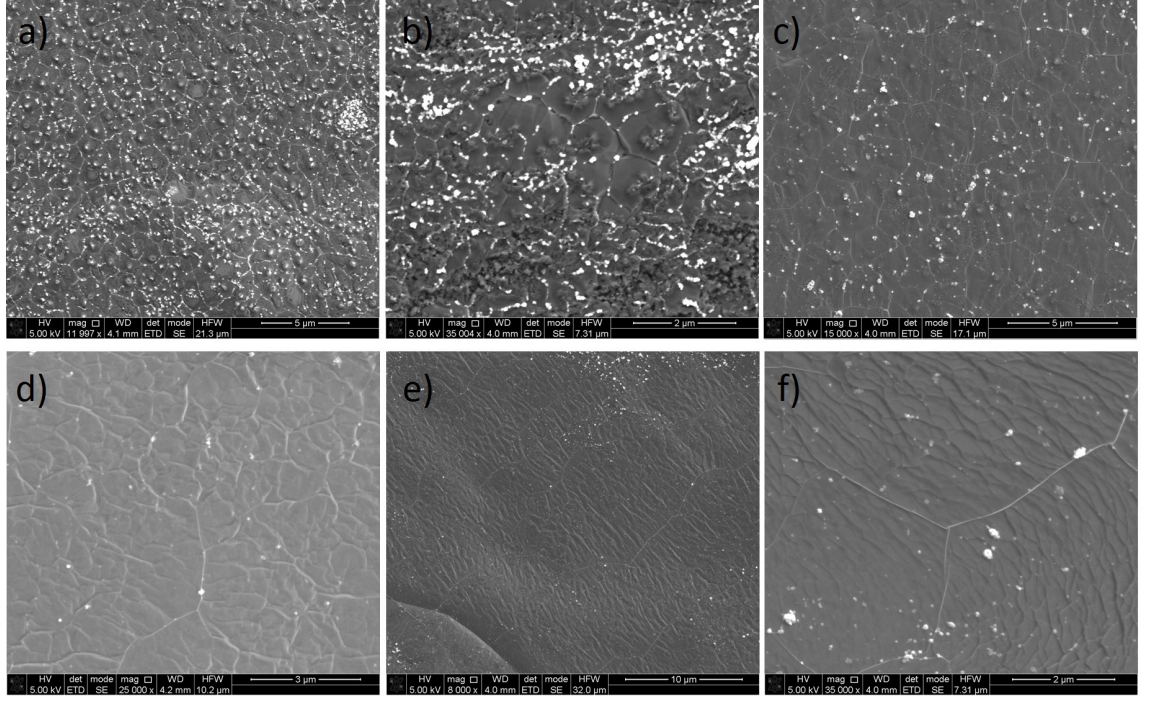
Figure 7.3: SEM images of graphene grown in the Hot-wall reactor for (a) 5 minutes, (b) 10 minutes, (c) 20 minutes, (d) 30 minutes and (e) 1 minute. (f) Close up image of a pleat defect junction.

Figure 7.3 shows graphene growth for various growth times under a flow of 30 sccm of CH_4, with 50 sccm of H_2/Ar_2. Fig. 7.3(a) shows graphene produced after a growth time of 5 minutes. Small irregular domains separated by lines of oxidation covered 95±2% of the surface with an average size of 1.2±0.5 μm^2. Oxidation along grain boundaries has previously been observed by Chen *et al.* and provides a simple method for determining the size of graphene grains on metals [25]. A large proportion (73%) of these domains exhibit "lump like" features, 0.03±0.01 μm^2 in area, towards the centre of the graphene flakes. These islands strongly resemble those observed by Paronyan *et al.* which are attributed to inhomogeneous graphene growth on rough areas of the substrate [26]. Upon increasing the growth time to 10 minutes, an increase in graphene quality can be observed with average domain size increasing to 2.1±0.5 μm^2, furthermore the proportion of these domains that show the "lump" structures is also reduced to ∼45% (Fig. 7.3(b)). This improvement in quality continues when the growth time is increased to 20 minutes with average graphene domain size increasing further to 3.6±1.5 μm^2, although an increased size

distribution is also observed (Fig. 7.3(c)). The overall shape of these domains also appears less irregular with many of the islands displaying a more hexagonal shape which is characteristic of high quality graphene [4,27]. After a 30 minute growth period a peak in graphene quality was found in which a pristine film was found to have formed over large proportions of the surface (Fig. 7.3(d)). The average grain size observed was found to increase significantly again to 15 ± 10 μm^2, although some domains were found to span areas as large as 40 μm^2. This increase in quality was corroborated by the first instances of graphene pleats, indicating that graphene sheets are now large enough to require the strain release by pleat formation. Further increases in growth time were not found to result in any further increase in quality, with negligible differences observed between growth for 30 minutes, and growth at 40, 50 and 60 minutes.

Although increases in graphene quality were observed with increasing growth time up to 30 minutes, unexpectedly, growth after 1 minute under the same flow was found to consistently produce the highest quality graphene. Graphene terraces were found to extend over distances as large as 100 μm, whilst pleat defects were significantly more prevalent as networks that extend over many microns (Fig. 7.3(e) and (f)). This behaviour differs significantly to that observed previously in other studies, in which consistent increases in high quality graphene island size were observed with increasing growth time [4,28]; however, substantial differences are apparent between the growth methods, including CH_4 and H_2 concentrations, which likely leads to the disparity, due to the high level of sensitivity displayed to these parameters [4, 20].

The high quality growth of a complete layer of graphene suggests an optimal concentration of carbon diffuses into the Cu substrate, during the first minute of growth. The self-limiting nature of graphene growth on the Cu substrate ensures that the graphene produced is predominantly of single-layer thickness, with the presence of strain releasing pleat defects indicating the film is of a high quality and relatively defect free. The drop in quality upon the increase in growth time to 5 minutes and to some degree longer growth periods, can be explained by the initial supersaturation of the substrate, followed by inadequate time for significant mass transport to occur. Upon cooling this results in the amorphous carbon blob like structures clearly observable in figures 7.3(a) and (b). When the growth time is increased further to 20 and 30 minutes the rate of carbon diffusion into the substrate will have slowed significantly, due to the saturation of the substrate, which combined with large areas of the substrate being covered with graphene, prevents further

CH$_4$ adsorption [7]. Therefore, the longer period under high temperatures allows the reorganisation of the carbon already on the surface via mass transport [29], which effectively redistributes the carbon atoms leading to a higher quality film. Furthermore, hydrogen, even at the lower concentrations used here, will act as an etching reagent to modulate the morphology of the film whilst the chamber remains at the growth temperature, resulting in a smoother homogeneous film [2, 20].
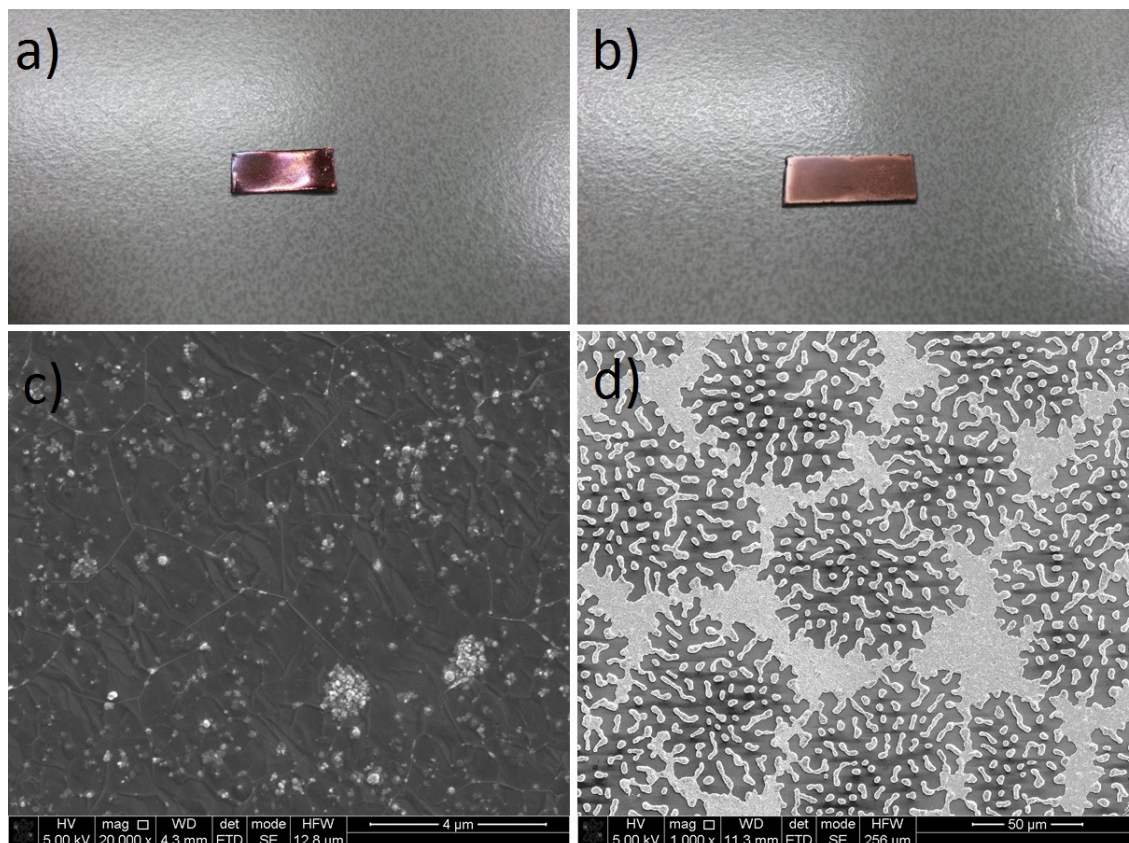
Figure 7.4: (a) Graphene film grown on a Cu foil. (b) Graphene film grown on Cu evaporated onto SiO$_2$. (c) Typical SEM image of the graphene film from the sample in (a). (d) Typical SEM image of the film from the sample in (b).

Figure 7.4 shows different Cu substrates on which graphene has been grown; (a) and (b) show a typical Cu foil substrate and an evaporated Cu substrate respectively. Whilst the normal Cu foil sample shows a pinkish sheen slightly darker than that observed for a clean Cu substrate, the evaporated substrate sample shows a light Cu colouring with a very clear contrast between the edges of the sample and the main central region, though a region towards the bottom right-hand corner shows a set of small spots. Upon imaging with SEM significant differences can be observed between growth on the Cu foil and the evaporated Cu substrate. Figure 7.4(c) shows a SEM image of a region of graphene on the Cu foil, which shows the expected high quality film with a small levels of oxidation/contamination on the surface. In contrast,

the sample grown on the evaporated Cu substrate shows large ($\sim$100 μm), roughly circular, dark areas punctuated by small islands, which upon post-growth annealing become small oxidised areas. In some regions these darker areas appear to merge and overlap much like typical graphene island growth on Cu foils. These islands could be mistaken for graphene, due to the similar contrast difference observed between dark regions and the lighter oxidised islands, however, EBSD maps of these regions suggest this is not the case. Figure 7.5 shows a region of dendritic islands and the EBSD map of the same area; the regions in green correspond to areas in which no Cu crystallographic information could be obtained. Therefore, rather than graphene, these areas are in fact regions in which no Cu is present and the SiO$_2$ substrate is now visible. It is therefore likely that the thin layer of Cu initially deposited is partially removed by the cleaning procedure and the pre-growth anneal under H$_2$/Ar$_2$ flow. Consequently, graphene growth cannot occur in these areas.
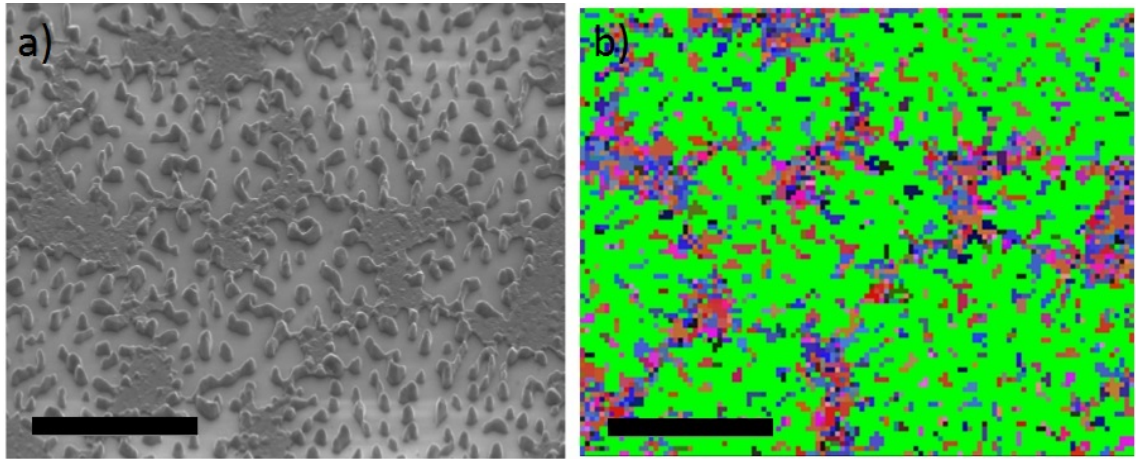
Figure 7.5: (a) SEM image of Cu evaporated onto SiO$_2$ after growth. (b) EBSD map of the region in image (a); green areas indicate an absence of Cu (Scale bar = 50 μm).

7.3.2 Cold-Wall Graphene Growth on Cu Foils

Figure 7.6 shows SEM images obtained from samples grown in the cold-wall graphene growth reactor for various time periods. Fig. 7.3(a) shows the results of growth for 5 minutes at a constant flow of 5 sccm of CH$_4$. Small rounded islands were found to form, with an average size of 0.9$\pm$0.5 μm^2 covering $\sim$22% of the surface. Islands exhibited a smooth, step free, structure indicating their composition is most likely thick amorphous carbon as none of the underlying Cu structure can be observed. Upon increasing the growth time to 10 minutes larger islands 15$\pm$7 μm^2 were observed covering 26$\pm$6% of the surface with significantly straighter edges and step
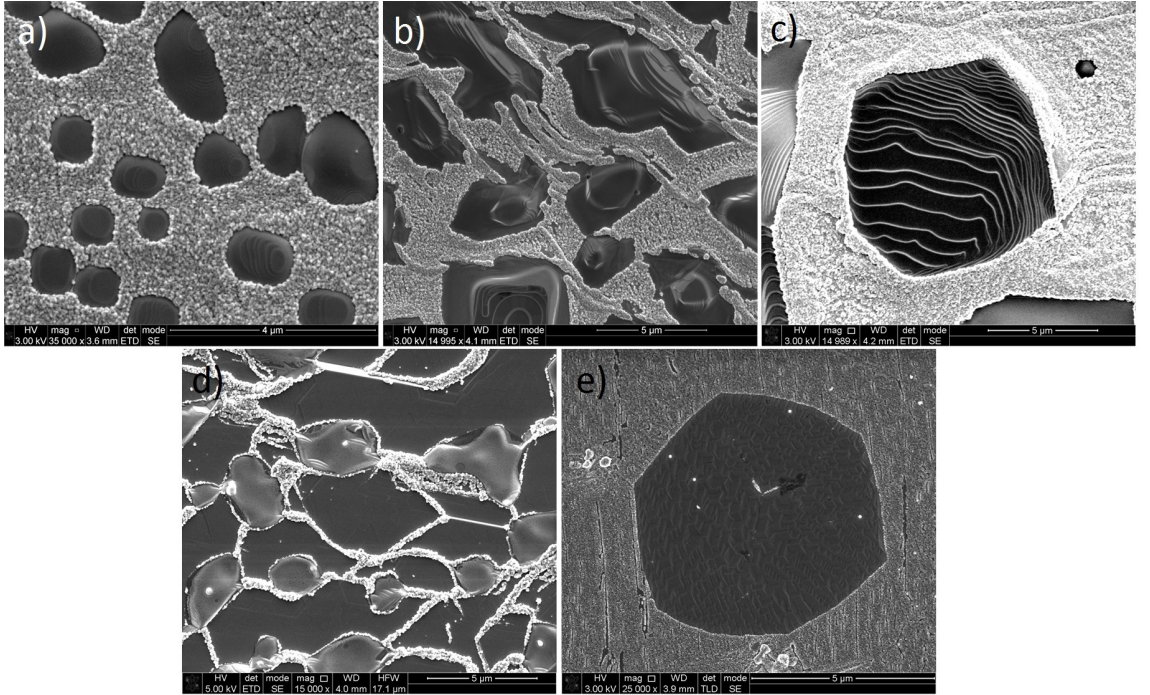
Figure 7.6: (a) Amorphous carbon islands formed on Cu after 5 minutes growth under 5 sccm of CH_4. (b) Predominantly amorphous carbon islands, showing some underlying step structure after 10 minutes under 5 sccm of CH_4. (c) Hexagonal partially graphitic islands after 20 minutes under 5 sccm of CH_4. (d) Interspersed graphene and amorphous carbon islands after 20 minutes growth under 10 sccm of CH_4. (e) Pristine hexagonal graphene flake produced after 20 minutes growth under 6 sccm CH_4, sample was annealed prior to growth under 1 slpm H_2/Ar_2 for 1 hour.

structures, however large rounded areas within these islands were still observed indicating that amorphous carbon continued to form during the growth phase in addition to graphene (Fig. 7.6(b)). By further increasing the growth time to 20 minutes an appreciable improvement in quality was observed, with large, 200 ± 50 μm^2, hexagonal shaped islands occurring. Some of these islands displayed clear underlying step structure, suggesting that monolayer graphene has formed on the surface (Fig. 7.6(c)), however, despite these improvements some areas continued to show amorphous carbon islands (Fig. 7.6(d)) indicating that growth across the entire sample remains inhomogeneous. Further increases in growth time were not found to significantly improve the quality of the graphene produced, although the concentration of islands was observed to increase marginally up to growth times of 1 hour.

The behaviour observed with increasing growth time follows a similar pattern to that observed in samples produced via hot wall growth for extended growth times, with increased graphene quality after longer syntheses. The increase in quality most likely arises in a similar way to that observed for hot wall growth, with the

extended time at 1000 °C allowing greater mass transport [7]. A significant difference between the two growth methods, was the continuity of the film with many small islands observed, rather than a continuous membrane. In part, this is likely to arise from the significantly lower CH_4 flow utilised in these studies, which would slow the rate of growth by reducing the carbon available in the process atmosphere [8]. When combined with the larger chamber, in which only a small localised region is heated, the substrate is likely to become saturated leading to the formation of islands, rather than supersaturated which would produce a complete film [8]. When increasing the CH_4 flow, a substantial increase in the surface coverage was observed. Figure 7.6(d) shows a graphene film produced after growth for 20 minutes under 10 sccm of CH_4, in which large flat graphene islands can be observed, with smaller amorphous carbon islands interspersed between, separated by lines of oxidation. Under these conditions, the average island size was found to be slightly smaller than that observed after growth under 5 sccm of CH_4, at 11.67$\pm$7.14 μm^2, however the surface coverage was significantly increased, to 94$\pm$3 %. The increased CH_4 concentration within the chamber will result in a higher concentration of graphene islands due to a significantly higher adsorption rate at the Cu surface, leading to supersaturation and subsequently a complete coverage.

Despite the improvement in graphene quality with increased growth time, the presence of amorphous islands and the significant concentration of large boundaries is a significant issue. Hence, further optimisation is required to increase the lateral dimensions of the graphene islands and eliminate amorphous carbon islands. This requires a systematic investigation of other parameters, such as the anneal time and hydrogen concentration. Both factors have been shown to have a significant effect either by reducing the number of nucleation sites on the substrate, which in turn reduces the number of grain boundaries in the film [16, 20] or by acting to limit the non-uniform, dendritic, growth of graphene islands [30]. Figure 7.6(e) shows the result of preliminary work investigating the influence of these parameters in the cold-wall system, in which a pristine hexagonal graphene island can be seen on a sample produced after a significantly longer anneal, under 1 slpm H_2. The islands observed on this sample showed a substantially higher quality in comparison to those observed on other samples. The preference for hexagonal, rather than dendritic, island growth strongly suggests that the shape of graphene domains is controlled by the increased hydrogen etching at the flake boundaries, as previously observed by Vlassiouk *et al.* [30]. However, despite the improvement observed under these conditions, reproducibility in the cold wall system was low due to a high degree of sensitivity to variables such as CH_4 concentration, growth temperature, chamber

pressure and cleanliness of the system. As such, the results observed at the higher hydrogen concentration and longer anneal time were not fully reproducible.

In conclusion, preliminary investigations into the growth of graphene on Cu substrates via hot-wall and cold-wall growth found a variation in quality with the methane flow used. In both cases increased growth time was found to significantly improve the quality of the graphene produced. In the hot-wall system this was characterised by a shift from a layer of small, amorphous islands to a pristine complete single layer, whilst cold-wall growth also showed a similar shift but with significantly lower coverage, with isolated amorphous islands transforming to small graphene islands. This was attributed to the reorganisation of carbon at the surface over longer periods producing pristine graphene layers. In contradiction to this trend however, the highest quality graphene was produced after a one minute growth step in the hot-wall system, which is believed to be due to an optimal level of carbon diffusion into the sample during this short time period. Hot-wall growth was also performed on evaporated Cu substrates, but these were found to be unsuitable as significant areas of Cu were removed by the cleaning and annealing phases, preventing the decomposition of carbon at the surface. Growth via the cold-wall system was able to produce graphene of an equal quality to that produced via hot-wall growth, when using high concentrations of H_2/Ar_2 and a long anneal time. The significant sensitivity of growth to small changes in chamber pressure and cleanliness, for example, is currently a weakness in this method. Therefore, in comparison to hot-wall CVD the cold-wall method is currently less attractive. Complete optimisation of either the hot-wall or cold-wall growth methods presents the first step in producing graphene samples from which a thorough kinetic growth model may be developed.

7.3.3 EBSD of Graphene on Cu

Figure 7.7(a) shows an SEM image obtained from graphene grown via hot-wall CVD growth for 1 minute under 30 sccm of CH_4 and 50 sccm of H_2/Ar_2 as outlined above. Two distinct regions are clearly visible corresponding to an area of high quality graphene, and an area of lower quality graphene islands with oxidised boundaries. Figure 7.7(b) shows the EBSD map of the region in (a), in which two crystal faces can be observed, either side of the grain boundary. This clearly shows significantly higher quality graphene forms on the lower index (212) Cu face, with the less homogeneous graphene forming on a higher index (136) surface. This behaviour is similar to that seen in previous studies in which the highest quality graphene was found to
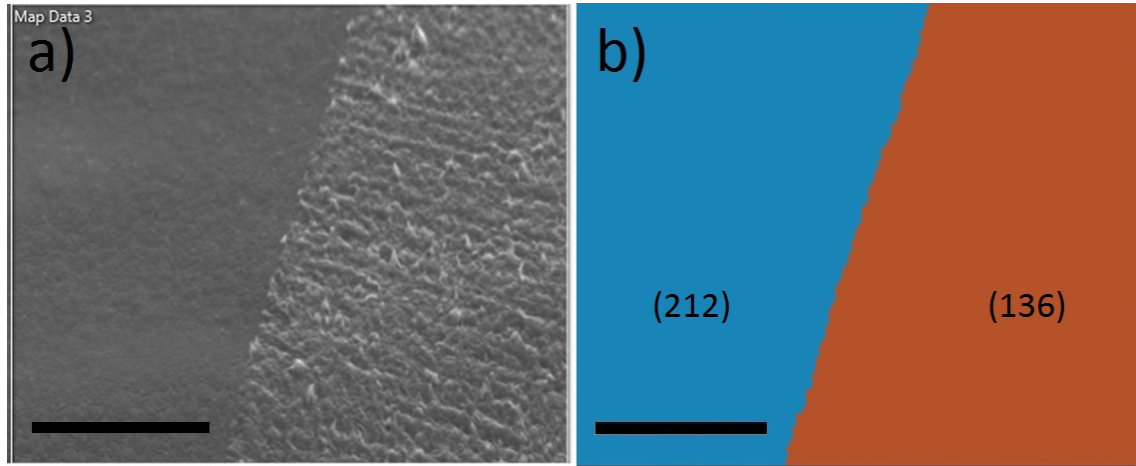
Figure 7.7: (a) SEM image of a high quality region of graphene grown on Cu (left) adjacent to a region of lower quality graphene (right) (scale = 10 μm). (b) EBSD map of the graphene regions in (a) showing two clear Cu faces.

grow quickly on lower index Cu faces, particularly the (111) face, due to rapid diffusion of carbon molecules on the Cu or pre-existing graphene, resulting in fast dendritic growth at the edges of the film [9, 20]. These results would suggest that the (212) plane, as a low index face similar to that of (111), produces a similar quality of graphene growth. In contrast, on vicinal planes, such as the (136) face, high concentrations of compact islands have typically been observed, in keeping with the grain boundary heavy region imaged [9]. This is proposed to result from significant nucleation at defect sites and steps [31], but is combined with reduced carbon diffusion which prevents supersaturation of these regions [8]. Consequently, the growth of small graphene islands is much more prevalent in these areas, as is observed in figure 7.7(a).

A similar behaviour can be observed in figure 7.8(a) which shows an SEM image of a region of graphene islands grown on a partially melted Cu substrate. The growth produces small interlocking islands with oxidised boundaries between, creating a mosaic like layer, rather than a continuous film. EBSD maps from regions of compact islands (Fig. 7.8(b)) reveal a highly polycrystalline surface beneath the graphene, with an average Cu grain size of 3±2 μm^2. It is likely that this arises from the rapid cooling after partial melting of the surface, which freezes the orientation of small grains before they can nucleate to produce the lowest energy (111) face [32]. The most prevalent crystal orientations were found to be (101) type faces, with a large degree of variation around this family of planes observed. The majority of grains exhibited higher index planes such as (203), (304), (405) and (506) as characterised by the large concentration of similarly coloured green regions in the
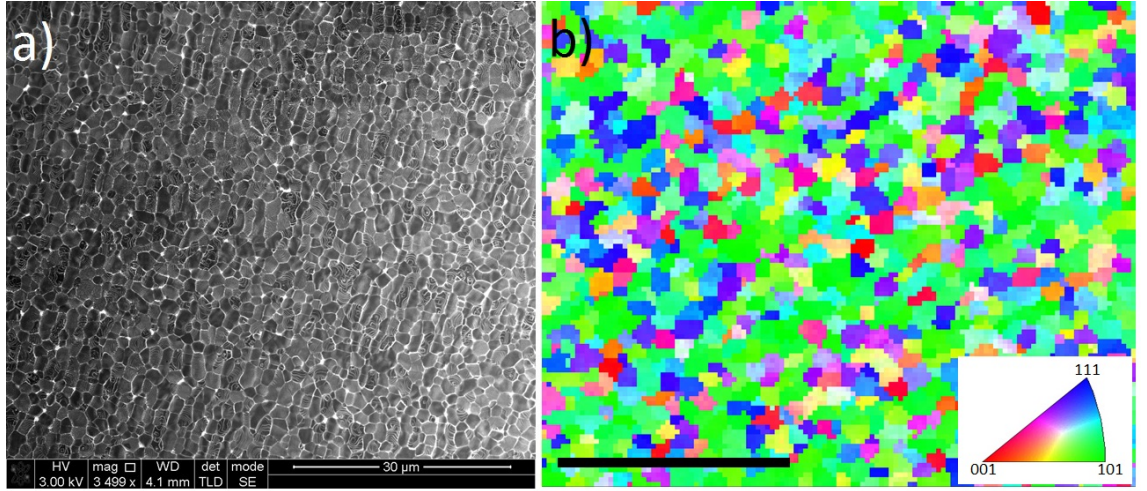
Figure 7.8: (a) Large area SEM image of mosaic like graphene islands after growth on a partially melted Cu substrate. (b) Large area EBSD map of a region of graphene islands, showing a highly polycrystalline Cu surface beneath (scale = 20 μm). (Inset) Surface orientation colour map.

EBSD map. However, despite this preference, a large degree of variation can be observed across the entire map, with significant regions of both (111) and (001) type planes also visible. The small graphene island size observed is in keeping with previous studies that suggest that high index faces produce compact graphene islands, due to inhibited carbon diffusion [9].

Upon higher resolution imaging, further features of the graphene growth become apparent. Figure 7.9(a) shows an area of graphene islands, in which two clear regions with different morphology can be observed. Higher resolution images of each region (Fig. 7.9(b) and (c)) show that graphene growth proceeds either on highly stepped Cu surfaces with elongated step edges or on square stepped Cu structures corresponding to screw dislocations. The two regions can easily be identified by the variation in the level of oxidation between islands, which was found to cover 13±2% of the surface in the region dominated by screw dislocations, in comparison with 8±1% observed on the "long step" regions. This is combined with a larger average island size observed, 8±4 μm^2, in the latter region with a large degree of anisotropy apparent, in comparison with an average area of 3±1 μm^2 obtained from the regions with screw dislocations.

Figure 7.9(d) shows the EBSD map obtained from an area of the partially melted Cu sample similar to that observed in (a), in which two different regions of islands growth was observed. The larger islands were observed on the left of the image, whilst the smaller areas of graphene that conform to the square pyramid-like struc-
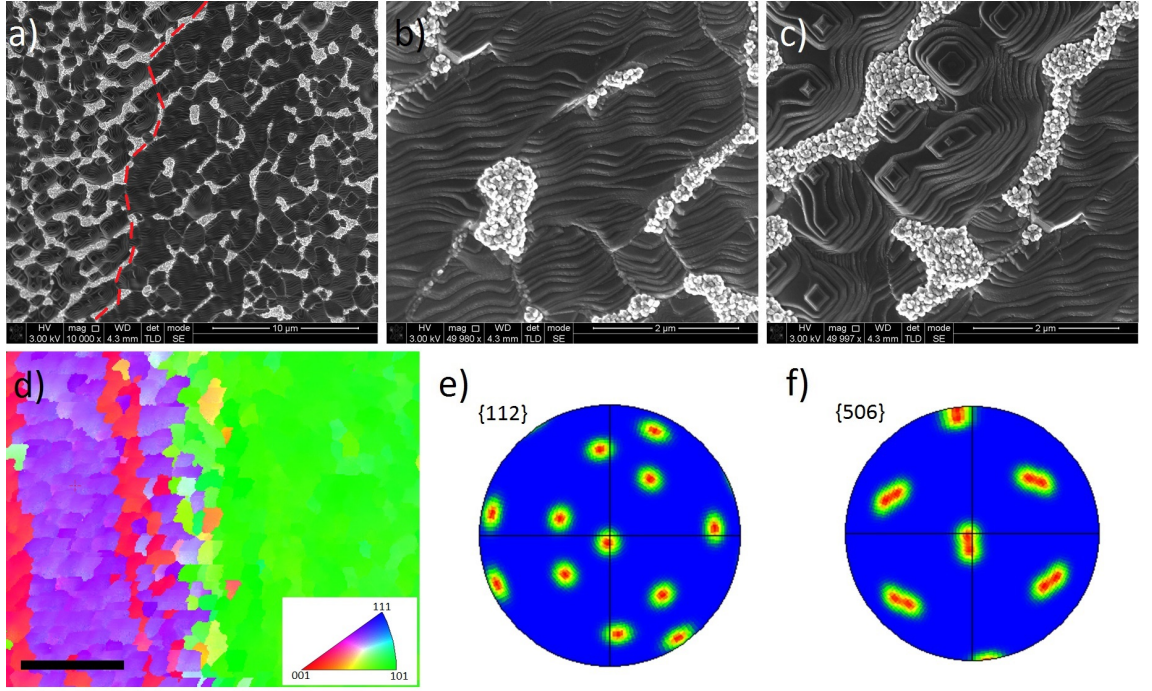
Figure 7.9: (a) SEM image of two regions of graphene islands meeting. (b), (c) Close up images of graphene-Cu islands either side of a grain boundary (red dashed line). (d) EBSD map obtained from a grain boundary region similar to that seen in (a); regions in purple correspond to the structures shown in (b) with Cu micrograin surfaces of (112), (115), (325), (315) and (326). Regions in green correspond to structures seen in (c) with Cu micrograin surfaces of (203), (304), (405) and (506) (10 μm Scale bar). (e) Pole figure obtained from the purple region on the EBSD map in (d) corresponding to the (112) plane. (f) Pole figure obtained from the green region of the EBSD map in (d) corresponding to the (506) plane.

tures were visible on the right. It can immediately be discerned that the two regions correspond to significantly different underlying Cu faces, with the (112) face predominantly in the region with larger islands, and the smaller islands on high index faces such as (506). This can be seen in the pole figures obtained from the two regions, which show high intensity spots corresponding to the predominant crystallographic orientations (Fig. 7.9(e) and (f)). What also becomes apparent is further variation in crystal face, with clear micro-crystal structure visible, corresponding to (203), (304), (405) and (506) surfaces from screw dislocation areas, and (112), (115), (325), (315) and (326) faces in the stepped region. Aligned (136) grains between the two areas can also be observed (orange), which appear to act as a boundary between the two regions, though no different graphene structures were observed on top of these faces, indicating that the growth mechanisms of the two large regions either side of these grains dominate how graphene grows in this smaller area.

Based on the variation in the shape and size of the islands observed it is highly

likely that the underlying micro-crystal structure has a significant effect on growth. Much like the rapid growth on the (111) surface seen previously in the literature [9, 10, 19, 20], it is likely that similar growth is to be expected on the predominantly (112) oriented faces. However, the presence of a high concentration of Cu grain boundaries due to the presence of the micro-crystal structure in these regions inhibits carbon diffusion on the surface due to the higher corrugation potential, resulting in two competing mechanisms, in that growth on the lower index (112) type surface is likely to proceed quickly and spill over onto the crystal faces around it, as seen previously by Wood *et al.* on the (111) face [9], whilst the growth is simultaneously limited due to the presence of the higher index grains, lowering the carbon diffusion rate. In smaller graphene islands on Cu screw dislocations, similar arguments can be made in that the underlying high index faces are likely to dramatically reduce the rate of carbon diffusion which, when combined with the increased reactive sites, will result in a high concentration of small graphene islands. Furthermore, the nucleation density and growth rate on the (101) face has previously been shown to be significantly lower than that observed on (111) grains [20], providing additional support for reduced growth on this family of planes, resulting in smaller islands.

A final feature to note is that graphene which forms on these textured regions, lacks any pleat defects, which, as discussed in Chapter 6, are indicative of the strain in the film, caused by thermal mismatch with the substrate. The absence of pleats, indicates that strain release via delamination is not required on these highly stepped structures. This indicates that the combination of an undulating surface and small island size provides sufficient routes for strain release for the film, despite the high degree of conformation to the surface [33]. This behaviour is in marked contrast to the extensive pleat networks typically observed on the high quality graphene films grown on solid Cu foils, as seen in figure 7.3(e). Further work should therefore be conducted to determine whether a dependence exists between the size of graphene islands and onset of pleat formation; whilst additional studies into the effects of growth on highly stepped surfaces may also be of interest.

In summary, the Cu surface facets were found to have a significant effect on graphene growth, with lower index crystal faces producing significantly higher quality graphene in comparison with higher order faces. The highest quality graphene was observed on surfaces closely related to the (111) face, with pristine islands observed prolifically on (212) grains. Studies on partially melted Cu substrates, showed a highly polycrystalline surface also results in significant variation in the rate at which graphene can grow. The micro-crystal structure of the substrate was

found to produce small compact graphene islands with further variation observed depending on the predominant surface. (112) Type surfaces exhibited highly concentrated Cu steps with a larger island size, whereas the higher index (506) surfaces showed smaller graphene islands formed on high concentrations of screw dislocations. The small island size observed is expected to arise due to the presence of large concentrations of reactive sites on these surfaces, inhibiting the diffusion of carbon atoms. Finally, no pleat formation was observed on the small graphene islands, suggesting the reduced island size and an undulating surface relieves strain on the graphene effectively.

7.4   Conclusions

Preliminary experiments were conducted into the CVD growth of graphene on Cu substrates via hot-wall and cold-wall methods. Longer growth times (30 minutes), via both methods, were found to produce higher quality graphene, with low quality graphene and amorphous carbon observed when shorter growth periods (5 minutes) were utilised. This is assigned to the longer growth step allowing sufficient time for carbon diffusion, following initial saturation or supersaturation, leading to the formation of high quality graphene. An exception was observed with the hot-wall method when a one minute growth period was used, which was found to produce a pristine graphene layer devoid of small islands. Cold-wall growth at lower CH_4 concentrations (5 sccm) was found to result in saturation, rather than supersaturation, of the Cu substrate leading to isolated island formation, with complete layers produced only once the methane flow was substantially increased. Very high quality graphene was produced in an isolated test when a long anneal under 1 slpm was performed, however results were irreproducible due to the system exhibiting a high degree of sensitivity to many factors, such as growth temperature and contamination.

Initial experiments were also conducted into the effects that different Cu crystal surfaces have on the quality of graphene grown by the two methods outlined within the chapter. High quality graphene was found to form on low index faces such (212) grains, whilst higher index planes presented lower quality graphene in the form of compact islands. This was attributed to reduced carbon diffusion on high index planes due to the presence of point defects and steps in these regions, leading to the formation of small islands, rather than a large scale film. Growth on par-

tially melted substrates, showed further variation in graphene due to the presence of a micro-crystal surface structure, which resulted in differing regions of compact, highly stepped islands and square pyramid structures in areas of Cu with high concentrations of screw dislocations. Graphene was found to grow conformally in these areas resulting in high concentrations of small islands. Finally, no pleat defects were observed on graphene grown on these areas, suggesting strain release via buckling does not occur when the underlying substrate is significantly undulating or when graphene sheet size is small.

7.5 References

[1] X. Li, W. Cai, J. An, S. Kim, J. Nah, D. Yang, R. Piner, A. Velamakanni, I. Jung, E. Tutuc, S. K. Banerjee, L. Colombo and R. S. Ruoff, *Science*, **324**(5932), 1312–1314 (2009).

[2] M. Losurdo, M. M. Giangregorio, P. Capezzuto and G. Bruno, *Phys. Chem. Chem. Phys.*, **13**(46), 20836–20843 (2011).

[3] L. Tao, J. Lee, H. Chou, M. Holt, R. S. Ruoff and D. Akinwande, *ACS Nano*, **6**(3), 2319–2325 (2012).

[4] A. W. Robertson and J. H. Warner, *Nano Lett.*, **11**(3), 1182–1189 (2011).

[5] X. Li, C. Magnuson, A. Venugopal, R. M. Tromp, J. B. Hannon, E. M. Vogel, L. Colombo and R. S. Ruoff, *J. Am. Chem. Soc.*, **133**(9), 2816–2819 (2011).

[6] W. Zhang, P. Wu, Z. Li and J. Yang, *J. Phys. Chem. C*, **115**(36), 17782–17787 (2011).

[7] K. Celebi, M. T. Cole, J. W. Choi, F. Wyczisk, P. Legagneux, N. Rupesinghe, J. Robertson, K. B. K. Teo and H. G. Park, *Nano Lett.*, **13**(3), 967–974 (2013).

[8] X. Li, C. W. Magnuson, A. Venugopal, J. An, J. W. Suk, B. Han, M. Borysiak, W. Cai, A. Velamakanni, Y. Zhu, L. Fu, E. M. Vogel, E. Voelkl, L. Colombo and R. S. Ruoff, *Nano Lett.*, **10**(11), 4328–4334 (2010).

[9] J. D. Wood, S. W. Schmucker, A. S. Lyons, E. Pop and J. W. Lyding, *Nano Lett.*, **11**(11), 4547–4554 (2011).

[10] L. Zhao, K. T. Rim, R. He, T. F. Heinz, A. Pinczuk, G. W. Flynn and A. N. Pasupathy, *Solid State Comm.*, **151**(7), 509–513 (2011).

[11] J. M. Wofford, S. Nie, K. F. McCarty, N. C. Bartelt and O. D. Dubon, *Nano Lett.*, **10**, 4890–4896 (2010).

[12] H. Chen, W. Zhu and Z. Zhang, *Phys. Rev. Lett.*, **104**(18), 186101 (2010).

[13] Y. A. Wu, A. W. Robertson, F. Schäffel, S. C. Speller and J. H. Warner, *Chem. Mater.*, **23**(20), 4543–4547 (2011).

[14] R. M. Jacobberger and M. S. Arnold, *Chem. Mater.*, **25**, 871–877 (2013).

[15] A. T. Murdock, A. Koos, T. B. Britton, L. Houben, T. Batten, T. Zhang, A. J. Wilkinson, R. E. Dunin-Borkowski, C. E. Lekka and N. Grobert, *ACS Nano*, **7**(2), 1351–1359 (2013).

[16] H. Wang, Q. Wang, Y. Cheng, K. Li, Y. Yao, Q. Zhang, C. DOng, P. Wang, U. Schwingenögl, W. Yang and X. X. Zhang, *Nano Lett.*, **12**(1), 141–144 (2012).

[17] D. Geng, B. Wu, Y. Guo, L. Huang, Y. Xue, J. Chen, G. Yu, L. Jiang, W. Hu and Y. Liu, *Proc. Nat. Aca. Sci. USA*, **109**(21), 7992–7996 (2012).

[18] Y. A. Wu, Y. Fan, S. Speller, G. L. Creeth, J. T. Sadowski, K. He, A. W. Robertson, C. S. Allen and J. H. Warner, *ACS Nano*, **6**(6), 5010–5017 (2012).

[19] H. Ago, Y. Ogawa, M. Tsuji, S. Mizuno and H. Hibikino, *J. Phys. Chem. Lett.*, **3**(16), 2228–2236 (2012).

[20] I. Vlassiouk, S. Smirnov, M. Regmi, S. P. Surwade, N. Srivastava, R. Feenstra, G. Eres, C. Parish, N. Lavrik, P. Datskos, S. Dai and P. Fulvio, *J. Phys. Chem. C*, **117**(37), 18919–18926 (2013).

[21] W. Cai, R. D. Piner, Y. Zhu, X. Li, Z. Tan, H. C. Floresca, C. Yang, L. Lu, M. J. Kim and R. S. Ruoff, *Nano Res.*, **2**(11), 851–856 (2009).

[22] Y. Lee, S. Bae, H. Jang, S. Jang, S.-E. Zhu, S. H. Sim, Y. I. Song, B. H. Hong and J.-H. Ahn, *Nano Lett.*, **10**(2), 490–493 (2010).

[23] V. Miseikis, D. Convertino, N. Mishra, M. Gemmi, T. Mashoff, S. Heun, N. Haghighian, F. Bisio, M. Canepa, V. Piazza and C. Coletti, *2D Mater.*, **2**(1), 014006 (2015).

[24] T. H. Bointon, M. D. Barnes, S. Russo and M. F. Craciun, *Adv. Mater.*, **27**(28), 4200–4206 (2015).

[25] S. Chen, L. Brown, M. Levendorf, W. Cai, S.-Y. Ju, J. Edgeworth, X. Li, C. W. Magnuson, A. Velamakanni, R. D. Piner, J. Kang, J. Park and R. S. Ruoff, *ACS Nano*, **5**(2), 1321–1327 (2011).

[26] T. M. Paronyan, E. M. Pigos, G. Chen and A. R. Harutyunyan, *ACS Nano*, **5**(12), 9619–9627 (2011).

[27] Z. Yan, J. Lin, Z. Peng, Z. Sun, Y. Zhu, L. Li, C. Xiang, E. L. Samuel, C. Kittrell and J. M. Tour, *ACS Nano*, **6**(10), 9110–9117 (2012).

[28] H. Wang, G. Wang, P. Bao, S. Yang, W. Zhu, X. Xie and W.-J. Zhang, *J. Am. Chem. Soc.*, **134**(8), 3627–3630 (2012).

[29] S. Bhaviripudi, X. Jia, M. S. Dresselhaus and J. Kong, *Nano Lett.*, **10**(10), 4128–4133 (2010).

[30] I. Vlassiouk, M. Regmi, P. Fulvio, S. Dai, P. Datskos, G. Eres and S. Smirnov, *ACS Nano*, **5**(7), 6069–6076 (2011).

[31] X. Li, W. Cai, L. Colombo and S. Ruoff, *Nano Lett.*, **9**(12), 4268–4272 (2009).

[32] D. Chatain, V. Ghetta and P. Wynblatt, *Interface Sci.*, **12**(1), 7–18 (2004).

[33] S. P. Koenig, N. G. Boddeti, M. L. Dunn and J. S. Bunch, *Nature Nanotechnol.*, **6**(9), 543–546 (2011).

Chapter 8

Summary and Further work

This chapter summarises the work presented in this thesis, followed by a discussion of further experiments that may be undertaken to extend the research performed herein.

8.1   Summary and Conclusions

At the beginning of this thesis, the properties exhibited by graphene were outlined, which has led to the growth and application of this material becoming significant areas of research in the last decade. The discussion also outlined the various methods by which graphene could be produced, from mechanical exfoliation to chemical vapour deposition, and their respective advantages and disadvantages. Chapter 4 presented a study of the optimisation of growth of graphene from SiC by varying the parameters of growth temperature, growth time and cooling rate. This investigation found that the quality of graphene grown depended strongly on the growth temperature, with higher temperatures (1775 - 1850 °C) producing significantly better graphene. However increasing the temperature further was found to produce undesirable etch pits. Similar results were observed when varying growth time, with longer periods at raised temperatures (∼60 minutes) producing higher quality graphene with minimal small islands. Cooling rate was not found to affect the quality of graphene, however increased contamination was observed after longer cooling periods. Therefore, it was suggested that in order to produce the highest quality of graphene via thermal processing of SiC(0001) wafers, a high growth temperature should be used, combined with a longer growth period. The optimised growth method outlined, provides an excellent alternative to mechanical exfoliation and CVD methods as a potential source of graphene for use in modern electronics.

In Chapter 4, the production of graphene nano-ribbons (GNRs) as a potential route to engineering electrical behaviour was also discussed. As the graphene bandgap can be tailored via variation in ribbon width, the production of ribbons using photolithography of SiC(0001) wafers, combined with the growth process outlined earlier in the chapter, was investigated as a method to grow large scale GNR nano-arrays. Experiments indicated that the quality of graphene nanoribbons produced was poor due to significant damage caused to the substrate by the etching process preventing normal graphene growth. Therefore, it is concluded that this method is unsuitable for producing graphene nano-ribbon arrays.

The effects of surface contamination were also described in Chapters 1 and 4, as its presence can cause degradation of many of the desirable properties of graphene. A simple technique was outlined in Chapter 4 to remove contamination from the surface of graphene grown on SiC(0001). Experiments showed that the technique was able to remove >99 % of noble metal contaminant layers of various thicknesses, with minimal damage caused to the graphene layer below. Furthermore, during

the course of this study, contamination caused by experimental techniques such as Auger electron spectroscopy (AES) was observed. This contamination showed a close resemblance to material previously referred to in the literature as "roughened" graphene. The cleaning method was found to also be able to remove this contamination without causing significant damage to the graphene. Therefore it can be concluded that metal contamination can be removed from graphene grown on SiC(0001) by this facile technique, allowing for the reuse of graphene samples.

In the introduction, the presence and effect of different defects was also discussed. One particular defect, the pleat, is discussed in Chapter 5 due to its presence as an almost universal feature in graphene-substrate systems. Experiments conducted in Chapter 5 studied the factors that affect the length, cross section, orientation and stability of pleats on graphene grown on SiC(0001). It was found that the size of pleats strongly depended upon the quality of the graphene produced, with a higher standard of graphene resulting in longer, taller and wider pleats, most likely due to the requirement of more strain release in the film due to the lack of defects. Orientation was found to strongly prefer a three-fold symmetry with pleats most commonly meeting at 120° angles. This three-fold combination of pleats has been attributed to it being more energetically favourable to produce junctions of three pleats rather than six, however continuum-energy calculations were unable to confirm this. Pleats were also found to follow the symmetry of the SiC(0001) substrate, which is thought to result in the least number of bonds broken between the graphitic buffer layer and the SiC substrate. Pleat stability was found to vary depending on a number of factors, with pleats on high quality graphene typically being dragged by the scanning tunnelling microscope (STM) tip. Pleats were found to increase significantly in stability at step edges and with the introduction of defects via ion bombardment or upon the deposition of small levels of adsorbates. This has been attributed to pleats pinning at reactive sites with which they interact strongly. Pleat defects were hence found to provide a qualitative measure of the quality of graphene on SiC(0001), whilst their stability and position may subsequently be manipulated.

As pleats are a universal feature of graphene-substrate systems they can provide substantial information on the substrate-overlayer interaction. The formation of buckles and pleats has been subject to studies performed on many different materials, however no such study has been applied to graphene. This is addressed in Chapter 5, in which a continuum energy model is developed to describe the formation of pleats, which allows the adhesion energy of graphene to SiC to be determined.

This model can be applied to any graphene-substrate system in which pleats form due to differences in thermal expansion allowing the adhesion energies of graphene to many different materials to be determined. Application of the model to graphene on SiC(0001) found an adhesion energy of $3.0\pm^{1.6}_{1.0}$ J/m^2, which is significantly higher than the adhesion energy observed for graphene on other substrates. This is attributed to the presence of the carbon-rich buffer layer, found between the substrate and the first true graphene layer, which forms strong covalent bonds with the SiC surface.

Chapter 6 also discusses the effect of defects in carbon nanostructures, particularly those that result from ion irradiation. The production of defects via ion bombardment has been significantly researched, particularly in graphite due to its use in nuclear reactors, despite this the intricacies of defect migration and agglomeration have not been fully pursued. This is of particular interest when comparing behaviour with more recently discovered carbon structures such as graphene. In order to address this, experiments in Chapter 6 explored the agglomeration of extrinsic defects on graphite upon annealing at various temperatures and for different lengths of time. Such defects were found to agglomerate after heating at 300 °C and then increased further in size when annealed at 750 °C resulting in larger defect structures with a corresponding drop in concentration. The defects were also found to align preferentially at graphite step edges, which is attributed to the regions of increased reactivity found in these areas effectively pinning them in place. Furthermore, preferential alignment of defects upon heating was also observed on terraces, with one or two preferential directions observed in a 300 nm^2 area. Upon performing RS it is suspected that this alignment corresponds to agglomeration along grain boundaries which, much like steps, provide pinning sites where defects can cluster.

Chapter 6 also examines the behaviour of defects on graphene grown on SiC(0001), which was found to differ significantly to that on graphite. Both intrinsic and extrinsic defects were observed after annealing at various temperatures, with no agglomeration or alignment observed. In the case of intrinsic defects this was attributed to their formation at high temperatures during growth, resulting in highly stable defect configurations. In the case of extrinsic defects, the origin of their increased stability in comparison to those produced on graphite is not understood. However, possible reasons for enhanced stability, such as the incorporation of Si into defects and variations in the surface energy landscape were discussed.

The influence of defects on local electronic structure was also studied in Chapter

6, with STS performed on the defects produced in both graphite and graphene. Ion bombardment induced defects on graphite were found to produce tunnelling spectra with increased conductance either side of the Fermi level, attributed to the conversion of the ordered graphite lattice to a disordered state. Other defects showed an alternative modification of the graphite LDOS, with asymmetries visible in both the valence and conduction bands, which are tentatively assigned to the presence of residual gas impurities. In both cases, the lack of increased LDOS at E_F strongly indicates that dangling bonds produced by the bombardment are saturated, either by gas adsorption or by lattice reconstruction. STS spectra were also obtained from intrinsic and extrinsic defects on graphene, in which features not typically observed on graphite were apparent. Very little variation was observed in the defects produced via ion bombardment, with resonant peaks visible at positive biases, suggesting similar defects at each bombardment site. The spectra obtained showed some similarities with those calculated for Stone-Wales and 555-777 defects in the literature, but further work is required before the exact defect structure can be determined.

The final chapter, Chapter 7, focussed on preliminary work on the growth of graphene on Cu by "hot-wall" and "cold-wall" CVD methods. In both cases, increased quality was observed with increased growth time, suggesting that a longer time at the growth temperature resulted in more effective reorganisation of carbon on the surface, following initial supersaturation. When comparing the two graphene growth methods, significant sensitivity to many environmental factors substantially reduced reproducibility, although there are a number of advantages in using this approach for cold-wall growth. Therefore, it was concluded that until the reproducibility of the cold-wall system is increased, hot-wall growth remains a more effective method for producing high quality graphene.

Electron Back-Scatter Diffraction (EBSD) was presented in Chapter 7 to determine how the Cu crystal face affects the growth of graphene. High index faces were found to significantly inhibit the growth of graphene resulting in the production of small, compact graphene islands, whereas growth on lower index faces, particularly those similar to the (111) plane, were found to produce the highest quality graphene. This was assigned to better diffusion of carbon on these surfaces in comparison to on high index planes, which are thought to reduce the mobility of carbon due to the large concentration of reactive sites. Growth on highly polycrystalline Cu surfaces was also investigated, with compact graphene islands of different morphologies observed on partially melted Cu substrates. These islands are likely to arise due to

the significant concentration of grain boundaries on the surface which limit diffusion of carbon resulting in isolated island formation. The different island morphologies observed were found to result from microcrystal structure on the surface in which larger crystals were made up of similarly oriented grains. Crystals made up of small grains closely related to the (112) plane were found to produce larger islands with a highly stepped structure, whilst those made up of high index (506) type grains resulted in a high concentration of screw dislocations upon which graphene would subsequently form small islands.

8.2   Further Work

As with any scientific endeavour, the work presented in this thesis poses new questions in addition to answering some of those existing. Considering the growth of graphene via the thermal decomposition of SiC(0001) first, contamination of the surface was found to occur upon cooling for longer time periods when varying the cooling rate. The source and makeup of this contamination is unknown. However, possible sources include the graphite heating elements which may degrade releasing material into the local atmosphere over time due to repeated thermal cycling; the chamber walls, which may release adsorbed atmospheric contamination. In order to determine whether these parts of the system are responsible for the observed contamination, the graphite heater should be replaced. This should be followed by repetition of the growth process with an extended cooling time. Should a large quantity of contamination still be observed, the source is unlikely to be from graphite heating elements. Careful cleaning of the chamber surfaces to reduce the level of atmospheric contamination that is adsorbed prior to growth should be conducted if contamination continues. Should contamination still be present after these steps, a significantly extended cooling step may be employed to produce a high level of contamination. With a high level of contamination on the surface, Auger electron spectroscopy (AES) may be implemented to reveal the elemental composition of the contamination and determine its source; further experiments and precautions may be performed upon the acquisition of new information. These minor experiments will result in the reduction of all contamination sources leading to significant increase in the quality of graphene produced.

Further investigation into the optimisation of graphene growth from SiC(0001) can be achieved by examination of an increased range of the growth temperatures

and growth time. Supplementary measurements with STM and AES would provide excellent complementary information to that outlined in Chapter 4, allowing perfect growth conditions to be achieved to consistently produce the highest quality graphene. Additional Raman measurements would also provide further confirmation of the level of quality obtained via this method.

Although the continuum energy model (Chapter 5) has been implemented successfully to determine the adhesion energy of graphene on SiC(0001), graphene has been grown on many other substrates, all of which exhibit pleat formation. Therefore, a natural progression for this work would be to apply the continuum energy model discussed to other graphene substrate systems and determine their respective adhesion energies. These values can be compared with those obtained previously to confirm the usefulness of the model or highlight any inaccuracies that may exist in the literature. Additionally, the model can currently only use pleats that form on terraces, as many pleats find their way to step edges, either by dragging or initial formation, adaptation of the model to incorporate these pleats would provide significantly more data with which to improve the accuracy of the adhesion energy values obtained. Finally, although this model can describe pleats that form due to the difference in thermal expansion between graphene and the substrate it is grown upon, graphene is often grown and then transferred to a different support. Pleat defects and ripples have also been observed on graphene transferred to such substrates as SiO_2; therefore measurement of these pleats and comparison to the model would be of significant interest.

Although significant characterisation of the defects that form on both graphite and graphene was carried out during the course of Chapter 6, due to time and resource limitations certain aspects of these defect structures remained unexplored. First, the exact structure of the defect agglomerations caused by ion bombardment remains unknown and could be addressed by TEM experiments. These measurements should be combined with further STS measurements, preferably taken at low temperature ($\sim$4 K), which would provide an insight into how larger regions of the reconstructed lattice affect the local density of states (LDOS). Furthermore, as discussed in Chapter 6, when performing STS, it was noted that the saturation of the dangling bonds that are produced upon the creation of vacancies, may result from residual gas species binding at these sites, rather than complete lattice reconstruction. In order to test whether this is the case, graphene/graphite samples should be bombarded to the same degree as in previous experiments, then exposed to high purity CO, O_2 or atomic H_2. Should the resulting STS spectra appear similar to

that observed previously, then the bonding of residual gas molecules to active sites is likely. However, should spectra show significantly different features, then complete reconstruction of the lattice without impurity molecules is more probable.

In Chapter 7 it was concluded that when growing graphene on Cu the hot-wall method was more effective, due to its superior reproducibility. However, many advantages to cold-wall growth were also discussed. Therefore, a complete optimisation of the cold-wall growth process is still required. Further experiments should employ a more stable heating method than the graphite heating slabs used in Chapter 7, ensuring growth is uniform across the substrate. Alternative gas atmospheres may also be tested, such as higher H_2 concentrations which may lead to cleaner Cu surfaces and moderated growth, resulting in higher quality graphene. Once optimised, reproducible growth is obtained, variation in the growth variables may be performed to develop a statistically thorough kinetic model to determine the accuracy of those in the literature. Finally, with the adaptability provided by the cold-wall system, layered structures may also be investigated, simply by supplying different gas mixtures, opening up a wide range of possibilities for device based research.

Appendix A

Linear Least Squares Fitting of Pleat Defect Height Profiles

```python
from numpy import cos, array, append, column_stack, savetxt
import pyspec
from pyspec.mpfit import *
from pyspec.fit import fit
from pyspec.fitfuncs import constant
from matplotlib.pyplot import figure, show

def cosinefit(x, p, mode='eval'):

        if mode == 'eval':
                out = array([])
                for i in range(0,len(x),1):
                        if x[i] <(p[2]-p[1]):
                                out = append(out,0.0)
                        elif x[i] >=(p[2]-p[1]):
                                if x[i]<=(p[2]+p[1]):
                                        out = append(out,p
                                            [0]/2.0*(1+cos(
                                            numpy.pi/p[1]*(x[
                                            i]-p[2])))))
                                else:
                                        out = append(out
```

```
                                              ,0.0)

#                    out = p[0]/2.0*(1+cos(numpy.pi/p[1]*(x-p[2])
   ))
        elif mode == 'params':
                out = ['d','b','Centre']
        elif mode == 'name':
                out = "George Special Function"
        elif mode == 'guess':
                out = [7.0e-10,5.0e-9,0.6e-8]
        else:
                out = []
        return out



data = loadtxt('p13.txt')
fig = figure()
ax = fig.add_subplot(111)
ax.plot(data[:,0],data[:,1],'b')
thefit = fit(x = data[:,0],y = data[:,1], funcs = [cosinefit
    ,constant],optimizer = 'mpfit')
thefit.go()
x,y = thefit.evalfitfunc(1000)
ax.plot(x,y,'r')
out = column_stack([x,y])
dof = len(x)-len(thefit.result)
error_out = thefit.stdev*sqrt(thefit._mpfit.fnorm/dof)
savetxt('p13fit.txt',out)
print thefit.result
print error_out
show()
```

Appendix B

Angular Intensity Distribution Code

```
from scipy.misc import imread, imrotate
from matplotlib.pyplot import figure, pause, show, draw,
    plot
from copy import copy
from numpy import *
imageadress = "/Users\George Wells\Documents\PhD Work\Defect
    Diffusion\defect1.jpg"

im1 = imread(imageadress)

no_rows, no_cols = shape(im1)[0:2]
large_dim = int(sqrt(no_rows**2+no_cols**2)+100)
bigim = zeros((large_dim, large_dim))
im3 = dot(im1[...,:3],[0.299,0.587,0.144])
#im3 = im1
bigim[(large_dim-no_rows)/2.0:large_dim-(large_dim-no_rows)
    /2.0,(large_dim-no_cols)/2.0:large_dim-(large_dim-no_cols
    )/2.0] = im3

y,x = ogrid[-large_dim/2.0:large_dim-large_dim/2.0, -
    large_dim/2.0:large_dim-large_dim/2.0]
mask = x*x + y*y <= ((min([no_rows, no_cols])/2.0)-5)**2
```

```
mask2 = mask==False
bigim[mask2] = 0.0
mask3 = zeros(shape(mask))
mask3[mask==True]=1
avX = sum(mask, axis= 0)
avX[avX ==0] = 1.0


figH,figW  = 7.5,5.5
b,l,r = 0.1,0.1,0.05
liH = 0.25
uiH = figW*(1-l-r)/figH
fig = figure('image',figsize= (figW,figH))
fig.clf()
axT = fig.add_axes([l,b+liH,1-l-r,uiH])
axB = fig.add_axes([l,b,1-l-r,liH])
axT.set_xticklabels([])
bigim2 = copy(bigim)
imageplot = axT.imshow(bigim2,'gray')
spectrum, = axB.plot(sum(bigim2,axis=0))#/avX)


axT.set_xlim(0,large_dim)
axB.set_xlim(0,large_dim)
show()
draw()

def rotateimage(angle, bigim=bigim2,mask = mask3):
        bigim2 = imrotate(bigim,angle)
        avX = sum(imrotate(mask,angle)/255.0,axis=0)
        avX[avX==0]=1.0
        ydata = sum(bigim2,axis=0)#/avX
        spectrum.set_ydata(ydata)
        imageplot.set_data(bigim2)
        draw()
        return max(ydata[len(ydata)/2.0-40:len(ydata)
            /2.0+40])
theta = arange(0,180,1)
thetarad = theta*pi/180.0
```

```
intensity = array([])
for i in theta:
        maxval =rotateimage(i)
        intensity= append(intensity ,maxval)
        #pause(0.001)

figure()
plot(theta,intensity)
out = column_stack([theta,intensity])
savetxt('C:\Users\George Wells\Documents\PhD Work\Defect
    Diffusion\AngleProfile1.txt',out)
```